MODELING TREACHER COLLINS SYNDROME AND DIRECTED DIFFERENTIATION OF BROWN ADIPOCYTES FROM HUMAN PLURIPOTENT STEM CELLS

by

JOHN W. AVERY III

(Under the Direction of Stephen Dalton)

Human pluripotent stem cells (hPSCs) are powerful tools to aid in the interrogation of the mechanisms of pathology of developmental disorders as well as modeling the development of embryonic and adult tissues. In this work, we attempted a patient-specific disease in a dish model of the craniofacial disorder Treacher Collins Syndrome (TCS) and the directed differentiation of brown adipocytes from hPSCs. The TCS model was unable to replicate the expected phenotype of reduced neural crest cell numbers or migratory potential. This shortcoming has been putatively attributed to reducing and high antioxidant conditions of the culture medium. Modulating brown adipocyte activity in humans has become an attractive therapeutic target for obesity and related metabolic disorders such as type 2 diabetes. Murine models suggest the brown adipose organ is capable of significant changes in body mass and circulating levels of insulin and glucose. Methods to interrogate human brown adipocyte functionality have been based on adult primary cells or overexpression systems. Here we report a robust and efficient chemically-defined method to differentiate human pluripotent stem cells into brown adipocytes through a developmentally appropriate paraxial mesoderm intermediate. These adipocytes display characteristics of mature brown adipocytes including marker expression, responsiveness

to stimulation, enhanced metabolic activity, thermogenic capacity, lipolysis, and utilization of fatty acids. These cells are capable of being maintained in culture for several weeks, are amenable to passage, and upon transplantation in mice can give rise to adipose depots that maintain both morphological and functional properties. We propose that these cells are appropriate for modeling brown adipocyte development in vivo, elucidating basic biological cell fate decisions and branch points and as a platform for high-throughput drug screening to identify putative therapeutic targets to combat obesity and related disorders.

INDEX WORDS: Brown adipocytes, human pluripotent stem cells, induced pluripotent stem cells, neural crest cells, paraxial mesoderm

MODELING TREACHER COLLINS SYNDROME AND DIRECTED DIFFERENTIATION OF BROWN ADIPOCYTES FROM HUMAN PLURIPOTENT STEM CELLS

by

JOHN W. AVERY III

BA, University of Georgia, 1997

BS, Kennesaw State University, 2007

MS, University of Georgia, 2010

A Dissertation Submitted to the Graduate Faculty of The University of Georgia in Partial Fulfillment of the Requirements for the Degree

DOCTOR OF PHILOSOPHY

ATHENS, GEORGIA

2017

MODELING TREACHER COLLINS SYNDROME AND DIRECTED DIFFERENTIATION OF BROWN ADIPOCYTES FROM HUMAN PLURIPOTENT STEM CELLS

by

JOHN W. AVERY III

Major Professor:	Stephen Dalton
Committee:	Richard Steet
	Takahiro Ito
	Amar Singh

Electronic Version Approved:

Suzanne Barbour
Dean of the Graduate School
The University of Georgia
August 2017

DEDICATION

This work is dedicated to my parents, John and Carolyn Avery, my wife, Heather Avery, my sister Leslie Avery, my best friends, John Keating and Jason Morris, and my children Cope, Elliot and Isla Avery. To my parents, you gave me the freedom to become whatever I wanted to and had enough knowledge and courage to let that play out. To my wife, you are the glue that holds it all together and the wheels that keep the whole thing rolling, without you I would go nowhere. To my sister, you always had my back- no matter what. To John and Jason, you have been constant reminders of what one is capable of accomplishing. To Cope, Elliot and Isla you are my source of inspiration- you allow me to see the world anew and as it may be. Thank you all.

ACKNOWLEDGEMENTS

I would like to thank Dr. Stephen Dalton for his direction and tireless belief that this story could be realized; I am sure that if we had known how difficult this project was going to be from the outset, we would have had second thoughts. To my lab mates, thank you for your expertise, your ideas, but most of all your levity. I would like to single out Liang Zhang for being and excellent mentee- making me a better mentor and scientist in the process.

TABLE OF CONTENTS

Page

LIST OF TABLES

Page

LIST OF FIGURES

Page

CHAPTER 1

INTRODUCTION AND LITERATURE REVIEW

PREFACE

In mammalian stem cell biology parlance, there is a tripartite hierarchical classification system based on the cells' competencies to develop into different cell types: totipotent, pluripotent, and multipotent (Figure 1.1). Totipotent stem cells have unlimited differentiation potential- that is they have the capacity to develop into every cell that forms the embryo (and subsequently, an adult) as well as the extra-embryonic placenta that provides nutrient, waste and gas exchange for the developing embryo. Potency becomes restricted as cells progress through development. Thus, pluripotent cells only have the capacity to give rise to the three embryonic germ layers: endoderm (organs, such as stomach, gastrointestinal tract and lungs); mesoderm (connective tissue, bone, muscle, adipose, and urogenital tract); ectoderm (hair, teeth, skin, and nervous tissue) (Figure 1.1). Critically, pluripotent cells can be isolated from the inner cell mass (ICM) (Figure 1.1) and maintained in vitro as embryonic stem cells (ESCs)(Rossant, 2008). The utility of potency is important to researchers, but so is the ability to self-renew, or the process of deriving more stem cells from parent stem cells, without loss of potential (Shenghui et al., 2009). In contrast, multipotent stem cells are lineage restricted and have limited self-renewal capacity. Each of these cell types play important roles in biological and clinical research.

Human ESCs are critical to biomedical research for a number of reasons. Many human diseases result from defects in a single cell type and ESCs can a theoretical unlimited source of

cell type for replacement therapies. Moreover, basic mechanisms of disease may be uncovered through in vitro differentiation using genetic knockdown, knockout, and knock-in experiments not possible in a human clinical setting. Critically, advances in cellular manipulation techniques mean that toti- and pluripotent stem cells can also be generated from mature cells by reprogramming (see Figure 1.2 for detailed descriptions) (Smith et al., 2016). Therefore, it is now possible to derived pluripotent stem cells from patients that may then be utilized to elucidate molecular mechanisms of disease for particular patients or groups of patients. This method of PSC derivation is called induced-pluripotentcy and will be discussed in detail in subsequent sections. Patient-derived pluripotent stem cells are extremely beneficial in disease states where symptoms are multifactorial and may exist of a spectrum of severity.

The work described herein focuses on the use of human ESCs and induced pluripotent stem cells (iPSCs) to examine the pathological mechanisms of Treacher Collins Syndrome (TCS) and directed differentiation of brown adipocytes. The basic biology of the human disease and brown adipocyte development and activity in humans are separately not well understood. Data suggest that TCS is a consequence of defects in neural crest cells (NCCs), which arise from the ectoderm. Brown adipocytes arise from a mesodermal cell origin but the derivation of these cells reliably from human PSCs has proven challenging. Because mature NCCs share much in common with mesenchymal stem cells, and, in fact, transit through a MSC-like phenotype on their way to giving rise to osteocytes, chondrocytes, and adipocytes (Menendez et al., 2013; 2011), we initially attempted to derive brown adipocytes from NCCs. The failure of which underscored the difficulty in directly differentiating brown adipocytes from hPSCs. However, hPSCs are an appropriate platform for interrogating the mechanism of disease and the basic biology of cell fate. Furthermore, the eventual success of the brown adipocyte platform may

generate more than basic understanding of brown adipogenesis, it may well serve as a drug-screening platform for putative therapeutic compounds that enhance brown adipocyte activity. The use of iPSCs may also uncover the patient-specific molecular causes as to why there is a large disparity among brown adipose tissue activity between high and low BMI patients.

Section 1. Neural Crest Cells and Treacher Collin Syndrome

Neural Crest Cells

Neural crest cells (NCCs) are a population of multipotent stem cells that emanate from the developing ectoderm during neural tube closure. NCCs emerge from the neural plate border between the neural plate and non-neural ectoderm as the neural tube closes. These cells migrate throughout the early embryo, eventually contributing to a wide range of cell types including bone, cartilage, adipose tissue, adrenal medulla, peripheral nervous system, melanocytes, and smooth muscle. Defects associated with the survival, migration or differentiation of these cells underpins the development of a broad class of diseases known as neurocristopathies. The molecular basis for neurocristopathies is poorly understood, in part because of limitations associated with the models used in their characterization. The recent development of iPSC technology combined with the availability of patient-derived cells opens up new opportunities to address the molecular basis of neurocristopathies. Technologies that allow iPSCs to be generated through cell reprogramming (Takahashi et al., 2007; Yu et al., 2007) have led to the development of powerful tools that can be used to model human disease and as platforms for drug discovery (Grskovic et al., 2011; Trounson et al., 2012). Disease modeling using iPSCs offers advantages over more traditional animal-based models and has tangible potential to advance molecular understanding of diseases that are poorly understood (Ebert et al., 2012). Most notably, patient-

derived iPSC models are more likely to completely and faithfully recapitulate the human disease state, particularly in cases where the disease is cell-autonomous. Access to patient-derived cells also allows for potential differences between individuals to be assessed. Induced PSCs are also well suited to modeling disease-related events that occur during development because iPSCs can be differentiated to a wide range of cell types by tightly controlled protocols. If disease progression is associated with a specific developmental defect, differentiation models should capture this and facilitate a more detailed molecular understanding that may then lead to new pathways of therapeutic intervention.

Neural Crest Cells and Neurocristopathies

Neural crest cells are a unique cell type that arise from the neural plate border of the developing neural tube and then migrate to diverse targets throughout the embryo where they differentiate and incorporate into functional tissue (Achilleos and Trainor, 2012; LaBonne and Bronner-Fraser, 1998; Le Douarin et al., 2008). In the human, NCCs are evident in the developing embryo during the third to fifth weeks of pregnancy, residing within the neural folds that marginate the neural plate from the non-neuroectoderm and the neuroectoderm (Figure1.1). Upon fusion of the neural folds, which ultimately yields the tube that will become the central nervous system, NCC undergo an epithelial to mesenchymal transition, delaminating from the roof plate of the newly form neural tube (Etchevers et al., 2006). NCCs then migrate throughout the body, where they differentiate into a variety of cell and tissue types. Defects associated with the emergence of NCCs from the neural plate border, their migration throughout the embryo, or their differentiation can contribute to a broad spectrum of defined diseases or syndromes, collectively known as neurocristopathies.

NCCs originate from four discrete segments (cranial, cardiac, vagal and trunk) along the neural tube's rostro-caudal axis. Figure 2.1 illustrates the corporal locations that NCCs are targeted to as they migrate away from different regions of the neural tube. Several prevalent neurocristopathies are listed that have specific relationships with the different populations of NCCs. Most of these arise from improper specification of neural crest cells, defective migration, compromised proliferation and/or decreased NCC survival. With relevance to TCS, cranial NCCs give rise to the bulk of the bone and cartilage that form scaffolding of the head and face and contribute to ganglia, smooth muscle, connective tissue and even pigment cells (Achilleos and Trainor, 2012).

The ultimate tissue identity at a particular site of differentiation is the product of an admixture of local extrinsic factors in the local embryonic microenvironment in conjunction with cell-intrinsic properties that tune the resident NCC responsiveness to particular cellular signals (Achilleos and Trainor, 2012; Hall, 2008). As a result, NCC migratory pathways and their fates are driven by the surrounding tissue as they develop within the neuroepithelium, delaminate from the roof plate of the neural primordium and from the ectoderm, mesoderm, and endoderm with which the NCCs interact during their migration (Etchevers et al., 2006).

Because NCC identity and migration are linked to the extrinsic signals from the layers with which they migrate through, it is feasible that patient-derived iPSCs differentiated to NCCs may not behave precisely as they might *in vivo* due to the lack of extrinsic factors produced by surrounding tissues. Many neurocristopathies, however, are cell autonomous disorders and manifest due to specific issues solely proceeding failures within the NCCs themselves. For example, problems with NCC differentiation appear to lead to a discrete set of developmental abnormalities such as dysmorphic cranial shape, mid-face hypoplasia, seizures and mental

retardation, fitting into a category known as craniosynostosis (Grskovic et al., 2011; Le Lièvre and Le Douarin, 1975; Trounson et al., 2012); whereas Treacher Collins Syndrome, marked by craniofacial features such as small noses, jaws, and ears, as well as cleft palate, appears to be a result of too few NCCs populating their target tissue as a consequence of a poor proliferation and survival (Ebert et al., 2012; Trainor, 2010). These conditions manifest at the same period of development, but the developmental problems presented are clinically discrete. Because NCC generation is transient during just a short window during development, a pool of sufficient, properly functioning NCC cells are critical to normal development.

The importance of understanding craniofacial defects, such as those brought about by TCS, cannot be overstated: fully one-third of all congenital defects involve craniofacial abnormalities (Achilleos and Trainor, 2012; LaBonne and Bronner-Fraser, 1998; Le Douarin et al., 2008; Trainor, 2010). The Centers for Disease Control and Prevention estimate that the lifetime healthcare cost of patients of cleft lip/palate alone approach $1 billion. It is impossible to quantitate the hardships both patients and their families encounter due to a lifetime of functional, aesthetic, and social consequences of craniofacial abnormalities (Trainor, 2010). Augmenting our understanding of the basic etiology and pathogenesis of Treacher Collins syndrome will not only help us comprehend, prevent, or treat this disease, but it may also have wide-ranging implications for congenital, craniofacial birth defects in general.

Treacher Collins Syndrome (TCS)

TCS is a rare condition affecting 1:50,000 live births (Trainor, 2010). TCS was initially described by Treacher Collins in 1900 (Collins, 1900) and clinically presents with a range of characteristics (Figure 2.5) including hypoplasia of the facial bones, cleft palate, external and

middle ear anomalies and defects in brain development (Trainor, 2013; 2010). Current treatment strategies for TCS patients are related to clinical management. Life threatening complications related to breathing and feeding problems are immediately apparent in the neonate. Excessively shortened lower jaws (micrognathia) impede feeding and tongue obstruction of the hypopharynx often requires emergency tracheostomy to maintain adequate pulmonary ventilation. Additionally, when specific developmental milestones have been reached, extensive reconstructive surgeries are implemented in attempt to restore the structure of the face. Management of the hard and soft tissues typically requires multiple surgeries and initially, depending on severity, palatal clefting is corrected in the earliest years of life (Cohen et al., 1995; Milligan et al., 1994; Poswillo, 1975; Teber et al., 2004; Trainor, 2010). Most TCS patients also require bone conducting hearing aids to permit hearing.

Multiple studies indicate that the majority of TCS cases can be attributed to mutations in the *TCOF1* gene on chromosome 5 (Trainor, 2010). *TCOF1* encodes the serine/alanine-rich nucleolar protein, treacle (Jabs et al., 1991; 1993; Sakai and Trainor, 2009; Trainor et al., 2008a; Wise et al., 1997). The *TCOF1* gene comprises 28 exons and can be differentially spliced to generate up to 6 known transcript variants (Cynthia Isaac, 2000; Dixon et al., 1997; Wise et al., 1997). Over 200 different mutations have been identified in *TCOF1* and many of these have implicated roles in TCS pathology including deletions, insertions, missense, nonsense and splicing mutations (Bowman et al., 2012). Deletions of 1-41 nucleotides are the most common and only exon 24 has been reported as a mutational hot spot with a common 5-bp deletion occurring with a frequency of 17% (Splendore et al., 2005). Almost half of all TCS cases have no previous family history and arise from *de novo* mutations (Jones et al., 1975; Trainor, 2010). Diagnosing TCS may often be confounded by the fact that a high degree of both inter- and intra-

familial phenotypic variations are commonly observed (Dixon et al., 1994; Marres et al., 1995). In many cases, TCS phenotypes are slight and go undiagnosed until an offspring or sibling displaying a more severe phenotype is diagnosed (Trainor, 2010).

The vast majority of mutations found within *TCOF1* result in the introduction of a premature-termination codon into the protein, suggesting that haploinsufficiency of treacle is mechanism underlying TCS (Edwards et al., 1997). Mouse models of TCS have demonstrated that normal *Tcof1* expression is critical to the formation, proliferation and survival of NCCs (Dixon et al., 2000; 2006). These studies, in conjunction with Gonzales et al. established that treacle participates in ribosome biogenesis and maturation, and that defects in *Tcof1* result in a diminished pool of mature ribosomes and compromised protein synthesis (Gonzales, 2005). The current view of TCS is that compromised ribosome biogenesis contributes to reduced numbers of emerging NCCs at the time of neural tube closure due to decreased proliferation and increased apoptosis (Dixon et al., 2006; Gonzales, 2005; Trainor, 2010). Jones et al. demonstrated that *Tcof1* haploinsufficiency in mice provokes p53-dependent apoptosis within the neuroepithelium of the neural crest, thus diminishing the NCC progenitor pool (Jones et al., 2008a).

In keeping with the hypothesis that impaired ribosome stress responses drive NCC loss, Jones et al. developed compound *Tcof1+/-:Trp53+/-* mice in which impaired p53 production lead to an improvement of the TCS phenotype in 75% of embryos (Jones et al., 2008a). Indeed, *Tcof1* haploinsufficient mice present with typical TCS-like loss of proper craniofacial architecture, and this feature was amended by diminution of p53 in the compound haploinsufficient *Tcof1:Trp53* mice (Figure 1.4a) (Jones et al., 2008a). It remains to be determined whether these same pathways are triggered and subsequent to impaired ribosome biogenesis in human TCS.

Both cell proliferation and cell survival reductions correlate to reduced mature ribosome production in this mouse model (Dixon et al., 2006) (Figure 1.4d), and in further studies, siRNA knock down of treacle in HeLa cells demonstrated a reduction in processed RNA (Figure 1.5a) (Valdez et al., 2004). Ribosome biogenesis is monitored by surveillance systems that constantly check levels of key source materials to ensure that a cell can meet the high demands of cell growth and division (Figure 1.5b) Ribosome biogenesis encompasses transcription, modification, and processing of rRNA, production of ribosomal proteins, and coordinated association of ribonucleoprotein particles to produce ribosomes (Deisenroth and Zhang, 2010a; 2011). Three key checkpoints are utilized wherein deficiencies in any may trigger a p53-dependent nucleolar stress response. These checkpoints are discrete phases of ribosome biogenesis: 1) rRNA transcription, 2) processing into mature rRNA species, 3) and assembly of ribonucleoprotein complexes and the small (40S) and large (60S) subunits (Deisenroth and Zhang, 2010a). Impaired rRNA biogenesis results in free ribosomal protein subunits, that have been shown to sequester Mdm2, which under normal conditions negatively regulate p53 through direct binding and masking of the DNA binding domain or by acting as an E3 ubiquitin ligase thereby preventing ubiquitin-mediated p53 destruction and leading to increased p53 activity and cell cycle arrest and/or apoptosis (Deisenroth and Zhang, 2011; Gazda and Sieff, 2006; Narla and Ebert, 2010).

Section 2. Obesity, the Adipose Organs and Adipogenesis

The meteoric rise in global obesity has driven a major push to understand human adipogenesis. Two principal adipose tissues exist: white adipose (WAT) and brown adipose (BAT). The discovery that humans possess active BAT has intensified the effort to fully

understand this tissue and its origins in part because of its potential in understanding and treating obesity. The utilization of BAT as an anti-obesity and metabolic disorder therapy holds great promise because of its ability to oxidize and thus clear serum triglycerides and glucose, resulting in heat production. Murine models demonstrate that increased BAT activity leads to resistance against metabolic diseases, such as obesity and type 2 diabetes. Adipocyte generation from mPSCs, however, has limited reproducibility and applicability to human cells so we propose to develop a model for human brown adipogenesis using hPSCs.

Obesity and Adipose Tissues

Obesity represents a major risk factor for increased morbidity and mortality. Obesity is difficult to clinically define due to disparities among metrics; however, it is characterized by the inequitable accumulation of excess white adipose tissue (WAT) in corporal deposits. Obesity is associated with a myriad of negative health outcomes such as type 2 diabetes, heart disease, insulin resistance, hyperglycemia, dyslipidemia, hypertension and many types of cancer (Billon et al., 2008; Bornfeldt and Tabas, 2011; GBD 2015 Obesity Collaborators, 2017; Harms and Seale, 2013; Lloyd-Jones et al., 2009). In 2012, 35.4% of adults and 17% of children in the United States were categorized as obese (GBD 2015 Obesity Collaborators, 2017; Gesta et al., 2008; Ogden et al., 2012; 2013). The worldwide prevalence of obesity has virtually doubled between 1980 and 2008 and currently affects over 500 million individuals (GBD 2015 Obesity Collaborators, 2017; Gesta et al., 2008; Perez Rodrigo, 2013; Rueda-Clausen et al., 2013). Critically, obesity has a major impact on the development and outcome of non-communicable diseases, which by 2020 are expected to cause 7 out of every 10 deaths in developing countries alone (Boutayeb and Boutayeb, 2005; GBD 2015 Obesity Collaborators, 2017; Gesta et al.,

2008; Ibrahim, 2010). Thus the burden of obesity is a global public threat. Improved knowledge of all aspects of adipose biology will be required to develop therapeutics aimed at countering this hazard.

Adipose tissue is composed of specialized cells whose primary role is energy homeostasis. In mammals, at least two types of adipocytes and their associated depots exist and function in opposing roles: white adipose tissue (WAT) manages triglyceride storage and mobilization for fasting energy needs, while brown adipose tissue (BAT) utilizes free fatty acids liberated from WAT to power an uncoupled process of cold or diet induced thermogenesis (Billon et al., 2008; Cristancho and Lazar, 2011; Harms and Seale, 2013; Yamamoto et al., 2010). Both tissues are essential to human health and exist in different depots. In humans, WAT is dispersed throughout the body with major intra-abdominal depots around the omentum, intestines, and perirenal areas, as well as in subcutaneous depots in the buttocks, thighs, and abdomen (Cannon and Nedergaard, 2004; Gesta et al., 2008). WAT can also be found in the retro-orbital space, on the face and extremities, and within the bone marrow (Figure 1.6, right) (Gesta et al., 2008; Lee et al., 2013a). Different adipose depots are responsive to different signals. For example, adipose tissues in the breasts and thighs are responsive to sex hormones, whereas adipose tissues of the neck and upper back are more responsive to glucocorticoids (Cannon and Nedergaard, 2004; Gesta et al., 2008; Ibrahim, 2010; Lee et al., 2013a), possibly owing to differential developmental origins (Bonnot, 1908; Cristancho and Lazar, 2011; Rasmussen, 1922; Yamamoto et al., 2010). In human fetuses and newborns, BAT depots compose a larger percentage of soft tissue composition than in adults and are found in axillary, cervical, perirenal, and periadrenal regions, whereas adult BAT is typically found in the cervical, supraclavicular and paraverterbral regions (Figure 1.6, left and inset)(Cannon and Nedergaard,

2004; Gesta et al., 2008; Lee et al., 2013a). Brown adipocytes differ from white adipocytes in that the latter are characterized by their round appearance, a large single lipid compartment (unilocular), and peripheral nuclear localization. In contrast, brown adipocytes are more polygonal in shape, smaller in size, maintain a central nucleus, hold numerous small lipid compartments (multilocular), and contain a multitude of well-developed mitochondria that occupy the vast majority of the cytoplasmic space (GARCIA et al., 2004; Hany et al., 2002; Lee et al., 2013a; 2011; Saito et al., 2009). Most importantly, brown adipocytes contain uncoupling protein 1 (UCP-1) within the inner membrane of their numerous mitochondria, which serves to uncouple oxidative phosphorylation and release energy in the form of heat as a protective measure against hypothermia (Cannon and Nedergaard, 2004; Cypess et al., 2009; Lee et al., 2013a). Although the tissue had been described in the adult human in the early 1900s (Bonnot, 1908; Casteilla et al., 2008; Rasmussen, 1922), BAT was thought to be inactive or insignificant outside of early infancy (Lee et al., 2013a; Sanchez-Gurmaches and Guertin, 2013). However, recent work using PET-CT scans have shown that BAT is present and active in human adults (GARCIA et al., 2004; Hany et al., 2002; Lee et al., 2011; Saito et al., 2009). Interestingly, and with possible clinical relevance, an inverse correlation between BAT amount/activity and body mass index (BMI) has been demonstrated (Cypess et al., 2009). These findings have generated hope for new potential therapeutic targets in the fight against obesity and obesity related diseases.

Murine and human fat deposits share some similarities, but differ in many of their characteristics, not only in their location but also in their activity, composition, and plasticity (Casteilla et al., 2008; Sanchez-Gurmaches and Guertin, 2014a). Research efforts to reveal preadipocyte and mature adipocyte identity, location, and function have largely been focused on

murine models. Further complicating matters, WAT depots within an individual have been shown to be heterogeneous in composition and function (Sanchez-Gurmaches and Guertin, 2013; 2014a). These depots are admixtures of not only of mature adipocytes but also of preadipocytes, fibroblasts, nerves, vascular cells, macrophages, and other cell types (Bornfeldt and Tabas, 2011; Harms and Seale, 2013; Lloyd-Jones et al., 2009; Sanchez-Gurmaches and Guertin, 2013).

Further still, there are many reports of disparities in lipogenic activity, cell dynamics, proliferative and differentiation capacity, as well as gene expression that occur in intra-WAT depots within both mice and humans (Edens et al., 1993; Gesta et al., 2006; Ogden et al., 2012; 2013; Rehrer et al., 2012; Sackmann-Sala et al., 2012; Sanchez-Gurmaches and Guertin, 2013; 2014a; Tchkonia et al., 2007; 2005; Yamamoto et al., 2010). Adding further complexity, a third type of adipocyte has been described that is found in WAT depots but is capable of assuming a BAT-like identity. This cell type is referred to by several monikers, such as a "brite" (contraction of BRown and whITE), "beige", "inducible brown," or "recruitable brown" adipocyte (Perez Rodrigo, 2013; Rueda-Clausen et al., 2013; Sanchez-Gurmaches and Guertin, 2013). These cells are morphologically indistinguishable from their neighbors within intra-WAT deposits; however, upon activation (in-vivo cold exposure or through β-adrenergic stimulation) these cells assume a more classical brown morphology and begin expressing UCP-1. There is considerable debate as to the origin of these brite cells and whether they significantly contribute to thermogenesis. The two opposing principal viewpoints are that the cells arise through trans-differentiation of resident white adipocytes (Figure 1.7 left) or from a population of distinct preadipocytes that reside in certain WAT depots (Figure 1.7 right) (Rosenwald and Wolfrum, 2014). It is clear that we do not yet have the data to fully appreciate the complexity of adipocyte

or adipose deposit character. This fact is also grossly manifested by the paucity of human data delineating the developmental origins of adipose tissue and adipogenesis.

Adipogenesis

The current paradigm based on murine models posits that adipogenesis occurs in two stages: 1) a commitment stage, wherein mesenchymal stem cells (MSCs) commit to a preadipocyte fate and 2) a terminal differentiation stage involving the maturation of the preadipocytes into functional adipocytes (Cristancho and Lazar, 2011). The term preadipocyte is applied retrospectively as they are defined as cells that are restricted to becoming adipocytes and must be confirmed upon differentiation- they do not spontaneously undergo terminal differentiation in the absence of exogenous adipogenic stimuli (Cristancho and Lazar, 2011). The process of adipocyte terminal differentiation occurs primarily through epigenomic activation of peroxisome proliferator-activated receptor-γ (PPARγ) and its coordination with CCAAT/enhancer-binding protein (C/EBP) transcription factors (Cristancho and Lazar, 2011; Lefterova et al., 2008; Nielsen et al., 2008).

The process of preadipocyte commitment is less well understood. The early steps of generation and commitment of MSCs to the preadipocyte lineage remain largely unknown (Billon and Dani, 2011; Billon et al., 2008). While MSCs are generally considered products of the mesoderm, populations of MSCs do arise from the ectoderm. The structures that comprise the head and neck, such as connective tissue, vascular smooth muscle, tendons, dermis, odontoblasts, cartilage, and bone arise from mesenchymal precursors of neural crest origin (Billon and Dani, 2011; Billon et al., 2008; Dupin et al., 2006; Le Douarin and Dupin, 2003; Le Douarin et al., 2004). Moreover, Morikawa et al. identified MSCs in the bone marrow (BM-

MSCs) from adult transgenic mice encoding neural crest-specific P0-Cre/EGFP and Wnt1-Cre/EGFP. These EGFP-positive MSCs formed spheres that expressed neural crest stem cell genes and were capable of differentiating into neurons, glial cells, and myofibroblasts, suggesting that bone marrow resident MSCs in adult mice have at least two developmental origins: mesoderm and ectoderm (Morikawa et al., 2009). Billon et al. 2007, utilized Sox10-Cre/YFP transgenic mice to label neural crest-derived cells (mesodermal cells lack Sox10 expression). YFP-labeled adipocytes were detected in adipose tissue in the head between the salivary gland and ear. However, adipocytes in other body locations were YFP negative, demonstrating that a subset of facial adipocytes originate from the neural crest and not the mesoderm (Billon et al., 2007; Majka et al., 2011). Takashima et al. 2007, showed similar results using Sox1-Cre/YFP murine ESCs (mESCs) and transgenic mice, however, their data suggest that an initial wave of MSCs originate from the NC, but that this population does not proliferate beyond the neonatal stage and is eventually replaced by MSCs derived from the mesoderm (Takashima et al., 2007). It has also been suggested that although bmMSCs do not enter the circulation, a population of hematopoietic cells with mesenchymal characteristics traffic outside of the marrow and home to other tissues. It is possible that some adipocytes may arise from marrow progenitors that then home to adipose depots and subsequently undergo preadipocyte commitment and subsequent adipocyte maturation (Crossno et al., 2006; Majka et al., 2011; Sera et al., 2009; Tomiyama et al., 2008).

Brown adipocytes are thought to be generated via two possible mechanisms (Figure 1.8). The first mechanism is based on evidence generated through murine genetic fate mapping, microarray analysis, and lineage tracing. Using genetic fate mapping, Atit et al. demonstrated that cells of the central dermomyotome (paraxial-mesodermal somatic structure of the vertebrate

embryo that gives rise to the dermis, dermatome, and muscle, myotome) that express homeobox transcription factor Engrailed-1 (En1) also gave rise to intrascapular BAT. Timmons et al. (Timmons et al., 2007) established that brown adipocytes originated from a distinct lineage from white adipocytes by using microarray analysis to compare and contrast global gene expression patterns in white and brown preadipocytes. Brown preadipocytes displayed a transcriptional signature enriched for members of the myogenic regulatory factor (MRF) family, including Myogenic factor 5 (*Myf5*), Myoblast determination protein (*MyoD*) and myogenin. These data were further supported by Seale et al. (Seale et al., 2008) using Myf5-Cre/YFP mice to show that skeletal muscle cells and brown adipocytes in intrascapular or perirenal adipose tissue expressed YFP; whereas, white adipocytes were YFP negative in all other depots (Majka et al., 2011). The genetic tracing experiments performed by Seale et al. did not establish that a unique $Myf5^{+}$ cell gave rise to both skeletal muscle and brown adipocytes. However, the authors suggest that a bipotnet muscle-brown fat precursor may exist as they were able to differentiate both a myoblast cell line and primary mouse myoblasts, isolated from postnatal skeletal muscle, into brown adipocytes in culture through ectopic expression of PR domain 16 (PRDM16) (Seale et al., 2008). They further established that PRDM16 acted as a positive regulator of brown adipogenesis through direct physical interaction and subsequent activation of the transcriptional activity of PPARγ and PPARγ coactivator-1a (PGC-1α) (Seale et al., 2009; 2008; 2007). The second mechanism occurs through the aforementioned trans-differentiation of mature unilocular white adipocytes to multilocular brown-like adipocytes, which was originally observed in rodent models exposed to chronic low temperature (Murano et al., 2005) or treatment with β3-adrenergic agonists (Cinti, 2009; Himms-Hagen et al., 2000). However, further studies showed that although these brown adipocytes are functionally thermogenic, they do not display signature

brown adipocyte gene markers such as *PDRM16* and that they continue to express white adipocyte markers (Petrovic et al., 2010). There is as of yet, no definitive agreement among the adipocyte research community as to which intrinsic and extrinsic factors lead to the "browning" process, what serves as a brite/beige progenitor, or if this process is significant in humans (Harms and Seale, 2013).

Developing human cellular models to understand brown fat adipogenesis. Both white and brown adipocytes share a common transcriptional program driven by PPARγ and C/EBP transcription factors (Figure 1.8) (Billon and Dani, 2011; Lefterova et al., 2008; Nielsen et al., 2008). PPARγ has so far been shown to be obligatory for the development of all adipocytes and is considered the master regulator of adipogenesis (Barak et al., 1999; Giralt and Villarroya, 2013a; Rosen and MacDougald, 2006). The C/EBP factors, two of which are critical- C/EBPα and C/EBPβ, sustain and support PPARγ: C/EBPα functions to maintain PPARγ expression, and both C/EBPα and C/EBPβ cooperatively regulate gene transcription to initiate, promote and maintain the differentiated state of adipocytes (ie, lipid metabolism, glucose metabolism, and insulin sensitivity) (Farmer, 2006; Giralt and Villarroya, 2013b; Mueller, 2013). C/EBPβ may be more critical to brown rather than white fat programs as a loss of C/EBPβ is associated with defective thermogenesis, whereas increasing amounts of C/EBPβ in white fat cells supports a brown fat transcriptional profile in some adipocytes (Carmona et al., 2005; Harms and Seale, 2013; Kajimura et al., 2009; Karamanlidis et al., 2007; Tanaka et al., 1997). As mentioned, the apparent molecular switch that differentiates brown from white adipogenic programs is PRDM16. PRDM16 binds to and coregulates C/EBPβ, PPARγ, and PGC-1α to stimulate brown fat–specific gene induction (Giralt et al., 2011; Hondares et al., 2011; Kajimura et al., 2009; Seale et al., 2007). Through positive feedback, PGC- 1α in turn coactivates PPARγ and is central

to the regulation of mature brown adipocyte functions such as mitochondrial biogenesis, oxidative metabolism, and thermogenesis (Barbera et al., 2001; Giralt and Villarroya, 2013b; Lin et al., 2005; Puigserver et al., 1998). PGC- 1α is also implicated as a critical factor in the browning process as many of the some 50 molecules identified to act in adipogenesis induce or repress the browning program through modulation of PGC-1α activity (Giralt and Villarroya, 2013b; Wu et al., 2013).

The developmental patterns of both brown and white adipose tissues are quite different, regardless of their shared transcriptional program. In mice and humans alike, brown adipose develops first during late gestation and is fully mature at birth when the requirements for non-shivering thermogenesis are greatest (Cannon and Nedergaard, 2004; Moulin et al., 2001; Nedergaard et al., 1986). White adipose development, on the other hand, occurs post-natally (Moulin et al., 2001). It stands to reason that the progenitors for these adipocytes are of different origin. Lineage tracing experiments (Table 1.1) support a shared origin between brown adipocytes and skeletal muscle, specifically those cells that are Myf5+ (Timmons et al., 2007). In addition, brown adipose has been demonstrated to share other expression similarities to skeletal muscle, such as paired box 7 (Pax7), which, along with paired box 3 (Pax3), are transcription factors that cooperate with Myf5 to drive myogenesis (Lee et al., 2013b; Lepper and Fan, 2010; Sanchez-Gurmaches and Guertin, 2014b). In fact, in the experiments performed by Lepper et al. (Lepper and Fan, 2010), using an inducible Pax7 reporter, the authors were able to demonstrate that the developmental divergence between BAT and muscle in mice occurs between E10.5 to E12.5 (Lee et al., 2013b).

Recent data however, have muddled the distinction between Myf5+ derived adipocytes. Sanchez-Gurmaches et al. (Sanchez-Gurmaches et al., 2012) demonstrated that a subset of WAT

arose from Myf5+ precursors in mice with conditional PTEN (phosphatase and tensin homolog) deletion (Figure 1.9). In preadipocyte differentiation, insulin is used to activate the PI3K (phosphatidylinositol 3-kinase) signaling pathway and stimulate adipogenesis (Cannon and Nedergaard, 2004; Rosen and MacDougald, 2006). PI3K activity is negatively regulated by *PTEN* and its conditional deletion in mice led to a concomitant increase in BAT and a drastic redistribution of WAT, with some WAT depots arising from the Myf5+ lineage (Figure 1.9a). These Myf5+ depots did not display characteristic brown adipocyte expression patterns measured by mRNA expression Figure 1.9b). The authors did not isolate the My5+ WAT cells to determine if they could be induced to become brite cells, and they acquiesce to the fact that it cannot be ruled out that given appropriate stimuli, these cells might be capable of brown-like activity. Thus, Myf5 cannot yet reliably be used to determine functionality or identity of adipocytes. Although these data indicate that WAT may be derived from Myf5+ or Myf5- lineages, no evidence exists that supports classical brown adipogenesis from non-Myf5 origins.

Despite a number of tracing studies using different markers (Table 1), a definition for proper preadipocytes distinctive to types of adipose tissue remains to be determined. And there is yet to be a defined developmental path delineating brown, white, or brite adipocytes from one another. It is possible that the $Myf5^{+}$ lineage has the capacity to selectively differentiate into the BAT, while $Myf5^{-}$ lineages selectively give rise to most adipocytes in the WAT depots. The cell types that are contained within adipocyte precursor pools are identified by cell surface markers, and how selective expansion of certain lineages might be determined is not known. It is also possible that $Myf5^{-}$ precursors have the ability to give rise to Myf5+ precursors within the progenitor pool leading to brown-like identities or capacities. However, data from brite adipocytes would not support this hypothesis: brite cells express lineage marks from the specific

depot that they originate. Brite cells originating from Myf5+ depots are also Myf5+, while those arising from Myf5- depots retain the Myf5- signature, even upon activation. (Sanchez-Gurmaches and Guertin, 2013; Sanchez-Gurmaches et al., 2012; Seale et al., 2008). To further complicate matters, Sanchez-Gurmaches and Guertin have recently demonstrated in the mouse through additional Myf5/Pax3 lineage tracing studies that adipocytes arise from multiple lineages that are heterogeneously and dynamically distributed throughout the animal (Figue 1.10) (Sanchez-Gurmaches and Guertin, 2014a). They posit four grounding concepts for adipogenesis:

1) adipocytes originate from multiple developmental lineages that are distributed heterogeneously in depot-specific patterns;
2) adipocyte lineage contribution to the mature adipocyte pool varies with age;
3) adipocyte lineages may selectively expand in response to certain factors;
4) adipocyte lineages can compensate for each other indicating that lineage plasticity exists.

It is evident then that the full picture of adipogenesis is extremely complex. If the paradigm above proves correct, then elucidating the basic biology of brown adipocyte origin and capacity for thermogenesis in the human through hPSCs will be paramount, as the multitude of cell lineages are exhaustive relative to MSCs and primary cells obtained from an adult. Moreover, because the lineage pool contribution may vary with age, hPSC derived brown adipocytes may have a greater capacity and range to demonstrate functionality, which is critical to developing drug screen platforms.

Generating a Brown Adipocyte Model form hPSCs

Generating brown adipocytes from hPSCs has proven difficult- to date, there are only three successful reports (Ahfeldt et al., 2012; Hafner et al., 2016; Nishio et al., 2012). Ahfeldt et al. used several over expression systems to derive functional brown adipocytes from hPSCs through an MSC state, however, untransduced cells were unable to display BA characteristics or functionality when exposed to there differentiation scheme (Ahfeldt et al., 2012). Nishio et al. serendipitously found the existence of brown adipose-like cell clusters surrounding the hematopoietic centers while attempting to develop a feeder-free system for hematopoietic differentiation of hPSCs. These cells were found to express PRDM16 and UCP1. Following this discovery, they developed a bipartite differentiation protocol using two hematopoietic cocktails (HCs) containing bone morphogenetic protein (BMP) 4 and 7 delivered sequentially (Nishio et al., 2012). This system does not generate morphologically distinct, intermediate MSCs in the presence of the HCs, but the derived cells do display similar expression characteristics to MSCs from various mesodermal developmental locations. Unfortunately, in our hands, this procedure has been irreproducible upon twelve distinct attempts. Recently, the procedure by Hafner also generates MSCs through embryoid body formation and cultivation of subsequent outgrowth (Hafner et al., 2016). This system, while novel, is extremely inefficient in its production of functional brown adipocytes. The Ahfeldt and Hafner methods rely on serum-based media, further limiting their clinical or drug screen utility. Only the hematopoietic cocktail based differentiation scheme was based on chemically defined media, however, reproducibility has been problematic. Furthermore, the reliance on MSC-like intermediates is restrictive, as they have limited self-renewal potential and inefficient adipocyte differentiation capacity (Chen et al., 2012; Sarugaser et al., 2009).

Figure 1.1- The stem-cell hierarchy. The totipotent zygote formed by the fusion of egg and sperm divides to form the inner cell mass (ICM) and the extra-embryonic (EE) tissue of the blastocyst. When isolated from the blastocyst in vitro, the cells of the ICM can be maintained in culture as pluripotent embryonic stem cell (ESC) lines. During the development of the embryo, the pluripotent stem cells in the ICM become increasingly restricted in their lineage potential and generate tissue-specific, multipotent stem cells. These include epidermal stem cells (bulge cells) that form skin and hair, haematopoietic stem cells in the bone marrow that give rise to all haematopoietic cells, neural stem cells in the subventricular zone of the brain, gastrointestinal tem cells that are located in the crypt of the small intestine, oval cells that give rise to liver (not shown), and mesenchymal stem cells that reside in the bone marrow and can form bone, stromal cells and adipocytes (not shown). (Eckfeldt et al., 2005)

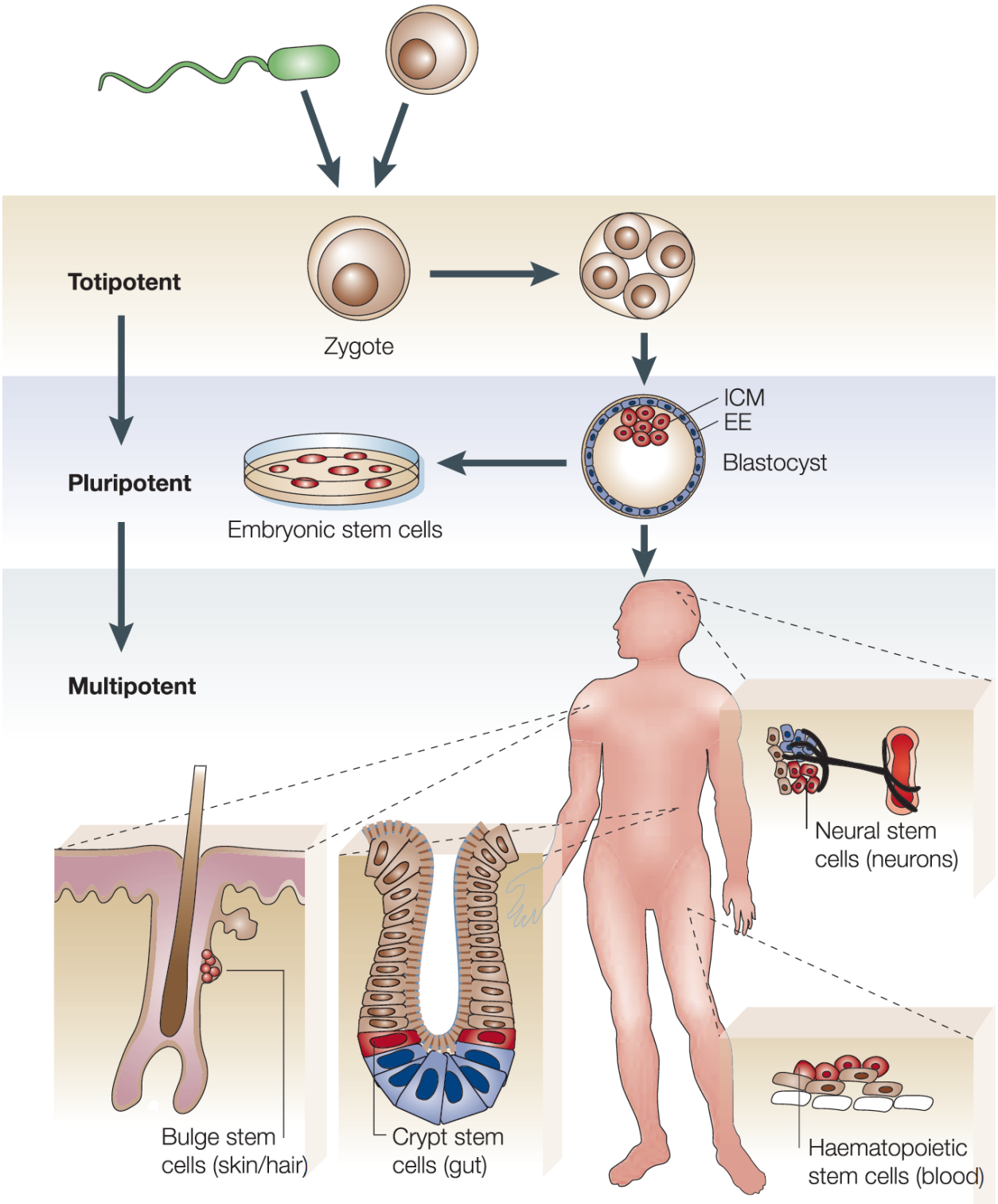
Totipotent
Zygote
Pluripotent
ICM
EE
Blastocyst
Embryonic stem cells
Multipotent
Neural stem cells (neurons)
Bulge stem cells (skin/hair)
Crypt stem cells (gut)
Haematopoietic stem cells (blood)

Figure 1.2 Approaches for reprogramming somatic nuclei. A somatic nucleus can be directed to an early embryonic state through three general approaches: somatic cell nuclear transfer (SCNT), fusion with embryonic stem cells (ES cells) and ectopic factor expression (direct reprogramming). In somatic nuclei, pluripotency-specific genes such as *Oct4* are epigenetically silenced. Nuclear potential scales from totipotent (the ability to generate an entire organism, including extra-embryonic and embryonic tissues) to unipotent. In SCNT, somatic nuclei are transferred into enucleated oocytes. Upon oocyte activation, maternal factors rapidly and globally remodel the somatic genome Successfully reprogrammed SCNT zygotes have restored totipotency and express select pluripotency factors, such as *Oct4*, that have developmental functions in both the early embryo and inner cell mass (ICM). After ~3–4 days, the ICM is formed in the blastocyst and developmental potency is restricted, producing pluripotent cells that contribute to the embryo proper, or from which ES cells can be derived. In experimentally induced ES cell fusion, a somatic cell is fused with a pluripotent cell. Reprogramming is initiated in the heterokaryon phase, during which both nuclei remain discrete, and includes global epigenetic remodelling that precedes the activation of pluripotent loci. In the late heterokaryon phase, select loci are activated through a process that may require DNA replication. The somatic and pluripotent nuclei fuse after cell division, and additional genes are then reprogrammed to consolidate the pluripotent network within the somatic genome. During direct reprogramming, OCT4, SRY-box 2 (SOX2), Krüppel-like factor 4 (KLF4) and MYC (OSKM) are introduced into somatic cells, which respond by increasing proliferation and undergoing local changes to their epigenome. Shortly afterwards, KLF4 induces epithelial genes, and genes supporting the mesenchymal state are repressed. Early responses do not include activation of true pluripotency-associated regulators, including *Oct4*. The transition from a factor-dependent, non-pluripotent

state to induced pluripotent stem cells (iPSCs) requires multiple divisions and an extended latency period under persistent ectopic OSKM expression. Complete reprogramming of the somatic nucleus occurs within a small percentage of responding cells and includes activation of the endogenous network, as well as consolidation of additional global epigenetic features of stable pluripotency. NT zygote, nuclear transfer zygote. (Smith et al., 2016)

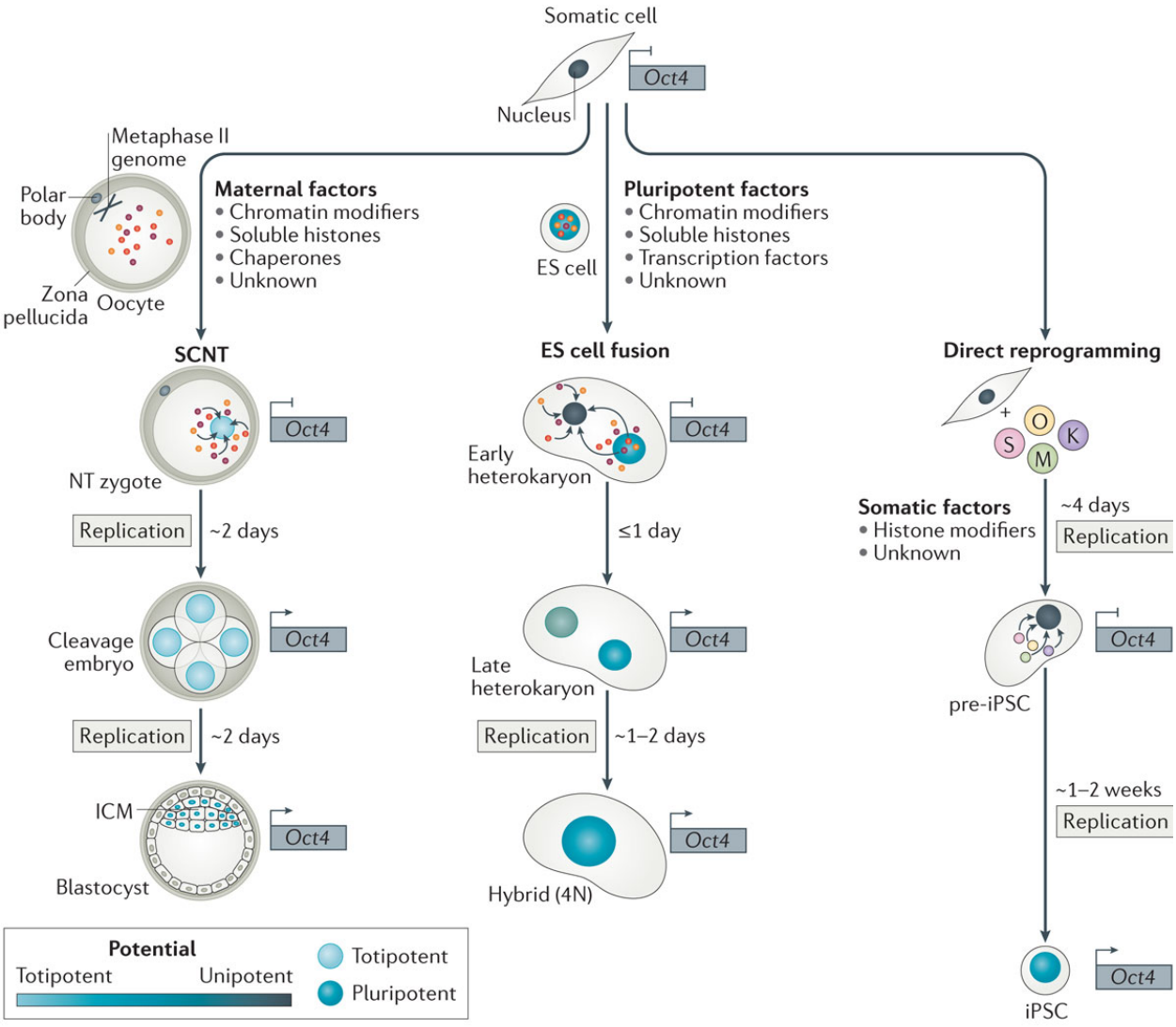
Somatic cell
Oct4
Nucleus
Metaphase II genome
Polar body
Zona pellucida
Oocyte
Maternal factors
• Chromatin modifiers
• Soluble histones
• Chaperones
• Unknown
ES cell
Pluripotent factors
• Chromatin modifiers
• Soluble histones
• Transcription factors
• Unknown
SCNT
ES cell fusion
Direct reprogramming
NT zygote
Replication
~2 days
Cleavage embryo
Replication
~2 days
ICM
Blastocyst
Early heterokaryon
≤1 day
Late heterokaryon
Replication
~1–2 days
Hybrid (4N)
O
S
M
K
Somatic factors
• Histone modifiers
• Unknown
~4 days
Replication
pre-iPSC
~1–2 weeks
Replication
iPSC
Potential
Totipotent
Unipotent
Totipotent
Pluripotent

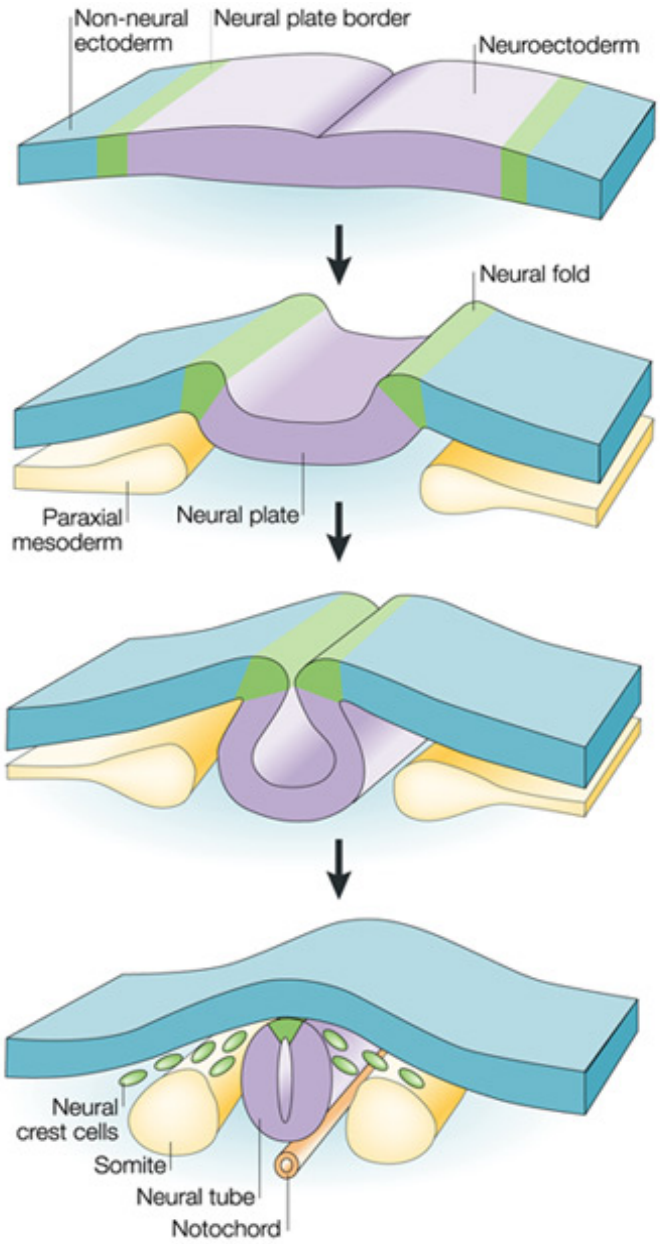

Figure1.3- Neural Crest Cell Origination. After gastrulation, NCCs are specified at the border of the neural plate and the non-neuroectoderm. During neurulation, the neural folds converge at the dorsal midline to form the neural tube. NCCs from the roof palte of the neural tube undergo an EMT, delaminating from the neuroepithelium and migrating throughout the periphery integrating nearly every organ (Gammill and Bronner-Fraser, 2003).

Figure 1.4- Phenotypic display of *Tcof1* haploinsufficiency in murine model of TCS. WT and compound *Tcof1:Trp53* haploinsufficiency yields viable adults, whereas *Tcof1*$^{+/-}$ is lethal. (a). Cartoon of the neuroepithelium and migration of neural crest cells (red) and apoptosis (blue cells) (panel b); late gestation craniofacial consequences in the corresponding genotypes: bone (red) and cartilage (blue) staining showed normal cranioskeletal patterning in E18.5 *Tcof1*$^{+/+}$ embryos (c, left); severe frontonasal hypoplasia and dysplasia in *Tcof1*$^{+/-}$ embryos (c, middle) and apparent rescue in *Tcof1*$^{+/-}$:*Trp53*$^{+/-}$ littermates (c, right). Staining for apoptosis (TUNEL, green) showed low endogenous levels of cell death in E8.5 wild-type embryos and elevated levels in *Tcof1*$^{+/-}$littermates (d, left, upper and lower). BrdU incorporation (red) into DAPI-stained nuclei (blue) of E9.0 embryos highlighted a concomitant decrease in cell proliferation in *Tcof1*$^{+/-}$ embryos (d, middle, upper and lower). Immunostaining for the 28S ribosomal protein (red) in E8.5 embryos uncovered deficient ribosome biogenesis in *Tcof1*$^{+/-}$ littermates (d, right, upper and lower). Flow diagram of the current model of the pathogenesis of TCS in mice (Trainor et al., 2008b) (Gonzales, 2005; Jones et al., 2008b; Valdez et al., 2004)

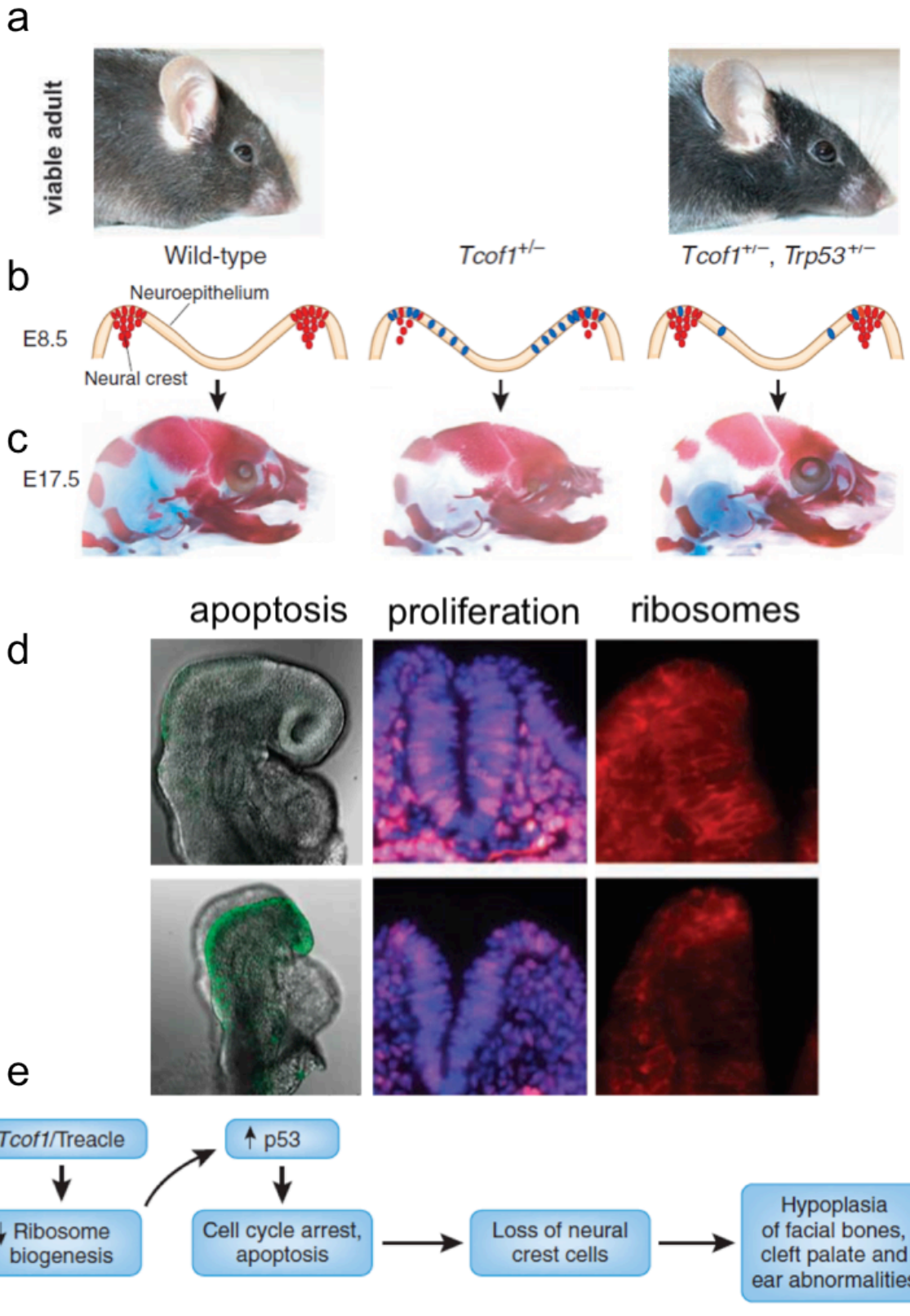
a
viable adult
Wild-type
Tcof1+/–
Tcof1+/–, Trp53+/–
b
Neuroepithelium
E8.5
Neural crest
c
E17.5
apoptosis
proliferation
ribosomes
d
e
↓Tcof1/Treacle
↑ p53
↓ Ribosome biogenesis
Cell cycle arrest, apoptosis
Loss of neural crest cells
Hypoplasia of facial bones, cleft palate and ear abnormalities

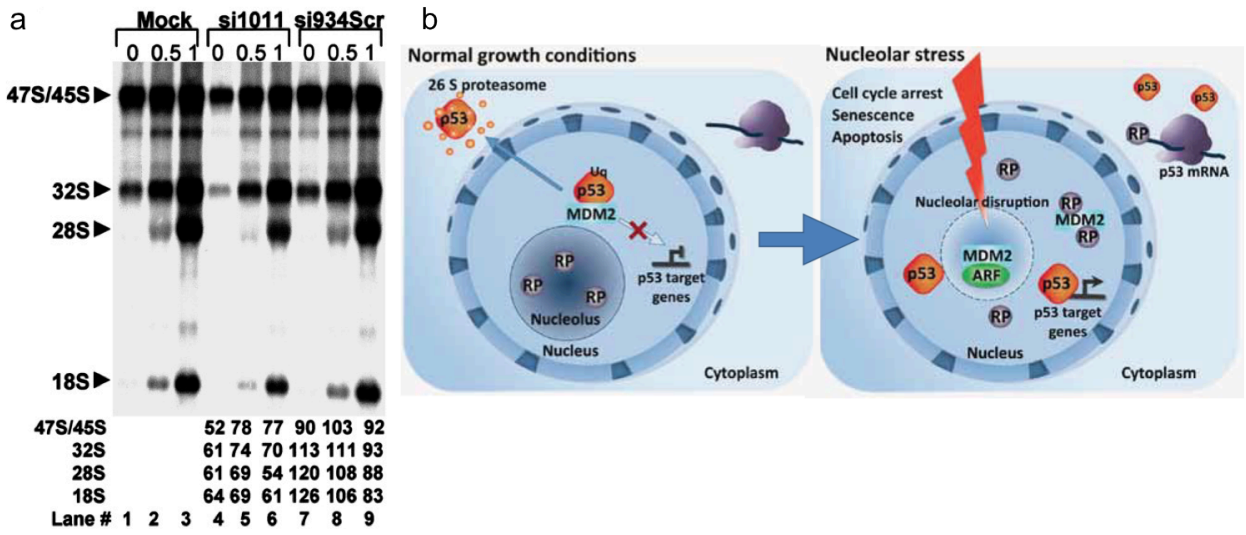

Figure 1.5- Effects of siRNA-mediated down-regulation of treacle on rRNA production and the ribosome surveillance system. HeLa cells were treated with 40 nM siRNA or mock-transfected. si1011 targets the TCOF1 mRNA and si934Scr is control siRNA. Total RNAs from 32P-metabolically labeled transfected HeLa cells were analyzed by gel electrophoresis. The chase times with nonradioactive phosphate are labeled 0, 0.5, and 1 h. The numbers below correspond to the amount of specific RNA band relative to mock-transfected samples (set at 100) (a). Under Normal growth conditions, ribosomal proteins, (RPs) are assembled in the nucleolus and transported to the cytoplasm to form functional ribosomes. MDM2 binds and monoubiquitylates p53 in the nucleoplasm, which promotes p53 proteasomal degradation (left panel). Under nucleolar stress conditions, RPs are released to the nucleoplasm where they can interact with MDM2 resulting in the suppression of p53 ubiquitination. The activation of p53 induces cell cycle arrest, apoptosis and/or senescence (b). (Deisenroth and Zhang, 2010b; Valdez et al., 2004)

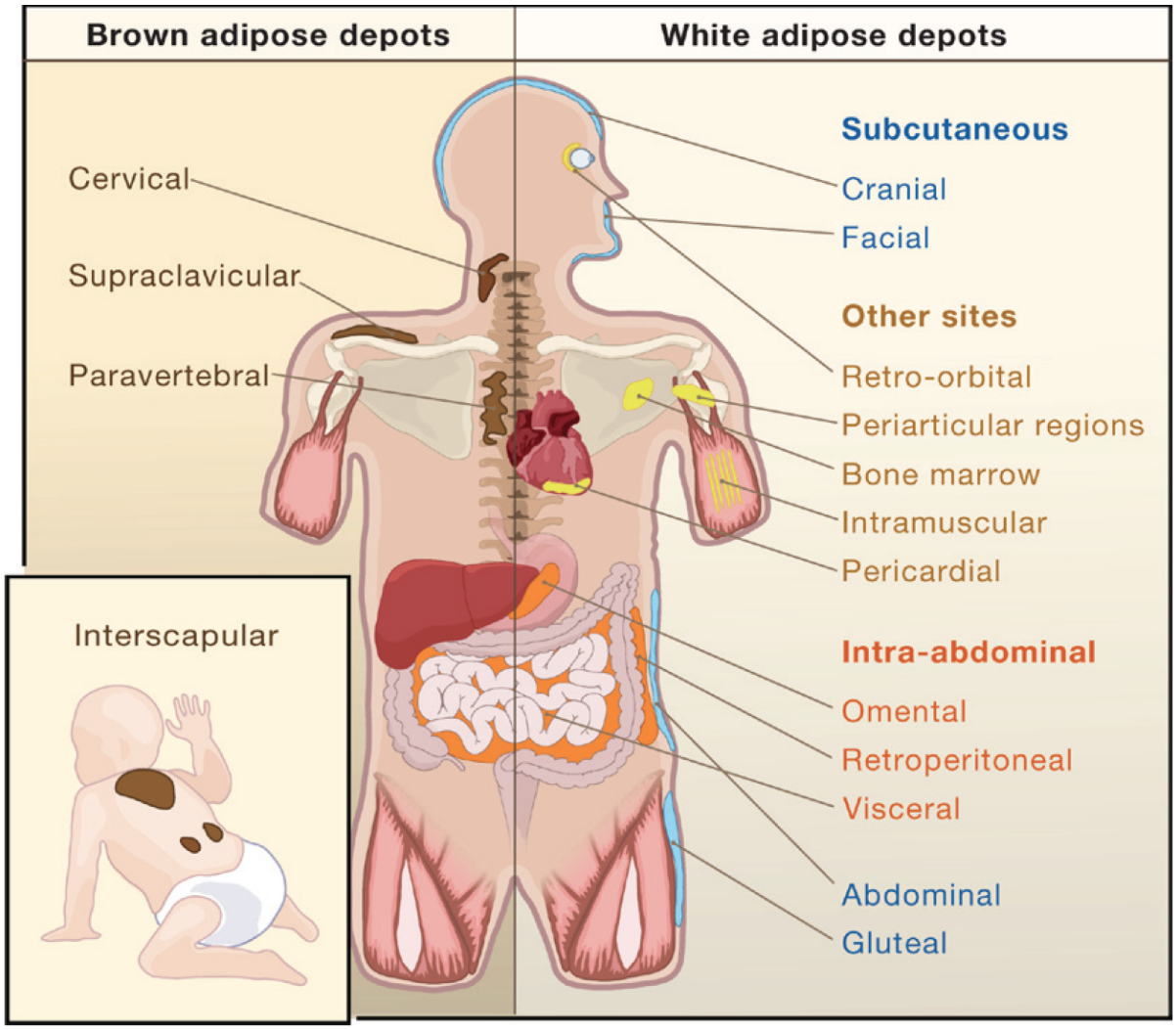

Figure 1.6- Corporal Location of adipose tissue in humans. Depots of WAT are found in various locations throughout the body, with subcutaneous and intra-abdominal depots representing the main compartments for fat storage. BAT is abundant at birth and still present in adulthood but to a lesser extent (Gesta et al., 2007).

Figure 1.7- Brite adipocyte formation-two potential models. Left: Adipocyte precursors within WAT develop into a homogenous population of mature white adipocytes. Upon cold adaptation, a subset of these transdifferentiates into thermogenic brite adipocytes. Right: Different subsets of the adipocyte precursor population within WAT develop into an apparently homogeneous but intrinsically heterogeneous population of cells with mature white adipocyte characteristics. One subset of these cells holds the potential to transform into thermogenic brite adipocytes upon cold adaptation, while the others remain white adipocytes (Rosenwald and Wolfrum, 2014).

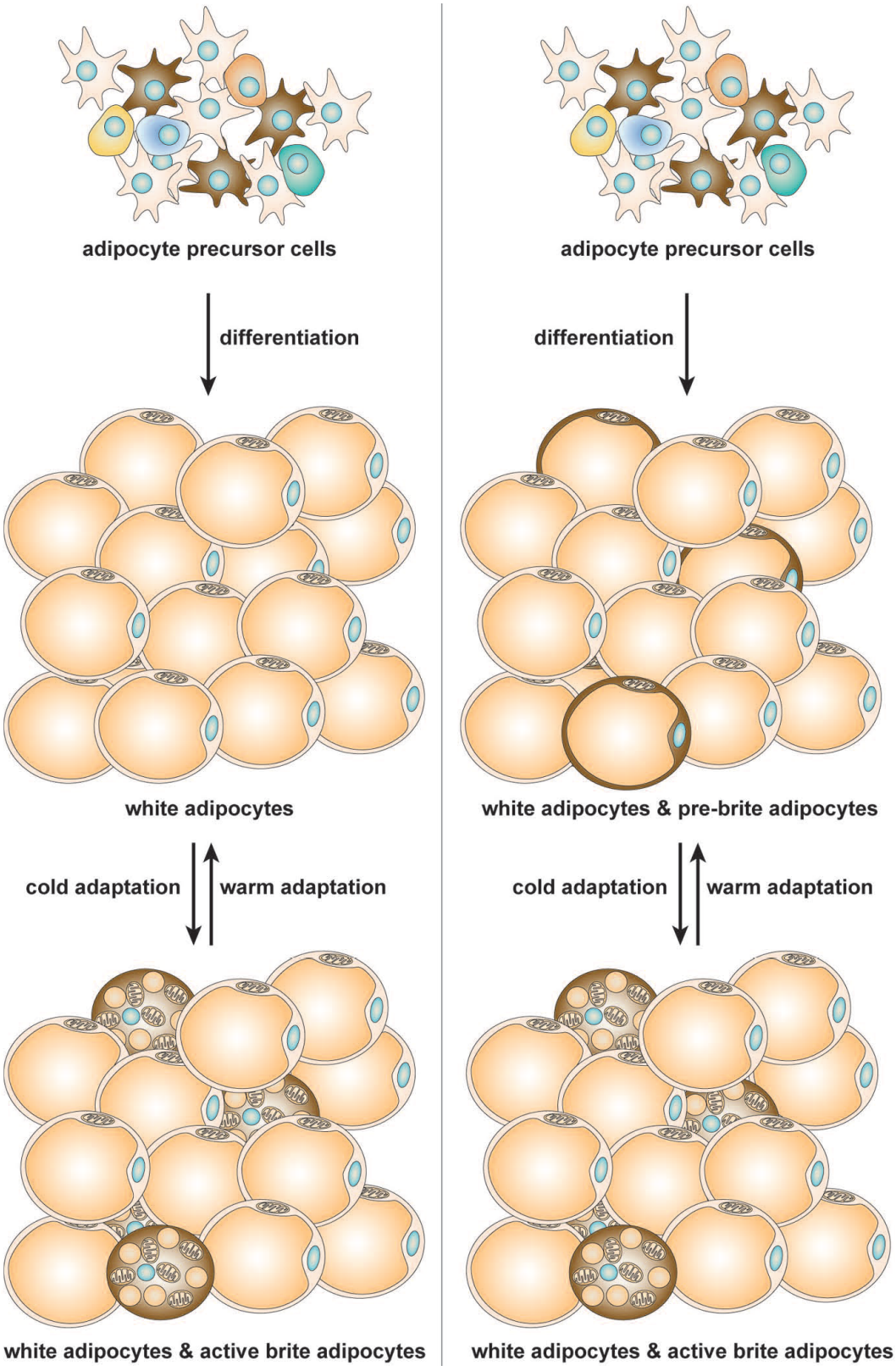
adipocyte precursor cells
differentiation
white adipocytes
cold adaptation
warm adaptation
white adipocytes & active brite adipocytes
adipocyte precursor cells
differentiation
white adipocytes & pre-brite adipocytes
cold adaptation
warm adaptation
white adipocytes & active brite adipocytes

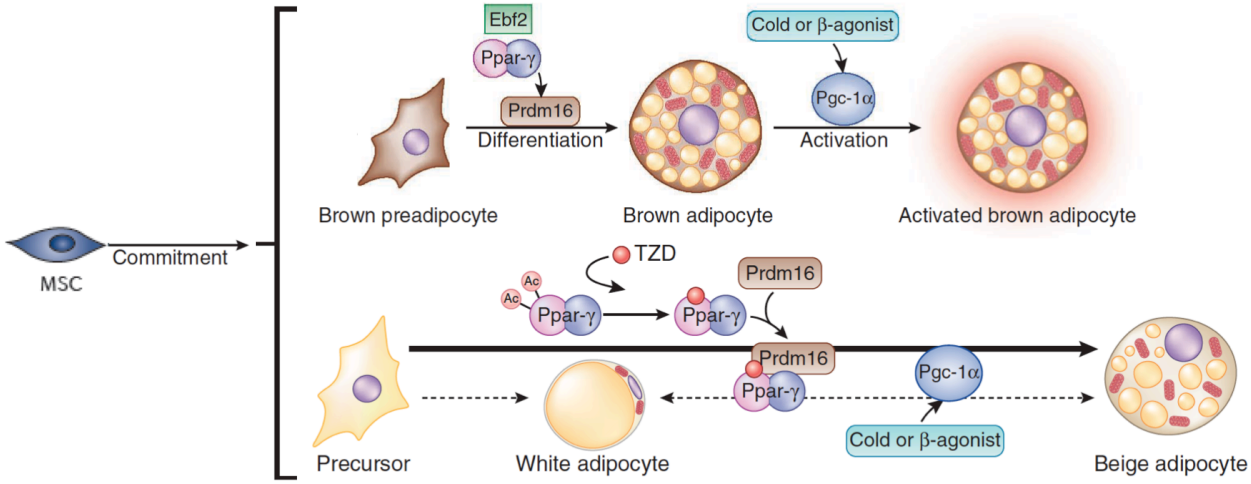

Figure 1.8- Proposed development of white, brown and beige adipocytes. (**Top**) Brown adipocytes are derived from a *Myf5*-expressing progenitor population. Ppar-γ promotes the expression of Prdm16, which drives a brown-fat cell fate. Thermogenesis in mature brown adipocytes is activated by β3 agonists released from sympathetic neuron signaling to increase the expression and activity of Pgc-1α, a transcriptional coactivator that coordinates gene programming in response to activation. (**Bottom**) white adipose precursors derive from non-*Myf5*-expressing progenitor populations. In WAT β-adrenergic stimulation triggers differentiation of precursor cells (large arrow) to beige fat; other mature white fat cells can transdifferentiate into beige cells (small dashed arrow). TZD agonists of Ppar-γ promote browning by increasing the stability of Prdm16 via deacetylation, which recruits Prdm16 to Ppar-γ target genes. β-adrenergic signaling drives the expression and activity of Pgc-1α in beige adipocytes (Harms and Seale, 2013).

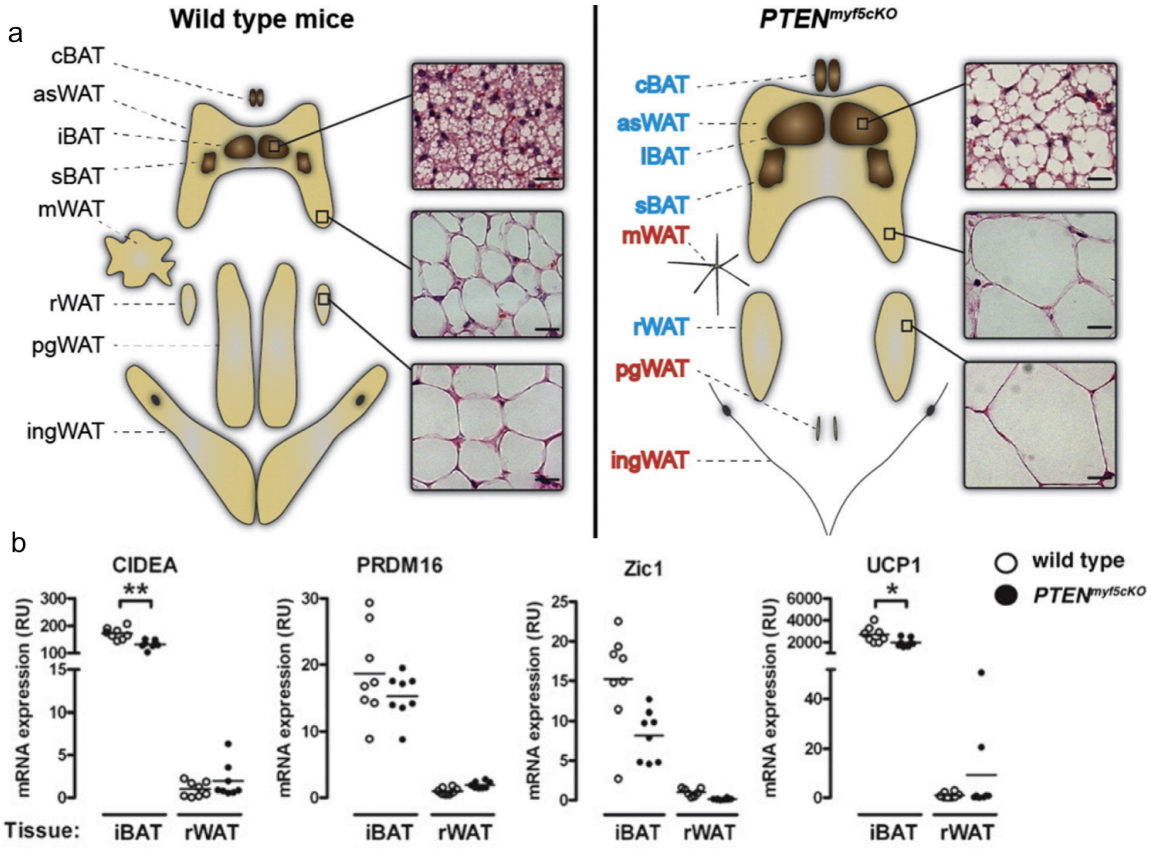

Figure 1.9- Deleting PTEN with Myf5-Cre in mice. Deleting PTEN with Myf5-Cre causes lipohypertrophy of the fat depots largely derived from Myf5+ adipocyte precursors (labeled in blue) and lipoatrophy of the fats that are largely Myf5neg (labeled in red). The overgrown fats are bigger because they contain more cells due to expansion of the Myf5+ adipocyte precursor cell population and bigger cells as a result of increased lipid content (histology insets). The absent fats are reduced to fibrotic tissue. WAT depots: anterior subcutaneous (asWAT); inguinal (ingWAT); perigonadal (pgWAT); retroperitoneal (rWAT); mesenteric (mWAT); BAT depots interscapular (iBAT), sub-scapular (sBAT), and cervical (cBAT) (a). qRT-PCR analysis of *Cidea, Prdm16, Zic1, Ucp1*, in whole iBAT and rWAT, representing classical brown (iBAT) and classical white (rWAT) depots (b) (Sanchez-Gurmaches et al., 2012).

Figure 1.10- Model depicting the Myf5-Cre and Pax3-Cre lineage-tracing patterns. (a) Anatomical disposition of BAT and WAT depots: Interscapular BAT (iBAT), subscapular BAT (sBAT), cervical BAT (cBAT), peri-aortic BAT (paBAT), peri-renal BAT (prBAT), anteriorsubcutaneous WAT (asWAT), posterior-subcutaneous WAT (psWAT), retroperitoneal WAT (rWAT), perigonadal WAT (pgWAT) and mesenteric WAT (mWAT) depots are indicated. (b) Anatomical distribution of Myf5-Cre-traced adipocytes in BAT and WAT The distribution is not significantly different between males and females. Anterior (A), posterior (P), dorsal (D) and ventral (V) are indicated. (c) Anatomical distribution of Pax3-Cre-traced adipocytes in BAT and WAT. Male and female distribution patterns are shown separately because of the gender-linked variation in paBAT and pgWAT (Sanchez-Gurmaches and Guertin, 2014a).

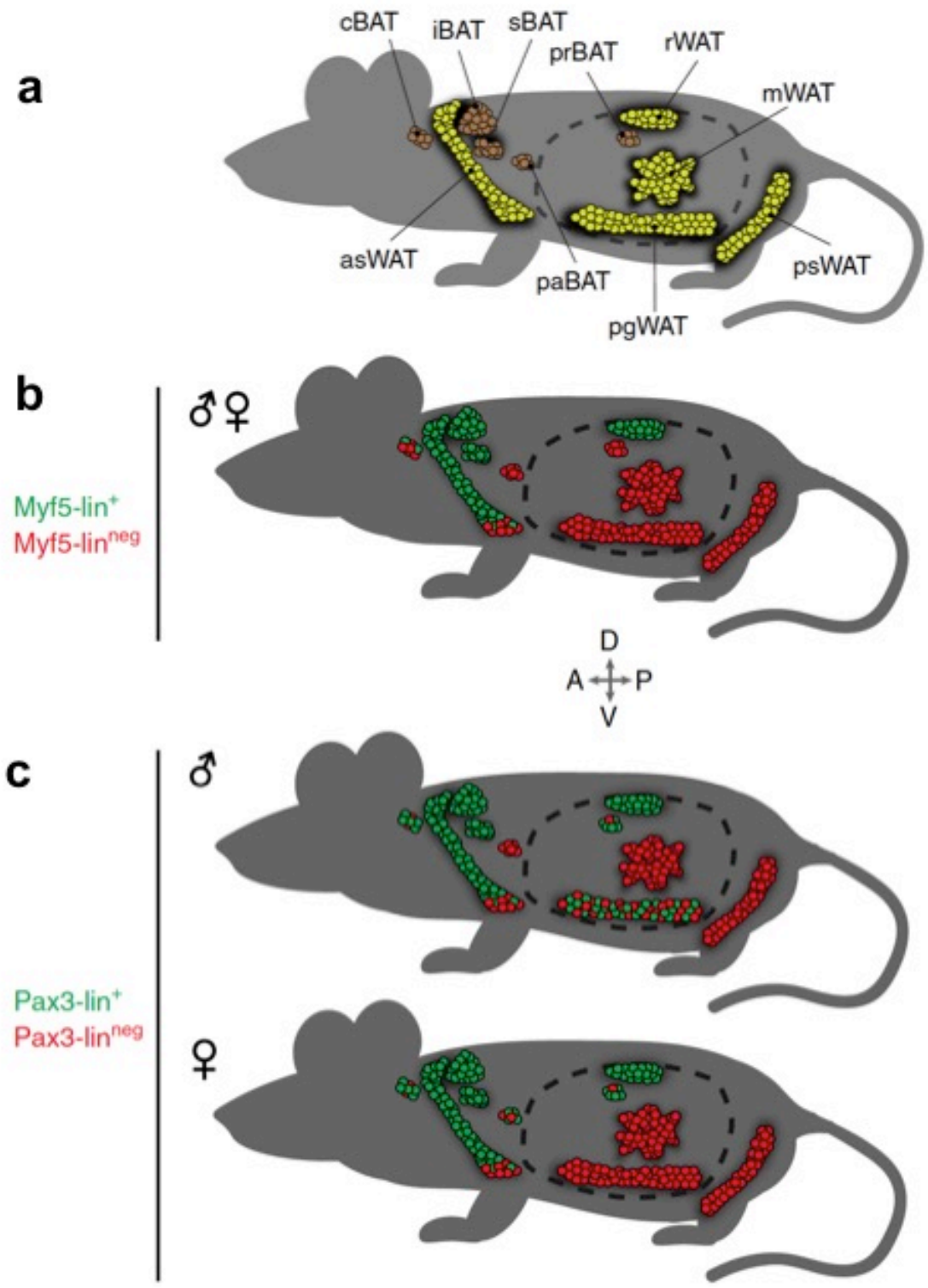
a
cBAT
iBAT
sBAT
prBAT
rWAT
mWAT
asWAT
paBAT
psWAT
pgWAT
b
♂♀
Myf5-lin+
Myf5-linneg
D
A
P
V
c
♂
♀
Pax3-lin+
Pax3-linneg

Table 1.1- Genetic tracing of adipocyte progenitors during development/adult adipose tissue

Lineage markers	Developmental origin	Lineage-derived adipose depots
Myf5	Paraxial mesoderm Myogenic	BAT (interscapular, perirenal) WAT
Pax7	Somite (dermomyotome) Myogenic	BAT (interscapular)
PDGFRβ	Mesenchyme MSC	WAT (retroperitoneal, inguinal)
PPARγ	Adipogenic	WAT (retroperitoneal, inguinal)
SM22	Vascular smooth muscle cells (VSMC)	Perivascular adipose tissue
Sox10	Neural crest	Facial WAT (salivary gland and ear)
VE-Cadherin	Endothelial cells	WAT and BAT
LysM	Myeloid cells	BM-derived adipocytes
PDGFRα	Paraxial mesoderm MSC	WA/ Inducible BA Inducible BA

(Lee et al., 2013b)

REFERENCES

Achilleos, A., and Trainor, P.A. (2012). Neural crest stem cells: discovery, properties and potential for therapy. Cell Research *22*, 288–304.

Ahfeldt, T., Schinzel, R.T., Lee, Y.-K., Hendrickson, D., Kaplan, A., Lum, D.H., Camahort, R., Xia, F., Shay, J., Rhee, E.P., et al. (2012). Programming human pluripotent stem cells into white and brown adipocytes. Nature Publishing Group *14*, 209–219.

Barak, Y., Nelson, M.C., Ong, E.S., Jones, Y.Z., Ruiz-Lozano, P., Chien, K.R., Koder, A., and Evans, R.M. (1999). PPAR gamma is required for placental, cardiac, and adipose tissue development. Molecular Cell *4*, 585–595.

Barbera, M.J., Schluter, A., Pedraza, N., Iglesias, R., Villarroya, F., and Giralt, M. (2001). Peroxisome proliferator-activated receptor alpha activates transcription of the brown fat uncoupling protein-1 gene. A link between regulation of the thermogenic and lipid oxidation pathways in the brown fat cell. J. Biol. Chem. *276*, 1486–1493.

Billon, N., Iannarelli, P., Monteiro, M.C., Glavieux-Pardanaud, C., Richardson, W.D., Kessaris, N., Dani, C., and Dupin, E. (2007). The generation of adipocytes by the neural crest. Development *134*, 2283–2292.

Billon, N., and Dani, C. (2011). Developmental Origins of the Adipocyte Lineage: New Insights from Genetics and Genomics Studies. Stem Cell Rev and Rep *8*, 55–66.

Billon, N., Monteiro, M.C., and Dani, C. (2008). Developmental origin of adipocytes: new insights into a pending question. Biol Cell *100*, 563–575.

Bonnot, E. (1908). The Interscapular Gland. Journal of Anatomy and Physiology *43*, 43.

Bornfeldt, K.E., and Tabas, I. (2011). Insulin resistance, hyperglycemia, and atherosclerosis. Cell Metabolism *14*, 575–585.

Boutayeb, A., and Boutayeb, S. (2005). The burden of non communicable diseases in developing countries. Int J Equity Health *4*, 2.

Bowman, M., Oldridge, M., Archer, C., O'Rourke, A., McParland, J., Brekelmans, R., Seller, A., and Lester, T. (2012). Gross deletions in TCOF1 are a cause of Treacher-Collins-Franceschetti syndrome. Eur J Hum Genet *20*, 769–777.

Cannon, B., and Nedergaard, J. (2004). Brown adipose tissue: function and physiological significance. Physiol. Rev. *84*, 277–359.

Carmona, M.C., Hondares, E., Rodríguez de la Concepción, M.L., Rodríguez-Sureda, V., Peinado-Onsurbe, J., Poli, V., Iglesias, R., Villarroya, F., and Giralt, M. (2005). Defective thermoregulation, impaired lipid metabolism, but preserved adrenergic induction of gene expression in brown fat of mice lacking C/EBPbeta. Biochem. J. *389*, 47–56.

Casteilla, L., Penicaud, L., Cousin, B., and Calise, D. (2008). Choosing an adipose tissue depot for sampling: factors in selection and depot specificity. Methods Mol Biol *456*, 23–38.

Chen, Y.S., Pelekanos, R.A., Ellis, R.L., Horne, R., Wolvetang, E.J., and Fisk, N.M. (2012). Small molecule mesengenic induction of human induced pluripotent stem cells to generate mesenchymal stem/stromal cells. Stem Cells Transl Med *1*, 83–95.

Cinti, S. (2009). Transdifferentiation properties of adipocytes in the adipose organ. Am. J. Physiol. Endocrinol. Metab. *297*, E977–E986.

Cohen, J., Ghezzi, F., Gonçalves, L., Fuentes, J.D., Paulyson, K.J., and Sherer, D.M. (1995). Prenatal sonographic diagnosis of Treacher Collins syndrome: a case and review of the literature. Am J Perinatol *12*, 416–419.

Collins, E.T. (1900). Case with symmetrical congenital notches in the outer part of each lower lid and defective development of the malar bones. Trans Ophthalmol Soc UK *20*, 191–192.

Cristancho, A.G., and Lazar, M.A. (2011). Forming functional fat: a growing understanding of adipocyte differentiation. Nat Rev Mol Cell Biol *12*, 722–734.

Crossno, J.T., Majka, S.M., Grazia, T., Gill, R.G., and Klemm, D.J. (2006). Rosiglitazone promotes development of a novel adipocyte population from bone marrow-derived circulating progenitor cells. J. Clin. Invest. *116*, 3220–3228.

Cynthia Isaac, K.L.M.W.A.P.J.D.M.J.D.E.W.J.U.T.M. (2000). Characterization of the Nucleolar Gene Product, Treacle, in Treacher Collins Syndrome. Molecular Biology of the Cell *11*, 3061–11.

Cypess, A.M., Lehman, S., Williams, G., Tal, I., Rodman, D., Goldfine, A.B., Kuo, F.C., Palmer, E.L., Tseng, Y.-H., Doria, A., et al. (2009). Identification and importance of brown adipose tissue in adult humans. N. Engl. J. Med. *360*, 1509–1517.

Deisenroth, C., and Zhang, Y. (2010a). Ribosome biogenesis surveillance: probing the ribosomal protein-Mdm2-p53 pathway. Oncogene *29*, 4253–4260.

Deisenroth, C., and Zhang, Y. (2010b). Ribosome biogenesis surveillance: probing the ribosomal protein-Mdm2-p53 pathway. Oncogene *29*, 4253–4260.

Deisenroth, C., and Zhang, Y. (2011). The Ribosomal Protein-Mdm2-p53 Pathway and Energy Metabolism: Bridging the Gap between Feast and Famine. Genes & Cancer *2*, 392–403.

Dixon, J., Brakebusch, C., Fassler, R., and Dixon, M.J. (2000). Increased levels of apoptosis in the prefusion neural folds underlie the craniofacial disorder, Treacher Collins syndrome. Human Molecular Genetics *9*, 1473–1480.

Dixon, J., Hovanes, K., Shiang, R., and Dixon, M.J. (1997). Sequence analysis, identification of evolutionary conserved motifs and expression analysis of murine tcof1 provide further evidence for a potential function for the gene and its human homologue, TCOF1. Human Molecular Genetics *6*, 727–737.

Dixon, J., Jones, N.C., Sandell, L.L., Jayasinghe, S.M., Crane, J., Rey, J.-P., Dixon, M.J., and Trainor, P.A. (2006). Tcof1/Treacle is required for neural crest cell formation and proliferation deficiencies that cause craniofacial abnormalities. Proc. Natl. Acad. Sci. U.S.a. *103*, 13403–13408.

Dixon, M.J., Marres, H.A., Edwards, S.J., Dixon, J., and Cremers, C.W. (1994). Treacher Collins syndrome: correlation between clinical and genetic linkage studies. Clin. Dysmorphol. *3*, 96–103.

Dupin, E., Creuzet, S., and Douarin, N. (2006). The Contribution of the Neural Crest to the Vertebrate Body. Advances in Experimental Medicine and Biology *589*, 96–119.

Ebert, A.D., Liang, P., and Wu, J.C. (2012). Induced pluripotent stem cells as a disease modeling and drug screening platform. J. Cardiovasc. Pharmacol. *60*, 408–416.

Eckfeldt, C.E., Mendenhall, E.M., and Verfaillie, C.M. (2005). The molecular repertoire of the "almighty" stem cell. Nat Rev Mol Cell Biol *6*, 726–737.

Edens, N.K., Fried, S.K., Kral, J.G., Hirsch, J., and Leibel, R.L. (1993). In vitro lipid synthesis in human adipose tissue from three abdominal sites. Am. J. Physiol. *265*, E374–E379.

Edwards, S.J., Gladwin, A.J., and Dixon, M.J. (1997). The mutational spectrum in Treacher Collins syndrome reveals a predominance of mutations that create a premature-termination codon. Am. J. Hum. Genet. *60*, 515–524.

Etchevers, H.C., Amiel, J., and Lyonnet, S. (2006). Molecular bases of human neurocristopathies. Adv. Exp. Med. Biol. *589*, 213–234.

Farmer, S.R. (2006). Transcriptional control of adipocyte formation. Cell Metabolism *4*, 263–273.

Gammill, L.S., and Bronner-Fraser, M. (2003). Neural crest specification: migrating into genomics. Nat Rev Neurosci *4*, 795–805.

GARCIA, C., VANNOSTRAND, D., MAJD, M., ATKINS, F., ACIO, E., SHEIKH, A., and BUTLER, C. (2004). Benzodiazepine-resistant ?brown fat? pattern in positron emission tomography: two case reports of resolution with temperature control. Molecular Imaging & Biology *6*, 368–372.

Gazda, H.T., and Sieff, C.A. (2006). Recent insights into the pathogenesis of Diamond-Blackfan anaemia. Br. J. Haematol. *135*, 149–157.

GBD 2015 Obesity Collaborators (2017). Health Effects of Overweight and Obesity in 195 Countries over 25 Years. N. Engl. J. Med. NEJMoa1614362.

Gesta, S., Blüher, M., Yamamoto, Y., Norris, A.W., Berndt, J., Kralisch, S., Boucher, J., Lewis, C., and Kahn, C.R. (2006). Evidence for a role of developmental genes in the origin of obesity and body fat distribution. Proc. Natl. Acad. Sci. U.S.a. *103*, 6676–6681.

Gesta, S., Tseng, Y.-H., and Kahn, C.R. (2007). Developmental Origin of Fat: Tracking Obesity to Its Source. Cell *131*, 242–256.

Gesta, S., Tseng, Y.-H., and Kahn, C.R. (2008). Developmental Origin of Fat: Tracking Obesity to Its Source. Cell *135*, 366–366.

Giralt, A., Hondares, E., Villena, J.A., Ribas, F., Díaz-Delfín, J., Giralt, M., Iglesias, R., and Villarroya, F. (2011). Peroxisome proliferator-activated receptor-gamma coactivator-1alpha controls transcription of the Sirt3 gene, an essential component of the thermogenic brown adipocyte phenotype. Journal of Biological Chemistry *286*, 16958–16966.

Giralt, M., and Villarroya, F. (2013a). White, Brown, Beige/Brite: Different Adipose Cells for Different Functions? Endocrinology *154*, 2992–3000.

Giralt, M., and Villarroya, F. (2013b). White, Brown, Beige/Brite: Different Adipose Cells for Different Functions? Endocrinology *154*, 2992–3000.

Gonzales, B. (2005). The Treacher Collins syndrome (TCOF1) gene product is involved in pre-rRNA methylation. Human Molecular Genetics *14*, 2035–2043.

Grskovic, M., Javaherian, A., Strulovici, B., and Daley, G.Q. (2011). Induced pluripotent stem cells —opportunities for disease modellingand drug discovery. Nat Rev Drug Discov 1–15.

Hafner, A.-L., Contet, J., Ravaud, C., Yao, X., Villageois, P., Suknuntha, K., Annab, K., Peraldi, P., Binetruy, B., Slukvin, I.I., et al. (2016). Brown-like adipose progenitors derived from human induced pluripotent stem cells: Identification of critical pathways governing their adipogenic capacity. Sci. Rep. *6*, 32490.

Hall, B.K. (2008). The neural crest and neural crest cells: discovery and significance for theories of embryonic organization. J. Biosci. *33*, 781–793.

Hany, T.F., Gharehpapagh, E., Kamel, E.M., and Buck, A. (2002). Brown adipose tissue: a factor to... [Eur J Nucl Med Mol Imaging. 2002] - PubMed - NCBI. European Journal of ….

Harms, M., and Seale, P. (2013). Brown and beige fat: development, functionand therapeutic potential. Nat Med *19*, 1252–1263.

Himms-Hagen, J., Melnyk, A., Zingaretti, M.C., Ceresi, E., Barbatelli, G., and Cinti, S. (2000). Multilocular fat cells in WAT of CL-316243-treated rats derive directly from white adipocytes. Am. J. Physiol., Cell Physiol. *279*, C670–C681.

Hondares, E., Rosell, M., Díaz-Delfín, J., Olmos, Y., Monsalve, M., Iglesias, R., Villarroya, F., and Giralt, M. (2011). Peroxisome proliferator-activated receptor α (PPARα) induces PPARγ coactivator 1α (PGC-1α) gene expression and contributes to thermogenic activation of brown fat: involvement of PRDM16. Journal of Biological Chemistry *286*, 43112–43122.

Ibrahim, M.M. (2010). Subcutaneous and visceral adipose tissue: structural and functional differences. Obesity Reviews *11*, 11–18.

Jabs, E.W., Li, X., Coss, C.A., Taylor, E.W., Meyers, D.A., and Weber, J.L. (1991). Mapping the Treacher Collins syndrome locus to 5q31.3----q33.3. Genomics *11*, 193–198.

Jabs, E.W., Li, X., Lovett, M., Yamaoka, L.H., Taylor, E., Speer, M.C., Coss, C., Cadle, R., Hall, B., and Brown, K. (1993). Genetic and physical mapping of the Treacher Collins syndrome locus with respect to loci in the chromosome 5q3 region. Genomics *18*, 7–13.

Jones, K.L., Smith, D.W., Harvey, M.A., Hall, B.D., and Quan, L. (1975). Older paternal age and fresh gene mutation: data on additional disorders. J. Pediatr. *86*, 84–88.

Jones, N.C., Lynn, M.L., Gaudenz, K., Sakai, D., Aoto, K., Rey, J.-P., Glynn, E.F., Ellington, L., Du, C., Dixon, J., et al. (2008a). Prevention of the neurocristopathy Treacher Collins syndrome through inhibition of p53 function. Nat Med *14*, 125–133.

Jones, N.C., Lynn, M.L., Gaudenz, K., Sakai, D., Aoto, K., Rey, J.-P., Glynn, E.F., Ellington, L., Du, C., Dixon, J., et al. (2008b). Prevention of the neurocristopathy Treacher Collins syndrome through inhibition of p53 function. Nat Med *14*, 125–133.

Kajimura, S., Seale, P., Kubota, K., Lunsford, E., Frangioni, J.V., Gygi, S.P., and Spiegelman, B.M. (2009). Initiation of myoblast to brown fat switch by a PRDM16-C/EBP-beta transcriptional complex. Nature *460*, 1154–1158.

Karamanlidis, G., Karamitri, A., Docherty, K., Hazlerigg, D.G., and Lomax, M.A. (2007). C/EBPbeta reprograms white 3T3-L1 preadipocytes to a Brown adipocyte pattern of gene expression. J. Biol. Chem. *282*, 24660–24669.

LaBonne, C., and Bronner-Fraser, M. (1998). Induction and patterning of the neural crest, a stem cell-like precursor population. J. Neurobiol. *36*, 175–189.

Le Douarin, N.M., and Dupin, E. (2003). Multipotentiality of the neural crest. Current Opinion in Genetics & Development *13*, 529–536.

Le Douarin, N.M., Calloni, G.W., and Dupin, E. (2008). The stem cells of the neural crest. Cell Cycle *7*, 1013–1019.

Le Douarin, N.M., Creuzet, S., Couly, G., and Dupin, E. (2004). Neural crest cell plasticity and its limits. Development *131*, 4637–4650.

Le Lièvre, C.S., and Le Douarin, N.M. (1975). Mesenchymal derivatives of the neural crest: analysis of chimaeric quail and chick embryos. J Embryol Exp Morphol *34*, 125–154.

Lee, P., Swarbrick, M.M., and Ho, K.K.Y. (2013a). Brown Adipose Tissue in Adult Humans: A Metabolic Renaissance. Endocrine Reviews *34*, 413–438.

Lee, P., Zhao, J.T., Swarbrick, M.M., Gracie, G., Bova, R., Greenfield, J.R., Freund, J., and Ho, K.K.Y. (2011). High prevalence of brown adipose tissue in adult humans. J. Clin. Endocrinol. Metab. *96*, 2450–2455.

Lee, Y.-H., Mottillo, E.P., and Granneman, J.G. (2013b). Adipose tissue plasticity from WAT to BAT and in between. BBA - Molecular Basis of Disease 1–12.

Lefterova, M.I., Zhang, Y., Steger, D.J., Schupp, M., Schug, J., Cristancho, A., Feng, D., Zhuo, D., Stoeckert, C.J., Liu, X.S., et al. (2008). PPARgamma and C/EBP factors orchestrate adipocyte biology via adjacent binding on a genome-wide scale. Genes & Development *22*, 2941–2952.

Lepper, C., and Fan, C.-M. (2010). Inducible lineage tracing of Pax7-descendant cells reveals embryonic origin of adult satellite cells. Genesis *48*, 424–436.

Lin, J., Handschin, C., and Spiegelman, B.M. (2005). Metabolic control through the PGC-1 family of transcription coactivators. Cell Metabolism *1*, 361–370.

Lloyd-Jones, D., Adams, R., Carnethon, M., De Simone, G., Ferguson, T.B., Flegal, K., Ford, E., Furie, K., Go, A., Greenlund, K., et al. (2009). Heart disease and stroke statistics--2009 update: a report from the American Heart Association Statistics Committee and Stroke Statistics Subcommittee. Circulation *119*, 480–486.

Majka, S.M., Barak, Y., and Klemm, D.J. (2011). Concise Review: Adipocyte Origins: Weighing the Possibilities. Stem Cells *29*, 1034–1040.

Marres, H.A., Cremers, C.W., Dixon, M.J., Huygen, P.L., and Joosten, F.B. (1995). The Treacher Collins syndrome. A clinical, radiological, and genetic linkage study on two pedigrees. Arch. Otolaryngol. Head Neck Surg. *121*, 509–514.

Menendez, L., Kulik, M.J., Page, A.T., Park, S.S., Lauderdale, J.D., Cunningham, M.L., and Dalton, S. (2013). Directed differentiation of human pluripotent cells to neural crest stem cells. Nature Protocols *8*, 203–212.

Menendez, L., Yatskievych, T.A., Antin, P.B., and Dalton, S. (2011). Wnt signaling and a Smad pathway blockade direct the differentiation of human pluripotent stem cells to multipotent neural crest cells. Proceedings of the National Academy of Sciences *108*, 19240–19245.

Milligan, D.A., Harlass, F.E., Duff, P., and Kopelman, J.N. (1994). Recurrence of Treacher Collins' syndrome with sonographic findings. Mil Med *159*, 250–252.

Morikawa, S., Mabuchi, Y., Niibe, K., Suzuki, S., Nagoshi, N., Sunabori, T., Shimmura, S., Nagai, Y., Nakagawa, T., Okano, H., et al. (2009). Biochemical and Biophysical Research Communications. Biochemical and Biophysical Research Communications *379*, 1114–1119.

Moulin, K., Truel, N., Andre, M., Arnauld, E., Nibbelink, M., Cousin, B., Dani, C., Penicaud, L., and Casteilla, L. (2001). Emergence during development of the white-adipocyte cell phenotype is independent of the brown-adipocyte cell phenotype. Biochem. J. *356*, 659–664.

Mueller, E. (2013). Biochimica et Biophysica Acta. BBA - Molecular Basis of Disease 1–6.

Murano, I., Zingaretti, M.C., and Cinti, S. (2005). Murano: The adipose organ of Sv129 mice contains... - Google Scholar. Adipocytes.

Narla, A., and Ebert, B.L. (2010). Ribosomopathies: human disorders of ribosome dysfunction. Blood *115*, 3196–3205.

Nedergaard, J., Connolly, E., and Cannon, B. (1986). Nedergaard: Brown adipose tissue in the mammalian neonate - Google Scholar. Brown Adipose Tissue.

Nielsen, R., Pedersen, T.A., Hagenbeek, D., Moulos, P., Siersbæk, R., Megens, E., Denissov, S., Børgesen, M., Francoijs, K.-J., Mandrup, S., et al. (2008). Genome-wide profiling of PPARgamma:RXR and RNA polymerase II occupancy reveals temporal activation of distinct metabolic pathways and changes in RXR dimer composition during adipogenesis. Genes & Development *22*, 2953–2967.

Nishio, M., Yoneshiro, T., Nakahara, M., Suzuki, S., Saeki, K., Hasegawa, M., Kawai, Y., Akutsu, H., Umezawa, A., Yasuda, K., et al. (2012). Production of Functional Classical Brown Adipocytes from Human Pluripotent Stem Cells usingSpecific Hemopoietin Cocktail without Gene Transfer. Cell Metabolism *16*, 394–406.

Ogden, C.L., Carroll, M.D., Kit, B.K., and Flegal, K.M. (2012). Prevalence of obesity in the United States, 2009-2010. NCHS Data Brief 1–8.

Ogden, C.L., Carroll, M.D., Kit, B.K., and Flegal, K.M. (2013). Prevalence of obesity among adults: United States, 2011-2012. NCHS Data Brief 1–8.

Perez Rodrigo, C. (2013). Current mapping of obesity. Nutr Hosp *28 Suppl 5*, 21–31.

Petrovic, N., Walden, T.B., Shabalina, I.G., Timmons, J.A., Cannon, B., and Nedergaard, J. (2010). Chronic peroxisome proliferator-activated receptor gamma (PPARgamma) activation of

epididymally derived white adipocyte cultures reveals a population of thermogenically competent, UCP1-containing adipocytes molecularly distinct from classic brown adipocytes. Journal of Biological Chemistry *285*, 7153–7164.

Poswillo, D. (1975). The pathogenesis of the Treacher Collins syndrome (mandibulofacial dysostosis). Br J Oral Surg *13*, 1–26.

Puigserver, P., Wu, Z., Park, C.W., Graves, R., Wright, M., and Spiegelman, B.M. (1998). A cold-inducible coactivator of nuclear receptors linked to adaptive thermogenesis. Cell *92*, 829–839.

Rasmussen, A.T. (1922). The Glandular Status of Brown Multilocular Adipose Tissue. Endocrinology *6*, 760–770.

Rehrer, C.W., Karimpour-Fard, A., Hernandez, T.L., Law, C.K., Stob, N.R., Hunter, L.E., and Eckel, R.H. (2012). Regional differences in subcutaneous adipose tissue gene expression. Obesity *20*, 2168–2173.

Rosen, E.D., and MacDougald, O.A. (2006). Adipocyte differentiation from the inside out. Nat Rev Mol Cell Biol *7*, 885–896.

Rosenwald, M., and Wolfrum, C. (2014). The origin and definition of brite versus white and classical brown adipocytes. Adipocyte *3*.

Rossant, J. (2008). Stem cells and early lineage development. Cell *132*, 527–531.

Rueda-Clausen, C.F., Padwal, R.S., and Sharma, A.M. (2013). New pharmacological approaches for obesity management. Nat Rev Endocrinol *9*, 467–478.

Sackmann-Sala, L., Berryman, D.E., Munn, R.D., Lubbers, E.R., and Kopchick, J.J. (2012). Heterogeneity among white adipose tissue depots in male C57BL/6J mice. Obesity *20*, 101–111.

Saito, M., Okamatsu-Ogura, Y., Matsushita, M., Watanabe, K., Yoneshiro, T., Nio-Kobayashi, J., Iwanaga, T., Miyagawa, M., Kameya, T., Nakada, K., et al. (2009). High incidence of metabolically active brown adipose tissue in healthy adult humans: effects of cold exposure and adiposity. Diabetes *58*, 1526–1531.

Sakai, D., and Trainor, P.A. (2009). Treacher Collins syndrome: unmasking the role of Tcof1/treacle. Int. J. Biochem. Cell Biol. *41*, 1229–1232.

Sanchez-Gurmaches, J., and Guertin, D.A. (2013). Biochimica et Biophysica Acta. BBA - Molecular Basis of Disease 1–12.

Sanchez-Gurmaches, J., and Guertin, D.A. (2014a). Adipocytes arise from multiple lineages that are heterogeneously and dynamically distributed. Nature Communications *5*, 4099.

Sanchez-Gurmaches, J., and Guertin, D.A. (2014b). Adipocyte lineages: Tracing back the origins of fat. Biochimica Et Biophysica Acta (BBA) - Molecular Basis of Disease *1842*, 340–351.

Sanchez-Gurmaches, J., Hung, C.-M., Sparks, C.A., Tang, Y., Li, H., and Guertin, D.A. (2012). PTEN loss in the Myf5 lineage redistributes body fat and reveals subsets of white adipocytes that arise from Myf5 precursors. Cell Metabolism *16*, 348–362.

Sarugaser, R., Hanoun, L., Keating, A., Stanford, W.L., and Davies, J.E. (2009). Human mesenchymal stem cells self-renew and differentiate according to a deterministic hierarchy. PLoS ONE *4*, e6498.

Seale, P., Kajimura, S., and Spiegelman, B.M. (2009). Transcriptional control of brown adipocyte development and physiological function--of mice and men. Genes & Development *23*, 788–797.

Seale, P., Bjork, B., Yang, W., Kajimura, S., Chin, S., Kuang, S., Scimè, A., Devarakonda, S., Conroe, H.M., Erdjument-Bromage, H., et al. (2008). PRDM16 controls a brown fat/skeletal muscle switch. Nature *454*, 961–967.

Seale, P., Kajimura, S., Yang, W., Chin, S., Rohas, L.M., Uldry, M., Tavernier, G., Langin, D., and Spiegelman, B.M. (2007). Transcriptional control of brown fat determination by PRDM16. Cell Metabolism *6*, 38–54.

Sera, Y., Larue, A.C., Moussa, O., Mehrotra, M., Duncan, J.D., Williams, C.R., Nishimoto, E., Schulte, B.A., Watson, P.M., Watson, D.K., et al. (2009). Hematopoietic stem cell origin of adipocytes. Exp. Hematol. *37*, 1108–20–1120.e1–4.

Shenghui, H., Nakada, D., and Morrison, S.J. (2009). Mechanisms of Stem Cell Self-Renewal. Annu. Rev. Cell Dev. Biol. *25*, 377–406.

Smith, Z.D., Sindhu, C., and Meissner, A. (2016). Molecular features of cellular reprogramming and development. Nature Publishing Group *17*, 139–154.

Splendore, A., Fanganiello, R.D., Masotti, C., Morganti, L.S.C., and Passos-Bueno, M.R. (2005). TCOF1 mutation database: novel mutation in the alternatively spliced exon 6A and update in mutation nomenclature. Hum. Mutat. *25*, 429–434.

Takahashi, K., Tanabe, K., Ohnuki, M., Narita, M., Ichisaka, T., Tomoda, K., and Yamanaka, S. (2007). Induction of Pluripotent Stem Cells from Adult Human Fibroblasts by Defined Factors. Cell *131*, 861–872.

Takashima, Y., Era, T., Nakao, K., Kondo, S., Kasuga, M., Smith, A.G., and Nishikawa, S.-I. (2007). Neuroepithelial Cells Supply an Initial Transient Wave of MSC Differentiation. Cell *129*, 1377–1388.

Tanaka, T., Yoshida, N., Kishimoto, T., and Akira, S. (1997). Defective adipocyte differentiation in mice lacking the C/EBPbeta and/or C/EBPdelta gene. Embo J. *16*, 7432–7443.

Tchkonia, T., Lenburg, M., Thomou, T., Giorgadze, N., Frampton, G., Pirtskhalava, T., Cartwright, A., Cartwright, M., Flanagan, J., Karagiannides, I., et al. (2007). Identification of depot-specific human fat cell progenitors through distinct expression profiles and developmental gene patterns. Am. J. Physiol. Endocrinol. Metab. *292*, E298–E307.

Tchkonia, T., Tchoukalova, Y.D., Giorgadze, N., Pirtskhalava, T., Karagiannides, I., Forse, R.A., Koo, A., Stevenson, M., Chinnappan, D., Cartwright, A., et al. (2005). Abundance of two human preadipocyte subtypes with distinct capacities for replication, adipogenesis, and apoptosis varies among fat depots. Am. J. Physiol. Endocrinol. Metab. *288*, E267–E277.

Teber, O.A., Gillessen-Kaesbach, G., Fischer, S., Böhringer, S., Albrecht, B., Albert, A., Arslan-Kirchner, M., Haan, E., Hagedorn-Greiwe, M., Hammans, C., et al. (2004). Genotyping in 46 patients with tentative diagnosis of Treacher Collins syndrome revealed unexpected phenotypic variation. Eur J Hum Genet *12*, 879–890.

Timmons, J.A., Wennmalm, K., Larsson, O., Walden, T.B., Lassmann, T., Petrovic, N., Hamilton, D.L., Gimeno, R.E., Wahlestedt, C., Baar, K., et al. (2007). Myogenic gene expression signature establishes that brown and white adipocytes originate from distinct cell lineages. Proc. Natl. Acad. Sci. U.S.a. *104*, 4401–4406.

Tomiyama, K., Murase, N., Stolz, D.B., Toyokawa, H., O'Donnell, D.R., Smith, D.M., Dudas, J.R., Rubin, J.P., and Marra, K.G. (2008). Characterization of transplanted green fluorescent protein+ bone marrow cells into adipose tissue. Stem Cells *26*, 330–338.

Trainor, P. (2013). Neural Crest Cells (Academic Press).

Trainor, P.A. (2010). Craniofacial birth defects: The role of neural crest cells in the etiology and pathogenesis of Treacher Collins syndrome and the potential for prevention. Am. J. Med. Genet. *152A*, 2984–2994.

Trainor, P.A., Dixon, J., and Dixon, M.J. (2008a). Treacher Collins syndrome: etiology, pathogenesis and prevention. Eur J Hum Genet *17*, 275–283.

Trainor, P.A., Dixon, J., and Dixon, M.J. (2008b). Treacher Collins syndrome: etiology, pathogenesis and prevention. Eur J Hum Genet *17*, 275–283.

Trounson, A., Shepard, K.A., and DeWitt, N.D. (2012). Human disease modeling with induced pluripotent stem cells. Current Opinion in Genetics & Development *22*, 509–516.

Valdez, B.C., Henning, D., So, R.B., Dixon, J., and Dixon, M.J. (2004). The Treacher Collins syndrome (TCOF1) gene product is involved in ribosomal DNA gene transcription by interacting with upstream binding factor. Proc. Natl. Acad. Sci. U.S.a. *101*, 10709–10714.

Wise, C.A., Chiang, L.C., Paznekas, W.A., Sharma, M., Musy, M.M., Ashley, J.A., Lovett, M., and Jabs, E.W. (1997). TCOF1 gene encodes a putative nucleolar phosphoprotein that exhibits mutations in Treacher Collins Syndrome throughout its coding region. Proc. Natl. Acad. Sci. U.S.A. *94*, 3110–3115.

Wu, J., Cohen, P., and Spiegelman, B.M. (2013). Adaptive thermogenesis in adipocytes: is beige the new brown? Genes & Development *27*, 234–250.

Yamamoto, Y., Gesta, S., Lee, K.Y., Tran, T.T., Saadatirad, P., and Ronald Kahn, C. (2010). Adipose Depots Possess Unique Developmental Gene Signatures. Obesity *18*, 872–878.

Yu, J., Vodyanik, M.A., Smuga-Otto, K., Antosiewicz-Bourget, J., Frane, J.L., Tian, S., Nie, J., Jonsdottir, G.A., Ruotti, V., Stewart, R., et al. (2007). Induced Pluripotent Stem Cell Lines Derived from Human Somatic Cells. Science *318*, 1917–1920.

CHAPTER 2

USING INDUCED PLURIPOTENT STEM CELLS AS A TOOL TO UNDERSTAND NEUROCRISTOPATHIES

Avery, J, Menendez, L, Cunningham, ML, Lovvorn, H N & Dalton, S. 2014. Using Induced Pluripotent Stem Cells as a Tool to Understand Neurocristopathies. In Neural Crest Cells: Evolution, Development and Disease. Elsevier Inc., pp. 441-459.

Reprinted here with permission from the publisher.

INTRODUCTION

Technologies that allow induced pluripotent stem cells (iPSCs) to be generated through cell reprogramming (Takahashi et al., 2007; Yu et al., 2007) have led to the development of powerful tools that can be used to model human disease and as platforms for drug discovery (Grskovic et al., 2011; Trounson et al., 2012). Disease modeling using iPSCs offers advantages over more traditional animal-based models and has real potential to advance molecular understanding of diseases that are poorly understood. Most notably, patient-derived iPSC models are likely to more completely and faithfully recapitulate the human disease state in cases where the disease is cell autonomous. This is particularly relevant where disease pathogenesis is multifactorial and dependent on the patient's genetic background. Access to patient-derived cells also allows for potential differences between individuals to be assessed. iPSCs are also well suited to modeling disease-related events that occur during development because iPSCs can be differentiated to a wide range of cell types by tightly controlled protocols. If disease progression is associated with a specific developmental defect, differentiation models should capture this and facilitate a more detailed molecular understanding that may then lead to new pathways of therapeutic intervention. As knowledge of progenitor differentiation pathways is gained from this technology, the potential for tissue engineering to repopulate defective cell types becomes more promising.

NEURAL CREST CELLS AND NEUROCRISTOPATHIES

Neural crest cells (NCCs) arise from the neural plate border, migrate to diverse targets throughout the embryo where they differentiate and incorporate into functional tissue (Achilleos

and Trainor, 2012; LaBonne and Bronner-Fraser, 1998; Le Douarin et al., 2008). Defects associated with the emergence of NCCs from the neural plate border, their migration throughout the embryo or their differentiation can contribute to a broad spectrum of defined diseases or syndromes, collectively known as neurocristopathies. This chapter will focus on how iPSC-based technologies can be used to gain a better understanding of neurocristopathies.

NCCs originate from four discrete segments (cranial, cardiac, vagal and trunk) along the neural tube's rostro-caudal axis. Figure 2.1 illustrates the corporal locations that NCCs are targeted as they migrate away from different regions of the neural tube. Several prevalent neurocristopathies are listed that have specific relationships with the different populations of NCCs. Most of these arise from improper specification of neural crest cells, defective migration, compromised proliferation and/or decreased NCC survival. Most of these aspects of neurocristopathies are likely to be cell autonomous and can therefore be approached using iPSCs as a tool.

Cranial NCCs give rise to the bulk of the bone and cartilage that form scaffolding of the head and face and contribute to ganglia, smooth muscle, connective tissue and even pigment cells[7]. NCCs emanating from the cardiac segment contribute to heart development by forming connective tissue associated with the great vessels, the aorticopulmonary septum, smooth muscle cells of the great arteries as well as celiac, superior, mesenteric, and aortic ganglia (Hall, 2008). Vagally-derived NCCs establish the ganglia of the enteric nervous system (ENS) and contribute to neurons of the parasympathetic nervous system (Achilleos and Trainor, 2012; Hall, 2008). Trunk NCCs establish the dorsal root ganglia, contribute to the lower sympathetic nervous system and the peripheral nervous system, as well as give rise to secretory cells of the endocrine system and to pigment cells of the skin (Achilleos and Trainor, 2012; Hall, 2008). Because of the multipotent nature of NCCs, neurocristopathies may take many and varied forms. These include

craniofacial defects (Treacher Collins syndrome), cardiac defects (CHARGE syndrome, Noonan/Leopard syndrome, 22q.11.2 deletion syndromes), enteric nervous system defects (Hirschsprung's disease), peripheral nervous system defects (familial dysautonomia) and melanocyte defects (Waardenburg syndrome, melanoma, piebaldism) (Figure 2.1). This chapter examines several conditions of NCC origin in which iPSCs have the potential to serve as tools to understand detailed aspects of disease progression. There are only a few reports describing the use of iPSCs for modeling neurocristopathies but as will be seen, these have provided encouraging outcomes that support their use as a tool in this important area.

The strategy for generating induced pluripotent stem cells (iPSCs) from patients with neurocristopathies and their subsequent characterization in vitro is similar to that of 'disease in a dish' modeling for other clinical conditions. Our laboratory uses Sendai virus particles to deliver the four reprogramming factors Oct4, Sox2, Klf4 and c-Myc to recipient donor cells that over three weeks are reprogrammed to a pluripotent state. For details about reprogramming procedures see Menendez et al. (Menendez et al., 2013). Once iPSC colonies are obtained, they are genotyped by fluorescence in situ hybridization (FISH) and subjected to G-band analysis to confirm that genetic aberrations have not been introduced during the reprogramming procedure. iPSC colonies are then transitioned to culture in chemically-defined media that is compatible with differentiation into lineages such as neural crest. Cell stocks are frozen at different stages to provide a tiered stock of low passage cells (Menendez et al., 2013).

METHODS FOR NCC DIFFERENTIATION FROM PLURIPOTENT STEM CELLS

Differentiation of human embryonic stem cell (hESCs) and iPSCs towards a neural crest cell fate offers great opportunities to study important aspects of early embryonic development

and also to elucidate molecular mechanisms related to human neurocristopathies. A general scheme for generation of patient-derived iPSCs is shown in Figure 2.2. The first reports of human cells differentiating to NCCs involved co-culture on PA6 stromal cells but this was relatively inefficient (Pomp et al., 2005) and obtaining highly-enriched populations required FACS (fluorescence-activated cell sorting) (Jiang et al., 2009). $Sox9^{+}$ $Ap2^{+}$ cells in these cultures however, could be further differentiated to peripheral neurons through a neurosphere intermediate stage demonstrating that they had developmental potential comparable to their embryonic counterparts(Pomp et al., 2008). A second method used co-culture of hESCs and the mouse stromal line MS5 to generate neural rosettes (Lee et al., 2007). This approach represents the adaptation of existing methods where contaminating NCCs were isolated from neural rosette cultures. A shortfall of this method is that it is inefficient and requires a labor-intensive FACS step.

More recently, methods have been developed that eliminate the need for stromal co-cultures, instead using chemically-defined media supplemented with small molecules and/or growth factors (Chambers et al., 2009; Curchoe et al., 2010; Lee et al., 2010). Most of these methods however, are inefficient and often still require a FACS step. To this point, no method had been developed for efficient, lineage-specific differentiation of human pluripotent cells to a NCC fate. This is obviously important if the development of neurocristopathies is to be understood at the molecular level. To solve this problem we developed a protocol using chemically-defined medium and two small molecule inhibitors, SB431542 (Lefty/Activin/TGFB inhibitor) and BIO (GSK3 Inhibitor/ Wnt activator) (Menendez et al., 2011). This method generates NCC cultures without other contaminating cell types under feeder-free conditions, within a relatively short time frame (10-15 days). NCCs produced by this method have similar

developmental potential to that described by other methods but do not require FACS isolation or co-culture steps. It is unclear if any of these methods generate NCCs that are patterned as is seen along the rostro-caudal axis during embryogenesis or, if they have broad NCC developmental potential. The paucity of molecular markers that discriminate between cranial, cardiac, vagal and trunk identities have made this question difficult to address. NCCs derived from human pluripotent cells can however, be further differentiated into peripheral neurons, adipocytes, bone, cartilage and smooth muscle, indicating that they possess cranial, cardiac and perhaps vagal NCC differentiation potential.

hESCs and iPSCs alike may be utilized to balance the *in vivo* and *in vitro* information garnered from neural crest development in model organisms. While many molecular markers and processes of neural crest development are shared between human and model organisms such as Xenopus, chick, and mouse, there are vast differences that require examination of human model systems (Stuhlmiller and García-Castro, 2012). In recent years, significant progress has been made in complementing our knowledge of human neural crest development and its distinctive variances. These advancements were achieved through exhaustive morphological analysis of early human neural crest development (O Rahilly and Müller, 2007), molecular profiling of human neural tube explants (Thomas et al., 2008), and marker analyses defining cranial and trunk regions from intact early human embryos (Betters et al., 2010). Despite these developments, stem cell technologies are recognized as much-needed tools that have the capacity to address limitations of studying the human model and further our understanding of molecular mechanisms that drive normal and aberrant neural crest development (Stuhlmiller and García-Castro, 2012).

NEUROCRISTOPATHIES

Familial dysautonomia

Familial dysautonomia (FD), also known as Riley-Day disease, is a rare disease in the general population but one that affects 1:3700 births from Jewish individuals of eastern European ancestry (Axelrod, 2005; Slaugenhaupt, 2002). Most notably, it impacts the autonomic and sensory nervous systems resulting in an age-increasing reduction of dorsal root ganglion and superior cervical sympathetic ganglion neurons. FD symptoms include the inability to produce tears, hypotonia and speech and growth developmental delays and only 50% of patients reach age 30 (Slaugenhaupt, 2002). FD patients also suffer from cardiac problems due to postural hypotension without compensatory tachycardia and episodic hypertension, as well as chronic kidney disease believed to be caused by the inability to regulate renal hemodynamics (Rekhtman et al., 2010; Slaugenhaupt, 2002). FD is an autosomal recessive disease where ~99% of affected patients have point mutations in the IkB kinase complex-associated protein (IkBKAP) gene, resulting in splicing defects and reduced IkBKAP expression (Lee and Studer, 2011).

In 2009, the Studer laboratory described the first use of iPSCs to model a neurocristopathy following the characterization of FD patient-derived cells (Lee et al., 2009). FD patient derived-iPSCs (FD iPSCs) differentiate to NCCs but show migratory defects and tissue-specific differences between mutant and wild-type IkBKAP transcripts, similar to that in seen in FD patient-derived tissue. Even though FD-NCCs differentiate to peripheral neurons, they do so at a reduced efficiency. Microarray analysis comparing wild-type and FD-NCCs identified 89 differentially expressed genes. Some of these are known to be involved in peripheral neurogenesis (SLC17A6, MAP4, INA, STMN2, and ASCL1) and were downregulated in FD-

NCCs relative to controls. Pharmacological evaluation of FD-NCCs was also used to evaluate the effects of potential therapeutics such as the plant hormone kinetin, which elevates the expression of wild-type IkBKAP. Under sustained exposure to kinetin, FD-NCCs showed elevated expression of wild type IkBKAP and increased differentiation to peripheral neurons. These observations illustrate how iPSC models can be used broadly for drug screening applications and therapeutic development. More generally, the study also shows the power of iPSCs as a tool to recapitulate and understand neurocristopathies.

Hirschsprung's Disease

Hirschsprung's disease (HSCR) is a developmental disorder arising from malformation of the enteric nervous system (ENS) within the hindgut (Parc et al., 1984; Whitehouse and Kernohan, 1948). At the tissue level HSCR is characterized by aganglionosis in the lower intestine resulting in loss of peristaltic activity due to the absence of peripheral neuron innervation, see Figure 2.3. Proper peristaltic activity requires the coordination of gut smooth muscle action via enteric nervous signaling. This signaling is propagated by plexuses of ganglia beneath the longitudinal muscle and within the intestinal submucosa. Normal proximal ganglionic colon is shown in Figure 2.3a (uppermost portion), contrasted against the contracted portion of aganglionic distal colon, which is unable to relax in the absence of neural crest-derived ganglia (lower portion of Figure 2.3a). Histologically, differences between ganglionic and aganglionic colon are apparent: ganglia (blue stars) are visible within the ganglionic portion of the proximal colon between the longitudinal and circular muscle layers (Figure 2.3c), but are absent from within the submucosal layer and exterior to the circular muscle layer in the aganglionic portion (Figure 2.3d). Diagnosis of HSCR is typically made postnatally due to

intestinal obstruction associated with the failure to pass meconium within the first 48 hours of life. Patients also display abdominal distension, vomiting and neonatal enterocolitis (Amiel et al., 2007a). Depending on the degree of severity for this disease, other individuals may be diagnosed later in infancy or even into adulthood with severe constipation, chronic abdominal distension, vomiting and failure to thrive (Amiel et al., 2007a; Parc et al., 1984).

Hirschsprung-associated aganglionosis presumably results from the migration failure of vagally and sacrally derived NCCs to reach their target in the developing hindgut between gestational weeks five and twelve (Amiel et al., 2007b; Kenny et al., 2010). The incidence of HSCR is approximately 1:5000 live births although the degree of aganglionosis and corresponding disease severity is variable and only presents as an isolated trait (aganglionosis not associated with other underlying causes) in ~70% of cases, whereas the remaining cases are observed as associated malformations of complex syndromes (Amiel et al., 2007b; Mundt and Bates, 2010). HSCR displays strong sexual dimorphism with males being affected up to two to four times more often/severe than females (Amiel et al., 2007a) (this is true overall but for short and long segment disease which are components of HSCR there is a recognized female predominance). There may also be ethnic disparities in terms of HSCR predisposition (Torfs et al., 1994).

In addition to Hirschsprung's syndromic or isolated nature, the disease may arise through familial or sporadic modes and may be further categorized into two subtypes depending on the degree of aganglionosis. Short-segment HSCR (S-HSCR) is the most common and affects the rectum and a short portion of the colon. Long-segment HSCR (L-HSCR) affects longer tracts of the colon and in severe cases, presents as total colonic (~10% of cases) or total intestinal aganglionosis (Brooks et al., 2005; Heanue and Pachnis, 2007). Although the vast majority of

patients with HSCR are sporadic, it can also be inherited. Isolated HSCR transmission is non-Mendelian implying that it is a multifactorial disease. The dissimilar characteristics of syndromic versus isolated HSCR can be striking: cases of isolated HSCR display lower penetrance in that genotypic abnormality leading to aganglionosis in one individual may not cause the same diseased phenotype in another individual, isolated cases also present with the greatest variability in the extent of aganglionosis, and isolated cases display the highest degree of male gender bias (Amiel et al., 2007a; Brooks et al., 2005).

Genetic heterogeneity in HSCR has been demonstrated with at least 10 specific genes suspected of contributing to pathogenesis (Amiel et al., 2007a). The two most commonly implicated genes in isolated HSCR are *RET* (rearranged during transfection) and *EDNRB* (endothelin receptor type B), with *RET* suffering coding sequence mutations in ~50% and 15-20% of familial versus sporadic HSCR cases, respectively (Amiel et al., 2007a). In addition to *RET* and *EDNRB*, mutations have been found within *GDNF*, *EDN3*, *ECE1*, *SOX10*, *ZFHX1B*, and *PHOX2B*. In the context of ENS development, these genes encode proteins that form a network of inter-related signaling pathways that are responsible for the development of enteric ganglia from NCCs; collectively and in coordinated fashion, these proteins regulate the survival, proliferation, migration and differentiation of NCCs in the developing ENS. Furthermore, HSCR has been associated with at least 32 syndromes and shows a strong association with Goldberg-Shprintzen and BRESHEK - brain abnormalities, retardation, ectodermal dysplasia, skeletal malformation, Hirschsprung's disease, ear/eye anomalies and kidney dysplasia (Amiel et al., 2007a). Chromosomal abnormalities in HSCR cases are less common although up to 10% of all HSCR cases are associated with trisomy 21(Amiel et al., 2007a).

Although several mouse models have identified genetic factors (such as *RET*) associated with HSCR and can recapitulate many features of human HSCR, the full genetic pathogenesis of this disease remains incomplete (Barlow et al., 2013). HSCR provides an excellent model for multigenic disease study and like many congenital disorders, lends itself extremely well to the use of iPSC technology. Although HSCR is likely to be multifactorial in nature, elucidating its pathogenesis can be approached with iPSC technology and various in vitro approaches including differentiation and migration assays. Hirschsprung's disease-specific iPSCs have already been generated and differentiated to neural crest in support of this general premise (Figure 2.4). Amenability to manipulation, scalability of disease-specific cell types, the capacity to focus on single or multiple targets simultaneously and the rapidity of phenotype assessment make iPSCs a potent tool for studying Hirschsprung's disease.

While mutations in *RET* coding sequences account for 50% of familial and 15–20% of sporadic HSCR cases, most familial HSCR cases show association with the *RET* locus by linkage analysis. Investigation into non-coding mutations has identified a single nucleotide polymorphism (SNP) within intron 1 that is far more frequently associated with HSCR than observed coding sequence mutations (Burzynski et al., 2009; Emison et al., 2005) . The detailed understanding of *RET* and its role in Hirschsprung's disease allows for a targeted approach to be used in iPSC-based models of the disease that are likely to generate important information. Additional evidence demonstrates that *RET* plays a role in HSCR symptoms associated with other congenital syndromes such as congenital central hypoventilation syndrome (CCHS). Alterations in RET expression or stability therefore appear to lie at the nexus for complex modes of HSCR pathogenesis. As previously mentioned, patients with PHOX2B mutations display the HSCR phenotype. The vast majority of CCHS patients also carry PHOX2B mutations

(Burzynski et al., 2009). Importantly, transmission of a *RET* hypomorphic allele in CCHS patients increases the risk for HSCR, implying an epistatic interaction between PHOX2B and RET in HSCR (Burzynski et al., 2009). Data generated in mice show that PHOX2B is required for RET expression in enteric NCCs and that mutant forms of PHOX2B are linked to compromised RET expression and thus, aganglionosis beyond the foregut (Burzynski et al., 2009; Pattyn et al., 1999). Furthermore, Down's Syndrome patients that concomitantly display HSCR also carry hypomorphic *RET* alleles (Amiel et al., 2007a; Burzynski et al., 2009). In mouse models of HSCR, reduced RET expression in $Ret^{9/-}$ mice (mice with a knocked-in RET^{9} isoform that has reduced expression) recapitulates many of the most common features of HSCR including distal colon aganglionosis, incomplete penetrance and confers a similar sex bias to that observed in humans (Burzynski et al., 2009; Uesaka et al., 2008). While mutations in other proteins such as EDNRB display colonic agangliosis, especially in closed populations such as Mennonite communities, the importance of RET mutations cannot be understated. Fully 5% of all HSCR cases involve only mutations in EDNRB and its ligand EDN3, which typically present with S-HSCR, however, in mouse studies concomitant mutations in both *Ret* and *Ednrb* lead to almost complete aganglionosis (Barlow et al., 2003; Heanue and Pachnis, 2007). In fact, mutation of the *RET* gene is now thought to be requisite in the majority of HSCR cases (Burzynski et al., 2009).

Together, these factors suggest that RET occupies a critical intersection between the monogenic and complex forms of HSCR pathogenesis. However, a complete molecular description of intestinal aganglionosis remains to be determined. Patient-specific iPSCs (see Figure 2.4) should prove an invaluable tool to determine these associations. As proof of concept, reprogramming of Hirschsprung's patient fibroblasts to iPSCs and their efficient differentiation

to NCCs are shown in Figure 2.4. Fibroblasts from an HSCR affected adult male with two affected children were collected (Figure 2.4a) and reprogrammed according to Menendez et al, 2013 (Menendez et al., 2013). Pluripotency was demonstrated following establishment of stem cell colonies by live alkaline phosphatase (AP) staining and immunofluorescence staining of three pluripotent markers– OCT4, NANOG, and SOX2 (Figures 2.4b-j). These iPSCs were then differentiated towards a NCC fate according to the method developed by Menendez et al, 2011(Menendez et al., 2013) Differentiation from iPSCs to NCCs was confirmed by flow cytometry (Figure 2.4k) using antibodies against the low-affinity nerve growth factor receptor (p75) and HNK-1, a glucoronyl transferase involved in neuronal cell surface protein glycosylation and neuronal cell adhesion. NCC differentiation was further confirmed by immunofluorescence using antibodies against AP-2B (activating enhancer binding protein 2 beta), p75 and HNK-1 (Figures 2.4l-n, p-r, and t-v). Increased staining for these markers correlated with loss of OCT4 and NANOG expression (Figure 2.4o). Figure 2.4s demonstrates typical NCC morphology upon differentiation. These cells are well suited to serve as an experimental platform to evaluate pathogenic mechanisms of HSCR.

Beyond replicating a 'disease in a dish,' a chief ambition in pluripotent cell research is the eventual reintroduction of normal cells as potential therapies for disease. This is also true in regards to understanding underlying mechanisms of disease pathogenesis. Often it is necessary for human pluripotent cells or tissues to be xenografted into model organisms to understand their behavior in an organismal context, or as in the case of NCCs, their proper proliferation, migration, and subsequent colonization of target tissue(s). However, reintroduction of pluripotent cells into model systems, such as Ret-/- mice, may encounter hurdles that are a consequence of non-cell autonomous effects. The obstacle of non-cell autonomous effects in

regards to NCC migration and ENS development was highlighted by Bogni et al., 2008 (Bogni et al., 2008). The authors demonstrated that murine intestinal ENS progenitors could be transplanted into Ret deficient hosts; however, while transplanted cells were able to fully colonize the entire length of the gastrointestinal tract in wild-type mice, transplanted cell migration was halted at the proximal foregut in Ret-/- mice (Bogni et al., 2008). Thus, it must be appreciated that surrogate disease systems, such as in RET-/- mice for HSCR for example, may display complications arising from factors extrinsic to deficiencies in the cell type under study and co-dependent on proper microenvironments and signaling milieus of target tissue(s).

Treacher Collins Syndrome

Treacher Collins syndrome (TCS) is a rare condition affecting 1:50,000 live births although some perinatal deaths have been reported and is typically associated with improper craniofacial architecture arising from insufficient generation of cranially fated NCCs (Figure 2.5) (Trainor, 2010). TCS was initially described by Treacher Collins in 1900 and clinically presents with a range of characteristics including hypoplasia of the facial bones, cleft palate, external and middle ear anomalies and defects in brain development (Cohen et al., 1995; Collins, 1900; Milligan et al., 1994; Poswillo, 1975; Stovin et al., 1960; Teber et al., 2004; Trainor, 2010). Multiple studies indicate that the majority of TCS cases can be attributed to mutations in the *TCOF1* gene on chromosome 5 (Jabs et al., 1991; 1993; Sakai and Trainor, 2009; Trainor et al., 2008; Wise et al., 1997). *TCOF1* encodes the serine/alanine-rich nucleolar protein, treacle (Cynthia Isaac, 2000; Dixon et al., 1997; Wise et al., 1997).

The *TCOF1* gene comprises 26 exons and can be differentially spliced to generate up to 6 transcript variants (Bowman et al., 2012). Over 200 different mutations have been identified in

TCOF1 and many of these have implicated roles in TCS pathology including deletions, insertions, missense, nonsense and splicing mutations (Splendore et al., 2005; Trainor, 2010). Deletions of 1-41 nucleotides in length are the most common class and only exon 24 has been reported as a mutational hot spot with a common 5-bp deletion occurring with a frequency of 17% of TCS cases (Splendore et al., 2005). Half of all TCS cases have no previous family history and arise from de novo mutation (Jones et al., 1975; Trainor, 2010). Diagnosing TCS may often be confounded by the fact that a high degree of both inter- and intra-familial phenotypic variations are commonly observed (Dixon et al., 1994; Marres et al., 1995). In many cases TCS phenotypes are mild and go undiagnosed until an offspring or sibling displaying a more severe phenotype is diagnosed (Trainor, 2010).

Mouse models of TCS have demonstrated that normal *Tcof1* expression is critical to the formation, proliferation and survival of NCCs (Dixon et al., 2000; 2006). These studies, in conjunction with Gonzales et al. established that Tcof1 participates in ribosome biogenesis and maturation, and that defects in Tcof1 result in a diminished pool of mature ribosomes and compromised protein synthesis (Gonzales, 2005). The current view of TCS is that compromised ribosome biogenesis contributes to reduced numbers of emerging NCCs at the time of neural tube closure due to decreased proliferation and increased apoptosis (Dixon et al., 2006; Gonzales, 2005; Trainor, 2010). Jones et al. (Jones et al., 2008) demonstrated that *Tcof1* haplo-insufficiency in mice provokes p53-dependent apoptosis within the neuroepithelium of the neural crest, thus diminishing the NCC progenitor pool. As a consequence, fewer proliferating NCCs emanate from the branchial arches to form the proper craniofacial architecture (Jones et al., 2008).

Collectively, data suggest that mutations within *Tcof1* result in aberrant NCC formation and survival. Subsequently, an insufficient number of cranially-fated NCCs are available to create the scaffold on which the head and face are constructed. This is a simplified scenario as the high degree of variability in disease severity suggests that a myriad of factors contribute to TCS. Likewise, the complete picture of the molecular function of the treacle protein is not well characterized. In addition to the aforementioned association in ribosome biogenesis, treacle may play other roles depending on its subcellular localization. Recently, Barlow et al. demonstrated that *Tcof1* may act as a modifier of *Pax3* during enteric nervous system development, wherein compound haplo-insufficient *Pax3:Tcof1* mice display an exacerbated phenotype of colonic aganglionosis - this implies that TCOF1 may also play a role in HSCR pathogenesis (Barlow et al., 2013). Animal models of TCS alone may be inadequate to fully characterize the role of treacle and its impact on TCS. A primary reason for this is that treacle conservation among vertebrates is low. For example, amino acid sequence identity between mice and human is only 62% and between *Xenopus* and human only 19% (Dixon et al., 1997; Gonzales, 2005). Mechanistic studies on human embryos are obviously not an option, making patient-specific iPSC technology an attractive tool for understanding the molecular pathogenesis of TCS. Furthermore, parallel studies between parent, offspring and sibling derived iPSCs and derivative NCCs are likely to yield a critical understanding relating to phenotype variability. Because TCS is thought to be a monogenic disease, mechanistic studies utilizing patient-specific iPSCs should be straightforward.

Currently, the Dalton laboratory has successfully generated patient-specific iPSCs from three different patients, two of which are siblings (Figure 2.5). Both the clinical and 3D computerized tomography (CT) scan images demonstrate several characteristics typical of TCS

patients including the variability of phenotype among family members: both exhibit the undersized jaw (micrognathia) (Figure 2.5a, b, e-g and red arrowheads), clefting of the inferolateral orbit (Figure 2.5a-d, f, g, and green arrowheads), as well as the zygomatic arch (Figure 2.5e, blue arrowheads). The male child exhibits more severe soft tissue involvement as noted by the increased downward slope of the eyes, eyelid coloboma and microtia (small ear) (Figure 2.5a & b). The external and middle ear malformations common to TCS necessitate the use of bone conducting hearing aids (Figure 2.5a & b, f & g).

Fibroblasts from these patients have been reprogrammed to iPSCs and differentiated to NCCs via the method presented in Menendez et al (Menendez et al., 2013). Studies to determine the nature of NCC defects are ongoing. Specifically, flow cytometric analyses of apoptosis are being employed to determine if similar phenomena observed in mice may be recapitulated in vitro. Additionally, identifying apoptotic maxima during differentiation to NCCs will guide future experiments to determine the role of treacle specific to its subcellular localization and involvement in NCC development.

CHARGE syndrome

CHARGE syndrome was defined in 1981 as an acronym for a collection of symptoms: coloboma of the eye, heart defects, atresia of the nasal choanae, retardation of growth and/or development, genital and/or urinary abnormalities and ear abnormalities and deafness (Pagon et al., 1981). CHARGE is an autosomal dominant disease affecting 1:10,000 births. Around 65% of these cases are a result of mutations in *CDH7*, an ATP-dependent chromatin remodeler gene (Jongmans et al., 2006). Due to the nature of CHARGE-associated symptoms it was originally

assumed to be a neurocristopathy but it was not until 2010 that direct evidence for this was obtained, using hESCs and their differentiation to neural crest cells (Bajpai et al., 2010).

CHARGE syndrome is an excellent example of how pluripotent stem cells have been used to gain a deeper insight into the molecular basis of a poorly understood condition. Using differentiation models, *CDH7* was identified as a key regulator of NCC formation and function (Bajpai et al., 2010). Genes impacted by *CHD7* include *TWIST, SLUG* and *SOX9*, all of which are critical for NCC migration. CHD7 functions by binding BRG1, a member of the PBAF chromatin-remodeling complex. Once in a complex, CDH7 and PBAF regulate expression of SOX9 and TWIST by binding H3K4me1-marked enhancer regions that control chromosome architecture and transcriptional activity (Bajpai et al., 2010). The use of patient-derived iPSCs (CHARGE-iPSCs) will be critical to unravel the molecular complexities of CHARGE syndrome. For example, CHARGE-iPSCs from patients harboring CDH7 mutations can be differentiated to NCCs to test if migration and/or differentiation is affected. Overexpression of *CDH7* should rescue the expression of genes like *SOX9* and *TWIST,* as well as the migration problems. Jongmans et al. (Jongmans et al., 2006) reported 67 different *CDH7* mutations in 69 CHARGE patients with no corresponding genotype/phenotype relationship. The use of iPSCs might help find such correlation, since they might result in different levels of *CHD7* expression during NCC differentiation, which could correlate with different NCCs defects.

Noonan and LEOPARD syndromes

LEOPARD syndrome is an acronym of its most common symptoms: lentigines, ECG conduction abnormalities, ocular hypertelorism, pulmonary stenosis, abnormal genitalia, retardations of growth, and deafness (Keyte and Hutson, 2012). Noonan syndrome symptoms

include dwarfism, hypertrophic cardiomyopathy, and craniofacial malformations and affects 1:1000-1:2500 births (Romano et al., 2010; Tullu et al., 2000). Around 50% of cases for Noonan syndrome and 80-90% of LEOPARD syndrome are caused by an allelic dominant mutation in *PTPN11*, a gene encoding the tyrosine phosphatase SHP2 (Digilio et al., 2006; Tartaglia et al., 2001). In Noonan patients most *PTPN11* mutations are gain of function, promote protein stabilization at the structural level and elevated mitogen-activated protein (MAP) kinases ERK1/2 activity (Tartaglia et al., 2001). In mice, this leads to reduced osteoblasts differentiation from NCCs and consequently, craniofacial defects. Treatment of mice with the ERK1/2 inhibitor U0126 restored normal craniofacial development (Nakamura et al., 2009b). In contrast to Noonan syndrome, LEOPARD syndrome mutations in *PTPN11* are frequently associated with loss of function. Mice with reduced SHP2 expression have a corresponding decreased ERK1/2 activity resulting in loss of NCC migration to the heart and cranial areas (Nakamura et al., 2009a). Complete loss of SHP2 in NCCs results in lower number of cells reaching the outflow tract cushions resulting in septation defects. Cranial NCCs migrated properly but failed to differentiate to osteoblasts, without any increase of apoptosis.

iPSCs from two LEOPARD syndrome patients (LEOPARD iPSCs) have been generated and used to study differentiation to cardiomyocytes (Carvajal-Vergara et al., 2010). Comparison of LEOPARD iPSCs to those from normal patients showed significant differences in the phosphoproteosome as well as decreased ability to respond to FGF activation of ERK. As described above, proper regulation of ERK is very important for NCC differentiation since either too much or too little ERK signaling leads to craniofacial and cardiac problems. LEOPARD and Noonan iPSCs will be very useful to study NCC differentiation and to verify if the defects seen in mouse are comparable to humans.

22q11.2 deletion syndromes

22q11.2 deletion syndromes, also called DiGeorge syndrome, Velocardiofacial syndrome and conotruncal anomaly face syndrome, affect 1:4000 to 1:1600 births. 95% of cases are caused by the de novo deletion of a 3Mb region in chromosome 22 at band q11.2 (Oskarsdottir et al., 2004; Shprintzen, 2008). There are more than 180 different clinical features associated to this spectrum of diseases, some of the most common being heart defects, palatal anomalies, vascular anomalies, psychiatric disorders, learning difficulties and immune disorders. The q11.2-deleted region contains 30-40 genes of developmental importance including *COMT, UFD1L, TBX1* and *DGRC8*. Cardiac defects for this syndrome have been associated with migration and survival defects in cardiac NCCs.

TBX1 encodes the transcription factor T-box 1 that although not expressed in NCCs, is necessary to regulate signaling molecules from the pharyngeal ectoderm and endoderm such as *GBX2, SLIT* and *FGF8*. Without these signals, mouse cardiac NCC migration to the fourth pharyngeal arch fails, resulting in pharyngeal abnormalities that resemble those seen in 22q11.1 syndrome (Calmont et al., 2009). Another important gene for NCCs in the 22q11.2 region is *DGCR8*. This gene encodes a protein critical for microRNA (miRNA) processing, and its conditional ablation in mouse NCCs results in severe cardiovascular malformations (Chapnik et al., 2012). Contrary to *TBX1* deficiency, these defects are due to an increase of apoptosis of cardiac neural crest cells just before they reach the outflow tract (Chapnik et al., 2012). Patient-specific iPSCs could be differentiated to neural crest and then implanted in mice to study migration to the branchial arches. Similar phenotypes to that seen in mouse models may be seen such as migration defects (*TBX1* mutants) or increased apoptosis (*DGCR8* mutations). It would

be interesting to see if NCCs from these patients show an increase of apoptosis in vitro, and if so, if it can be rescued by overexpressing *DGCR8*.

Waardenburg syndrome

Waardenburg syndrome (WS) is an autosomal dominant disease affecting 1:42,000 births. WS symptoms include deafness, constipation, partial albinism, dystopia canthorum and in some cases, atrial septal defects and spina bifida (Banerjee, 1986). Patients are classified as type I, II, III or IV depending on the combination of symptoms they present. Up to six genes have been linked to the disease: *PAX3* in 90% of type I and III, *MITF* in type II (15%), *EDN3* and *EDNRB* in type II (<5%) and type IV (20-30%), *SOX10* in type II (15%) and type IV (50%), and *SNAI2* in type II (<5%) (Pingault et al., 2010). Approximately 70% of patients with type II and 15-35% of type IV patients do not exhibit mutations in these six genes. Most cases of type I WS are due to loss of function mutations in *PAX3*, an important regulator of early neural crest specification. There are more than 70 reported point mutations of *PAX3* in type I WS, with no correlation between them and the severity of the syndrome (Pingault et al., 2010). Most mutations affect the *PAX3* DNA binding domain or its homeodomain. In mouse models, *PAX3* mutations lead to increased apoptosis that could be rescued by p53 mutations (Wang et al., 2011). Since *PAX3* is a gene expressed very early during neural crest specification, differentiation of WS iPSCs (iPSCs derived from WS patients) to NCCs might be the only way to study the effects these multiple mutations have in early human NCC differentiation. For example, iPSCs from patients with different mutations could show different degrees of apoptosis. Experiments with mouse fibroblast show that mutations in PAX3 not only affect the DNA binding ability but its nuclear localization (Corry et al., 2010), therefore iPSCs could show a

similar defect in WS patients. Type IV WS, also referred as Waardenburg-Shah syndrome, presents an association of hypopigmentation and Hirschsprung's disease. Around 50% of those patients carry mutations in SOX10 and mouse models have shown it is very important for NCC differentiation to glial cells and melanocytes (Mollaaghababa and Pavan, 2003; Pingault et al., 2010; Southard-Smith et al., 1999). Both *PAX3* and *SOX10* control *MITF* expression, a gene required for melanocyte differentiation. WS-iPSCs could be differentiated to NCCs and then to melanocytes. Since both *PAX3* and *SOX10* regulate early melanocyte differentiation, iPSCs offer the opportunity to study early steps as opposed to the study of mature melanocytes. Furthermore, in those WS-iPSCs that present defects in melanocyte differentiation and *MITF* expression, microarray analysis could point to some unknown *MITF* regulator, which could be mutated in those patients and be the cause of the phenotypic variability or explain WS cases with unknown mutation. It is important to point out that the methods utilized to differentiate NCCs into melanocytes are currently inefficient- an important technical barrier that must be overcome in order to study pathologies such as WS (Clewes et al., 2011).

Piebaldism

Piebaldism is characterized by the absence of melanocytes in patches of skin and hair and the by presence of a white forelock in ~90% of patients. Piebaldism is a rare autosomal dominant disorder in which ~75% of cases are due to mutations in the *KIT* gene. The KIT protein is a receptor tyrosine kinase, and it activates multiple signaling cascades such as phosphatidylinositol 3'-kinase (PI3'-kinase), Src Family Kinase (SFK), MAP kinase and phospholipase C and D pathways (Lennartsson and Rönnstrand, 2012). KIT is a receptor for the stem-cell growth factor expressed in NCC-derived melanoblasts and it is required for their migration (Ezoe et al.,

1995). Melanoblasts also show increased apoptosis under conditions where KIT signaling is compromised (Ito et al., 1999).

Although piebaldism is mostly considered a cosmetic defect, the study of iPSCs from these patients could help understand how deregulation of *KIT* affects melanocyte differentiation. For example, they could help understand if, in humans, *KIT* mutations result in an increase of apoptosis during melanoblast differentiation, a migration defect of the NCCs or a combination of both, and microarray analysis could point to new *KIT* targets in human melanocytes. Piebaldism iPSCs can also be use similarly to FD-iPSCs for drug screens. Piebaldism patient derived-melanocytes could be screened for activation of KIT downstream pathways and those drugs could be potentially used in topic ointments to treat piebaldism.

CONCLUDING COMMENTS

Development of technology for the derivation of patient-specific pluripotent cells represents a major leap forward for modeling and potentially treating human disease (Southard-Smith et al., 1999). These tools will be a valuable part of deciphering disease pathogenesis and are likely to uncover aspects of human disease that would be unanticipated from other approaches. Several reports have already described the use of iPSC technology to model neurocristopathies. One potential outcome of this is the development of new therapeutics from iPSC-based drug screens. Although animal models have been critical to reach our current level of understanding, patient-derived iPSC models are likely to take this to the next level particularly in the area of personalized medicine.

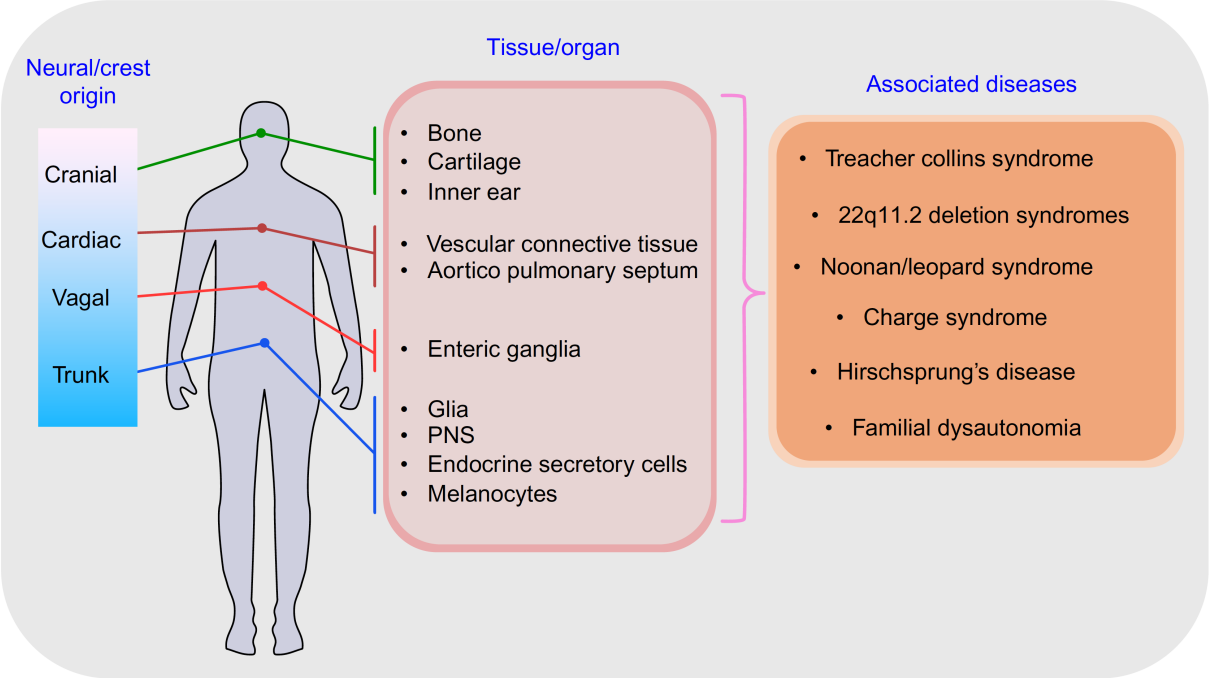

Figure 2.1- Depiction of neural crest cell (NCC) origin along the rostro-caudal axis of the neural tube with corresponding tissues and associated diseases in humans. In vertebrates, the neural tube gives rise to neural crest cells, which then migrate from distinct regions along the neuraxis to specific areas of the organism where they differentiate into an extremely diverse array of tissues. As a consequence of NCC multipotency, perturbations in NCC differentiation, migration, proliferation, and/or survival may lead to a wide variety of associated diseases, termed neurocristopathies, which may primarily be limited to one type of tissue, such as the enteric nervous system observed in Hirschsprung's disease, or affect many tissue types as observed in LEOPARD syndrome. (PNS, peripheral nervous system).

Figure 2.2- Patient-specific cells, such as dermal fibroblasts, are collected via biopsy or operative incision. The isolated fibroblasts are amplified in culture prior to reprogramming (red box). Various transduction methods have been developed to introduce reprogramming factors; iPSC induction via Sendai virus delivery allows for transient expression of *OCT4, SOX2, KLF4* and c-*MYC* that yields colonies of reprogrammed pluripotent cells (green box) within 3 weeks when kept on a feeder layer of irradiated mouse embryonic fibroblasts. Reprogrammed cells are adapted to feeder free culture and are genotyped for quality control to ensure no genetic aberrations are introduced during reprogramming. The patient-specific iPSCs are then transitioned to defined media to assess their capacity to differentiate into cells that are representative of the endoderm, mesoderm, and ectoderm, such as neural crest cells (blue box). Genetic and functional assays may demonstrate that these cells are disease-specific cells, which can authentically replicate the 'disease in a dish,' and are powerful tools for disease modeling and high-throughput drug screening.

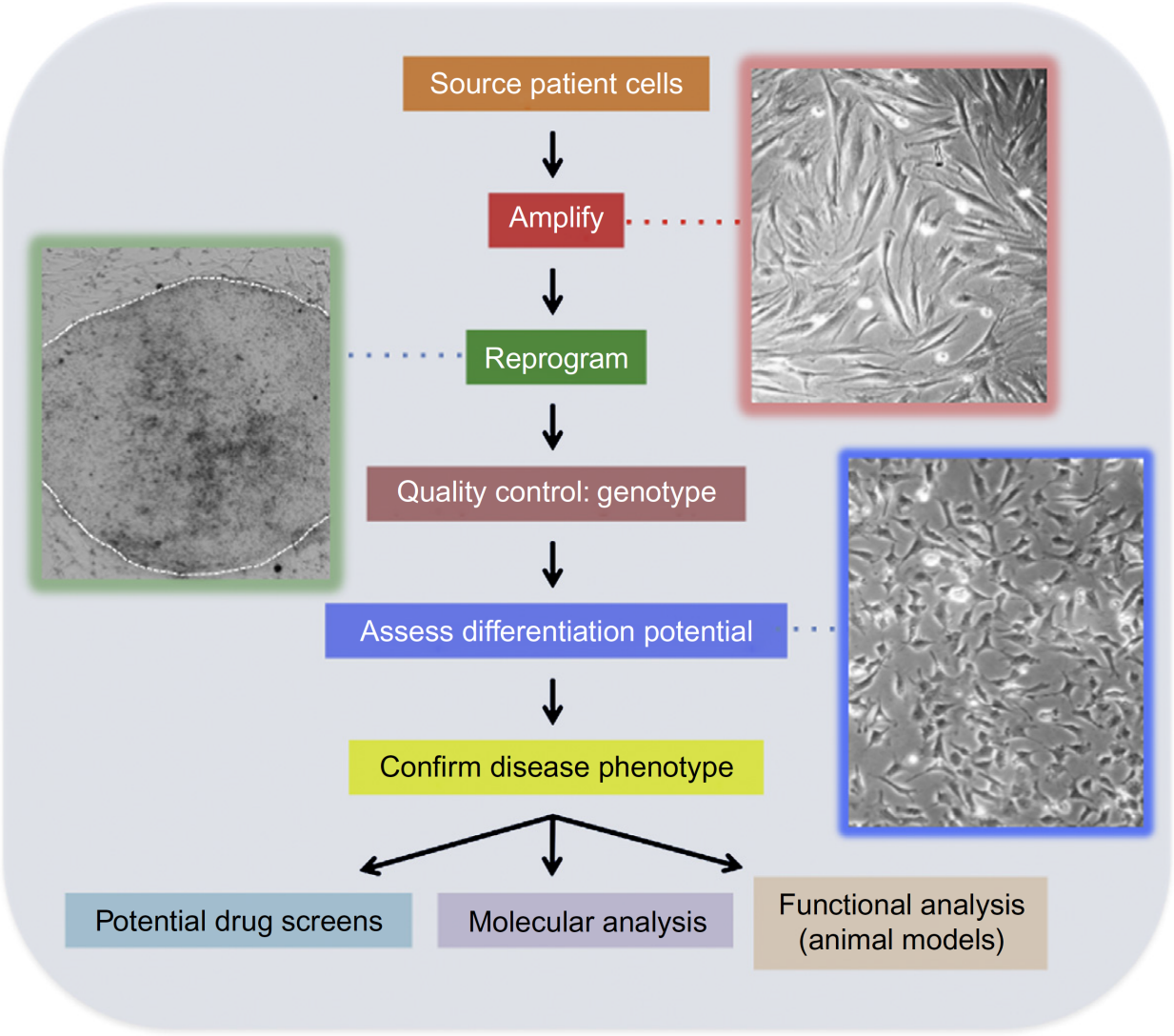
Source patient cells
Amplify
Reprogram
Quality control: genotype
Assess differentiation potential
Confirm disease phenotype
Potential drug screens
Molecular analysis
Functional analysis
(animal models)

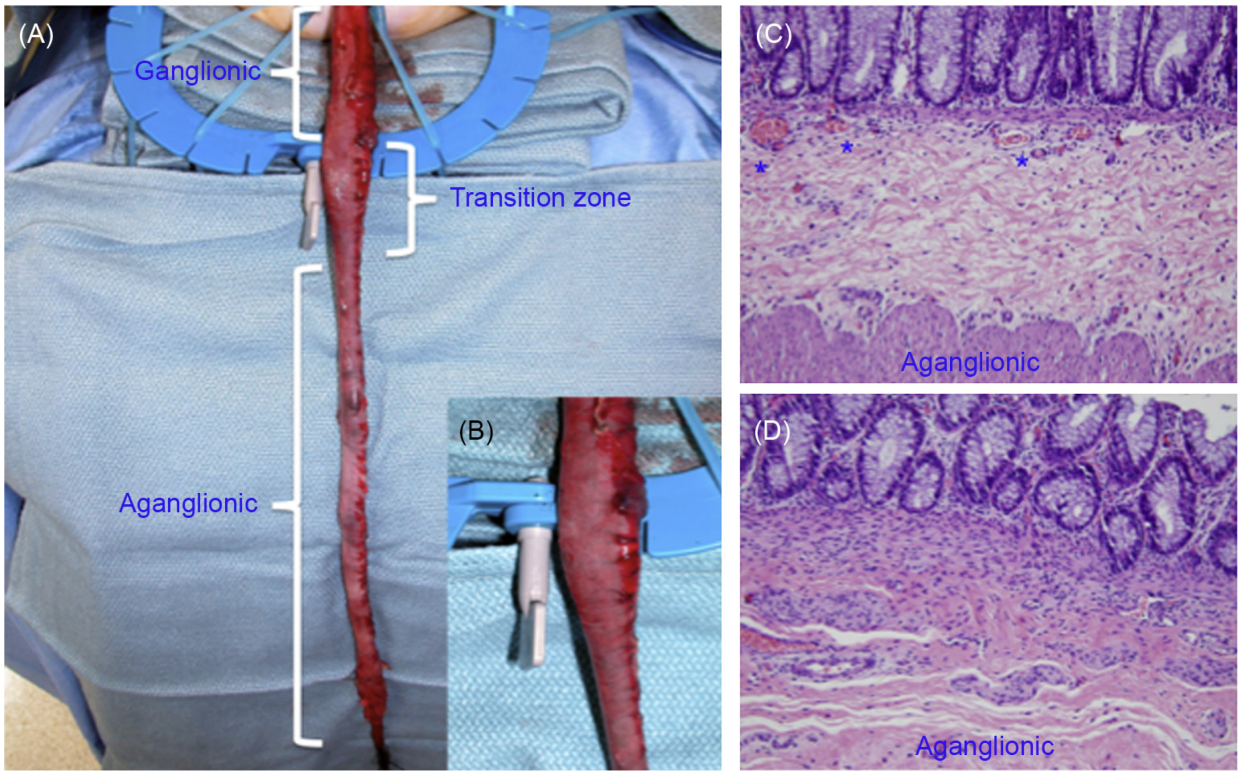

Figure 2.3- An aganglionic distal colon from a Hirschsprung's disease patient. (**a**) Operative photograph depicting long segment aganglionic colon, which is contracted relative to the more proximal normal caliber colon. (**b**) Enlargement of operative photograph of the transition zone between normal and aganglionic colon. The normal ganglionated colon is at top of photo; the transition zone is the middle tapered segment of colon and on microscopy has rare ganglia; and the contracted aganglionic colon appears at the bottom of the image. (**c**) High power (400x) photomicrograph of normal ganglion cells populating the proximal resected colon (ganglia are denoted by blue stars). The layer of ganglia appears between the outer and inner muscle layers of the colon. (**d**) Low power (200x) photomicrograph of aganglionic segment. Sub-mucosa in this region contains numerous hypertrophic nerve twigs.

Figure 2.4- Hirschsprung's disease (HSCR) iPSCs and neural crest cells (NCCs). (a) Bright field image of HS fibroblasts before reprogramming. Immunocytochemistry analysis of HSCR iPSCs shows they are positive for pluripotent markers such as OCT4, NANOG (**b-e**) and SOX2 (**h-j**). (**f**) Alkaline phosphatase (AP) staining of a reprogrammed HSCR iPSC colony. (**g**) Bright field image of a reprogrammed HSCR colony. (**k**) Flow cytometry analysis of HSCR iPSCs and HSCR NCCs at day 20, showing an increase of p75+/HNK1+ population in NCCs. Double positive cells are shown in the circled area. HSCR NCCs are positive for AP2 (**l-o**), p75 (**p-r**) and HNK1 (**t-v**) but negative for OCT4 and NANOG (**o**). (**s**) Bright field image of HSCR NCCs at day 20. Scale bars, 100 μM.

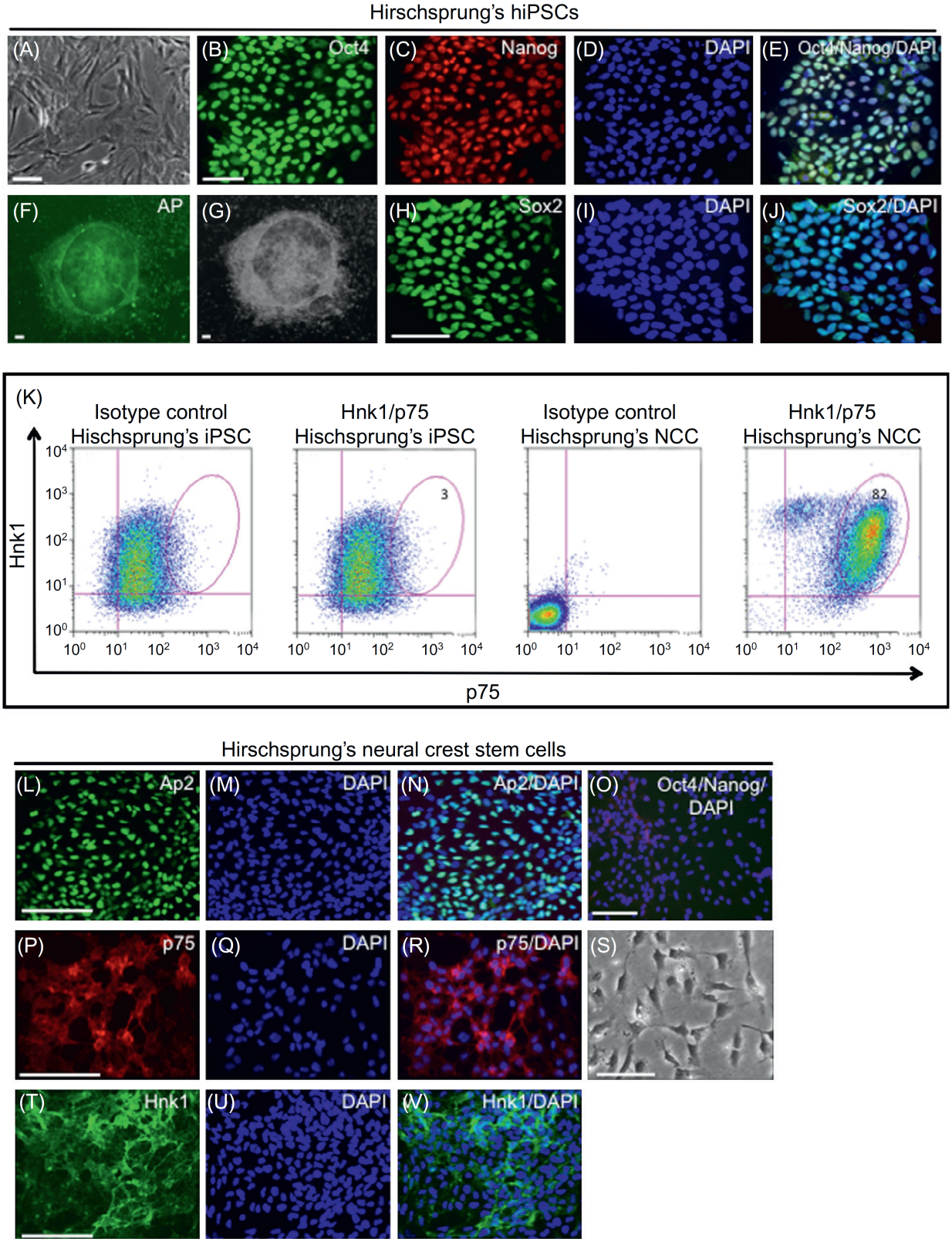
Hirschsprung's hiPSCs
(A)
(B) Oct4
(C) Nanog
(D) DAPI
(E) Oct4/Nanog/DAPI
(F) AP
(G)
(H) Sox2
(I) DAPI
(J) Sox2/DAPI
(K)
Isotype control
Hischsprung's iPSC
Hnk1/p75
Hischsprung's iPSC
Isotype control
Hischsprung's NCC
Hnk1/p75
Hischsprung's NCC
Hnk1
p75
3
82
Hirschsprung's neural crest stem cells
(L) Ap2
(M) DAPI
(N) Ap2/DAPI
(O) Oct4/Nanog/ DAPI
(P) p75
(Q) DAPI
(R) p75/DAPI
(S)
(T) Hnk1
(U) DAPI
(V) Hnk1/DAPI

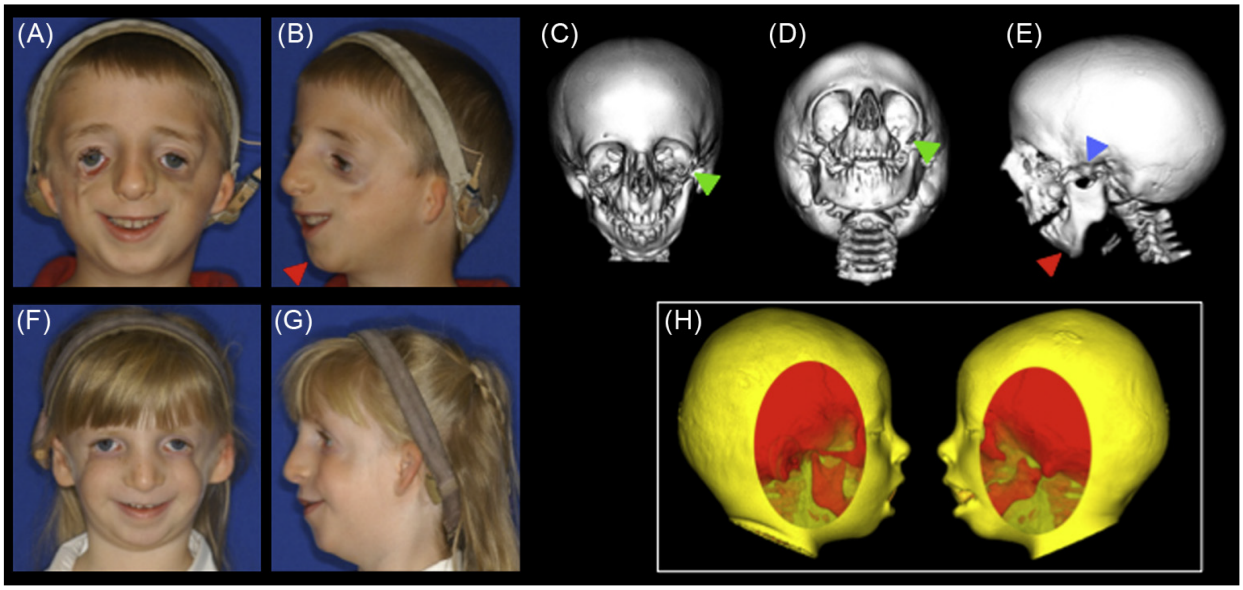

Figure 2.5- Examples of hereditary and sporadic conditions affecting craniofacial structures derived from cranial neural crest. (**a-g**) Clinical and 3D computerized tomography (CT) scan images of Treacher Collins Syndrome patients demonstrating lateral oblique orbital clefts (green arrowheads), micrognathia (red arrowheads), zygomatic arch clefts (blue arrowhead), facial soft tissue deficiency, microtia and auditory canal atresia (**a-e**). Images (**f**) and (**g**) demonstrate the phenotypic variability in TCS in the sister of (**a**). Note the less severely affected facial soft tissue and ear involvement. Middle ear ossicular chain malformations necessitate the use of bone conduction hearing aids (**a, f**). Craniofacial microsomia (**h**) is a sporadic condition affecting the same neural crest derivatives as in TCS but usually presenting with asymmetric involvement. Windows in 3D reconstructions of soft and skeletal tissues demonstrates the asymmetric mandibular dysplasia and zygomatic arch clefting.

REFERENCES

Achilleos, A., and Trainor, P.A. (2012). Neural crest stem cells: discovery, properties and potential for therapy. Cell Research *22*, 288–304.

Amiel, J., Sproat-Emison, E., Garcia-Barcelo, M., Lantieri, F., Burzynski, G., Borrego, S., Pelet, A., Arnold, S., Miao, X., Griseri, P., et al. (2007a). Hirschsprung disease, associated syndromes and genetics: a review. Journal of Medical Genetics *45*, 1–14.

Amiel, J., Sproat-Emison, E., Garcia-Barcelo, M., Lantieri, F., Burzynski, G., Borrego, S., Pelet, A., Arnold, S., Miao, X., Griseri, P., et al. (2007b). Hirschsprung disease, associated syndromes and genetics: a review. Journal of Medical Genetics *45*, 1–14.

Axelrod, F.B. (2005). Familial dysautonomia: a review of the current pharmacological treatments. Expert Opin Pharmacother *6*, 561–567.

Bajpai, R., Chen, D.A., Rada-Iglesias, A., Zhang, J., Xiong, Y., Helms, J., Chang, C.-P., Zhao, Y., Swigut, T., and Wysocka, J. (2010). CHD7 cooperates with PBAF to control multipotent neural crest formation. Nature *463*, 958–962.

Banerjee, A.K. (1986). Waardenburg's syndrome associated with ostium secundum atrial septal defect. Journal of the Royal Society of Medicine *79*, 677–678.

Barlow, A.J., Dixon, J., Dixon, M., and Trainor, P.A. (2013). Tcof1 acts as a modifier of Pax3 during enteric nervous system development and in the pathogenesis of colonic aganglionosis. Human Molecular Genetics *22*, 1206–1217.

Barlow, A., de Graaff, E., and Pachnis, V. (2003). Enteric nervous system progenitors are coordinately controlled by the G protein-coupled receptor EDNRB and the receptor tyrosine kinase RET. Neuron *40*, 905–916.

Betters, E., Liu, Y., Kjaeldgaard, A., Sundström, E., and García-Castro, M.I. (2010). Analysis of early human neural crest development. Developmental Biology *344*, 578–592.

Bogni, S., Trainor, P., Natarajan, D., Krumlauf, R., and pachnis, V. (2008). Non-cell-autonomous effects of Ret deletion in early enteric neurogenesis. Development *135*, 3007–3011.

Bowman, M., Oldridge, M., Archer, C., Rourke, A.O.A., McParland, J., Brekelmans, R., Seller, A., and Lester, T. (2012). Gross deletions in TCOF1 are a cause of Treacher–Collins–Franceschetti syndrome. *20*, 769–777.

Brooks, A.S., Oostra, B.A., and Hofstra, R.M.W. (2005). Studying the genetics of Hirschsprung's disease: unraveling an oligogenic disorder. Clin Genet *67*, 6–14.

Burzynski, G., Shepherd, I.T., and Enomoto, H. (2009). Genetic model system studies of the development of the enteric nervous system, gut motility and Hirschsprung's disease. *21*, 113–127.

Calmont, A., Ivins, S., Van Bueren, K.L., Papangeli, I., Kyriakopoulou, V., Andrews, W.D., Martin, J.F., Moon, A.M., Illingworth, E.A., Basson, M.A., et al. (2009). Tbx1 controls cardiac neural crest cell migration during arch artery development by regulating Gbx2 expression in the pharyngeal ectoderm. Development *136*, 3173–3183.

Carvajal-Vergara, X., Sevilla, A., D'Souza, S.L., Ang, Y.-S., Schaniel, C., Lee, D.-F., Yang, L., Kaplan, A.D., Adler, E.D., Rozov, R., et al. (2010). Patient-specific induced pluripotent stem-cell-derived models of LEOPARD syndrome. Nature *465*, 808–812.

Chambers, S.M., Fasano, C.A., Papapetrou, E.P., Tomishima, M., Sadelain, M., and Studer, L. (2009). Highly efficient neural conversion of human ES and iPS cells by dual inhibition of SMAD signaling. Nat Biotechnol *27*, 275–280.

Chapnik, E., Sasson, V., Blelloch, R., and Hornstein, E. (2012). Dgcr8 controls neural crest cells survival in cardiovascular development. Developmental Biology *362*, 50–56.

Clewes, O., Narytnyk, A., Gillinder, K.R., Loughney, A.D., Murdoch, A.P., and Sieber-Blum, M. (2011). Human Epidermal Neural Crest Stem Cells (hEPI-NCSC)—Characterization and Directed Differentiation into Osteocytes and Melanocytes. Stem Cell Rev and Rep *7*, 799–814.

Cohen, J., Ghezzi, F., Gonçalves, L., Fuentes, J.D., Paulyson, K.J., and Sherer, D.M. (1995). Prenatal sonographic diagnosis of Treacher Collins syndrome: a case and review of the literature. Am J Perinatol *12*, 416–419.

Collins, E.T. (1900). Case with symmetrical congenital notches in the outer part of each lower lid and defective development of the malar bones. Trans Ophthalmol Soc UK *20*, 191–192.

Corry, G.N., Raghuram, N., Missiaen, K.K., Hu, N., Hendzel, M.J., and Underhill, D.A. (2010). The PAX3 Paired Domain and Homeodomain Function as a Single Binding Module In Vivo to Regulate Subnuclear Localization and Mobility by a Mechanism That Requires Base-Specific Recognition. Journal of Molecular Biology *402*, 178–193.

Curchoe, C.L., Maurer, J., McKeown, S.J., Cattarossi, G., Cimadamore, F., Nilbratt, M., Snyder, E.Y., Bronner-Fraser, M., and Terskikh, A.V. (2010). Early acquisition of neural crest competence during hESCs neuralization. PLoS ONE *5*, e13890.

Cynthia Isaac, K.L.M.W.A.P.J.D.M.J.D.E.W.J.U.T.M. (2000). Characterization of the Nucleolar Gene Product, Treacle, inTreacher Collins Syndrome. Molecular Biology of the Cell *11*, 3061–11.

Digilio, M.C., Sarkozy, A., Pacileo, G., Limongelli, G., Marino, B., and Dallapiccola, B. (2006). PTPN11 gene mutations: linking the Gln510Glu mutation to the "LEOPARD syndrome phenotype". Eur. J. Pediatr. *165*, 803–805.

Dixon, J., Brakebusch, C., Fassler, R., and Dixon, M.J. (2000). Increased levels of apoptosis in the prefusion neural folds underlie the craniofacial disorder, Treacher Collins syndrome. Human Molecular Genetics *9*, 1473–1480.

Dixon, J., Hovanes, K., Shiang, R., and Dixon, M.J. (1997). Sequence analysis, identification of evolutionary conserved motifs and expression analysis of murine tcof1 provide further evidence for a potential function for the gene and its human homologue, TCOF1. Human Molecular Genetics *6*, 727–737.

Dixon, J., Jones, N.C., Sandell, L.L., Jayasinghe, S.M., Crane, J., Rey, J.-P., Dixon, M.J., and Trainor, P.A. (2006). Tcof1/Treacle is required for neural crest cell formation and proliferation deficiencies that cause craniofacial abnormalities. Proc. Natl. Acad. Sci. U.S.a. *103*, 13403–13408.

Dixon, M.J., Marres, H.A., Edwards, S.J., Dixon, J., and Cremers, C.W. (1994). Treacher Collins syndrome: correlation between clinical and genetic linkage studies. Clin. Dysmorphol. *3*, 96–103.

Emison, E.S., McCallion, A.S., Kashuk, C.S., Bush, R.T., Grice, E., Lin, S., Portnoy, M.E., Cutler, D.J., Green, E.D., and Chakravarti, A. (2005). A common sex-dependent mutation in a RET enhancer underlies Hirschsprung disease risk. Nature *434*, 857–863.

Ezoe, K., Holmes, S.A., Ho, L., Bennett, C.P., Bolognia, J.L., Brueton, L., Burn, J., Falabella, R., Gatto, E.M., and Ishii, N. (1995). Novel mutations and deletions of the KIT (steel factor receptor) gene in human piebaldism. Am. J. Hum. Genet. *56*, 58–66.

Gonzales, B. (2005). The Treacher Collins syndrome (TCOF1) gene product is involved in pre-rRNA methylation. Human Molecular Genetics *14*, 2035–2043.

Grskovic, M., Javaherian, A., Strulovici, B., and Daley, G.Q. (2011). Induced pluripotent stem cells — opportunities for disease modelling and drug discovery. Nat Rev Drug Discov *10*, 915–929.

Hall, B.K. (2008). The neural crest and neural crest cells: discovery and significance for theories of embryonic organization. J. Biosci. *33*, 781–793.

Heanue, T.A., and Pachnis, V. (2007). Enteric nervous system development and Hirschsprung's disease: advances in genetic and stem cell studies. Nat Rev Neurosci *8*, 466–479.

Ito, M., Kawa, Y., Okura, M., Baba, T., Kubota, Y., Mizoguchi, M., Ono, H., and Nishikawa, S.-I. (1999). Removal of Stem Cell Factor or Addition of Monoclonal Anti-c-KIT Antibody Induces Apoptosis in Murine Melanocyte Precursors. Journal of Investigative Dermatology *112*, 796–801.

Jabs, E.W., Li, X., Coss, C.A., Taylor, E.W., Meyers, D.A., and Weber, J.L. (1991). Mapping the Treacher Collins syndrome locus to 5q31.3----q33.3. Genomics *11*, 193–198.

Jabs, E.W., Li, X., Lovett, M., Yamaoka, L.H., Taylor, E., Speer, M.C., Coss, C., Cadle, R., Hall, B., and Brown, K. (1993). Genetic and physical mapping of the Treacher Collins syndrome locus with respect to loci in the chromosome 5q3 region. Genomics *18*, 7–13.

Jiang, X., Gwye, Y., McKeown, S.J., Bronner-Fraser, M., Lutzko, C., and Lawlor, E.R. (2009). Isolation and Characterization of Neural Crest Stem Cells Derived From In Vitro–Differentiated Human Embryonic Stem Cells. Stem Cells and Development *18*, 1059–1070.

Jones, K.L., Smith, D.W., Harvey, M.A., Hall, B.D., and Quan, L. (1975). Older paternal age and fresh gene mutation: data on additional disorders. J. Pediatr. *86*, 84–88.

Jones, N.C., Lynn, M.L., Gaudenz, K., Sakai, D., Aoto, K., Rey, J.-P., Glynn, E.F., Ellington, L., Du, C., Dixon, J., et al. (2008). Prevention of the neurocristopathy Treacher Collins syndrome through inhibition of p53 function. Nat Med *14*, 125–133.

Jongmans, M.C.J., Admiraal, R.J., van der Donk, K.P., Vissers, L.E.L.M., Baas, A.F., Kapusta, L., van Hagen, J.M., Donnai, D., de Ravel, T.J., Veltman, J.A., et al. (2006). CHARGE syndrome: the phenotypic spectrum of mutations in the CHD7 gene. Journal of Medical Genetics *43*, 306–314.

Kenny, S.E., Tam, P.K.H., and Garcia-Barceló, M. (2010). Hirschsprung's disease. Seminars in Pediatric Surgery *19*, 194–200.

Keyte, A., and Hutson, M.R. (2012). The neural crest in cardiac congenital anomalies. Differentiation *84*, 25–40.

LaBonne, C., and Bronner-Fraser, M. (1998). Induction and patterning of the neural crest, a stem cell-like precursor population. J. Neurobiol. *36*, 175–189.

Le Douarin, N.M., Calloni, G.W., and Dupin, E. (2008). The stem cells of the neural crest. Cell Cycle *7*, 1013–1019.

Lee, G., and Studer, L. (2011). Modelling familial dysautonomia in human induced pluripotent stem cells. Philosophical Transactions of the Royal Society B: Biological Sciences *366*, 2286–2296.

Lee, G., Chambers, S.M., Tomishima, M.J., and Studer, L. (2010). Derivation of neural crest cells from humanpluripotent stem cells. Nature Protocols *5*, 688–701.

Lee, G., Kim, H., Elkabetz, Y., Shamy, Al, G., Panagiotakos, G., Barberi, T., Tabar, V., and Studer, L. (2007). Isolation and directed differentiation of neural crest stem cells derived from human embryonic stem cells. Nat Biotechnol *25*, 1468–1475.

Lee, G., Papapetrou, E.P., Kim, H., Chambers, S.M., Tomishima, M.J., Fasano, C.A., Ganat, Y.M., Menon, J., Shimizu, F., Viale, A., et al. (2009). Modelling pathogenesis and treatment of familial dysautonomia using patient-specific iPSCs. Nature *461*, 402–406.

Lennartsson, J., and Rönnstrand, L. (2012). Stem Cell Factor Receptor/c-Kit: From Basic Science to Clinical Implications. Physiol. Rev. *92*, 1619–1649.

Marres, H.A., Cremers, C.W., Dixon, M.J., Huygen, P.L., and Joosten, F.B. (1995). The Treacher Collins syndrome. A clinical, radiological, and genetic linkage study on two pedigrees. Arch. Otolaryngol. Head Neck Surg. *121*, 509–514.

Menendez, L., Kulik, M.J., Page, A.T., Park, S.S., Lauderdale, J.D., Cunningham, M.L., and Dalton, S. (2013). Directed differentiation of human pluripotent cells to neural crest stem cells. Nature Protocols *8*, 203–212.

Menendez, L., Yatskievych, T.A., Antin, P.B., and Dalton, S. (2011). Wnt signaling and a Smad pathway blockade direct the differentiation of human pluripotent stem cells to multipotent neural crest cells. Proceedings of the National Academy of Sciences *108*, 19240–19245.

Milligan, D.A., Harlass, F.E., Duff, P., and Kopelman, J.N. (1994). Recurrence of Treacher Collins' syndrome with sonographic findings. Mil Med *159*, 250–252.

Mollaaghababa, R., and Pavan, W.J. (2003). The importance of having your SOX on: role of SOX10|[dagger]| in the development of neural crest-derived melanocytes and glia. Oncogene *22*, 3024–3034.

Mundt, E., and Bates, M.D. (2010). Genetics of Hirschsprung disease and anorectal malformations. Seminars in Pediatric Surgery *19*, 107–117.

Nakamura, T., Gulick, J., Colbert, M.C., and Robbins, J. (2009a). Protein tyrosine phosphatase activity in the neural crest is essential for normal heart and skull development. Proceedings of the National Academy of Sciences *106*, 11270–11275.

Nakamura, T., Gulick, J., Pratt, R., and Robbins, J. (2009b). Noonan syndrome is associated with enhanced pERK activity, the repression of which can prevent craniofacial malformations. Proceedings of the National Academy of Sciences *106*, 15436–15441.

O Rahilly, R., and Müller, F. (2007). The development of the neural crest in the human. J Anatomy *211*, 335–351.

Oskarsdottir, S., Vujic, M., and Fasth, A. (2004). Incidence and prevalence of the 22q11 deletion syndrome: a population-based study in Western Sweden. Archives of Disease in Childhood *89*, 148–151.

Pagon, R.A., Graham, J.M., Zonana, J., and Yong, S.L. (1981). Coloboma, congenital heart disease, and choanal atresia with multiple anomalies: CHARGE association. J. Pediatr. *99*, 223–227.

Parc, R., Berrod, J.L., Tussiot, J., and Loygue, J. (1984). [Megacolon in adults. Apropos of 76 cases]. Ann Gastroenterol Hepatol (Paris) *20*, 133–141.

Pattyn, A., Morin, X., Cremer, H., Goridis, C., and Brunet, J.F. (1999). The homeobox gene Phox2b is essential for the development of autonomic neural crest derivatives. Nature *399*, 366–370.

Pingault, V., Ente, D., Dastot Le Moal, F., Goossens, M., Marlin, S., and Bondurand, N. (2010). Review and update of mutations causing Waardenburg syndrome. Hum. Mutat. *31*, 391–406.

Pomp, O., Brokhman, I., Ben-Dor, I., Reubinoff, B., and Goldstein, R.S. (2005). Generation of peripheral sensory and sympathetic neurons and neural crest cells from human embryonic stem cells. Stem Cells *23*, 923–930.

Pomp, O., Brokhman, I., Ziegler, L., Almog, M., Korngreen, A., Tavian, M., and Goldstein, R.S. (2008). PA6-induced human embryonic stem cell-derived neurospheres: a new source of human peripheral sensory neurons and neural crest cells. Brain Res. *1230*, 50–60.

Poswillo, D. (1975). The pathogenesis of the Treacher Collins syndrome (mandibulofacial dysostosis). Br J Oral Surg *13*, 1–26.

Rekhtman, Y., Bomback, A.S., Nash, M.A., Cohen, S.D., Matalon, A., Jan, D.M., Kaufmann, H., Axelrod, F.B., Radhakrishnan, J., and Appel, G.B. (2010). Renal transplantation in familial dysautonomia: report of two cases and review of the literature. Clin J Am Soc Nephrol *5*, 1676–1680.

Romano, A.A., Allanson, J.E., Dahlgren, J., Gelb, B.D., Hall, B., Pierpont, M.E., Roberts, A.E., Robinson, W., Takemoto, C.M., and Noonan, J.A. (2010). Noonan syndrome: clinical features, diagnosis, and management guidelines. Pediatrics *126*, 746–759.

Sakai, D., and Trainor, P.A. (2009). Treacher Collins syndrome: unmasking the role of Tcof1/treacle. Int. J. Biochem. Cell Biol. *41*, 1229–1232.

Shprintzen, R.J. (2008). Velo-cardio-facial syndrome: 30 Years of study. Developmental Disabilities Research Reviews *14*, 3–10.

Slaugenhaupt, S.A. (2002). Genetics of familial dysautonomia. Tissue-specific expression of a splicing mutation in the IKBKAP gene. Clin. Auton. Res. *12 Suppl 1*, I15–I19.

Southard-Smith, E.M., Angrist, M., Ellison, J.S., Agarwala, R., Baxevanis, A.D., Chakravarti, A., and Pavan, W.J. (1999). The Sox10(Dom) mouse: modeling the genetic variation of Waardenburg-Shah (WS4) syndrome. Genome Research *9*, 215–225.

Splendore, A., Fanganiello, R.D., Masotti, C., Morganti, L.S.C., and Passos-Bueno, M.R. (2005). TCOF1 mutation database: novel mutation in the alternatively spliced exon 6A and update in mutation nomenclature. Hum. Mutat. *25*, 429–434.

Stovin, J.J., Lyon, J.A., Jr, and Clemmens, R.L. (1960). Mandibulofacial dysostosis. Radiology.

Stuhlmiller, T.J., and García-Castro, M.I. (2012). Current perspectives of the signaling pathways directing neural crest induction. Cell. Mol. Life Sci. *69*, 3715–3737.

Takahashi, K., Tanabe, K., Ohnuki, M., Narita, M., Ichisaka, T., Tomoda, K., and Yamanaka, S. (2007). Induction of Pluripotent Stem Cells from Adult Human Fibroblasts by Defined Factors. Cell *131*, 861–872.

Tartaglia, M., Mehler, E.L., Goldberg, R., Zampino, G., Brunner, H.G., Kremer, H., van der Burgt, I., Crosby, A.H., Ion, A., Jeffery, S., et al. (2001). Mutations in PTPN11, encoding the protein tyrosine phosphatase SHP-2, cause Noonan syndrome. Nat. Genet. *29*, 465–468.

Teber, O.A., Gillessen-Kaesbach, G., Fischer, S., Böhringer, S., Albrecht, B., Albert, A., Arslan-Kirchner, M., Haan, E., Hagedorn-Greiwe, M., Hammans, C., et al. (2004). Genotyping in 46 patients with tentative diagnosis of Treacher Collins syndrome revealed unexpected phenotypic variation. Eur J Hum Genet *12*, 879–890.

Thomas, S., Thomas, M., Wincker, P., Babarit, C., Xu, P., Speer, M.C., Munnich, A., Lyonnet, S., Vekemans, M., and Etchevers, H.C. (2008). Human neural crest cells display molecular and phenotypic hallmarks of stem cells. Human Molecular Genetics *17*, 3411–3425.

Torfs, C.P., Velie, E.M., Oechsli, F.W., Bateson, T.F., and Curry, C.J.R. (1994). A population-based study of gastroschisis: Demographic, pregnancy, and lifestyle risk factors. Teratology *50*, 44–53.

Trainor, P.A. (2010). Craniofacial birth defects: The role of neural crest cells in the etiology and pathogenesis of Treacher Collins syndrome and the potential for prevention. Am. J. Med. Genet. *152A*, 2984–2994.

Trainor, P.A., Dixon, J., and Dixon, M.J. (2008). Treacher Collins syndrome: etiology, pathogenesis and prevention. Eur J Hum Genet *17*, 275–283.

Trounson, A., Shepard, K.A., and DeWitt, N.D. (2012). Human disease modeling with induced pluripotent stem cells. Current Opinion in Genetics & Development *22*, 509–516.

Tullu, M.S., Muranjan, M.N., Kantharia, V.C., Parmar, R.C., Sahu, D.R., Bavdekar, S.B., and Bharucha, B.A. (2000). Neurofibromatosis-Noonan syndrome or LEOPARD Syndrome? A clinical dilemma. J Postgrad Med *46*, 98–100.

Uesaka, T., Nagashimada, M., Yonemura, S., and Enomoto, H. (2008). Diminished Ret expression compromises neuronal survival in the colon and causes intestinal aganglionosis in mice. J. Clin. Invest. *118*, 1890–1898.

Wang, X.D., Morgan, S.C., and Loeken, M.R. (2011). Pax3 Stimulates p53 Ubiquitination and Degradation Independent of Transcription. PLoS ONE *6*, e29379.

Whitehouse, F.R., and Kernohan, J.W. (1948). Myenteric plexus in congenital megacolon; study of 11 cases. Arch Intern Med (Chic) *82*, 75–111.

Wise, C.A., Chiang, L.C., Paznekas, W.A., Sharma, M., Musy, M.M., Ashley, J.A., Lovett, M., and Jabs, E.W. (1997). TCOF1 gene encodes a putative nucleolar phosphoprotein that exhibits mutations in Treacher Collins Syndrome throughout its coding region. Proc. Natl. Acad. Sci. U.S.a. *94*, 3110–3115.

Yu, J., Vodyanik, M.A., Smuga-Otto, K., Antosiewicz-Bourget, J., Frane, J.L., Tian, S., Nie, J., Jonsdottir, G.A., Ruotti, V., Stewart, R., et al. (2007). Induced Pluripotent Stem Cell Lines Derived from Human Somatic Cells. Science *318*, 1917–1920.

CHAPTER 3

METHODS FOR DERIVATION OF MULTIPOTENT NEURAL CREST CELLS FROM HUMAN PLURIPOTENT STEM CELLS

Avery, J & Dalton, S. 2016. Methods for Derivation of Multipotent Neural Crest Cells Derived from Human Pluripotent Stem Cells. Methods Mol Biol. *1341*, 197–208.

SUMMARY/ABSTRACT

During development, multipotent neural crest stem cells (NCSCs) produce a wide assortment of cell/tissue types in vivo. These cells/tissue types include melanocytes, peripheral neurons, smooth muscle, bone, cartilage as well as adipose. The protocol detailed below describes a highly efficient method to reliably produce, lineage-specific differentiation of human pluripotent stem cells (hESC/hiPSC) to a NCSC fate. This is accomplished through a chemically defined medium containing a duo of small molecule inhibitors under feeder-free growth conditions. This method drives the conversion of human pluripotent cells to NCSCs in as few as 15 days. Subsequent to differentiation, the NCSCs are capable of being driven to common neural crest descendant cell types. This protocol may lead to an increase in the basic biology of NCSCs as well as disease pathogenesis as a result of impaired NCSC development/migration, particularly when coupled to the reprogramming of patient-derived cells.

Key Words: Neural Crest Cells, human pluripotent stem cells, human embryonic stem cells, human induced pluripotent stem cells

1. INTRODUCTION

Neural crest stem cells (NCSCs) arise from the neural plate border during closure of the burgeoning neural tube. NCSCs delaminate from the roof plate and migrate to distinct targets throughout the developing embryo where they differentiate to form varied functional tissue (Avery et al., 2013; Betancur et al., 2010; Le Douarin and Dupin, 2003; Lee et al., 2010). Migrating NCSCs maintain a characteristic phenotype, however, NCSC point of origin and local microenvironments encountered during migration influence cell and ultimately tissue fate (Achilleos and Trainor, 2012; Hall, 2008; LaBonne and Bronner-Fraser, 1998; Le Douarin et al., 2008). NCSCs originate from four separate compartments (cranial, cardiac, vagal and trunk), which lie along the rostro-caudal axis of the developing neural tube (Achilleos and Trainor, 2012). As a result of the multipotent nature of NCSCs, aberrations that are associated with the development of NCSCs from the neural plate border, their migration within the embryo and/or their terminal differentiation lead to a wide variety of diseases or syndromes, known as neurocristopathies (Etchevers et al., 2006). The study of neural crest biology has clear basic science and clinical relevance: NCSCs have been dubbed the "fourth germ layer" due to their mulitpotentcy, and the diseases that are a consequence of improper NCSC development or migration span many organ systems that can have debilitating and even lethal outcomes.

The strategy developed by our lab and outlined here was driven by previous studies in neuroectoderm specification (Chambers et al., 2009; Lee et al., 2010). Previous differentiation models lead to low efficiency derivation of NCSCs by utilizing concurrent inhibition of both transforming growth factor (TGF)-β- and bone morphogenetic protein (BMP)-dependent Smad signaling. The predominant cell type within these culture systems displays a neural progenitor cell (NPC) phenotype with high expression of PAX6. Moreover, these systems were laborious,

often relying on feeder layer co-culture and subsequent FACS enrichment steps (Chambers et al., 2009; Jiang et al., 2009; Lee et al., 2010; 2007; Pomp et al., 2005; 2008). In an effort to alleviate the aforementioned shortcomings, we have developed a highly efficient, single-step method for the generation of NCSCs from human pluripotent stem cells (Menendez et al., 2013; 2011). The protocol described here is feeder-free and requires no enrichment steps with typical population yields of ≥ 90% NCSC phenotype. To accomplish this, we coupled Smad inhibition to enhanced activation of the Wnt pathway by utilizing small-molecule inhibitors of TGF-β signaling (SB431542) and glycogen synthase kinase 3 [GSK3 inhibitor IX (BIO)]. In addition to highly efficient differentiation and ease of culture, the differentiated NCSC populations are capable of being stably maintained for greater than 30 passages. The differentiated NCSCs are also capable of being further differentiated into a multitude of additional fates such as mesenchymal stem cells, peripheral neurons, adipocytes, smooth muscle cells, chondrocytes and osteocytes (Menendez et al., 2011; 2013). Importantly, these cells are also capable of clonal expansion and can be resuscitated after cryopreservation with no loss in potency or self-renewing potential.

2. MATERIALS

2.1 Media Preparation

Special care should be made to prepare all media using freshly thawed factors from frozen aliquots. Bulk media preparation (greater than 500 mL) should be avoided. Unless otherwise stated, all media should be utilized within seven days of preparation. For the most consistent and reliable results, maintenance and differentiation media should be prepared, as needed, every one to two days. When not in use, media must be refrigerated at +4°C.

Collagenase IV Dissociation Solution: Combine enough collagenase IV powder and DMEM/F12 (1:1) to reach a final concentration of 400 units/mL (*see* **Note 1**). Filter-sterilize the solution and store at 4°C for a week. Alternatively, the solution may be placed in aliquots and stored at -20°C for up to 2 months.

StemPro® hESC Culture Medium: StemPro® should be mixed according to the manufacturer's instructions.

Basal Defined Medium: For each 500mL of basal defined medium, combine 50 mL of a 20% (vol/vol) stock solution of Probumin®, 5 mL of penicillin (10,000 IU) and Streptomycin (10,000 µg/ml) 100x, 5 mL of L-alanyl-l-glutamine (43.44 mg/mL) 100x, 5 mL of MEM non-essential amino acids, 0.5 mL of trace elements A 1,000x, 0.5 mL of trace elements B 1,000x, 0.5 mL of trace elements C 1,000x (Cellgro), 0.9 mL of 2-mercaptoethanol, transferrin (10 µg/mL), (+)-sodium L-ascorbate (50 µg/mL), and reach final volume of 500mL by adding 432 mL of DMEM/F12 (1:1). Filter sterilize (0.22 µm pore) and store at 4°C for up to two weeks for use with maintenance and differentiation media preparation (*see* **Note 2**).

Human Embryonic Stem Cell (hESC) Maintenance Medium. Add the following factors to the basal defined medium with the specified final concentrations: Heregulin β-1 (10 ng/mL), Activin A (10 ng/mL), LONG® R3 IGF-I (200 ng/mL), and Fgf2 (8 ng/mL) (*see* **Notes 2 & 3**).

Neural crest differentiation medium. Add the following factors and inhibitors to the basal defined medium with the specified final concentrations: Heregulin β-1 (10 ng/mL), LONG® R3 IGF-I (200 ng/mL), and FGF2 (8 ng/mL), GSK3 inhibitor IX (BIO) (2 µM), and SB431542 (20 µM) (*see* **Notes 2-4**).

2.2 Equipment Preparation

Geltrex™ LDEV-Free, hESC-Qualified, Reduced Growth Factor Basement Membrane Matrix -coated plates**:** Prepare 1mL aliquots of Geltrex™ according to manufacturer's protocol (*see* **Note 5**). Thaw a 1-ml aliquot of Geltrex ™ and dilute it to 1:30 or 1:200 (*see* **Notes 6 & 7**) in DMEM/F12 before plating. Add 1.5 mL of the Geltrex™ dilution to a 35-mm tissue culture plate or 3mL of the final dilution to a 60-mm tissue culture plate. Incubate coated plates at 37C for at least 1hour prior to use.

3. METHODS

This neural crest differentiation protocol works equally well for hESCs or hiPSCs, however, cultures must be adapted to feeder-free and single-cell growth conditions.

3.1 Adaptation of hESC and hiPSC cultures to feeder-free conditions.

Skip to step 3.2 (Adaptation of hESC/hiPSC cultures to single-cell growth conditions) if hESC/hiPSC cultures are already maintained in feeder-free conditions.

It is advisable to only passage one well/plate at a time and to work as quickly as possible through each step.

1. Once colonies reach proper confluence, aspirate the culture medium and wash with 1x PBS (*see* **Note 8**); aspirate the PBS and add enough collagenase IV dissociation solution to fully cover one well/plate (*see* **Notes 9-11**).

2. Manual passage of the colonies yields the most uniform results and leads to improved survival upon passage. Many methods can be used for manual passage, however, the most facile method utilizes the StemPro® EZ™ Passage Tool (*see* **Note 12**).

3. Upon addition of the collagenase IV solution, immediately begin manual passage. Once colonies have been cut into pieces, incubate them in the collagenase solution at 37°C for 5–30 min or until the colony fragments begin to lift up from the plate; observe the colonies under the microscope periodically to detect this change (*see* **Note 13**).

4. Gently collect the colonies using a 5 mL pipette and place in a 15-mL conical tube. If the colonies are difficult to remove by gentle pipetting, you may use a cell scraper to gently detach them from the plate (*see* **Note 14**). Once the cells have been collected in the conical tube, wash the plate with 2-5 mL of 1 x PBS (depending on well/plate size) to collect remaining colonies in the dish and to dilute the collagenase in the conical tube (See note 15). Centrifuge the cells for 4 min at 200g at RT.

5. Carefully aspirate the collagenase/PBS supernatant and resuspend the cell pellet in 4 mL of pre-equilibrated StemPro™ medium.

6. Plate the cells using a 1:4 (vol/vol) ratio (*see* **Note 16**) onto freshly prepared Geltrex-coated plates. Add pre-equilibrated StemPro® medium for a total volume of 2mL for a 35-mm dish and a total volume of 4mL for a 60-mm dish.

7. Maintain the cells at 37 °C in a 5% CO_2 incubator and replenish spent medium with fresh pre-equilibrated StemPro® medium every day. Repeat steps 1-7 as necessary until colonies begin to need passaging every 4-5 days (*see* **Notes 17** & **18**). The colonies may be kept in this manner indefinitely, however, for neural crest differentiation, they must be adapted to Accutase passage for single-cell culture as described below.

3.2 Accutase® and single-cell culture adaptation

1. When hESC/hiPSC colonies have become adapted to Geltrex™, they must be further adapted to Accutase® dissociation and single-cell culture before they may be differentiated to neural crest stem cells. Aspirate the StemPro® medium and add enough Accutase® cell dissociation reagent to cover the plate (~2mL/ 60-mm dish). Leave the dish at room temperature (RT) for 5-10 minutes, checking frequently to ensure that the colonies begin to conform to a rounded shape and the colony edges begin to detach from the plate but are still loosely adherent (*see* **Note 19**).

2. Gently collect the colonies using a 5 mL pipette and place in a 15-mL conical tube and centrifuge the cells for 4 min at 200*g* at RT.

3. Carefully aspirate the Accutase® supernatant and resuspend the cells in 4–5 ml of StemPro® medium, if the cells are still quite sensitive to Accutase® treatment or hESC maintenance medium, if they have become well tolerant of Accustase®. While adapting the cells to Accutase®, it is best to pass at a ratio of 1:2, until passaging is required every 4-5 days (*see* **Notes 20-22**).

4. Count the cells with a hemocytometer and replate them at a density of ~5-8 x 10^4 cells/cm^2. Once the cells have become well adapted to Accutase® passage they may be passed without cell number determination at a 1:4 to 1:5 (vol/vol) ratio on a Geltrex™-coated plate.

5. Maintain the cells at 37°C in a 5% CO_2 incubator and replenish spent medium with fresh pre-equilibrated medium every day. Human ESCs maintained in these conditions should remain positive for pluripotent markers such as *SOX2, OCT4* and *NANOG*.

3.3 Differentiation of hESC to Neural Crest Stem Cells (NCSCs)

1. When hESC plates have reach 75-85% confluence, they are ready to be passaged and replated for differentiation into NCSCs. Aspirate hESC maintenance medium from culture dish and add enough Accutase® cell dissociation reagent to cover the plate (~2mL/ 60-mm dish). Leave the dish at room temperature (RT) for 5-10 minutes, checking frequently to ensure that the cells conform to a rounded shape, but are still loosely adherent (*see* **Note 19**).

2. Collect the cells in a 15-ml tube and centrifuge for 4 min at 200*g* at room temperature.

3. Aspirate the supernatant and resuspend the cells in 4–5 ml of pre-equilibrated hESC maintenance medium.

4. Count the cells with a hemocytometer and replate them at a seeding density of ~9 - 9.2 x 10^4 cells/cm^2 onto Geltrex™-coated plates in hESC pre-equilibrated maintenance medium.

5. After 24 hours, aspirate the hESC maintenance medium, wash the cells with 1xPBS, (*see* **Note 23**) and replace with neural crest differentiation medium.

6. Replenish spent medium with fresh neural crest differentiation medium every day.

7. Differentiating cells will reach 75-85% confluence within 3-4 days and density/morphology should be monitored daily. Morphological changes should become apparent around days 4-5 (*see* **Figure 3.1B**) after exposure to neural crest differentiation medium, and subsequent neural crest morphology should become apparent between 7–12 days of differentiation in neural crest differentiation medium (*see* **Figure 3.1B**).

8. Upon reaching proper confluence (75-85%), typically every 3-4 days, the differentiating cells should be passed using Accutase® according to the method described above and continued to be

reseeded in neural crest differentiation medium at the same density.

9. NCSC identity can be analyzed as early as 15 days post initial exposure to neural crest differentiation medium However, it may take up to 21 days to reach full maturity (*See* **Figure 3.1**). Analyses include immunocytochemistry, flow cytometry and/or qRT-PCR. If you are using immunocytochemistry, NCSCs should be positive for NCSC markers such as p75, Hnk1, AP2. Flow cytometric analysis of NCSCs should yield p75+ and Hnk1+ cell populations. If you carry out RT-PCR, NCSCs should express genes such as *PAX3*, *AP2*, *ZIC1*, *SOX9* and *SOX10*, among others. (*See* **Figure 3.1**)

Notes

Note 1: If unit concentrations of collagenase IV are not given, use 1mg/mL.

Note 2: To ensure proper concentration of growth factors, it is best to follow strict aseptic technique with no need to filter the medium; however, if factors or other reagents are shared or their handling/aliquoting can not be accounted for, the medium must be filter-sterilized using a 0.22 μm pore.

Note 3: Media should be pre-equilibrated to 37°C prior to use.

Note 4: The use of commercially available stem cell media, such as StemPro® or mTesR®, is not recommended for this protocol, as the presence of Activin A and/or TGF-β inhibits efficient NCSC differentiation. Additionally, the use of serum-rich or KSR media is also not recommended due to the undefined nature of their components and poor efficiency in NCSC yield.

Note 5: In our lab, we initially aliquot 1mL containing a 1:1 solution of Geltrex™: DMEM/F12 by adding 5mL of ice cold DMEM/F12 to 5mL of frozen Geltrex™ and allow the mix to

completely thaw on ice before thoroughly mixing by pippetting. It is important to work quickly as Geltrex™ will gel in 5-10 minutes at temperatures above 15°C. To avoid the solution reaching this temperature, we keep the aliquoted tubes on ice until we finish portioning out the solution. These aliquots are immediately frozen (-20°C) for later use.

Note 6: When adapting cells to feeder free conditions, we utilize a 1:30 dilution of Geltrex™ to DMEM/F12. This is met by diluting a 1mL aliquot of 1:1 Geltrex™: DMEM/F12 as in Note 5 into a further 14mL of DMEM/F12 for a final volume of 15mL. The cellular stress upon change from the feeder layer to Geltrex™ appears to be lessened by using this higher concentration, as cell survival is enhanced. After 2-3 passages, the cells may be transitioned further to a Geltrex™:DMEM/F12 dilution of 1:200. Cell survival and spontaneous differentiation are unaffected, while considerable cost savings can be attained by this increased dilution.

Note 7: For best results, coated plates may be kept for five days at 37°C in a 5% CO_2 incubator, provided the plates are not allowed to dry out. Take care to monitor coated plates and add additional DMEM/F12 if needed after solidification to prevent drying. Alternatively, the plates may be wrapped with Parafilm™ and stored at 4°C for no greater than two weeks.

Note 8: You may use PBS with or without Ca^{2+}/Mg^{2+}, as they do not affect collagenase activity. The wash step is included to rid the plate of components that may inhibit or reduce collagenase IV activity, such as Fe^{2+}.

Note 9: Prior to beginning any plating or dissociation work with cells, ensure that you have Geltrex-coated plates prepared and that they are ready to be utilized.

Note 10: Prior to adding the dissociation solution, it is critical to evaluate the colonies for spontaneous differentiation. Observe the plate under an inverted scope and identify colonies that show evidence of differentiation or that are too large (excessively large colonies are more prone

to differentiation). Use an indelible marker to indicate on the plate where the colonies you wish to remove are so that you may remove them in the biological safety cabinet. Appropriate colony morphology is indicated by round, well-defined, homogenous colonies that are tightly packed; the cells within retain a characteristic high nuclear to cytoplasmic ratio and display easily identifiable nucleoli. Remove unwanted colonies by first aspirating the culture medium then etching a line around and through the colony(ies) using a 20uL pipette tip or 20-22G- 1½ needle (this guards against removing the underlying feeder layer in a sheet and prevents removing the colonies you wish to pass). Using a sterile Pasteur pipette, gently slide the pipette along the colony edges and center, being careful to observe and prevent any pulling from the feeder layer. You must work quickly to avoid drying of the plate. Once the colonies are removed, wash with 1x PBS; replace aspirated PBS with fresh hESC maintenance medium. If more than 10% of the colonies in a well/plate are of an inappropriate morphology, the culture is unreliable and should be discarded; you must examine your media preparation as well as your technique to maintain proper hESC identity.

Note 11: When working with multiple wells/plates of cells, it is critical to add the cell dissociation solution one well/plate at a time. For example, if using a 6 well plate, add the solution to one well and proceed to the next step with that well before moving on to the next well. This is time consuming but yields the most reliable results and protects cells from over exposure to the dissociation solution.

Note 12: The StemPro® EZ™ Passage Tool separates the colonies into optimally sized, uniform pieces, which survive passage with greater frequency and yield "goldilocks" colonies that are not too large or too small- leading to decreased spontaneous differentiation and more reliable culture. When attempting to pass several wells/plates the StemPro® EZ™ Passage Tool allows the

greatest time savings and therefore the least amount of exposure of the culture to contaminants. Use one Tool per well/plate.

Note 13: Once you have scraped the colonies in one well containing the collagenase solution, you may begin the process for other wells/plates now- **do not** exceed 6 wells/plates at one time, as time will become a limiting factor for good technique and ultimately culture survival/reliability.

Note 14: Too much or too vigorous pipetting will damage your colonies or reduce their size to suboptimal dimensions. Gentle pipetting 2-3x should be enough to remove the colonies from the plate. If this is not enough, you may not have incubated the cells in collagenase solution long enough. You may use gentle scraping with a sterile cell scraper, but make sure to add PBS or hESC medium to the plate first.

Note 15: Adding PBS to the collagenase solution accomplishes two goals: 1) it makes aspirating the supernatant from the conical tube after centrifugation easier, as an undiluted viscous collagenase solution can easily pull the entire pellet with it, and 2) it further dilutes the collagenase to be removed- if collagenase is not removed, the colonies will not adhere well, thus leading to reduced plating efficiency and spontaneous differentiation.

Note16: It is a good idea to use two Geltrex™ plates and two MEF plates and place 1 mL of the 1:4 (vol/vol) colony/StemPro® dilution onto each plate; that way, the two MEF plates serve as reserves in the event the cells do not survive well on the new Geltrex™ plates. If the colonies are successful upon transitioning to Geltrex™, then the two reserve MEF plates make great frozen stocks should you need to return to MEF plates in the future.

Note 17: Reaching a point at which colonies need to be passed every 4-5 days may take 2-3 weeks for reliable passaging and survival on Geltrex™.

Note 18: As with culturing hESC colonies on feeders, passage the colonies when any of the following criteria are observed: 1) colonies are becoming too large, 2) colonies are becoming too dense (proximity to neighboring colonies decreases or colonies begin touching), 3) spontaneous differentiation begins, or 4) 10 days pass between passages and the colonies have not violated the 3 preceding criteria.

Note 19: Overly confluent cells require longer Accutase® incubation; it is not optimal for the cells to fully detach, and not to pipette too much, as this decreases cell health.

Note 20: The cells may take up to 3 weeks to become adapted to Accutase treatment.

Note 21: In order to subsequently differentiate the cells, they should be passaged in hESC maintenance medium (not in a commercial stem cell medium) at least twice prior to switching to neural crest differentiation medium. Differentiation efficiency is dramatically reduced if the cells have not been adapted to the maintenance medium prior to any attempts at differentiation toward NCSCs.

Note 22: Avoid exceeding densities over 85-90% confluence in single cell culture conditions, as this dramatically increase spontaneous differentiation and decreases reliable differentiation to lineage specific cell types later on. Also, it is best not to plate at densities, which lead to excessive passage, i.e. cultures should not need passing more than every 4 days.

Note 23: It is critical to wash the cells with PBS in order to remove any remaining Activin A in the medium. The presence of any Activin A will reduce the NCSC differentiation.

Figure 3.1- Characteristics of NCSC differentiation from hPSCs. Morphological appearance of NCSCs during differentiation: NCSCs lose tight colony morphology, cell size becomes reduced, cell shape becomes increasingly stellate, and the cellular nucleus:cytoplasm ratio is reduced relative to hPSCs, 10X magnification, scale bar = 100um (A); Genetic markers of NCSC during differentiation, expression is relative to undifferentiated hESCs (WA09), the *x*-axis corresponds to day of differentiation. The suite of genetic markers typical of NCSCs display a general pattern of increased expression as early as d3 (SOX9) with maxima reached as the differentiation proceeds from d15-d18. Once the NCSC phenotype has been reached, expression patterns stabilize to d18 levels and remain until further differentiation (data not shown) (B); Immunofluorescence of characteristic NCSC cell surface (HNK1 and p75) and transcription factor (AP2) markers at d18, 20X magnification, scale bar = 50um (C); Flow cytometric analysis of NCSC cell surface markers during differentiation (D).

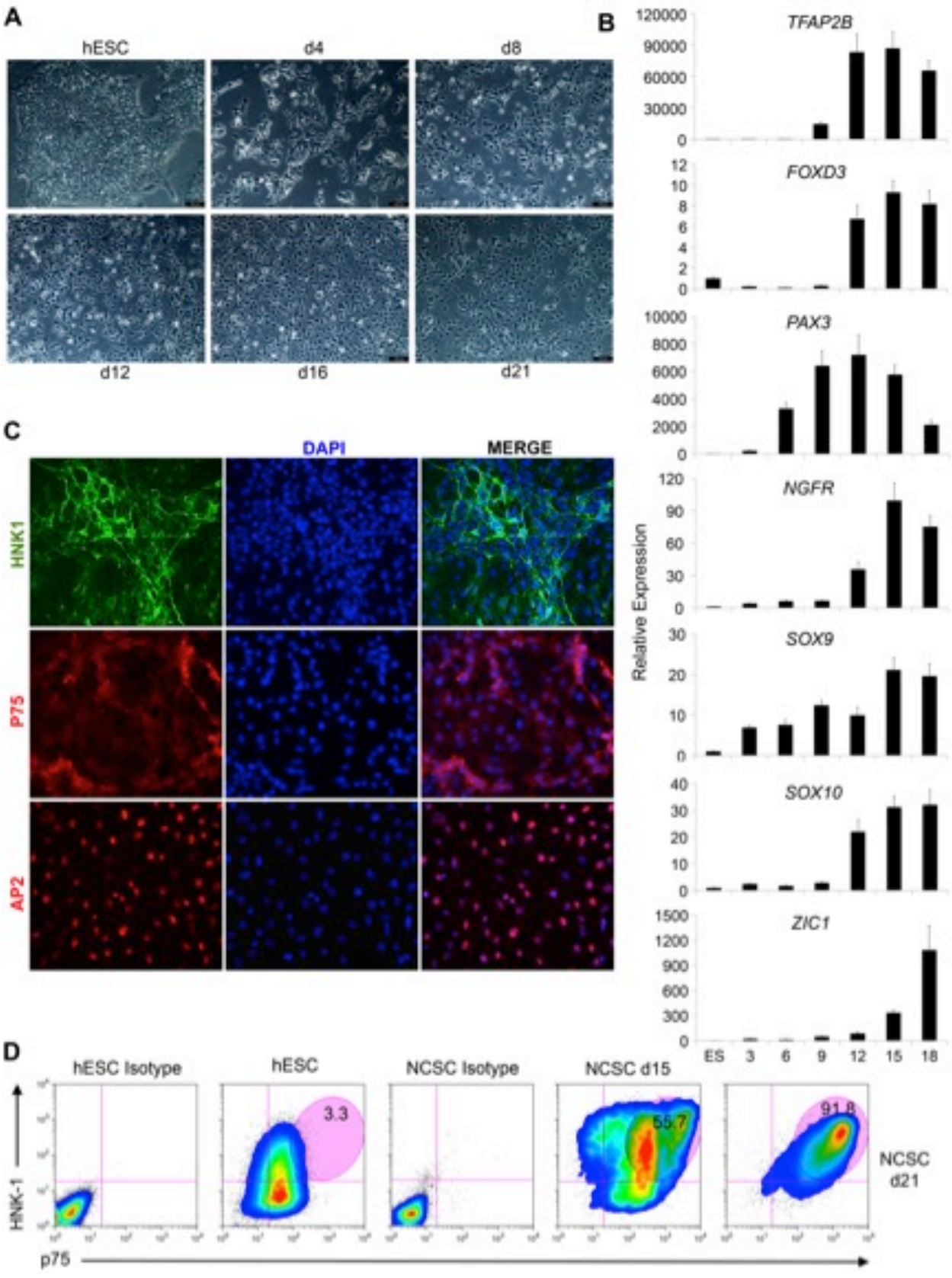
A
hESC
d4
d8
d12
d16
d21
B
TFAP2B
FOXD3
PAX3
NGFR
SOX9
SOX10
ZIC1
Relative Expression
ES
3
6
9
12
15
18
C
DAPI
MERGE
HNK1
P75
AP2
D
hESC Isotype
hESC
NCSC Isotype
NCSC d15
NCSC d21
3.3
55.7
91.8
HNK-1
p75

REFERENCES

Achilleos, A., and Trainor, P.A. (2012). Neural crest stem cells: discovery, properties and potential for therapy. Cell Research *22*, 288–304.

Avery, J., Menendez, L., Cunningham, M.L., Lovvorn, H.N., III, and Dalton, S. (2013). Chapter 21 - Using Induced Pluripotent Stem Cells as a Tool to Understand Neurocristopathies (Boston: Elsevier Inc.).

Betancur, P., Bronner-Fraser, M., and Sauka-Spengler, T. (2010). Assembling Neural Crest Regulatory Circuits into a Gene Regulatory Network. Annu. Rev. Cell Dev. Biol. *26*, 581–603.

Chambers, S.M., Fasano, C.A., Papapetrou, E.P., Tomishima, M., Sadelain, M., and Studer, L. (2009). Highly efficient neural conversion of human ES and iPS cells by dual inhibition of SMAD signaling. Nat Biotechnol *27*, 275–280.

Etchevers, H.C., Amiel, J., and Lyonnet, S. (2006). Molecular bases of human neurocristopathies. Adv. Exp. Med. Biol. *589*, 213–234.

Hall, B.K. (2008). The neural crest and neural crest cells: discovery and significance for theories of embryonic organization. J. Biosci. *33*, 781–793.

Jiang, X., Gwye, Y., McKeown, S.J., Bronner-Fraser, M., Lutzko, C., and Lawlor, E.R. (2009). Isolation and Characterization of Neural Crest Stem Cells Derived From In Vitro–Differentiated Human Embryonic Stem Cells. Stem Cells and Development *18*, 1059–1070.

LaBonne, C., and Bronner-Fraser, M. (1998). Induction and patterning of the neural crest, a stem cell-like precursor population. J. Neurobiol. *36*, 175–189.

Le Douarin, N.M., and Dupin, E. (2003). Multipotentiality of the neural crest. Current Opinion in Genetics & Development *13*, 529–536.

Le Douarin, N.M., Calloni, G.W., and Dupin, E. (2008). The stem cells of the neural crest. Cell Cycle *7*, 1013–1019.

Lee, G., Chambers, S.M., Tomishima, M.J., and Studer, L. (2010). Derivation of neural crest cells from humanpluripotent stem cells. Nature Protocols *5*, 688–701.

Lee, G., Kim, H., Elkabetz, Y., Shamy, Al, G., Panagiotakos, G., Barberi, T., Tabar, V., and Studer, L. (2007). Isolation and directed differentiation of neural crest stem cells derived from human embryonic stem cells. Nat Biotechnol *25*, 1468–1475.

Menendez, L., Kulik, M.J., Page, A.T., Park, S.S., Lauderdale, J.D., Cunningham, M.L., and Dalton, S. (2013). Directed differentiation of human pluripotent cells to neural crest stem cells. Nature Protocols *8*, 203–212.

Menendez, L., Yatskievych, T.A., Antin, P.B., and Dalton, S. (2011). Wnt signaling and a Smad pathway blockade direct the differentiation of human pluripotent stem cells to multipotent neural crest cells. Proceedings of the National Academy of Sciences *108*, 19240–19245.

Pomp, O., Brokhman, I., Ben-Dor, I., Reubinoff, B., and Goldstein, R.S. (2005). Generation of peripheral sensory and sympathetic neurons and neural crest cells from human embryonic stem cells. Stem Cells *23*, 923–930.

Pomp, O., Brokhman, I., Ziegler, L., Almog, M., Korngreen, A., Tavian, M., and Goldstein, R.S. (2008). PA6-induced human embryonic stem cell-derived neurospheres: a new source of human peripheral sensory neurons and neural crest cells. Brain Res. *1230*, 50–60.

CHAPTER 4

EXAMINING NEURAL CREST CELL SURVIVAL AND PROLIFERATION USING PATIENT-DERIVED IPSCS TO DEVELOP AN IN VITRO MODEL OF TREACHER COLLINS SYNDROME

INTRODUCTION

Neural crest cells (NCCs) are a population of multipotent stem cells that emanate from the developing ectoderm during neural tube closure. The early development and mulitpotentcy of NCCs makes this cell type well suited to studying models of differentiation, tissue development, and disease pathogenesis. The objective of this proposal is to explore two aspects of NCC biology: to develop an *in vitro* model of Treacher Collins Syndrome (TCS) and to develop a model of human brown adipogenesis. TCS is a congenital disorder characterized by improper craniofacial architecture arising from aberrant NCC colonization. TCS arises from mutations within *TCOF1* and functional complications of its product, treacle. The molecular pathogenesis of TCS is poorly understood, although animal models suggest that treacle is a modulator of ribosome biogenesis. *Tcof1* haploinsufficient mice show reduced ribosome maturation, leading to activation of stress surveillance mechanisms, and subsequent NCC death. However, animal models may not be capable of illuminating a comprehensive picture of TCS in humans and are not well suited for its detailed dissection. We intended to overcome these obstacles by elucidating the molecular basis for TCS utilizing patient-derived, induced pluripotent stem cells (iPSCs).

In addition to the decreased survival of NCC-derived cells in the *Tcof* haploinsufficient mouse model, NCC proliferative capacity is impaired as measured by Brdu incorporation in *Tcof1*$^{+/-}$ embryos versus WT cohorts (Dixon et al., 2006) (Figure 9, d). Control experiments transplanting WT hindbrain neuroepithileum in cultured E8 *Tcof1*$^{+/-}$ embryos displayed minimal apoptosis, whereas the same cells transplanted from *Tcof1*$^{+/-}$ into WT embryos exhibited significant apoptosis (Dixon et al., 2006). These data support the conclusion that the observed phenotype is cell autonomous and not driven by factors extrinsic to the NCCs, thus, patient-derived cells should be capable of displaying a diseased phenotype in culture conditions.

These preliminary studies in murine models of TCS have demonstrated that *Tcof1* haploinsufficiency results in decreased survival of NCCs. While these reports demonstrated craniofacial abnormalities, these studies have been characterized in genetically manipulated mice, which do not faithfully recapitulate TCS beyond late gestation, as this genotype is lethal. In addition these models demonstrate that burgeoning NCCs have defects in proliferation. Neither survival nor proliferation has ever been measured in developing human NCCs or subsequent cell types.

By comparing patient-derived vs. WT iPSC survivability during NCC differentiation, we hypothesized that TCS-derived cells would undergo excessive cell death leading to a reduced pool of NCC-derived cells or that there would be a reduction in proliferative capacity of patient-derived cells during the differentiations. The data presented here do not support these predictions.

RESULTS

The first step in developing an iPSC-based disease model is to reprogram patient-derived cells. Our lab was uniquely positioned to undertake the proposed research because we have extensive experience using iPSC technology, maintain access to a TCS patient pool, have generated iPSC lines from TCS patient cells, and have differentiated these lines to a NCC lineage via our established protocols (Figure 4.1) (Menendez et al., 2013; 2011). Our established protocol for NCC differentiation, delivers fully differentiated NCCs between 18-21 days in NCC culture (Figure 4.2) (Menendez et al., 2013). We utilized a Sendai virus based commercial reprogramming strategy to deliver the four reprogramming factors Oct4, Sox2, Klf4 and c-Myc to recipient donor cells, which, over a course of three to four weeks after the initial delivery of reprogramming factors, are reprogrammed to a pluripotent state. The advantage of this approach is that the Sendai virus does not integrate into the host cell genome. The cells are monitored for the appearance of characteristic colonies (Figure 4.1b). Once iPSC colonies are obtained, we confirm pluripotentcy markers utilizing immunofluorescence. Upon confirmation that the cells have been reprogrammed, low passage lots are serially frozen. The cells are genotyped by fluorescence in situ hybridization (FISH) and subjected to G-band analysis to confirm that genetic aberrations have not been introduced during the reprogramming procedure. Induced PSC colonies are then transitioned to culture in chemically-defined media that is compatible with differentiation into lineages such as NCCs (Menendez et al., 2013).

Two TCS-patient derived cell lines have been generated thus far with 5 clones in each line. Several WT iPSC lines have been evaluated for their ability to become NCCs. Kinetics of NCC differentiation were matched between TCS-derived iPSC cells and WT iPSC controls. Of these assays, the K3 line has shown to be the best parallel comparator to the TCS lines tested

(Figure 4.3 and data not shown). TCS cell lines are designated by the three letter term TCO, their cell line number, followed by their clone number. The two lines in current use are TCO1 and TCO3. Neural crest cell differentiation of iPSCs is accomplished through our established protocol (Menendez et al., 2011; 2013). NCC morphology wass apparent within 10-14 days and cells are assayed for NCC markers by flow cytometry, IF, and/or qRT-PCR. Positive NCC markers for IF include p75, Hnk1, AP2 and FoxD3, negative markers for iPSCs Sox2, Oct4, Nanog. NCCs were p75+ and Hnk1+ during flow cytometric analysis and qRT-PCR analysis demonstrated upregulated expression of genes such as *NGFR*, *PAX3, TFAP2, ZIC1, SOX9* and *SOX10* (Figures 3.1, 4.2).

In order to establish a model to investigate patient-derived cell survival relative to WT during NCC differentiation, a flow cytometric protocol was established based on a previous report of monitoring cell survival of hESCs utilizing the vital stain propidium iodide (PI) and a mitochondrial membrane potential (MMP) sensitive dye $DiIC_1(5)$ (Edel et al., 2011). This protocol was adapted and optimized for our culture conditions. The assay is both sensitive and specific enough to detect cell survival, which has been demonstrated by us in both WA09 hESCs and differentiated NCCs (Figures 4.4, 4.5). The readouts for cell death were loss of mitochondrial membrane potential via the potential sensitive dye 1,1',3,3,3',3'-hexamethylindodicarbo-cyanine iodide [$DiI_1(5)$] and the ability to take up the vital stain propidium iodide (PI). The maintenance of the DiIC dye is dependent on the inside-negative transmembrane potential maintained by functional mitochondria, loss of which is indicative of a failure to thrive and precedes an apoptotic program. Viability is established by high DiIC stain, exclusion of PI; as an internal control, the protonophore carbonyl cyanide *m*-chlorophenylhydrazone (CCCP) was used to disrupt the mitochondrial membrane potential. Both

apoptosis and necrosis will be induced as positive controls of cell death- apoptosis: 10uM camptothecin x 4hrs; necrosis: incubation at 65°C for 30 minutes, respectively. We attempted several methods of cell death interrogation, however, only the current method delivers consistent results. Using Annexin V to measure phosphatidylserine exposure to the extracellular leaflet, which is routinely used to assay apoptosis, was the least reliable. This unreliability has been documented and is inherent to adherent cell culture (Bundscherer et al., 2013; van Engeland et al., 1996).

We measured survivability every two days from D0-D21 or until cell markers indicative of NCC differentiation reach cell markers indicative of NCC differentiation reach their maxima. A combination of reduced MMP and low PI staining was used to establish cell death due to apoptosis, whereas, high PI positive staining will indicate necrotic death or secondary necrosis. Transitional, or secondary necrosis is a hallmark of late apoptosis and includes low MMP. Interestingly, our NCC time course data does not display the same cellular apoptotic behavior as expected from murine studies. During differentiation of WT vs Treacher Collins cells to NCC, no significant differences in levels of cells death were apparent (Figures 4.4, 4.5). The WT K3 cells displayed the same characteristics as the TCO-derived cells throughout the differentiations with regard to cells death. The assay profiles for necrosis and camptothecin induced apoptosis were also no different. Additionally, we performed poly (ADP-ribose) polymerase-1 (PARP-1) cleavage analysis via western blot. Cleaved PARP-1 is a sensitive indirect assay to detect activation of the executioner Caspase-3, which PARP-1 is a target of. In agreement with the flow cytometric data, PARP-1 cleavage was not different between WT K3 cells and TCO-derived cells during NCC differentiation (data not shown).

In proliferation studies, we enumerated cell numbers every three days during differentiation. We employed a very sensitive flow cytometry cell counting method utilizing the CountBright absolute counting beads (Figure 4.5). We complexed these beads with a fluorescent 7-AAD (7-amino-actinomycin D) vital stain. 7AAD has a high DNA binding constant and is efficiently excluded by intact cells, thus we could reliably count total cell numbers between passages and enumerate any loss in proliferation due to dead cells. By comparing the ratio of bead events to cell events, absolute numbers of cells in the sample were calculated. We predicted that a decrease or delay in proliferation would be observed by a decrease in absolute cell number as compared to WT-derived cells. However, no significant differences in cell number were observed between TCS and WT cells (Figure 4.5). Differentiation of iPSCs to NCCs in our culture system may not be fully representative of the cell identity upon delamination from the neural crest *in vivo*, and thus may not be able to recapitulate the evidence for increased apoptosis observed in murine studies (Figure 9). We propose that the differentiation of patient-derived NCCs to MSCs may more accurately depict the *in vivo* cell state and properly portray a more EMT-like phenotype. If so, we expect a decrease in survival of patient-derived cells during the differentiation (Dixon et al., 2000; 2006; Jones et al., 2008).

TCOF1/Treacle expression patterns have been investigated in the context of adult patient fibroblasts, transformed cells such as 293T cells, and murine embryonic NCCs. However, these are static representations and do not reflect the complexity of treacle that may exist during the course of NCC differentiation during human embryogenesis. To investigate treacle expression during differentiation, we compared WT to patient-derived cells during our established NCC differentiation protocol. Figure 4.3 displays western blot data from the results of a 21-day differentiation time course of K3 WT and TCO1-2 patient-derived cells. Treacle expression is

dynamic, and it is immediately apparent that treacle undergoes some form of processing during the differentiation from the iPSC state to the NCC lineage. A low molecular weight form of treacle predominates in the first days of differentiation as the identity of the cell remains iPSC-like (Figure 4.3c,d); however, by day 6, treacle begins a shift toward a high molecular weight form, which becomes the predominate form as the cells become more NCC-like. The evolution to the higher MW form appears delayed in the WT cells, as the patient-derived cells display the high MW form by day 8, whereas the WT cells do not display the pattern until day 10. The patterns occur despite qPCR data indicating that treacle message is unchanged between the two cell types (data not shown). To determine if the treacle protein was degraded in a selective manner, the 26S specific inhibitor, MG132 was added to mature NCC cell culture. Addition of MG132 leads to a reappearance of the low MW in both patient-derived and WT NCCs, while control culture without the 26S inhibitor retained the high MW form of treacle (Figure 4.3e). Although not conclusive, these data and the fact that message remains constant suggest that treacle expression is regulated in a post-translational manner during differentiation from iPSC to NCC. Interestingly, the message for the NCC specific transcript *TFAP2B* in TCO-derived cells displayed reduced kinetics in is upregulation compared to WT K3 (Figure 4.3). From days 4-10 of the 21 day differentiation, TCO-derived cells had significantly less relative expression. This difference was abolished by D12 as the kinetics equalized. Furthermore, immunofluorescent microscopy of the TFAP2B protein demonstrated no differences in protein expression in mature NCCs. Therefore, determining transcript and protein expression of TCOF1 and treacle during MSC and later differentiations may be more critical to determining the molecular basis of TCS than in burgeoning NCCs.

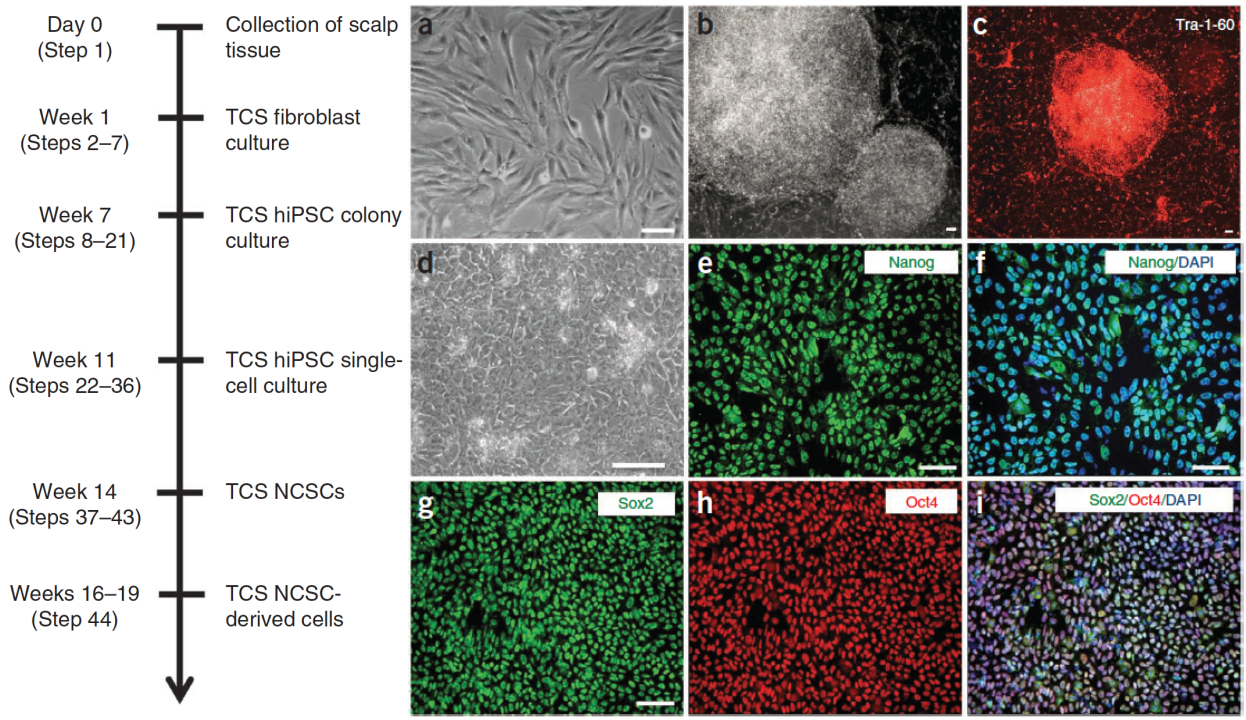

Figure 4.1- Schematic timetable of TCS hiPSC induction and differentiation to NCSCs and Generation of hiPSCs from TCS patients. (**a**) TCS fibroblasts seeded before viral transduction. (**b**,**c**) TCS hiPSC colonies grown after reprogramming (**b**) can be stained with Tra-1-60 antibody (**c**) (Steps 1–13). (**d**) After several passages, colonies can be adapted to single-cell culture conditions. (**e**–**i**) TCS hiPSCs should express pluripotent markers Nanog (**e**,**f**), Sox2 (**g**,**i**) and Oct4 (**h**,**i**) (Steps 14–36). Scale bars, 100 μM. (Menendez et al., 2013)

Figure 4.2- Differentiation of TCS hiPSCs to NCSCs. (**a**,**b**) Bright-field images of TCS NCSCs after day 3 (d3) and day 8 (d8) of differentiation (Steps 40–41). (**c**,**d**) Immunocytochemistry analysis shows that TCS hiPSCs are negative for p75 and low to moderate for Hnk1 expression before differentiation to NCSCs. (**e**–**i**) At day 16 of differentiation (Step 42), TCS NCSCs are positive for p75 (**e**), Hnk1 (**f**), AP2 (**g**) and FoxD3 (**h**) and negative for Sox2 and Oct4 (**i**). Scale bars, 100 μM. (**j**) Flow cytometry analysis for TCS hiPSCs before and after neural crest differentiation. The percentage of p75 + Hnk1 + cells is shown in the graph in the circled areas. (**k**) Real-time PCR data showing the expression of *PAX3*, *ZIC1*, *TFAP2A*, *SOX9*, *SOX10* and *P75NTR* in TCS NCSCs relative to TCS hiPSCs (Step 42). P0, passage 0; P2, passage 2; TC, Treacher-Collins (Syndrome). (Menendez et al., 2013)

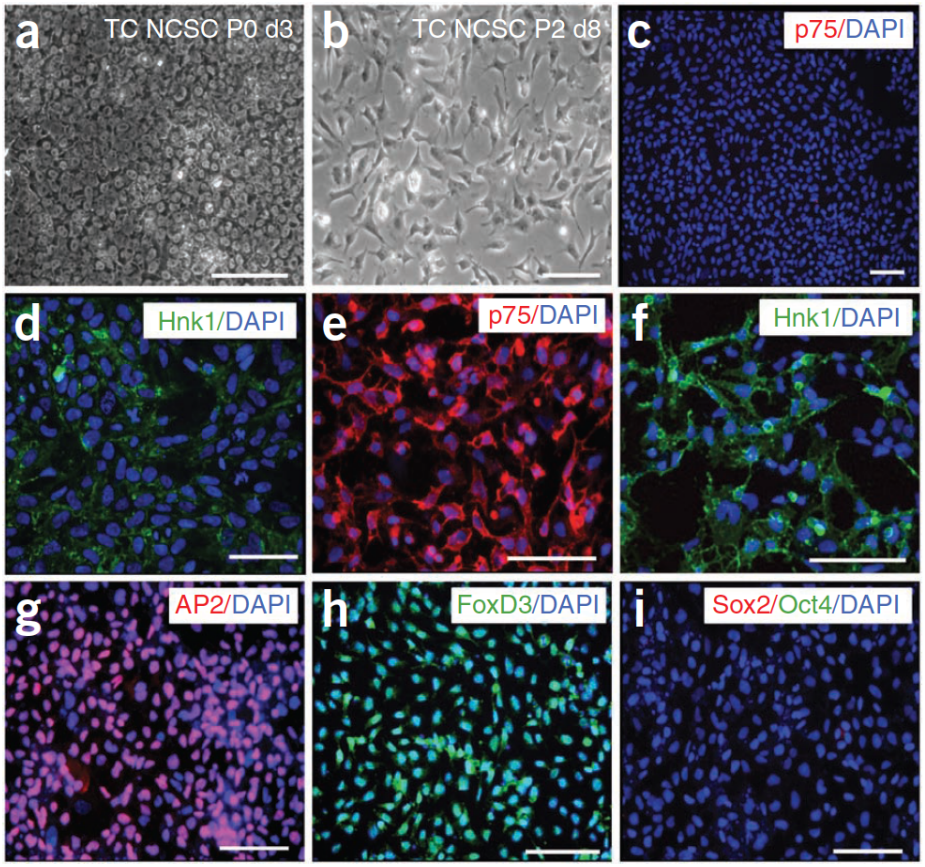
a
TC NCSC P0 d3
b
TC NCSC P2 d8
c
p75/DAPI
d
Hnk1/DAPI
e
p75/DAPI
f
Hnk1/DAPI
g
AP2/DAPI
h
FoxD3/DAPI
i
Sox2/Oct4/DAPI

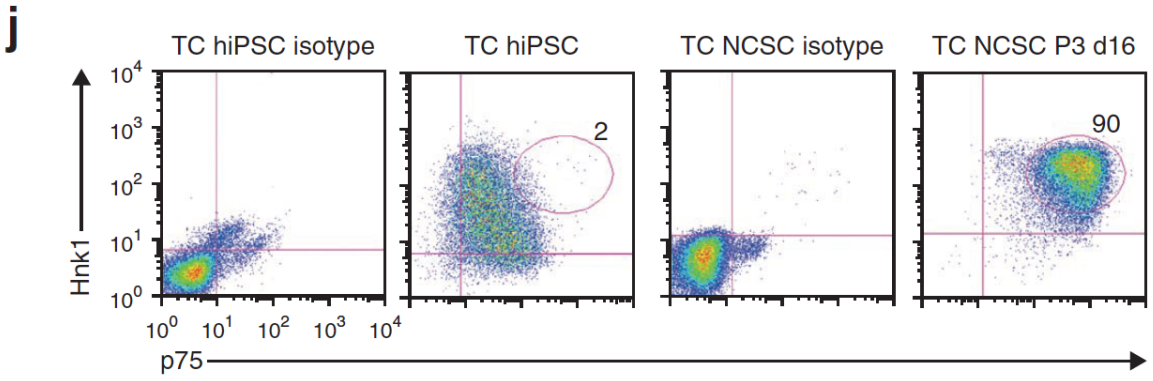
j
TC hiPSC isotype
TC hiPSC
TC NCSC isotype
TC NCSC P3 d16
2
90
Hnk1
p75
10^0
10^1
10^2
10^3
10^4

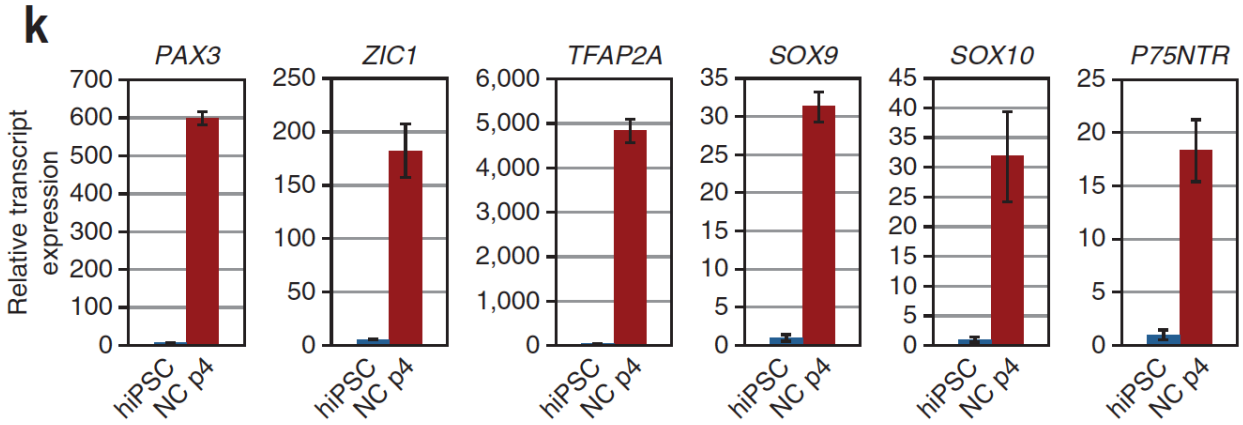
k
PAX3
ZIC1
TFAP2A
SOX9
SOX10
P75NTR
Relative transcript expression
hiPSC
NC p4

Figure 4.3. Protein and gene expression analysis of WT iPSC vs. TCS-derived cells. Immunofluorescent analysis of Treacle expression and TFAP2, a canonical NCC marker at D21 (final day of differentiation) 40x (a). qRT-PCR analysis of TFAP2 expression from D0-D21 of NCC differentiation. (*) $p = 0.0228$; (***) $p = .0009$; (****) $p \leq 0.0001$. Western Blot analysis of Treacle in patient-derived vs WT K3 cells: Treacle expression during NCC development days 0-21, patient derived (c), WT (d); d21 NCC Treacle expression pattern with or without 4hr treatment with MG-132 [10μM], a 26S proteasome inhibitor which reduces 26S proteasomal degradation (e).

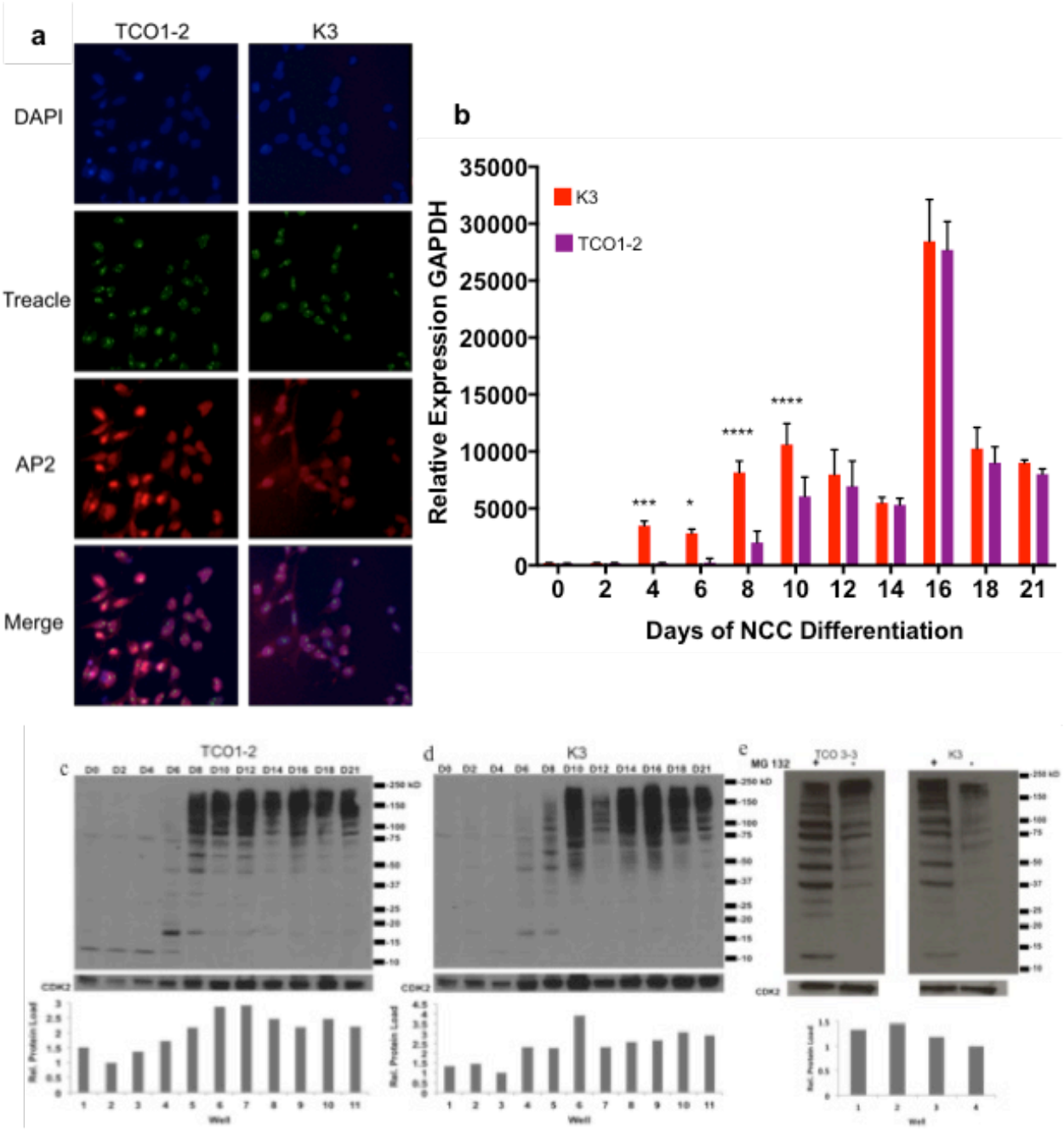
a
TCO1-2
K3
DAPI
Treacle
AP2
Merge
b
Relative Expression GAPDH
35000
30000
25000
20000
15000
10000
5000
0
K3
TCO1-2
***
*
****
****
0 2 4 6 8 10 12 14 16 18 21
Days of NCC Differentiation
c
TCO1-2
d
K3
e
MG 132
TCO 3-3
K3
CDK2
Rel. Protein Load
Well

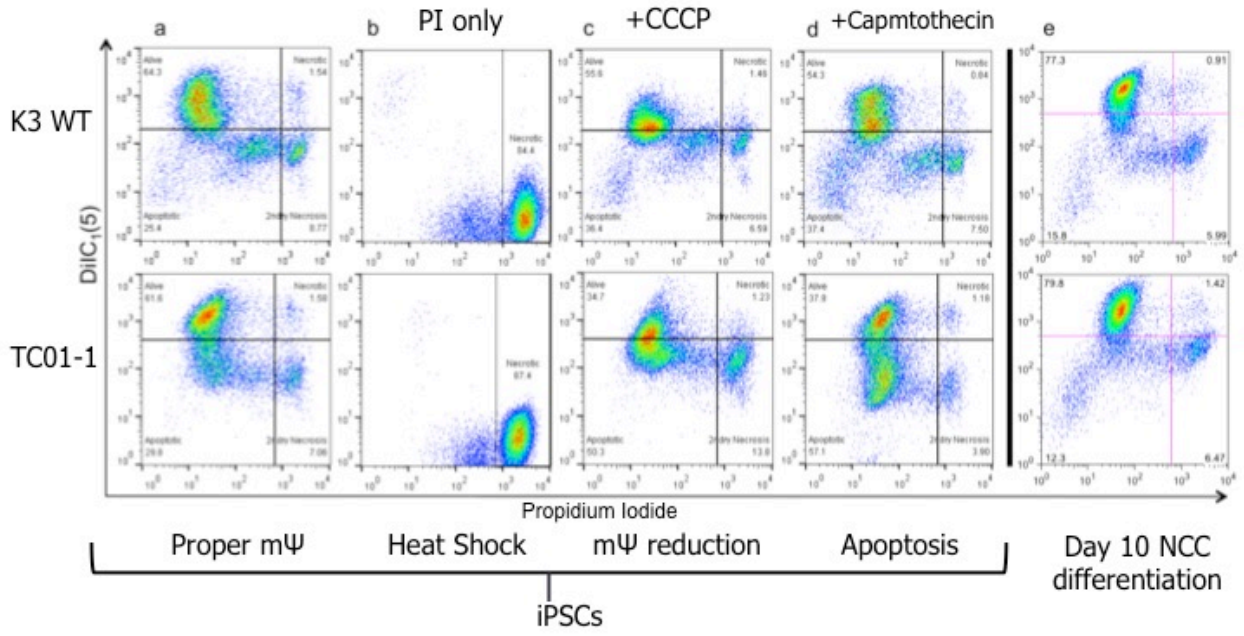

Figure 4.4- Flow cytometric analysis of iPSC and NCC cell death. K3 iPSCs were evaluated along with TCO1-1 iPSCs (bottom row) to demonstrate the potential use of this assay to measure cell death during differentiation to NCC phenotype (cells were from Day 8 of differentiation. Cells displaying proper mitochondrial membrane potential (MMP) (a); dead cells after heat shock treatment (b); display of shift in membrane potential with 3uM CCCP (oxidative phosphorylation uncoupler) control (c); Cell death induced by known apoptotic inducing agent, camtpothecin (10uM x 4hrs) (d); Day 10 differentiation of WT K3 (top) and TCO1-1 (bottom) (e), showing no differences in cell death between cell lines as seen in (a); data are representative of 21 day time course between three Treacher Collins and one WT induced pluripotent line (K3).

Figure 4.5- Flow cytometric analysis of iPSC and NCC cell death in conjunction with proliferation analysis using CountBright™ absolute counting beads. Day 12 K3 iPSCs were evaluated along with TCO1-1 iPSCs. Cells displaying proper mitochondrial membrane potential (MMP); dead cells after heat shock treatment display of shift in membrane potential with 3uM CCCP (oxidative phosphorylation uncoupler) control; Cell death induced by known apoptotic inducing agent, camtpothecin (10uM x 4hrs) (left); CountBright absolute bead counting using WT ESC, iPSC, and TCO1-1 cells. Dead cells were excluded by gating out the &AAD positive cells. Total cell number for D12 is shown on the upper right, whereas the mean of six separate experiments, each for all three TCO lines vs K3 WT cells are enumerating in the XY plot (bottom).

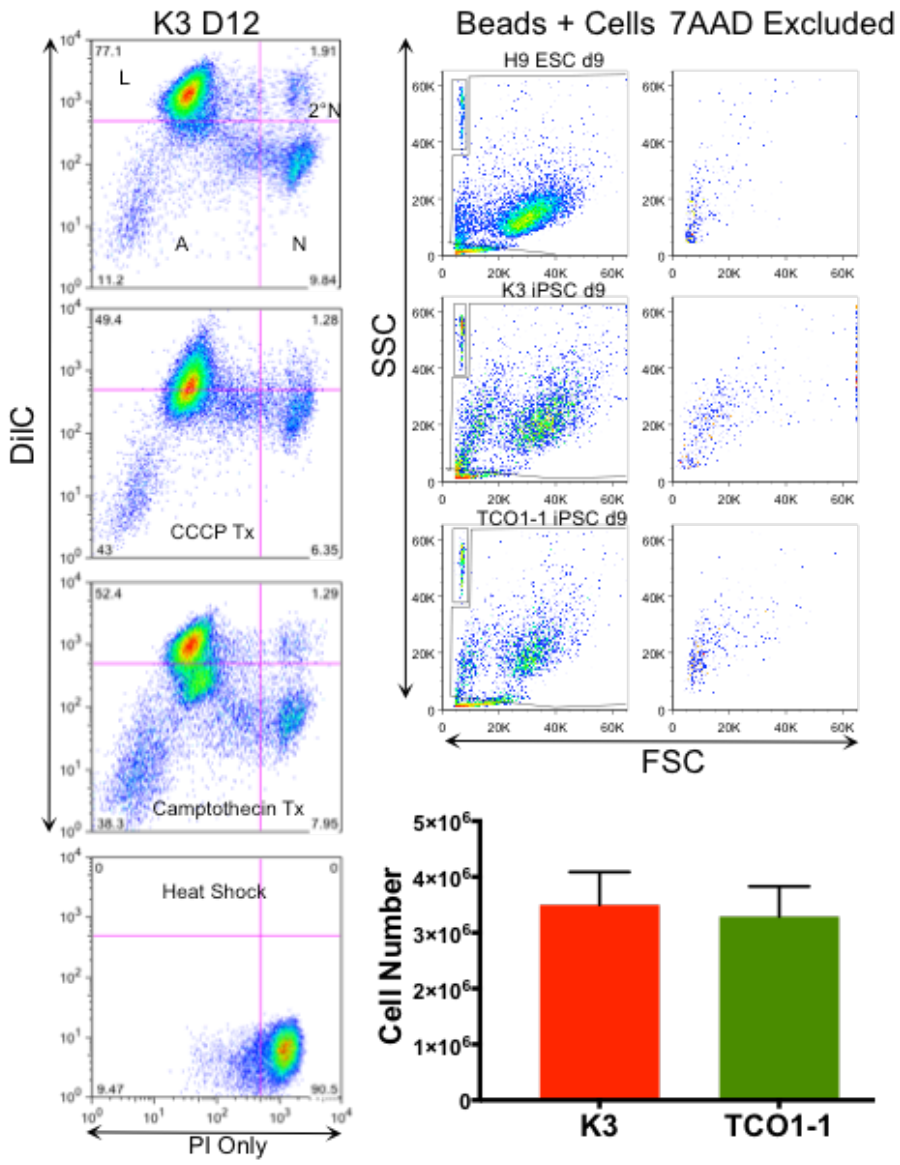
K3 D12
Beads + Cells 7AAD Excluded
DiIC
PI Only
L
A
N
CCCP Tx
Camptothecin Tx
Heat Shock
H9 ESC d9
K3 iPSC d9
TCO1-1 iPSC d9
SSC
FSC
Cell Number
K3
TCO1-1

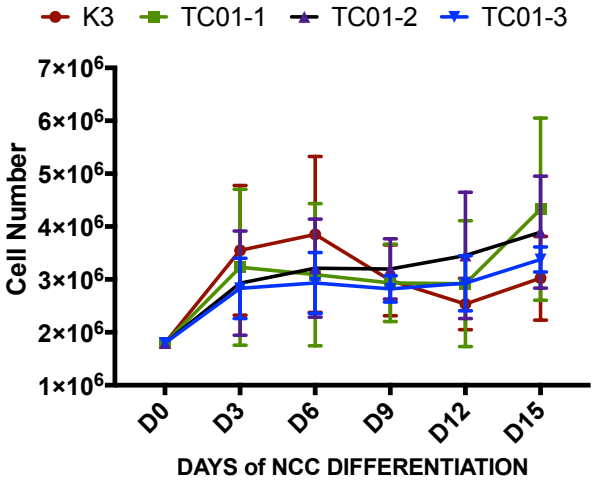
K3
TC01-1
TC01-2
TC01-3
Cell Number
DAYS of NCC DIFFERENTIATION
D0
D3
D6
D9
D12
D15

Table 4.1- Treacher Collins Syndrome patient lines with corresponding mutations

Cell Line	Nutide Δ	Consequence	Exon	Exon position	iPSC on MEFS	iPSC Feeder Free
TCO1	3540-3541 del GA	Frameshift	21	3287–3369	√	√
TCO3	159 G>C	Trp53Cys	2	109–164	√	√

REFERENCES

Bundscherer, A., Malsy, M., Lange, R., Hofmann, P., Metterlein, T., Graf, B.M., and Gruber, M. (2013). Cell harvesting method influences results of apoptosis analysis by annexin V staining. Anticancer Res. *33*, 3201–3204.

Dixon, J., Brakebusch, C., Fassler, R., and Dixon, M.J. (2000). Increased levels of apoptosis in the prefusion neural folds underlie the craniofacial disorder, Treacher Collins syndrome. Human Molecular Genetics *9*, 1473–1480.

Dixon, J., Jones, N.C., Sandell, L.L., Jayasinghe, S.M., Crane, J., Rey, J.-P., Dixon, M.J., and Trainor, P.A. (2006). Tcof1/Treacle is required for neural crest cell formation and proliferation deficiencies that cause craniofacial abnormalities. Proc. Natl. Acad. Sci. U.S.a. *103*, 13403–13408.

Edel, M.J., Menchon, C., Vaquero, J.M.A., and Izpisua Belmonte, J.C. (2011). A protocol to assess cell cycle and apoptosis in human and mouse pluripotent cells. Cell Commun. Signal *9*, 8.

Jones, N.C., Lynn, M.L., Gaudenz, K., Sakai, D., Aoto, K., Rey, J.-P., Glynn, E.F., Ellington, L., Du, C., Dixon, J., et al. (2008). Prevention of the neurocristopathy Treacher Collins syndrome through inhibition of p53 function. Nat Med *14*, 125–133.

Menendez, L., Kulik, M.J., Page, A.T., Park, S.S., Lauderdale, J.D., Cunningham, M.L., and Dalton, S. (2013). Directed differentiation of human pluripotent cells to neural crest stem cells. Nature Protocols *8*, 203–212.

Menendez, L., Yatskievych, T.A., Antin, P.B., and Dalton, S. (2011). Wnt signaling and a Smad pathway blockade direct the differentiation of human pluripotent stem cells to multipotent neural crest cells. Proceedings of the National Academy of Sciences *108*, 19240–19245.

van Engeland, M., Ramaekers, F., and Schutte, B. (1996). A novel assay to measure loss of plasma membrane asymmetry during apoptosis of adherent cells in culture. Cytometry.

CHAPTER 5

DIRECTED DIFFERENTIATION OF BROWN ADIPOCYTES FROM HUMAN PLURIPOTENT STEM CELLS

INTRODUCTION

The imposing health effects of obesity are global. Current worldwide estimates place greater than two billion adults as overweight with almost half qualifying as obese (BMI>30) (GBD 2015 Obesity Collaborators, 2017; Ng et al., 2014). Obesity is no longer a burden to developed nations; developing countries are suffering similar rates of obesity and associated diseases (GBD 2015 Obesity Collaborators, 2017; Ng et al., 2014). Excess adiposity is associated with and also increases the liability of chronic diseases such as type-2 diabetes, heart disease, insulin resistance, hyperglycemia, dyslipidemia, hypertension, many types of cancer, in addition to increased susceptibility to infection (Bornfeldt and Tabas, 2011; Huttunen and Syrjanen, 2013; Karlsson and Beck, 2010; Lloyd-Jones et al., 2009; Ng et al., 2014). Studies show that global obesity rates continue to dramatically rise and by 2030, it is estimated that the prevalence of obesity will increase by an additional 33% (Finkelstein et al., 2009). Critically, excess adiposity is a modifiable risk factor, however, therapeutic strategies must be developed to augment behavioral interventions to combat this major public health concern.

Several independent groups identified functional brown adipose tissue (BAT) in adult humans almost a decade ago (Cypess et al., 2009; Saito et al., 2009; van Marken Lichtenbelt et al., 2009; Virtanen et al., 2009). Present in many animals, BAT utilizes glucose and free fatty

acids to drive a non-shivering source of emergency heat production called thermogenesis. Because of its specialized function, BAT serves as a sink for serum glucose and free fatty acids. The importance of this tissue discovery in adult humans is apparent in light of BAT's considerable beneficial effects observed in murine studies (Gunawardana and Piston, 2012; 2015; Liu et al., 2013; Stanford et al., 2013). Moreover, the relative mass and activity levels of human brown adipocyte depots have been inversely correlated to body mass (Cypess et al., 2009; Saito et al., 2009; Virtanen et al., 2009). It stands to reason then that examining methods to augment BAT mass and/or activity in humans has received intense interest in recent years.

Both an understanding of BAT basic biology and development coupled to discovering mechanisms of activation are critical in developing therapeutic strategies to combat obesity and obesity associated diseases. Lineage tracing experiments suggest that brown adipocytes share a common progenitor with skeletal muscle and arise from the dermomyotome of the paraxial mesoderm and assume the fate of brown adipocyte under control of the master switch, PR domain zinc finger protein 16 (PRDM16) (Lepper and Fan, 2010; Sanchez-Gurmaches and Guertin, 2014; Sanchez-Gurmaches et al., 2012; Seale et al., 2008; Wang et al., 2014). However, recent data comparing murine and adult human brown adipocytes suggest that human brown adipocyte identity and relatedness to classical murine brown adipocytes are issues far from resolved (Shinoda et al., 2015). Thus, a human cell-based system capable of deciphering developmental and functional queries concerning brown adipocytes would be indispensible.

The current repertoire of human-cell-based models of brown adipogenesis relies on primary tissue derived stem cells (ADSCs), overexpression systems, or methods relating to hematopoietic development (Ahfeldt et al., 2012; Elabd et al., 2009; Nishio et al., 2012; Pisani et al., 2011). These methods have limited utility in examining the suggested developmental path of

brown adipocyte origin, as well as limited use in functional screens, such as high throughput drug screens due to inherent problems with scalability, proliferative potential, reduced differentiation potential or clinical relevance to glucose and lipid metabolism (Chen et al., 2012). We therefore sought to derive brown adipocytes using a developmentally appropriate pathway from human pluripotent stem cells. We first developed a novel rotational suspension culture system to reliably generate early dermomyotome-like cells that were capable of generating UCP1+ brown adipocytes. To our knowledge we are the first to derive functional brown adipocytes via a dermomyotome-like cell using directed differentiation in chemically defined media in the absence of genetic programming. Molecular and functional interrogation of differentiated brown adipocytes demonstrated that they have a high degree of UCP1 expression as validated by RT-qPCR, immunofluorescent microscopy, and flow cytometry. Brightfiled microscopy revealed the presence of extensive multilocular lipid droplets, which were surrounded by numerous UCP1+ mitochondria as reveled by staining with the neutral LipidTox® and MitoTracker® stains and UCP1 antibody. These data were further supported via ultrastructural analysis through electron microscopy. Stimulation through known brown adipocyte activators, norepinephrine, isoproterenol, and forskolin was demonstrated and measured by RT-qPCR, free glycerol release, and extracellular flux analysis. Similarly, oxidative capacity of exogenous and endogenous fatty acids was demonstrated by extracellular flux analysis. These data establish that our system mimics early development and provides a means by which to derive faithful and functional brown adipocytes capable of responding to stimulatory cues in vitro through increased uncoupling and substrate utilization. Therefore, this system provides a platform by which to interrogate both human brown adipocyte development and functional responses such as evaluating drug candidates that lead to activation.

RESULTS

Directed Differentiation of human PSCs into Dermomyotome-like Paraxial Mesoderm

Lineage tracing studies demonstrate that brown adipocytes arise from the dermomytome of the paraxial mesoderm sharing a common pool of myogenic factor 5 (MYF5) positive progenitors with skeletal muscle cells (Atit et al., 2006; Lee et al., 2013; Lepper and Fan, 2010; Sanchez-Gurmaches and Guertin, 2014; Seale et al., 2008; Timmons et al., 2007). To develop an in vitro analog to brown adipocyte development, we sought to derive brown adipocytes from a MYF5+ dermomytome-like origin. By utilizing a defined, multistep, mesoderm cocktail, we successfully established a highly efficient in vitro culturing system that yields dermomytome-like cells from hPSCs. Differentiation of hPSCs toward a paraxial mesoderm (PM) fate is accomplished by a three-step approach (Figure 5.1). First, feeder-free hPSCs are suspended in rotational suspension-culture in our defined hPSC maintenance medium supplemented with Y-27632 dihydrochloride for 24 hours to suppress anoikis. After an additional 24 hours in the hPSC maintenance medium, the resulting spheres are driven toward a mes-endoderm identity via utilization of paraxial mesoderm medium 1 (PMM1): low concentration BMP4, high bFGF, in combination with rapamycin for 48 hours; then dermomytome identity is achieved through simultaneous inhibition of endogenous BMP signaling via Noggin and activation and stabilization of WNT signaling through paraxial mesoderm medium 2 (PMM2): a WNT cocktail composed of WNT3a, the GSK-3 inhibitor, BIO, and the cAMP agonist Forskolin for an additional 96 hours in the presence of high bFGF and Rapamycin (Cheung et al., 2014; Shelton et al., 2014; Xu et al., 2013; 2011; Zhang et al., 2008; Zhou et al., 2009). A primary three-gene suite was selected to monitor the progression of dermomytome specification: Forkhead Box C1 (*FOXC1*), Myogenic Factor 5 (*MYF5*) and Paired Box 3 (*PAX3*). Both *MYF5* and *PAX3* began

modest upregulation of expression after 48-hour sphere formation (Figure 5.2). *FOXC1* upregulation kinetics were not appreciable until exposure to PMM1 (Figure 5.2). All three genes begin extensive upregulation upon exposure to PMM2 (Figure 5.2). In addition to the three-gene suite, a number of additional genes were examined. Coincident with additional paraxial mesoderm associated genes, expression of *PAX1 or PAX9* genes were undetectable- indicating paraxial mesoderm identity did not extend to the sclerotome (Figure 5.4 and data not shown). Furthermore, the lateral plate marker *NKX2.5* was lowly expressed until the final day of differentiation where it reached a maxima of 28 fold increase- a value nearly 10 fold lower than observed in splanchnic mesoderm differentiations. (Figure 5.4 and data not shown). Because sphere formation mimics embryoid body formation, we sought to determine the contribution of other transcripts demonstrative of lineages proximal to paraxial mesoderm during development in addition to lateral plate, such as neural tube and ectoderm marks during the differentiation. The neural tube mark *PAX6* was lowly detected and unchanging during the differentiation as were the neural fold mark *SOX1*, neural crest mark *FOXD3* and the epithelial mark *CDH1* (Figure 5.4).

Myogenic factor 5-protein expression was interrogated by western blot on the final day of differentiation and compared to cells differentiated to definitive endoderm as a negative control (Figure 5.3). Both iPSCs and ESCs demonstrated significant MYF5 expression by day 8 of the PM differentiation. Enumeration of cellular expression of the three-gene suite at the end of PMM2 was interrogated through immunofluorescent microscopy and flow cytometry (Figure 5.3 and 5.4). Sectioned cryopreserved spheres displayed a near uniform expression of the entire three-gene suite (Figure 5.3). Additionally, flow cytometric analysis demonstrates that the differentiation is highly efficient with consistent yields greater than 90% MYF5+/FOXC1+ and

MYF5+/PAX3+ (Figure 5.3). Additionally, the cell surface markers CD29, CD34, and PDGRFα have been found on the surface of presumptive murine brown adipocyte precursors (Wang et al., 2014); we found these marks to be present on our dermomytome-like cells as well (Figure 5.4). Taken together, these findings support the establishment of a highly efficient differentiation of a dermomyotome-like population from hPSCs.

Differentiated Adipocytes Display Genotypic and Morphological Characteristics Consistent with Brown Identity

We attempted to drive brown adipocyte differentiation using a suite of factors known to support adipogenesis as well as brown adipocyte commitment (Choy and Derynck, 2003; Nedergaard et al., 2005; Noguchi et al., 2007; Tseng et al., 2008), in a defined medium, albeit not previously utilized in concert (Figure 5.5). Single-cell dissociated PM plated in brown adipocyte differentiation medium (BAD) did not display morphology consistent with mesenchymal stem cells (Figure 5.6): they maintained a small stellate shape, reproduced quickly and became readily compact. Moreover, during the course of differentiation, the cells form a three-dimensional structure up to 75 um thick (Figure 5.12, 5.13 and 5.14). The appearance of lipid droplets was readily visible as early as day 16 but more consistently by day 21 of brown adipocyte differentiation (Figure 5.6). Unlike MSCs, in which differentiation to adipocytes is more efficient when the MSCs are grown to confluence prior to differentiation, PM cells continue down the mesoderm lineage if placed in any medium that does not contain the BAD factors and do not differentiate efficiently when plated at densities that represent near confluence for their size- ~250K cells/cm2 (data not shown).

To investigate transcript level analysis, we carried out RT-qPCR for a group of marker genes known to be fundamental to adipogenesis, brown specification, commitment or thermogenic function. Increases in fold expression of the adipogenic transcripts ADIPOQ, FABP4 and PPARγ preceded and were coincident with droplet formation, as were increases in the brown adipocyte specific transcripts EBF2, ENDRB and PRDM16 (Figure 5.7). FABP4 experienced the greatest change, reaching 10K-fold increase within eight days post PM, with a sustained maximum 1M-fold increase by 24 days post PM (Figure 5.7). Both PPARγ and PRDM16 attained their maxima at d24, immediately preceding the onset of significant UCP1 expression (Figures 5.7 and 5.8). Critically, the mature brown adipocyte genes governing fatty acid transport, packaging, and droplet containment, CD36, ELOVL3, CIDEA and PLIN1 were dramatically upregulated during brown adipocyte differentiation (Figure 5.8). Along with the brown fat specific mark PDK4, which displayed a 10K-fold increase over the PM control, the cAMP responsive genes regulating mitochondrial biogenesis and adaptive thermogenesis (PGC1-α, IRF4, DIO2 and UCP1) were upregulated and sensitive to stimulation with forskolin at d36 post PM (Figures 5.7 and 5.8). Importantly, UCP1 expression and responsiveness to stimulation was maintained in long-term culture (>21 days post reaggregation) (Figures 5.11, 5.12, 5.13, 5.19 and 5.22). Studies have implicated Forkhead Box C2 (FOXC2) in browning of WAT in mice, as well as a leaning phenotype in transgenic expression, coupled with improved insulin sensitivity and reduced circulating triacylglycerides (Kim et al. 2005 Cederberg 2001). In our brown adipocyte differentiation, FOXC2 is moderately upregulated relative to PM; however, the transcript is upregulated over 60-fold in PM relative to pluripotent cells (Figure 5.4 and 5.9). FOXC2 CT values consistently hover between 27 and 29 throughout the differentiation (data not shown). The beige fat markers CD137 and TMEM26 were lowly expressed during the brown

adipocyte differentiation and were equal to or down regulated relative to PM expression by day 36 of the brown adipocyte differentiation (Figure 5.9). Together, these observations are consistent with a transcriptional regulatory program associated with developing and mature brown adipocytes.

Flow cytometric analysis of the brown adipocyte differentiation demonstrated that by 30 days post establishment of paraxial mesoderm, double UCP1/LipdTox Red positive cells comprised 45% of the cell population (FIG 4.9). In accordance with transcript data, UCP1 protein expression rapidly increased in under a week, with the double UCP1+/LTR+ population rising to 63% by day 36 of the brown adipocyte differentiation (Figure 5.10). The effects of forskolin stimulation on UCP1 expression were evident as the cAMP agonists pushed the UCP1+/LTR+ population to 72%.

As the differentiation progressed passed d36, lipid droplet accumulation became so great as to reduce the functionality of flow cytometry due to the inherent difficulty in dissociating, collecting, labeling, and washing those cells with the highest lipid densities. However, dissociation, reaggregation of the brown adipocytes in suspension culture between d36-d42, and replating the reaggregates in outgrowth culture reduced the number of non-lipid containing/UCP1 negative cells (Figure 5.6, 5.11, 5.12 and 5.13). Upon replating, outgrowths rapidly colonize the plate, again in a three-dimensional fashion, with lipid droplets forming extensively throughout all layers (Figures 5.6, 5.11, 5.12, 5.13 and 5.14). This architecture was in stark contrast to white adipocytes differentiated from commercially available adipocyte derived-stem cells, which maintained a sheet-like architecture and a vastly reduced level of lipid droplet formation (Figure 5.15).

Confocal immunofluorescent microscopy also demonstrated a tighter three-dimensional packing of brown adipocyte nuclei, a greater degree of spherical droplet packaging, higher mitochondrial density, and high UCP1 staining relative to differentiated white adipocytes (Figures 5.11, 5.12 and 5.13). Interestingly, differentiated white adipocytes were not completely devoid of UCP1 expression, possibly owing to the nature of the ADSCs from patient-lipid aspirate. Furthermore, these patient-derived ADSCs never adopt mature white adipocyte unilocularity as observed in vivo. Z-stacking the layers of the brown adipocyte culture revealed a mixed orientation of the substructres- the nuclei and mitochondria generally occupied a position proximal to the growth surface, while the lipid droplets with the greatest lipid content were situated more superficially (Figures 5.12 and 5.13).

Brown adipocytes have characteristic internal features associated with their thermo-capable function. This list of features principally includes multilocular lipid droplets with numerous resident mitochondria coextensively populating the cytoplasmic space. To examine the ultrastructural features of brown adipocytes, outgrowths were grown on coverslips after reaggregation and examined after d60 by transmission electron microscopy (Figure 5.16). Our differentiated brown adipocytes confirmed the presence of numerous lipid droplets surrounded by abundant mitochondria, which were concentrated in the portions of the cytosol containing the lipid droplets (Figure 5.16). The external features of brown white adipocytes were interrogated by scanning electron microscopy. For SEM, two modes of electron capture were employed: backscatter detection and secondary electron detection. Both methods yield relative three-dimensional structural information, however, backscatter detection can penetrate to a greater depth due to its perpendicular position to the incident beam of electrons. Importantly, the lipid fixative osmium tetroxide imparts an enhanced scattering effect to lipids and therefore lipid

droplets appear brighter than the surrounding structures using backscatter detection. Within SEM samples, the three-dimensional architecture of the brown adipocytes is readily apparent compared to the ADSC differentiated white adipocytes (Figure 5.14 and 5.15). Prominent multilocular lipid compartments are found throughout- both on top and underneath the culture structure and to a greater extent than that observed within the white adipocyte culture Figure 5.14 and 5.15).

Differentiated Brown Adipocytes Demonstrate Functional Capacity in Response to Stimuli

The hallmark function of brown adipocytes is their capacity to uncouple the proton motive force from ATP generation and instead drive heat production from the electrochemical gradient. This process is driven by mitochondrial UCP1. Activation of UCP1 in vitro can be realized though several means: stimulation through free fatty acids and agonism of β-adrenergic receptors and adenylyl cyclase. In addition to the genotypic and morphological evidence that our cells were brown adipocytes, we sought to establish their functional capacity upon stimulation with a variety of activating agents. Three methods of analysis were employed: oxygen consumption rate (OCR), extracellular acidification rate (ECAR), and free glycerol analysis to describe their potential for increased mitochondrial activity, enhanced glucose utilization, and propensity to undergo lipolysis, respectively.

To analyze the functional metabolism of the these cells in response to stimulation, we plated brown adipocyte outgrowths in 24 well Seahorse plates and cultured the cells for an additional 21 days in BAD2. Control cells were differentiated PM or white adipocytes. Upon acute exposure to 1uM norepinephrine (NE), brown adipocytes significantly increased their basal oxygen consumption by 45.3% over that of untreated brown adipocytes (Figure 5.17).

Oxygen consumption remained elevated over that of untreated cells for the duration of the assay until the proton gradient was abolished by the antimycin A/rotenone injection. Both maximum respiration and uncoupled respiration were significantly greater in the NE treated samples than the untreated brown adipocytes (Figure 5.17). Oxygen consumption in PM control cells was markedly less in both treated and untreated samples. Moreover, NE had no effect on the oxygen consumption rate of PM cells at any point during the assay (Figure 5.17). There were no differences observed in basal oxygen consumption and maximal oxygen consumption upon FCCP induced uncoupling in PM cells. Importantly, however, PM cells were significantly more glycolytic as measured by ECAR (Figure 5.17). PM cells displayed a mean basal ECAR 63.5% greater than that of brown adipocytes and a mean maximum ECAR 65.2% greater than brown adipocytes. Glycolysis was only significantly, albeit mildly, increased upon NE stimulation in BA, and this effect was eliminated upon oligomycin injection, indicating that NE alone was not sufficient for maintaining glucose utilization, but that NE was capable of increasing mitochondrial activity as measured by significant elevations in oxygen consumption and uncoupled respiration, the latter presumably by increased UCP1 activity.

Overnight stimulation with 100uM isoproterenol (ISO) lead to a significant increase in basal oxygen consumption (+41%) relative to untreated BA (Figure 5.18). However, ISO was unable to significantly alter maximal respiration or uncoupled respiration among BA samples. Again, glycolysis was not significantly different in BA ECAR readings (Figure 5.18). As observed in the NE treatment assay, PM control cells were mainly glycolytic, and ISO treatment did not significantly alter oxygen consumption or glycolytic rates between treated and untreated PM samples (Figure 5.18). It is important to note that PM cells are differentiated in the presence of forskolin. It is therefore feasible that stimulation by adrenergic reception and subsequent PKA

activation is impotent in PM cells owing to a maximum respiratory state having already been achieved through FSK.

Both NE and ISO activate brown adipocytes through β-adrenergic reception and downstream signaling through cAMP and PKA (Collins et al., 2010; Rubio et al., 1995). In contrast, the adenylyl cyclase agonist forskolin (FSK) bypasses receptor-mediated responses while still raising cAMP levels and subsequent PKA activity (Seamon et al., 1981). During extracellular flux analysis, overnight treatment with 10uM FSK had a drastic effect on differentiated BA metabolism (Figure 5.19). Basal OCR levels were increased by 91.7% over that of untreated BA cells. Additionally, FSK treated cells reached a maximum OCR 22.7% greater than untreated BA cells. Most importantly, FSK was capable of increasing uncoupled respiration by over 110% relative to untreated BA cells (Figure 5.19). Unlike treatment with NE or ISO, stimulation of BA cells by FSK, dramatically increased glycolysis as measured by ECAR. Treated cells maintained increased glycolysis throughout the flux assay with a mean ECAR value 35% greater than that of untreated cells (Figure 5.19). Differentiated white adipocytes did not increase their oxygen consumption or glycolysis in response to FSK treatment. As expected, white adipocyte OCR values were much less than that of their brown counterparts. Basal respiration of both groups of white adipocytes was only 31.7% of untreated BA cells and 16.5% of FSK treated BA cells. While WA cells were capable of increasing their oxygen usage during FCCP uncoupling, unlike PM cells, their BA counterparts consumed 208% and 278% more pmoles of oxygen per minute among the untreated and treated BA groups, respectively (Figure 5.19). Thus in our extracellular fulx analyses, our differentiated brown adipocytes have a greater metabolic response to direct cAMP agonism than through β-adrenergic stimulation.

Brown adipocytes maintain a large capacity for metabolic modulation. In addition to beta adrenergic or cAMP driven processes, BA cells utilize both endogenous and exogenous fatty acids (FAs) through B-oxidation (Mottillo et al., 2012; Townsend and Tseng, 2014; Yu et al., 2002). Endogenous FAs are garnered from within resident brown adipocyte lipid droplets, whereas exogenous FAs are transported from the extracellular milieu. We sought to determine the ability of our differentiated brown adipocytes to oxidize palmitate for fuel relative to differentiated white adipocytes. Cells were maintained in minimal medium for 24 hours to shift their energy demands toward their intercellular stores of lipids. Cells were either given etomoxir (ETO), the irreversible inhibitor of carnitine palmitoyltransferase-1 (CPT-1) to inhibit transport of fatty acids into the mitochondrial inner membrane, or vehicle. Immediately prior to beginning the efflux analysis, cells were also either given BSA conjugated palmitate or BSA alone. The effects from exogenous fatty acid utilization can be computed by comparing the Palm:BSA-ETO samples to the BSA-ETO samples (Figures 5.20 and 5.21). The fraction of respiration attributable to endogenous fatty acid utilization can be enumerated by comparing the BSA-ETO to BSA+ETO samples (Figures 5.20 and 5.21). From these OCR graphs, we can conclude that exogenous FAs have a greater metabolic modulatory capacity in our cells than endogenous FAs (Figure 5.20). Cells receiving palmitate but not ETO demonstrated a significant increase in oxygen demands due to increased fatty acid oxidation of exogenous FA (Figure 5.20). Palmitate enabled cells to reach a respiratory maximum equal to that of adrenergic or cAMP stimulated samples (Figure 5.20). Furthermore, palmitate also led to an increased capacity for uncoupled respiration by UCP1 (Figure 5.20). As expected, white adipocytes experienced no significant changes attributable to exogenous fatty acid utilization, and their OCR profiles mirrored those observed in FSK treated experiments (Figure 5.20). We were limited in our understanding of

glycolysis rates in this assay as changes in ECAR values could not be isolated simply to changes in lactate production. Because β-oxidation produces large amounts of CO_2, acidification could solely be a consequence of this process and not increased glycolysis. In order to determine changes in glycolysis, a glycolytic inhibitor such as 2-Deoxy-D-Glucose (2-DG)- a glucose analog that inhibits glycolysis via its actions on hexokinase- would need to be utilized. In the present study, this proved difficult, as the 4 injection ports in the flux analyzer plate were already occupied and the etomoxir and palmitate had to be added directly to the plate.

We can compare cell-to-cell and treatment-to-treatment effects in all the cell types analyzed by extracellular flux by comparing the cellular energy phenotypes. Direct energy phenotype analysis is accomplished by plotting oxygen consumption versus extracellular acidification rates in a scatter plot (Figure 5.22). These analyses reveal that PM cells primarily utilize aerobic glycolysis as their source of energy production, with nearly no shift toward increased oxidative capacity even upon FCCP uncoupling. Furthermore, PM cells do not readily respond to stimulation by NE or ISO as their energy utilization does not change from unstimulated samples. On the other hand, BA cells stimulated with either NE or ISO have significantly higher basal respiration rates upon stimulation. In both instances, the stimulated basal conditions are more glycolytic than their unstimulated cohorts, however, this is lost upon FCCP uncoupling. Differentiated BA cells do have a large shift toward a balanced ox-phos:oxidative energy utilization, indicating a greater reliance on high energy systems, possibly including β-oxidation of endogenous fatty acids. White adipocytes do not respond to cAMP agonism through forskolin administration. They have a slight shift toward an oxidative phenotype when FCCP uncoupled, but these results are independent of forskolin stimulation. Brown adipocytes have a dramatic shift in energy system utilization balance when administered

forskolin. Forskolin-stimulated basal oxygen consumption is the maximum of the untreated samples. Moreover, the amount of glucose utilized in the forskolin-stimulated samples exceeds that of the unstimulated basal cohorts. Fatty acid utilization drives a significant change in oxidative capacity for brown adipocytes and this graph reveal that ADSC-derived white adipocytes do shift their utilization preference. These cells are all kept in a substrate-limited medium prior to the assay, and in contrast to the medium of forskolin assay, these cells utilize their endogenous fatty acids to the limit of their capacity. Without the inclusion of a glycolytic inhibitor, any increase in ECAR must be assumed to be derived from fatty acid β-oxidation.

In addition to increased usage of oxygen, glucose, and FAs, brown adipocytes maintain the ability to undergo increased rates of lipolysis upon stimulation (Roberts et al., 1986; Townsend and Tseng, 2014; Yu et al., 2002). We compared the ability of our differentiated brown adipocytes to undergo lipolysis compared to iPSCs and differentiated white adipocytes under unstimulated and stimulated conditions (Figure 5.23). We measured the release of free glycerol over eight hours with or without administration of FSK at time "0". Induced pluripotent stem cells showed no response to stimulation by FSK, as expected. Differentiated white adipocytes showed a significant increase upon stimulation at the eight-hour time point; however, this effect was significantly lower than that of stimulated brown adipocytes at both time points. Stimulated brown adipocytes nearly doubled and tripled the amount of lipolysis relative to stimulated white adipocytes at four and eight hours, respectively. Stimulated white adipocytes experienced no significant difference from unstimulated brown adipocytes at either four or eight hours. These data clearly indicate that our brown adipocytes are extremely lipolytic under basal conditions and are inducible by FSK to undergo greater lipolysis.

We have demonstrated an efficient method to generate dermomyotomal-like cells of the paraxial mesoderm from hPSCs. Furthermore, we have shown that these cells can be readily differentiated to adipocytes that maintain brown-like gene signatures with the canonical developmental and functional brown adipocyte genes, with the most critical being UCP1. UCP1 expression is sensitive to the know human brown adipocyte stimulant forskolin. Beyong the morphological and genotypic similarities to classical brown adipocytes, these cells maintain a functional repertoire commensurate with reported utilities of brown adipocytes both in vivo and in vitro. We conclude that these cells are brown adipocytes. We are the first to report these cells from a developmentally appropriate progenitor from hPSCs in a chemically-defined method. We propose that these cells are highly suitable for both developmental studies of brown adipocyte origin and maturation and bifurcation form shared the shared lineage with skeletal myocytes. Moreover, their responsiveness to stimulation, scalability and long-term culture potential make them an excellent candidate for high throughput-screens.

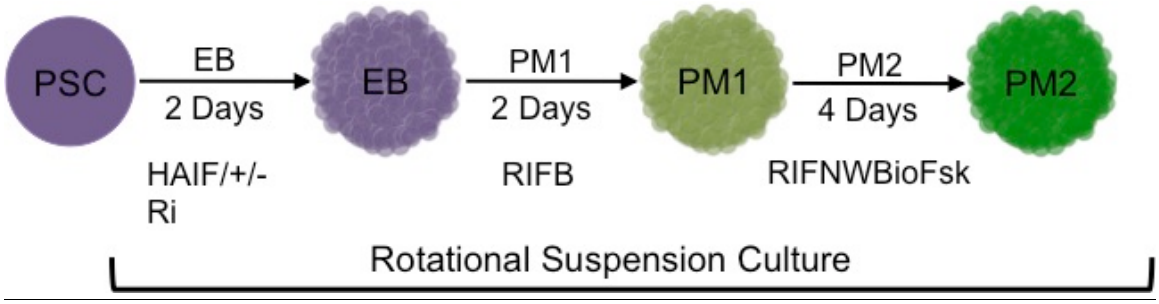

Figure 5.1- Visual scheme for paraxial mesoderm differentiation from hPCS. Human PSCs are dissociated from adherent culture and placed in rotational suspension for the duration of the PM differentiation. H= Hergeulin, A = Activin, I = IGF-1, F = bFGF, Ri= Y-27632 dihydrochloride, R = Rapamycin, B = BMP4, N = Noggin, W = Wnt3A, Bio, = BIO, FSK = Forskolin. For detailed description of protocol see materials and methods.

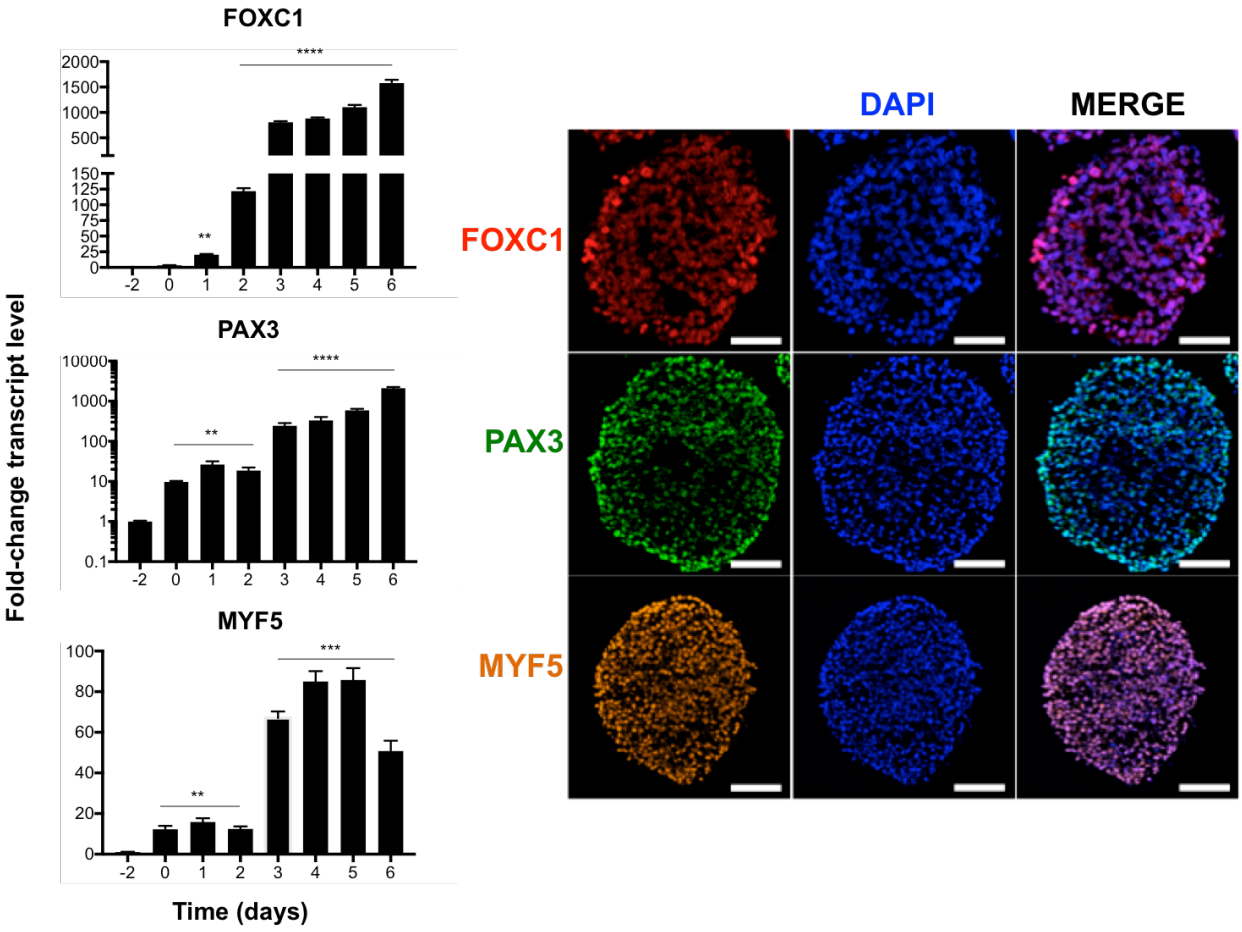

Figure 5.2- Confirmation of paraxial mesoderm identity by transcript and protein expression. Time course of mean transcript change of 9 biological replicates (±SEM) during K3 iPSC paraxial mesoderm differentiation relative to iPSC adherent cells (Day-2). Fold change normalized to 18S rRNA. (a). Protein expression interrogation through immunofluorescent microscopy of fixed paraxial mesoderm spheres on final day of paraxial mesoderm differentiation (b). **≤0.01, ***≤0.001; 20X magnification, scale bar = 100um.

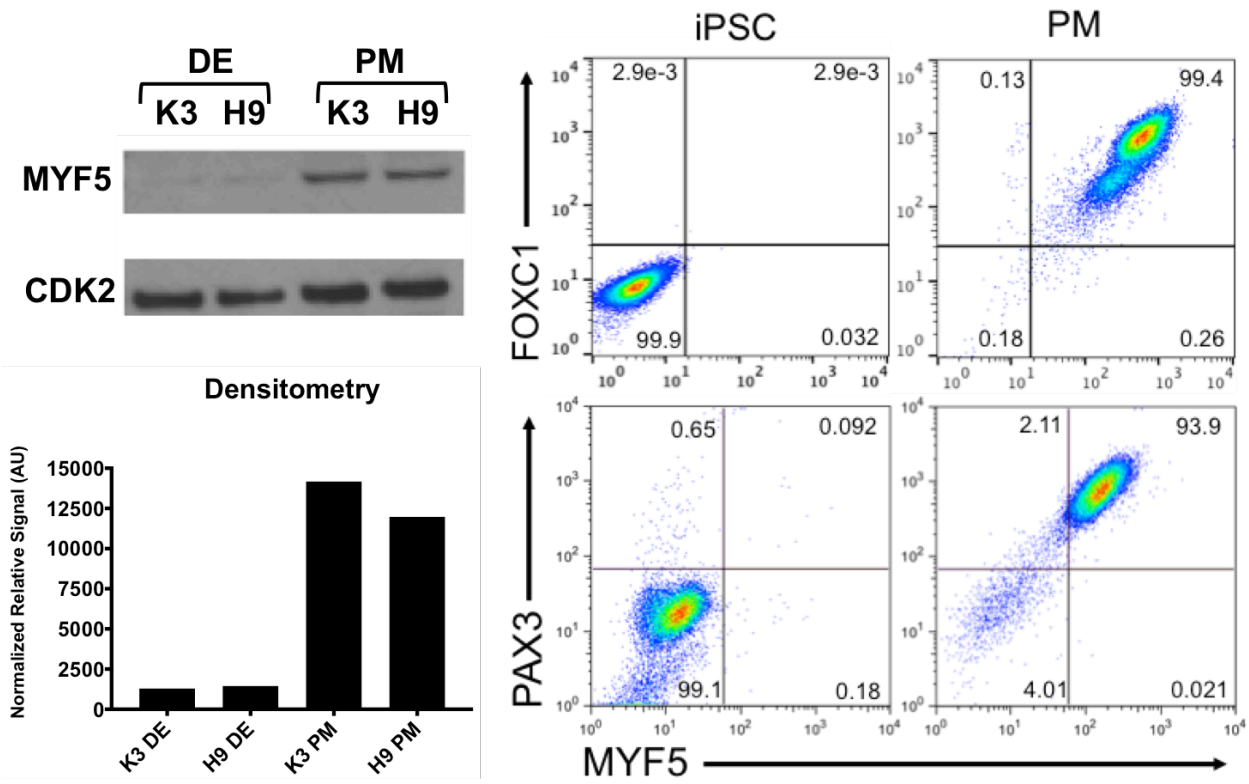

Figure 5.3- Protein quantification and enumeration of paraxial mesoderm cells. Western blot analysis of human MYF5 protein in K3 iPSCs and H9 ESCs on final day of paraxial mesoderm differentiation as compared to definitive endoderm expression of MYF5 and CDK2 loading control (a) Densitometry quantitation of PM and DE MYF5 expression (b). Representative flow cytometric analysis of biological replicates of PM proteins on final day of differentiation comparing undifferentiated iPSC profiles to fully differentiated PM samples (c).

Figure 5.4- Additional transcript and protein analysis of paraxial mesoderm cells. Mean transcript expression change (±SEM) for known dermomytomal genes from 9 biological replicates, including FOXC2, MRF4 (MYF6), MSGN1, PAX7, PRRX1, SIX1 and TBX6; ealry neuroepithelial marks CDH1 and SOX1, neural crest mark FOXD3, neural tube mark PAX6, and lateral plate mark NKX2.5 (a). Fold expression relative to 18S rRNA, only upregulation given significance. Flow cytometric analysis of cell surface markers from paraxial mesoderm cells after differentiation, CD29, PDGFRa, and CD34 have been demonstrated to be present on brown preadipocytes from Myf5+ cells in murine studies (b) blue histogram = isotype control, pink histogram = conjugated antibody against cell surface mark..

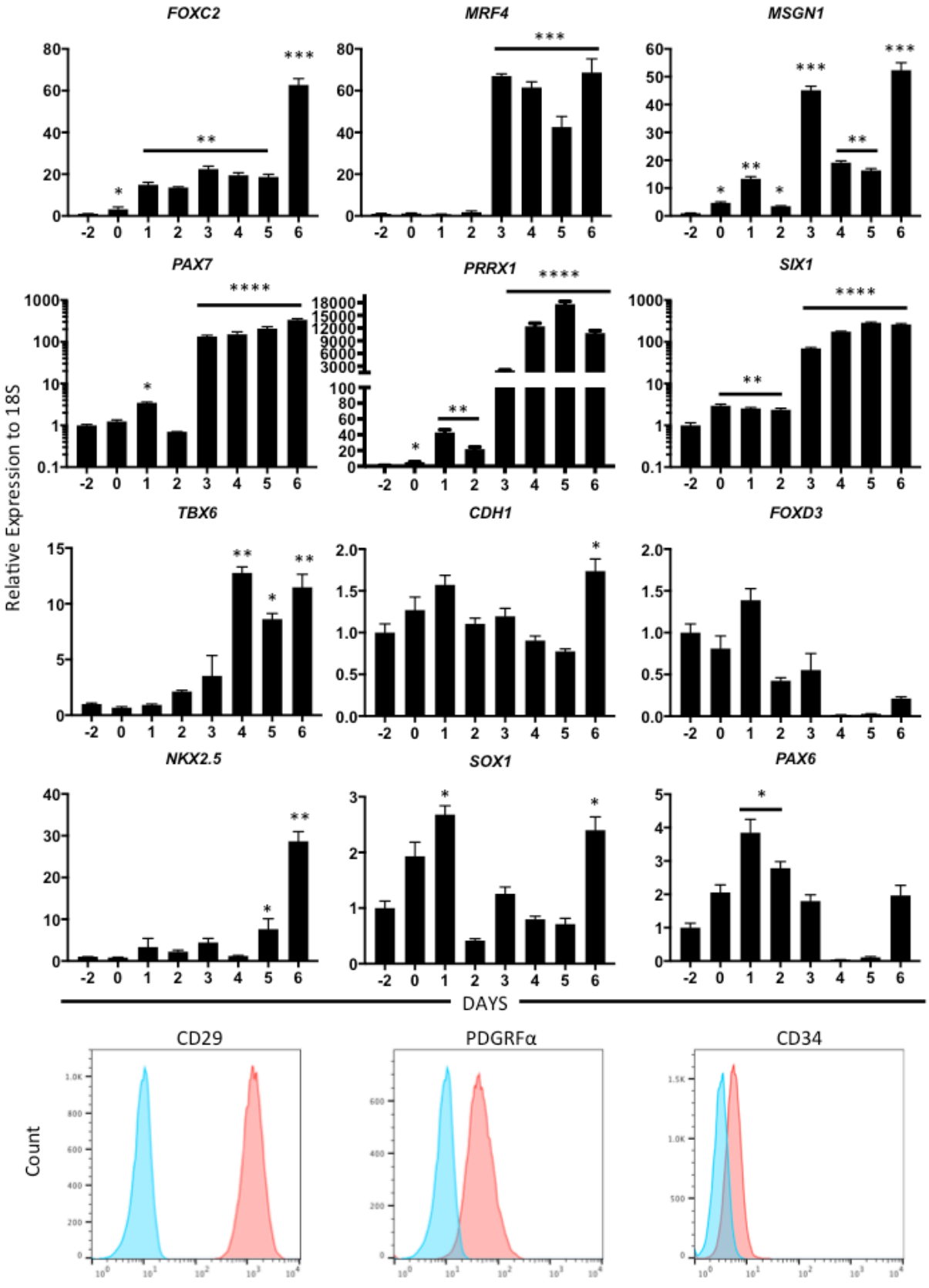
FOXC2
MRF4
MSGN1
PAX7
PRRX1
SIX1
TBX6
CDH1
FOXD3
NKX2.5
SOX1
PAX6
Relative Expression to 18S
DAYS
CD29
PDGRFα
CD34
Count

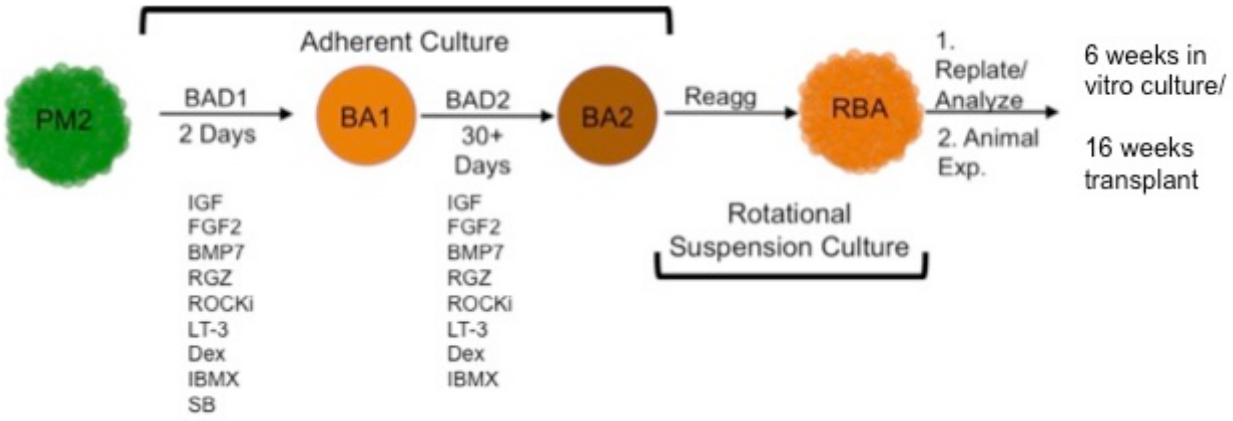

Figure 5.5- Brown adipocyte differentiation scheme from paraxial mesoderm. See materials and methods form detailed description.

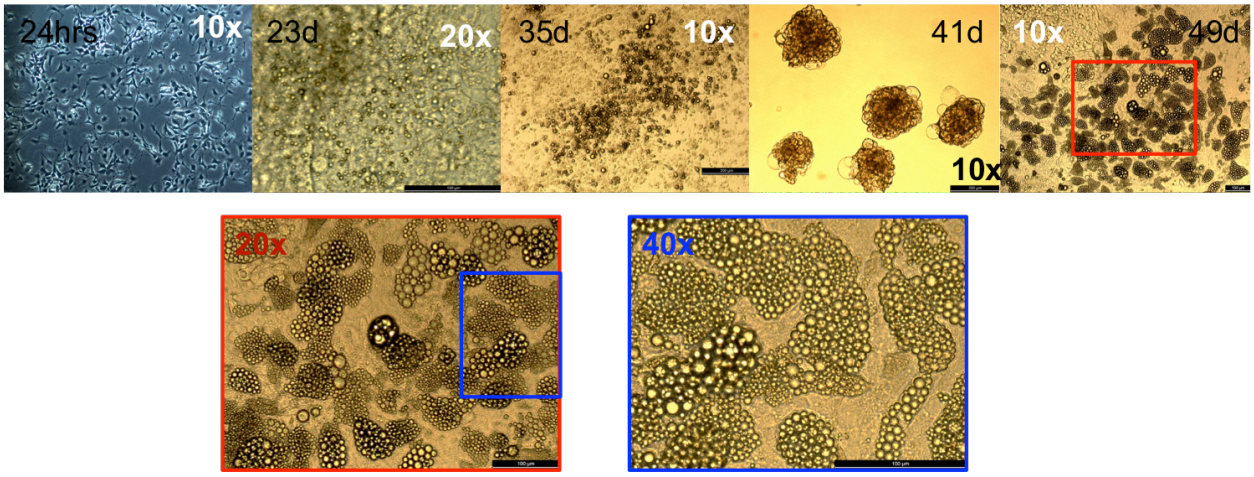

Figure 5.6- Brightfield images chronicling evolution of brown adipocyte differentiation and lipid droplet formation. PM (a), early lipid droplet formation in BA at day 23 (b) extensive droplet formation by day 35 (c), reaggregation of brown adipocytes in suspension culture (d), prolific droplet formation one week after replating aggregates (e-f).

Figure 5.7 Time course of known transcripts required for adipogenesis during differentiation of K3 paraxial mesoderm to brown adipocytes up to reaggregation. Common transcripts to both brown and white adipogenesis (ADIPOQ, FABP4 and PPARγ). Brown adipocyte specific transcripts known to be required for proper specification (EBF2, ENDRB, PRDM16) and activity (PGC1-α and IRF4). Only upregulation given significance, **≤0.01, ***≤0.001, ****≤0.0001.

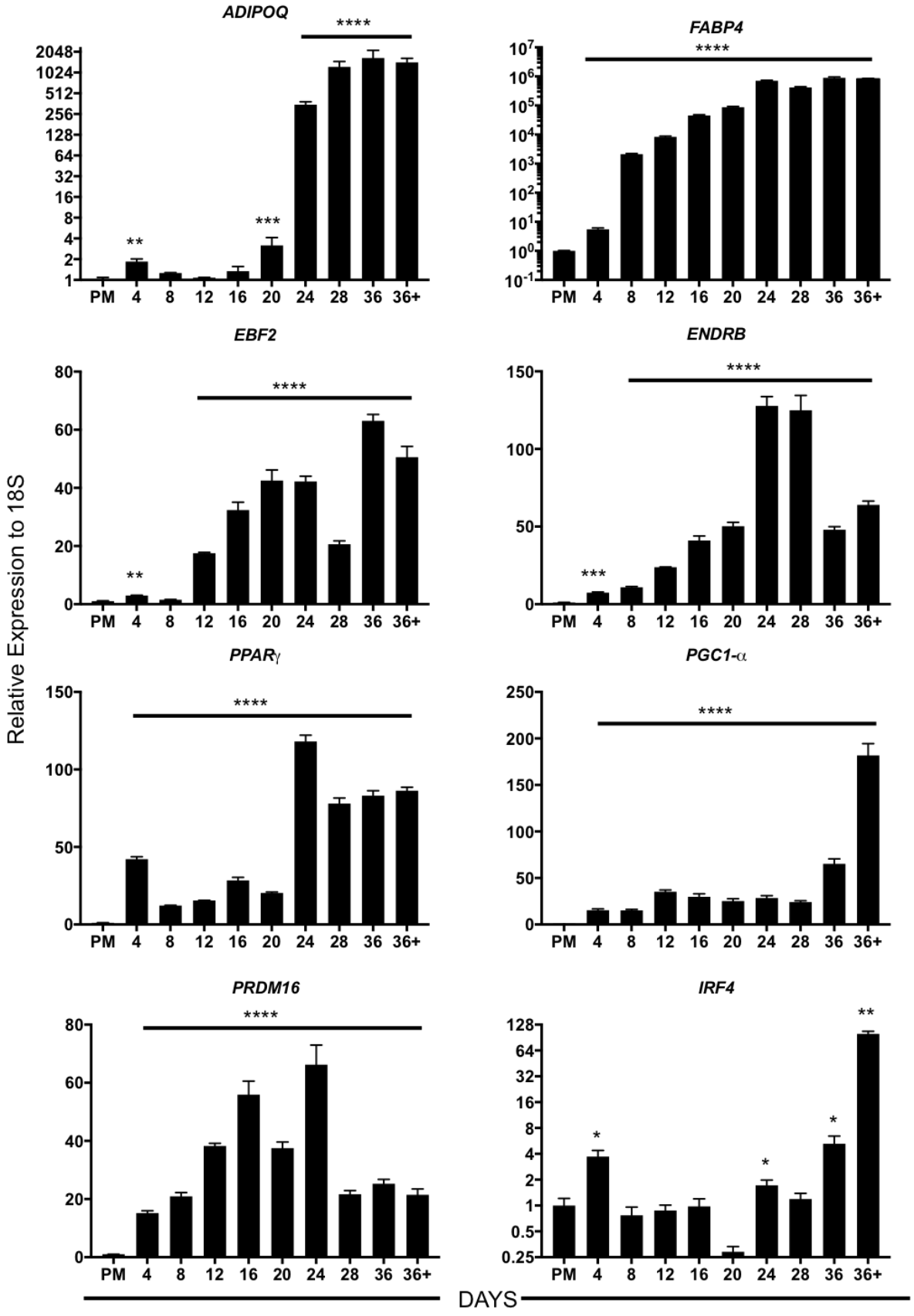
ADIPOQ
FABP4
EBF2
ENDRB
PPARγ
PGC1-α
PRDM16
IRF4
Relative Expression to 18S
DAYS
PM 4 8 12 16 20 24 28 36 36+

Figure 5.8- Time course of known transcripts of mature brown adipocytes during differentiation of K3 paraxial mesoderm to brown adipocytes up to reaggregation. Only upregulation given significance, **≤0.01, ***≤0.001, ****≤0.0001.

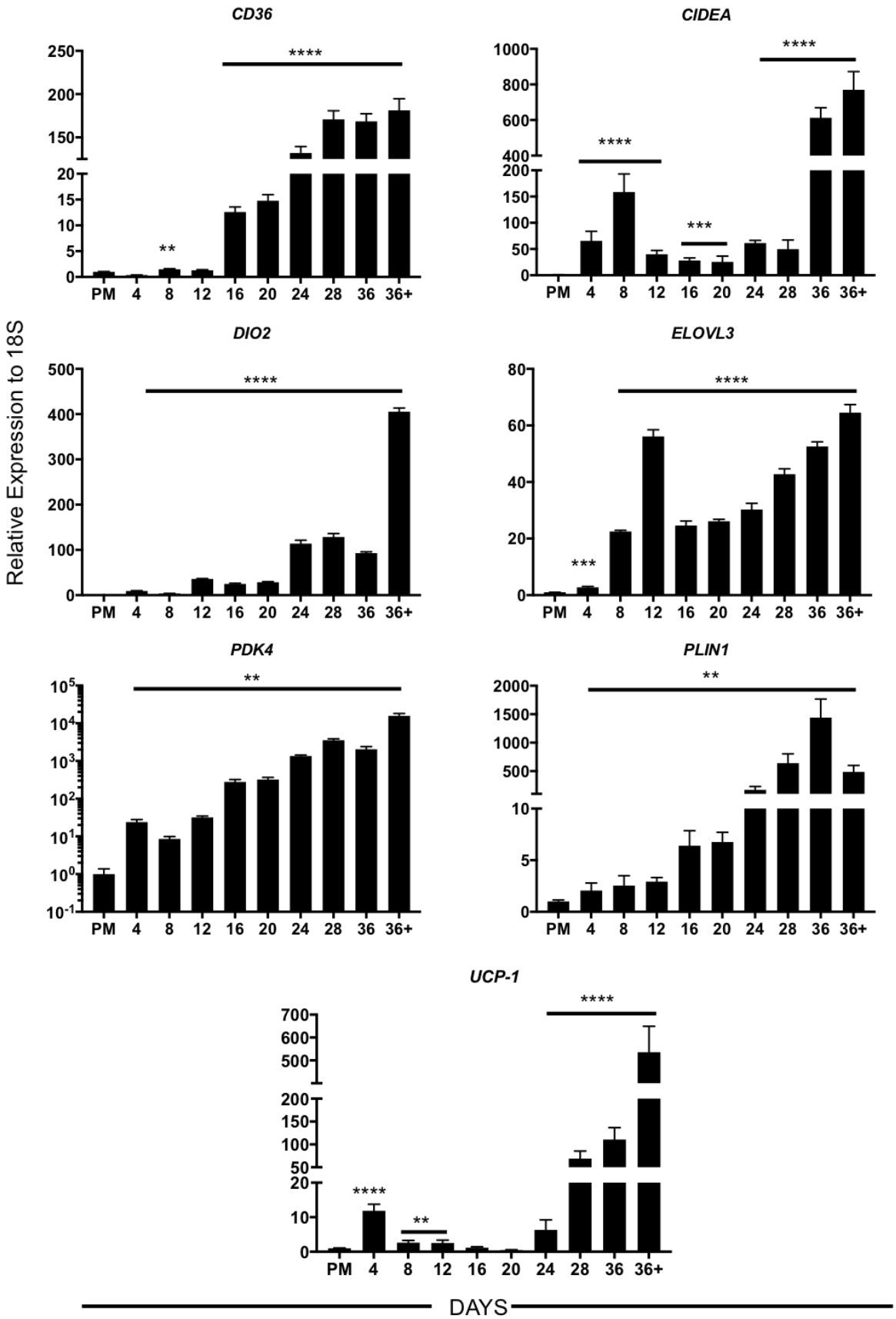
CD36
CIDEA
DIO2
ELOVL3
PDK4
PLIN1
UCP-1
Relative Expression to 18S
PM 4 8 12 16 20 24 28 36 36+
DAYS

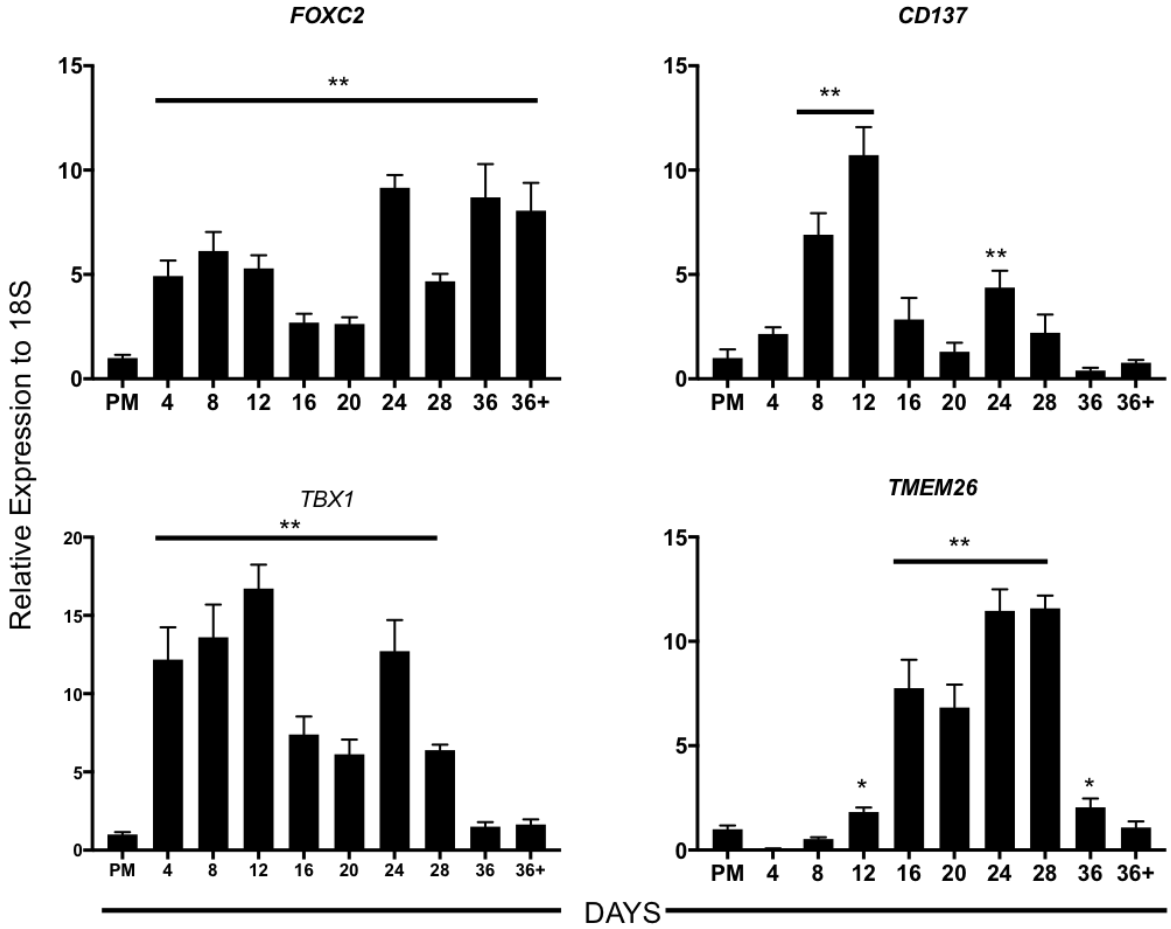

Figure 5.9- Time course of putative transcripts for human brown or beige specification during differentiation of K3 paraxial mesoderm to brown adipocytes up to reaggregation. FOXC2 is a putative mark for brown adipocyte specification; CD137, TBX1 and TMEM26 are thought to identify beige cells. Only upregulation given significance determined by multiple Student's t-test, **≤0.01, ***≤0.001, ****≤0.0001.

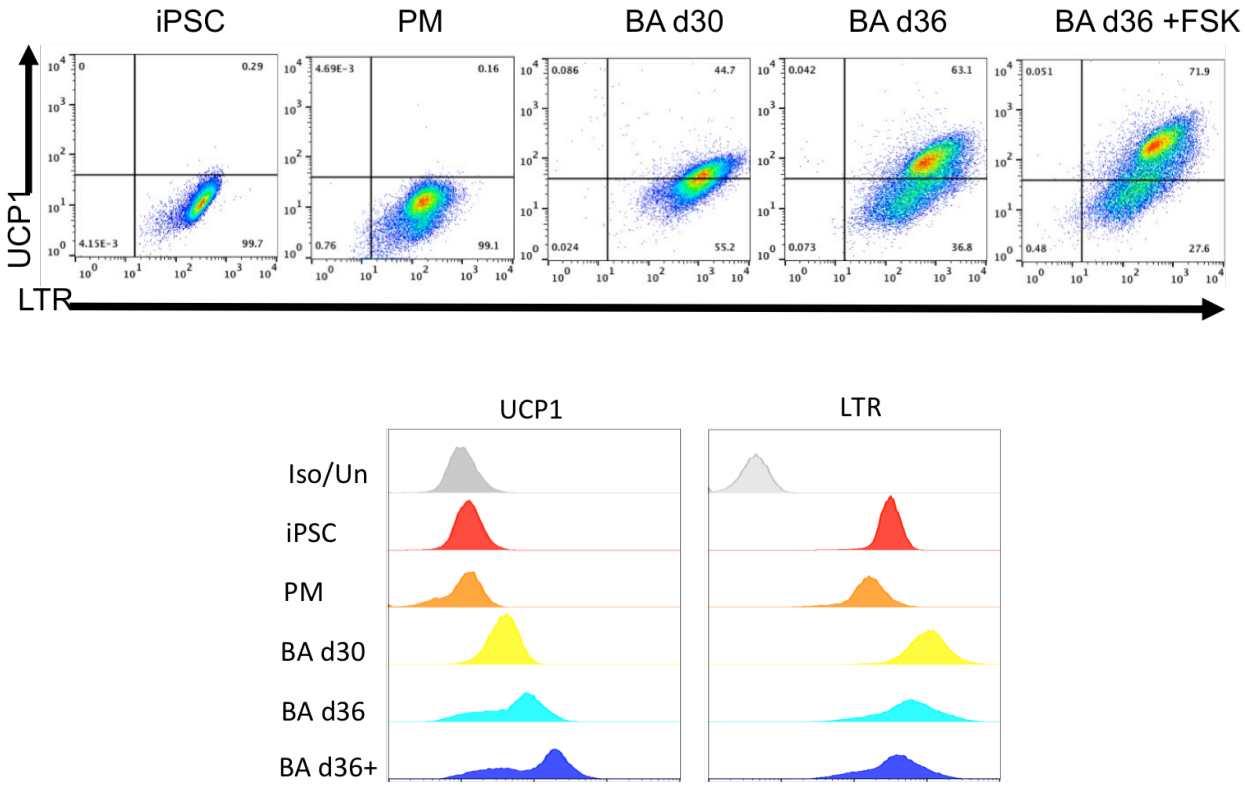

Figure 5.10- Flow cytometric analysis of brown fat specific protein Uncoupling Protein 1. Flow profile of appearance of UCP1 expression from iPSC through paraxial mesoderm and brown adipocytes in conjunction with LipidTox Red (LTR) with and without stimulation with forskolin (FSK) (a). Histogram analysis of the above flow profile (b).

Figure 5.11 Immunofluorescent confocal microscopy of white and brown adipocytes. Interrogation of lipid droplet formation (LTG), UCP1 expression and localization to the mitochondria (MitoTracker), in ADSC-derived both white (day 21) and iPSC (K3 and N4)-derived brown adipocytes (day 57).

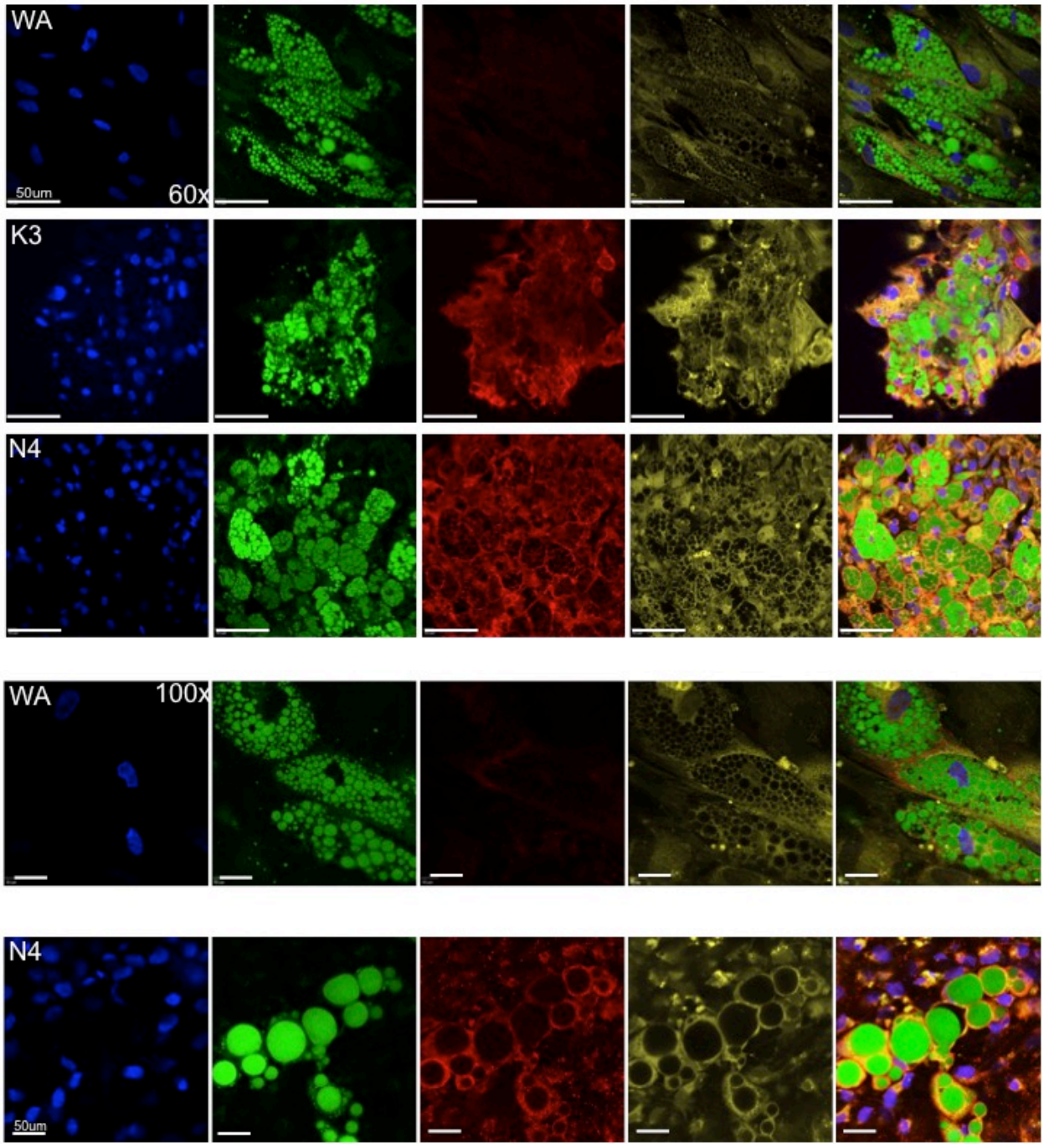
WA
50um
60x
K3
N4
WA
100x
N4
50um

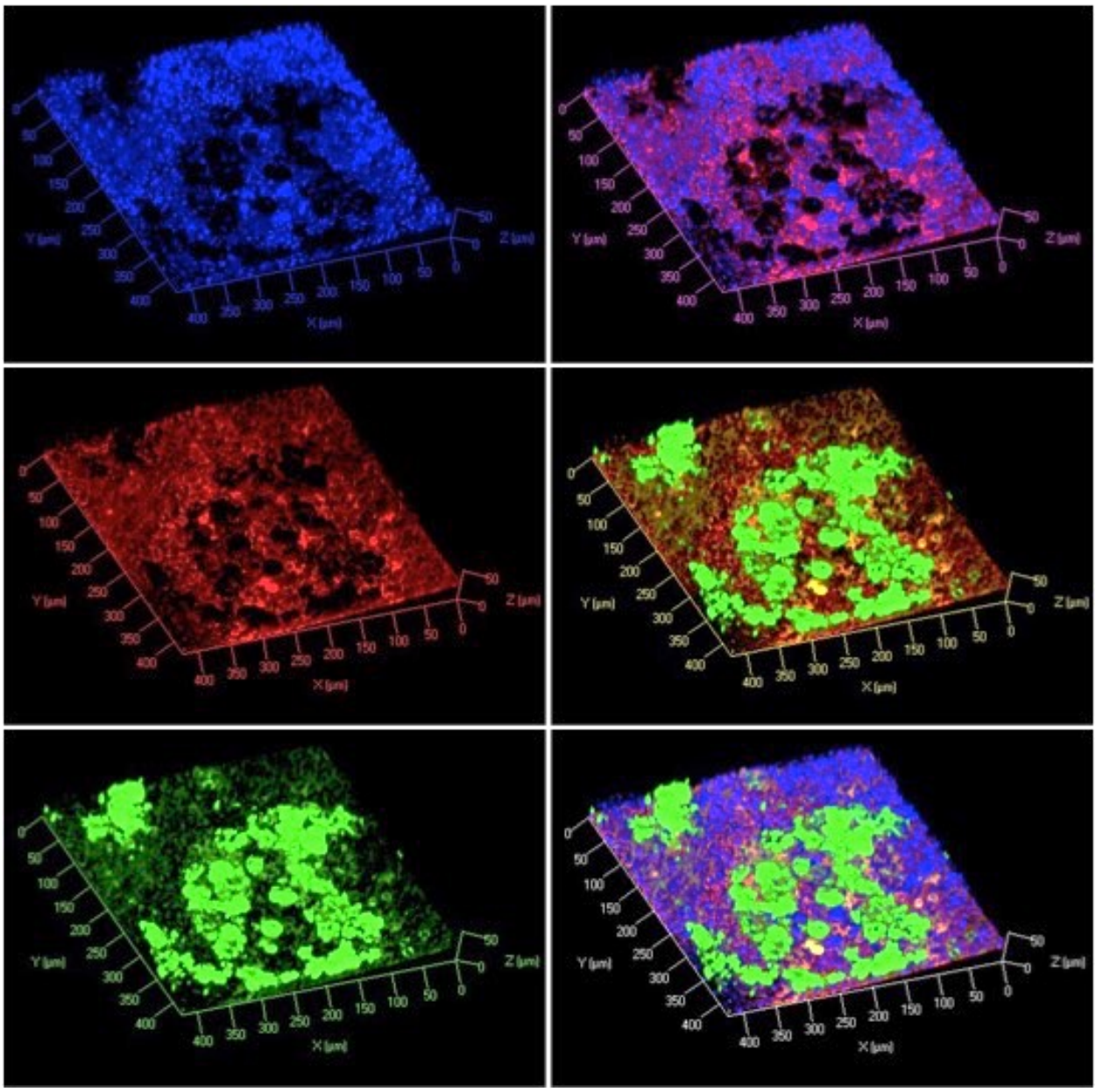

Figure 5.12- Confocal three-dimensional Z-stack analysis of brown adipocytes. Day 57, K3 brown adipocytes showing the spatial arrangement of nuclei (blue), UCP1+ mitochondria (red) and lipid droplets (green). The lipid droplets appear more superficial to the nuclei and mitochondria in their arrangement within cell culture. Maginifaction = 20x, thickness of stack = 50um.

Figure 5.13- Immunofluorescent confocal microscopic interrogation and localization of nuclei (blue), lipid droplet formation (green) and UCP1 expression (red) in day 57 hESC (H7 and H9)-derived brown adipocytes. Split screen of H9 brown adipocytes (a); 3-D Z-stack merge of H9 brown adipocytes (b), 3-D cambered Z-stack of H9 adipocytes (60um stack) (c). Split screen of H7 brown adipocytes (d), enlarged merge of H7 brown adipocytes (e). 20X magnification, scale bar = 50um.

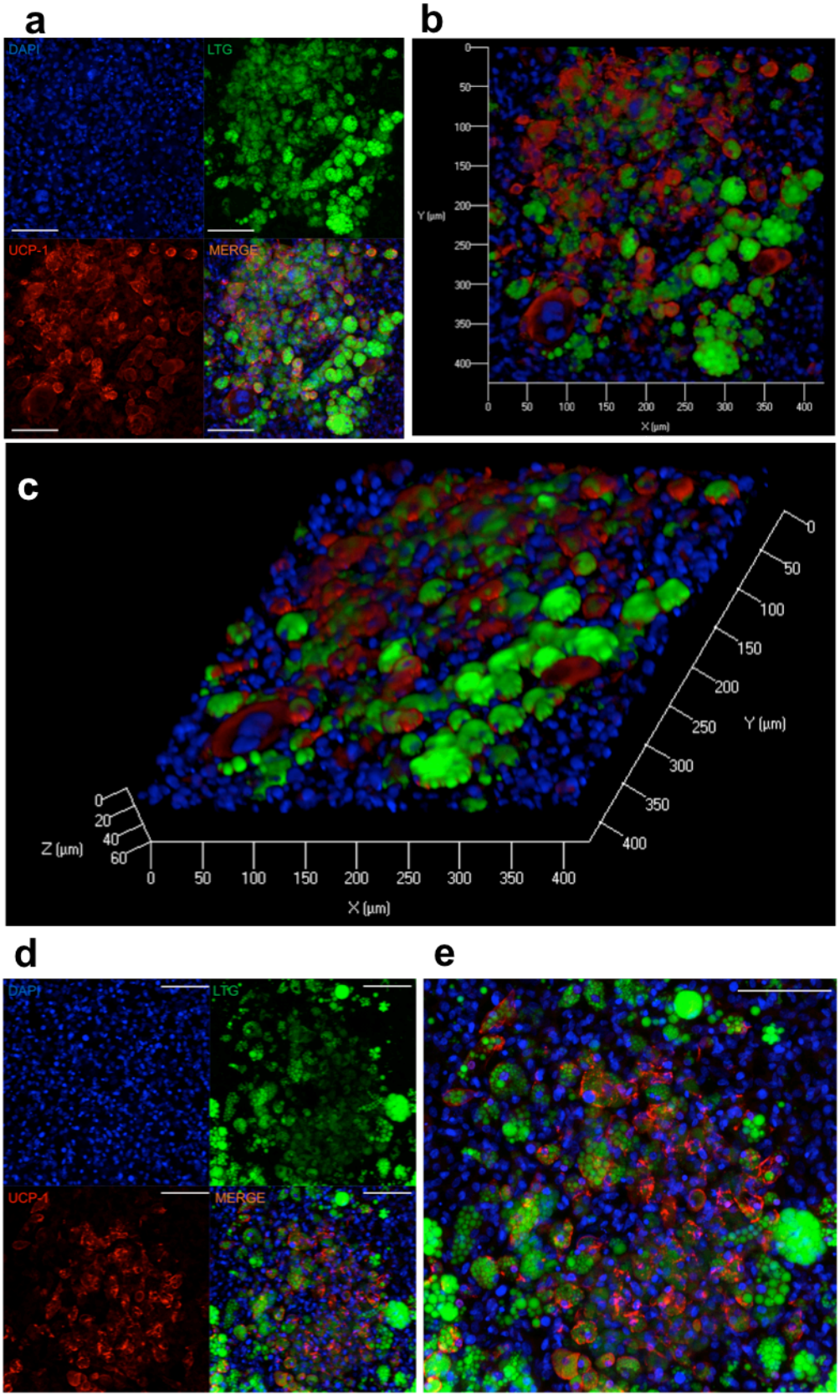
a
DAPI
LTG
UCP-1
MERGE
b
Y (μm)
X (μm)
c
Z (μm)
X (μm)
Y (μm)
d
DAPI
LTG
UCP-1
MERGE
e

Figure 5.14- Scanning electron micrographs of K3 brown adipocytes. Representative images of day 60 K3 brown adipocytes using both backscatter and secondary electron capture methods. The droplets in the backscatter capture method appear more intense due to high reflection of osmium tetroxide.

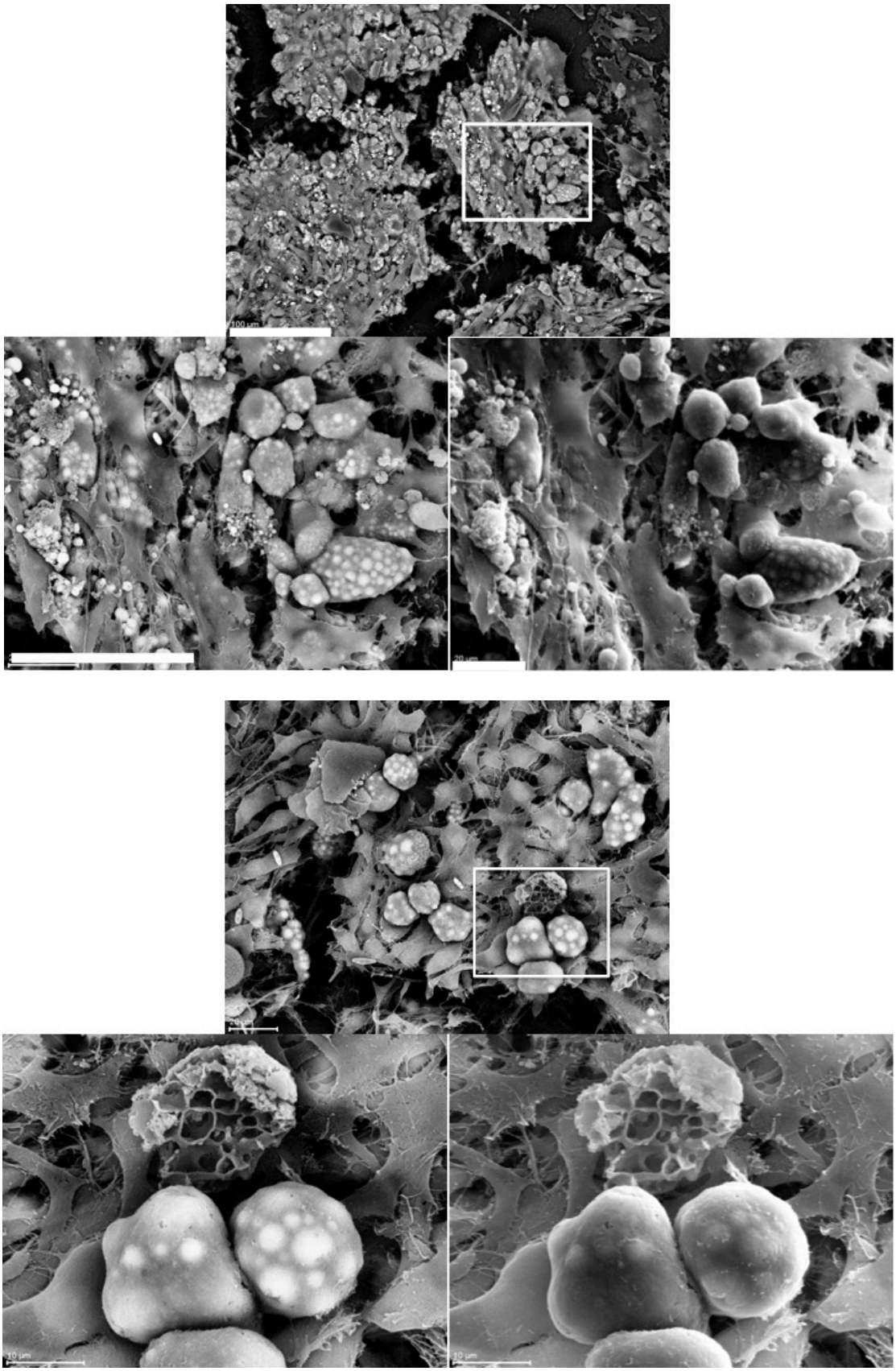

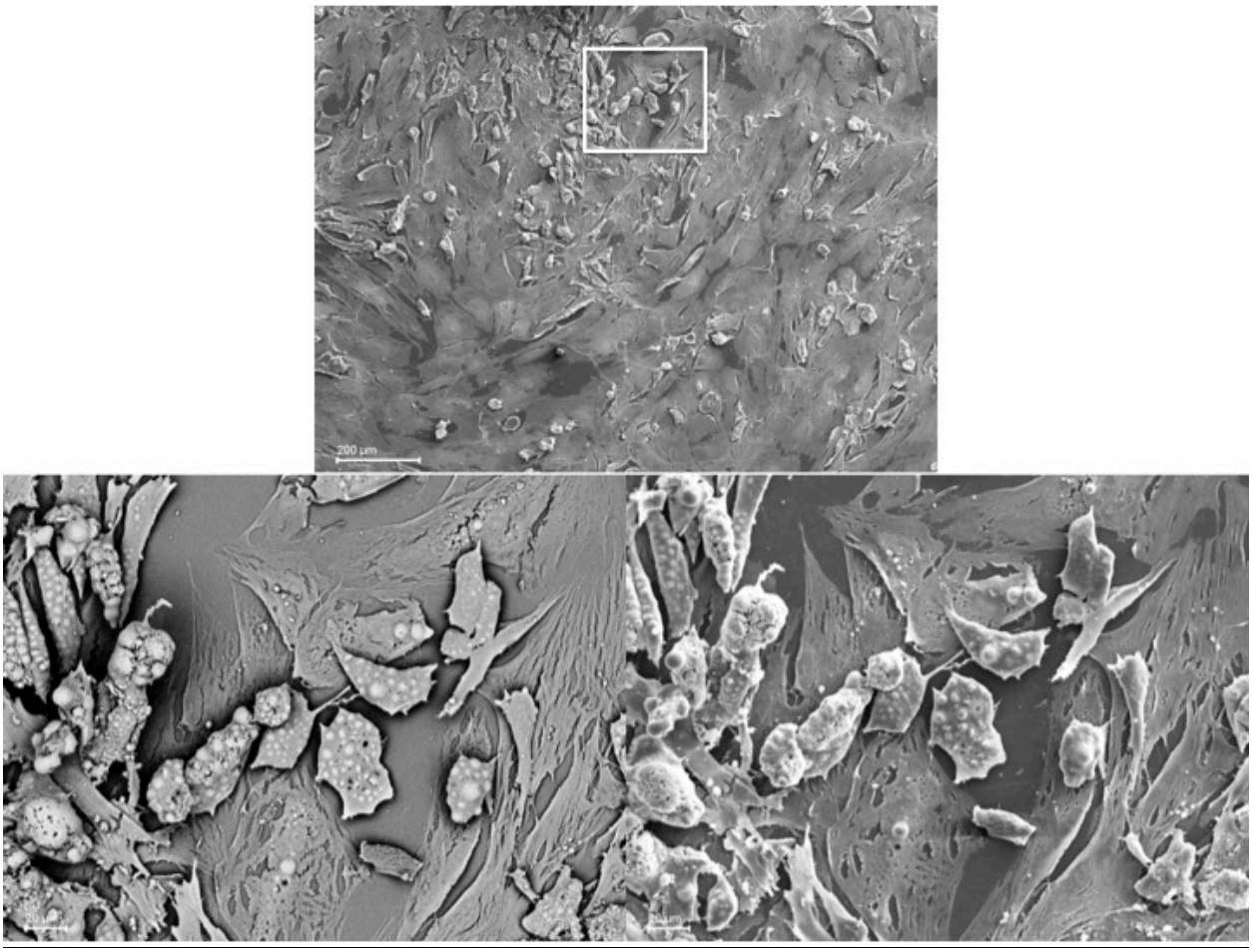

Figure 5.15- Scanning electron micrographs of ADSC-derive white adipocytes.

Representative images of ADSC-derive white adipocytes at day 21 using both backscatter and secondary electron capture methods. The droplets in the backscatter capture method appear more intense due to high reflection of osmium tetroxide.

Figure 5.16- Transmission electron micrographs of K3 brown adipocytes. Representative TEM images of day 60 K3 brown adipocytes. LD = lipid droplets, N= nuclei, mt= mitochondria.

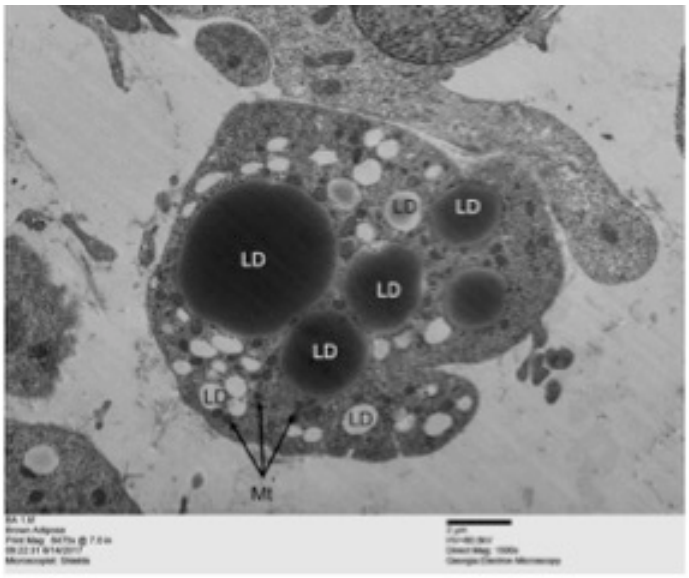
LD
LD
LD
LD
LD
LD
LD
Mt

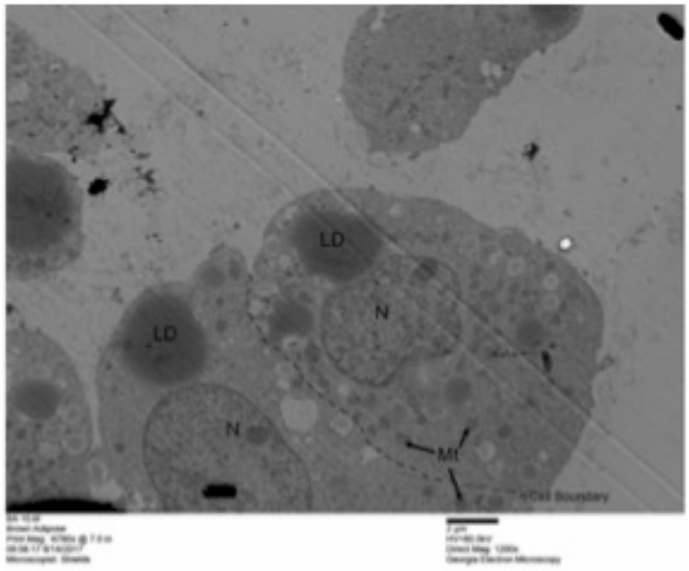
LD
N
LD
N
Mt
Cell Boundary

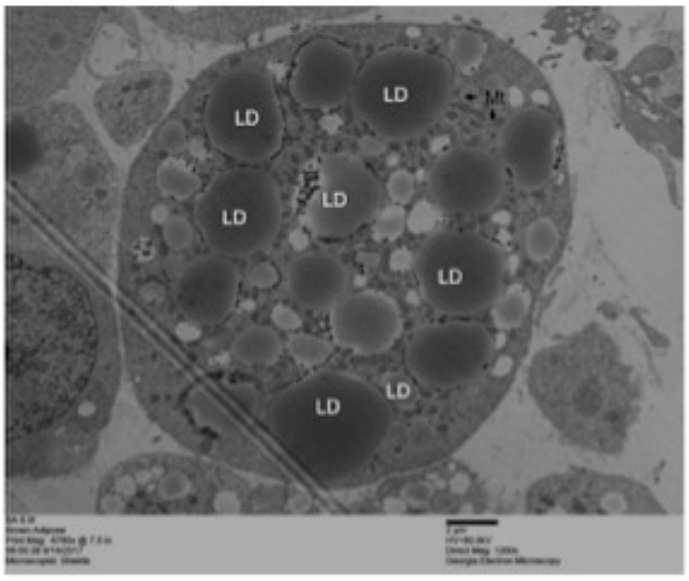
LD
LD
Mt
LD
LD
LD
LD
LD

5.17- Extracellular Flux Analysis of Norepinephrine Treated K3 Brown Adipocytes. Day 56-60 K3 brown adipocytes and paraxial mesoderm + 3days were treated or not with 1uM norepinephrine in Seahorse XFe24 plates and analyzed to their response to the Mito Stress Test. The data presented are mean data from 6 wells for each (BA) and 4 wells for each (PM). All samples were normalized to protein content. Significance was determined by One-way Anova, *≤0.05 **≤0.01, ***≤0.001, ****≤0.0001

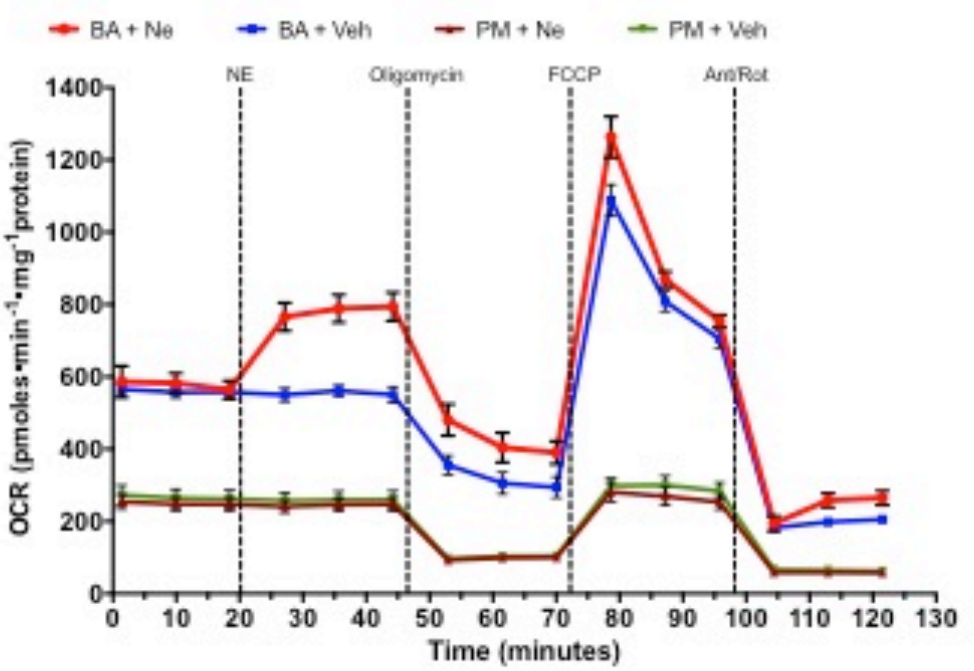
BA + Ne
BA + Veh
PM + Ne
PM + Veh
NE
Oligomycin
FCCP
Ant/Rot
OCR (pmoles•min-1•mg-1protein)
Time (minutes)

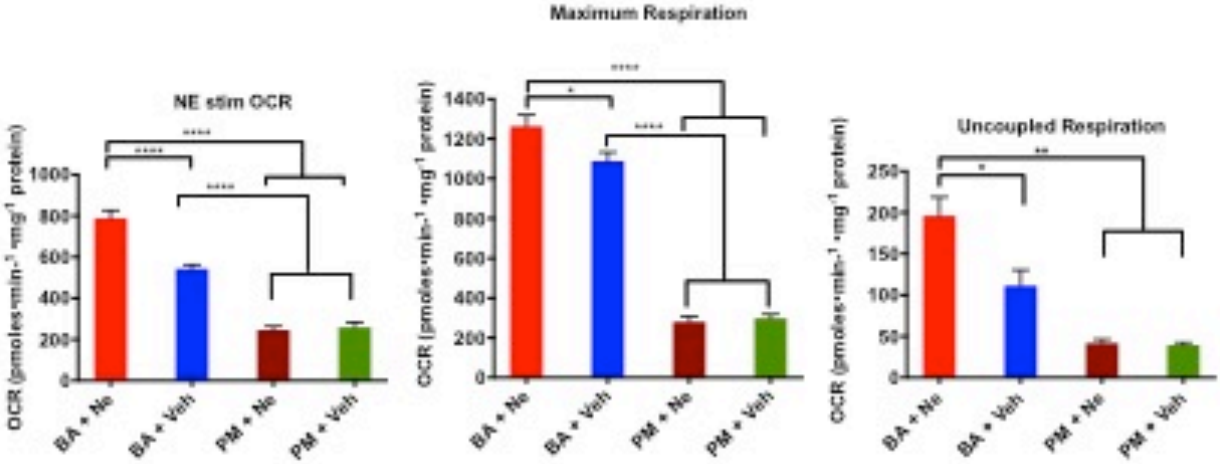
Maximum Respiration
NE stim OCR
Uncoupled Respiration
BA + Ne
BA + Veh
PM + Ne
PM + Veh

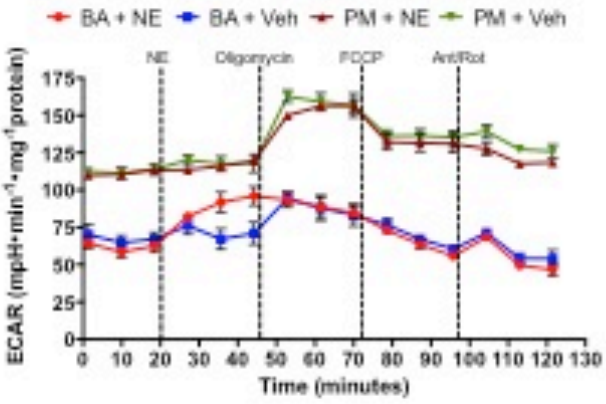
BA + NE
BA + Veh
PM + NE
PM + Veh
NE
Oligomycin
FCCP
Ant/Rot
ECAR (mpH•min-1•mg-1protein)
Time (minutes)

Figure 5.18- Extracellular Flux Analysis of Isoproterenol Treated K3 Brown Adipocytes. Day 56-60 K3 brown adipocytes and paraxial mesoderm + 3days were treated or not with 100 uM isoproterenol overnight in Seahorse XFe24 plates and analyzed to their response to the Mito Stress Test. The data presented are mean data from 6 wells for each (BA) and 4 wells for each (PM). All samples were normalized to protein content. Significance was determined by One-way Anova, *≤0.05 **≤0.01, ***≤0.001, ****≤0.0001

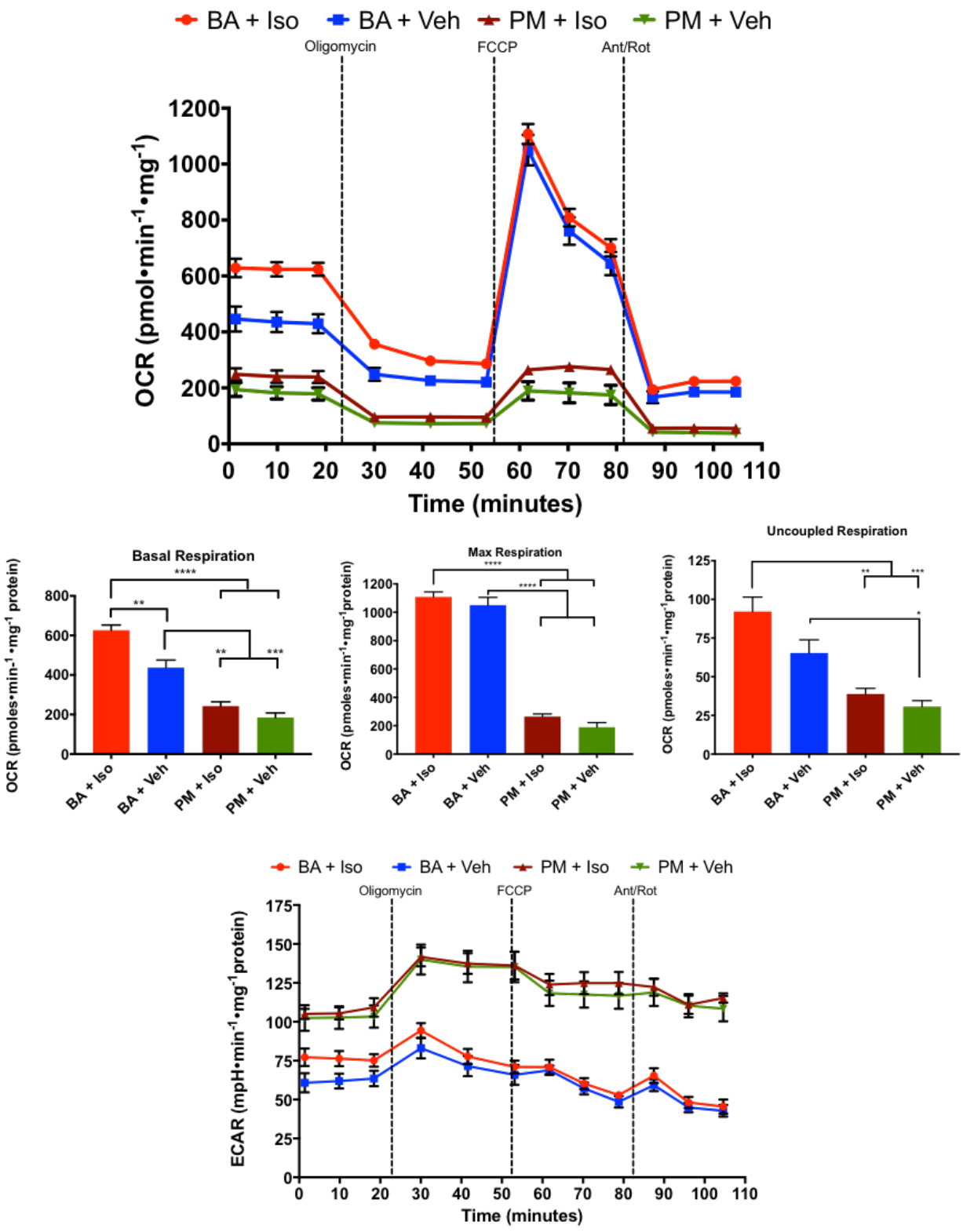
BA + Iso
BA + Veh
PM + Iso
PM + Veh
Oligomycin
FCCP
Ant/Rot
OCR (pmol•min-1•mg-1)
Time (minutes)
Basal Respiration
Max Respiration
Uncoupled Respiration
OCR (pmoles•min-1•mg-1protein)
ECAR (mpH•min-1•mg-1protein)

Figure 5.19- Extracellular Flux Analysis of Forskolin Treated K3 Brown Adipocytes. Day 56-60 K3 brown adipocytes and day 21-25 ADSC-derived white adipocytes were treated or not with 10 uM forskolin overnight in Seahorse XFe24 plates and analyzed to their response to the Mito Stress Test. The data presented are mean data from 34 wells (BA+FSK; WA +FSK) and 18 wells (BA+Veh; WA+Veh). All samples were normalized to protein content. Significance was determined by One-way Anova, *≤0.05 **≤0.01, ***≤0.001, ****≤0.0001.

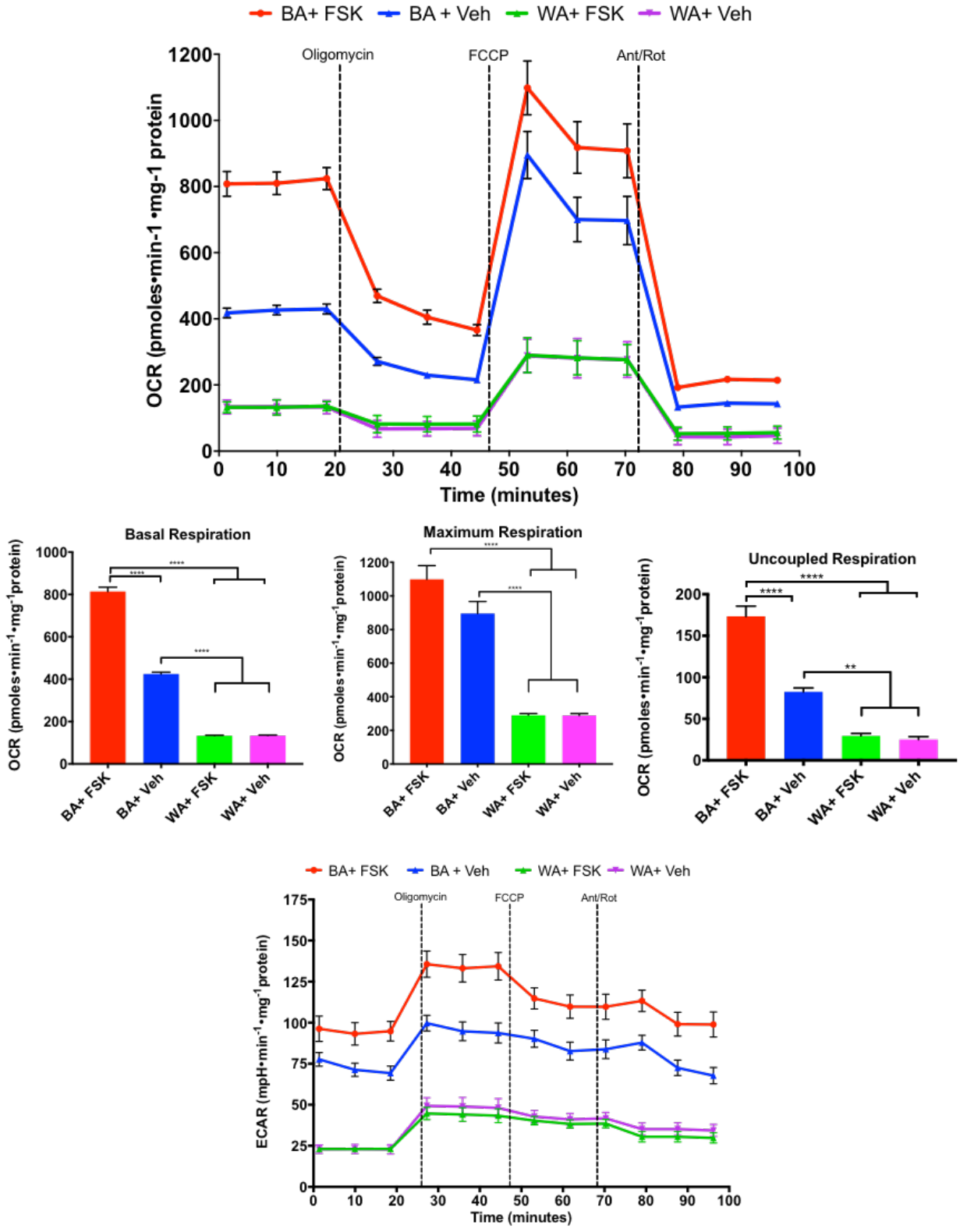
BA+ FSK
BA + Veh
WA+ FSK
WA+ Veh
Oligomycin
FCCP
Ant/Rot
OCR (pmoles•min-1 •mg-1 protein
Time (minutes)
Basal Respiration
Maximum Respiration
Uncoupled Respiration
OCR (pmoles•min-1•mg-1protein)
ECAR (mpH•min-1•mg-1protein)

Figure 5.20-21 Extracellular Flux Analysis of Fatty Acid Oxidation in K3 Brown Adipocytes. 64-66 K3 brown adipocytes and day 21-22 ADSC-derived white adipocytes were treated or not with 150uM palmitate conjugated to BSA and with or without the irreversible CPT1 inhibitor etomoxir (ETO) in Seahorse XFe24 plates and analyzed to their response to the Mito Stress Test. The data presented are mean data from 10 wells of each condition except 7 wells for WA+ Palm-BSA+ETO. All samples were normalized to protein content. Significance was determined by One-way Anova, *≤0.05 **≤0.01, ***≤0.001, ****≤0.0001.

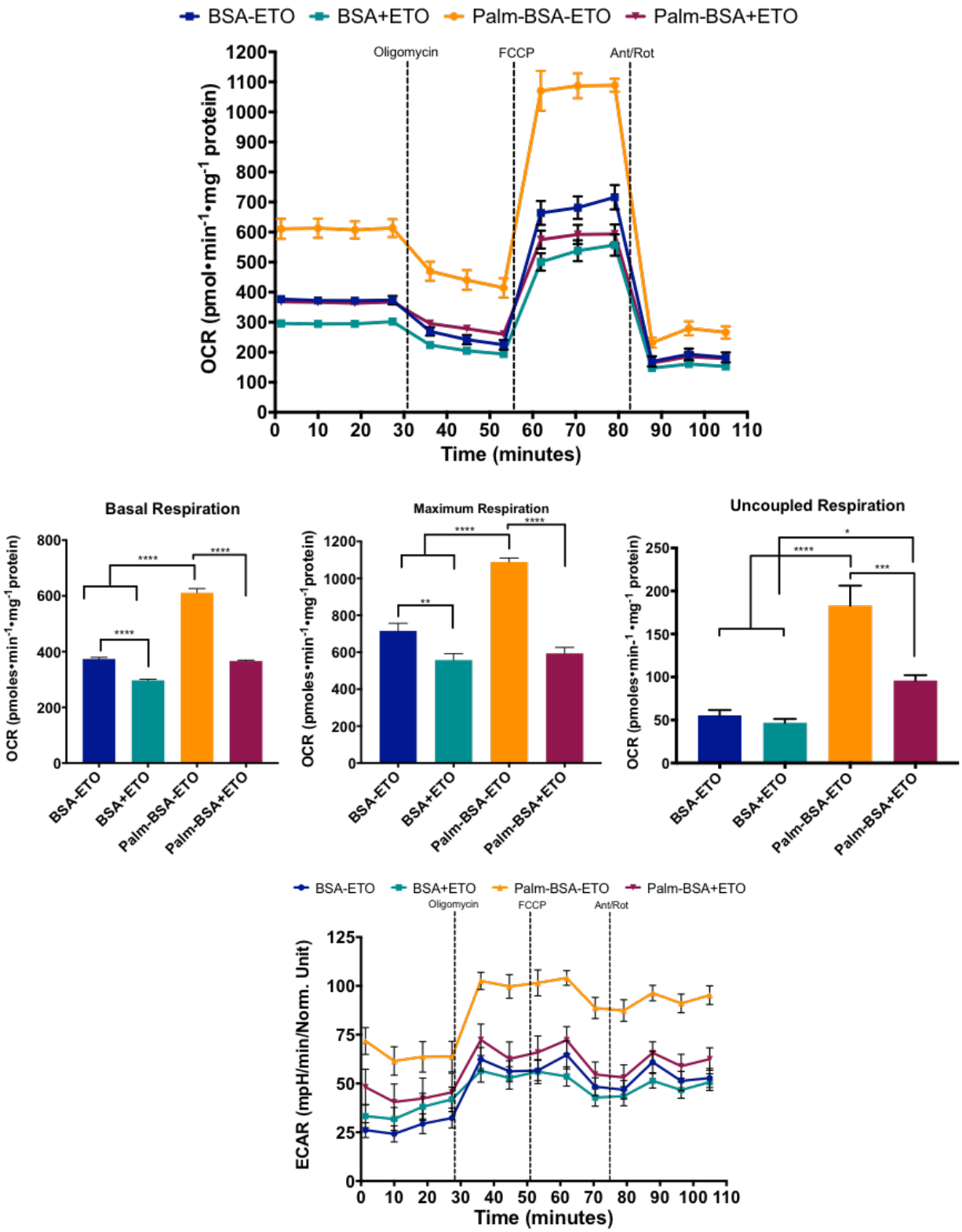
BSA-ETO
BSA+ETO
Palm-BSA-ETO
Palm-BSA+ETO
Oligomycin
FCCP
Ant/Rot
OCR (pmol•min-1•mg-1 protein)
Time (minutes)
Basal Respiration
Maximum Respiration
Uncoupled Respiration
OCR (pmoles•min-1•mg-1protein)
ECAR (mpH/min/Norm. Unit)

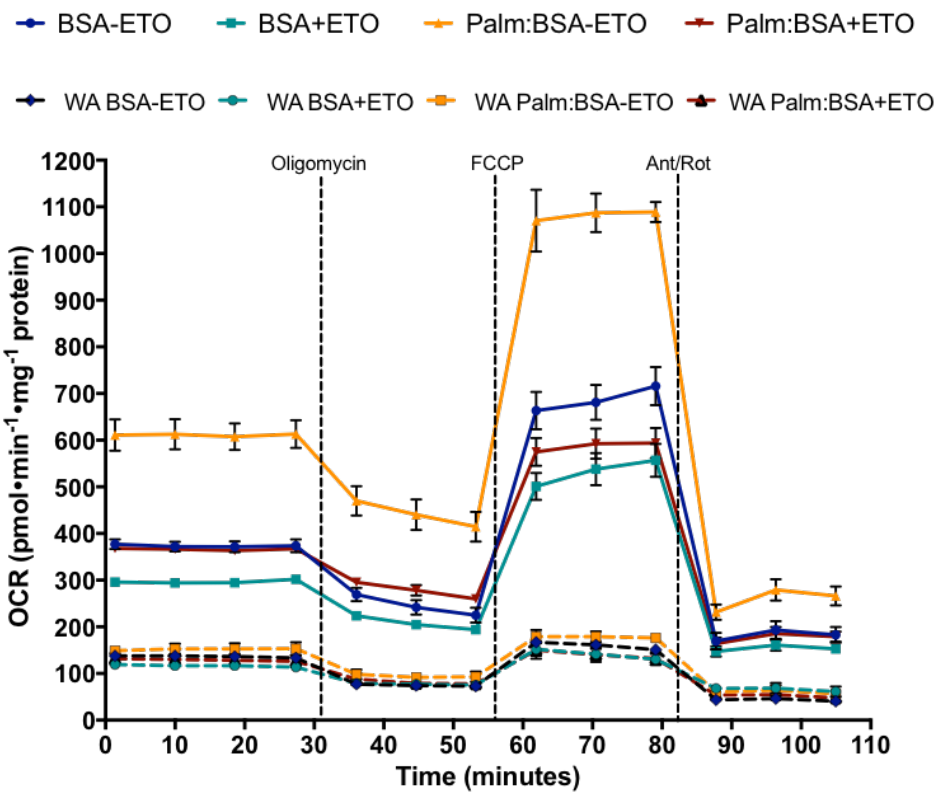
BSA-ETO
BSA+ETO
Palm:BSA-ETO
Palm:BSA+ETO
WA BSA-ETO
WA BSA+ETO
WA Palm:BSA-ETO
WA Palm:BSA+ETO
Oligomycin
FCCP
Ant/Rot
OCR (pmol•min-1•mg-1 protein)
Time (minutes)

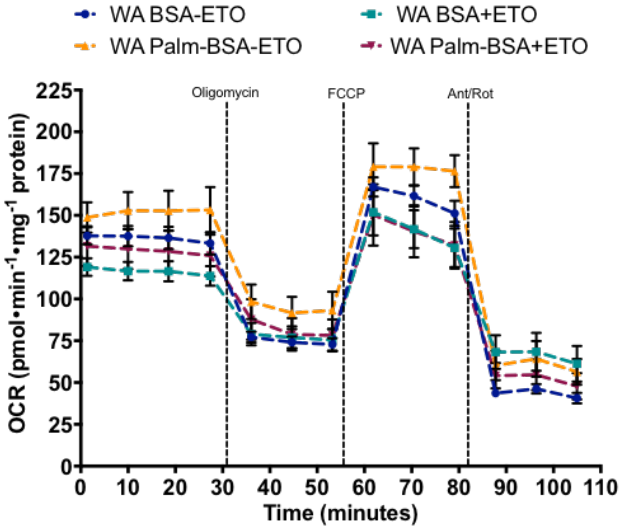
WA BSA-ETO
WA BSA+ETO
WA Palm-BSA-ETO
WA Palm-BSA+ETO
Oligomycin
FCCP
Ant/Rot
OCR (pmol•min-1•mg-1 protein)
Time (minutes)

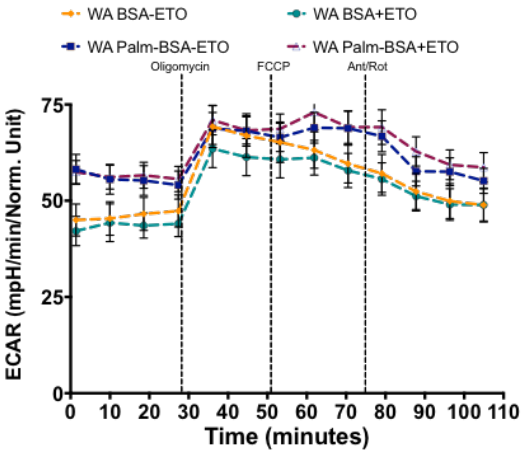
WA BSA-ETO
WA BSA+ETO
WA Palm-BSA-ETO
WA Palm-BSA+ETO
Oligomycin
FCCP
Ant/Rot
ECAR (mpH/min/Norm. Unit)
Time (minutes)

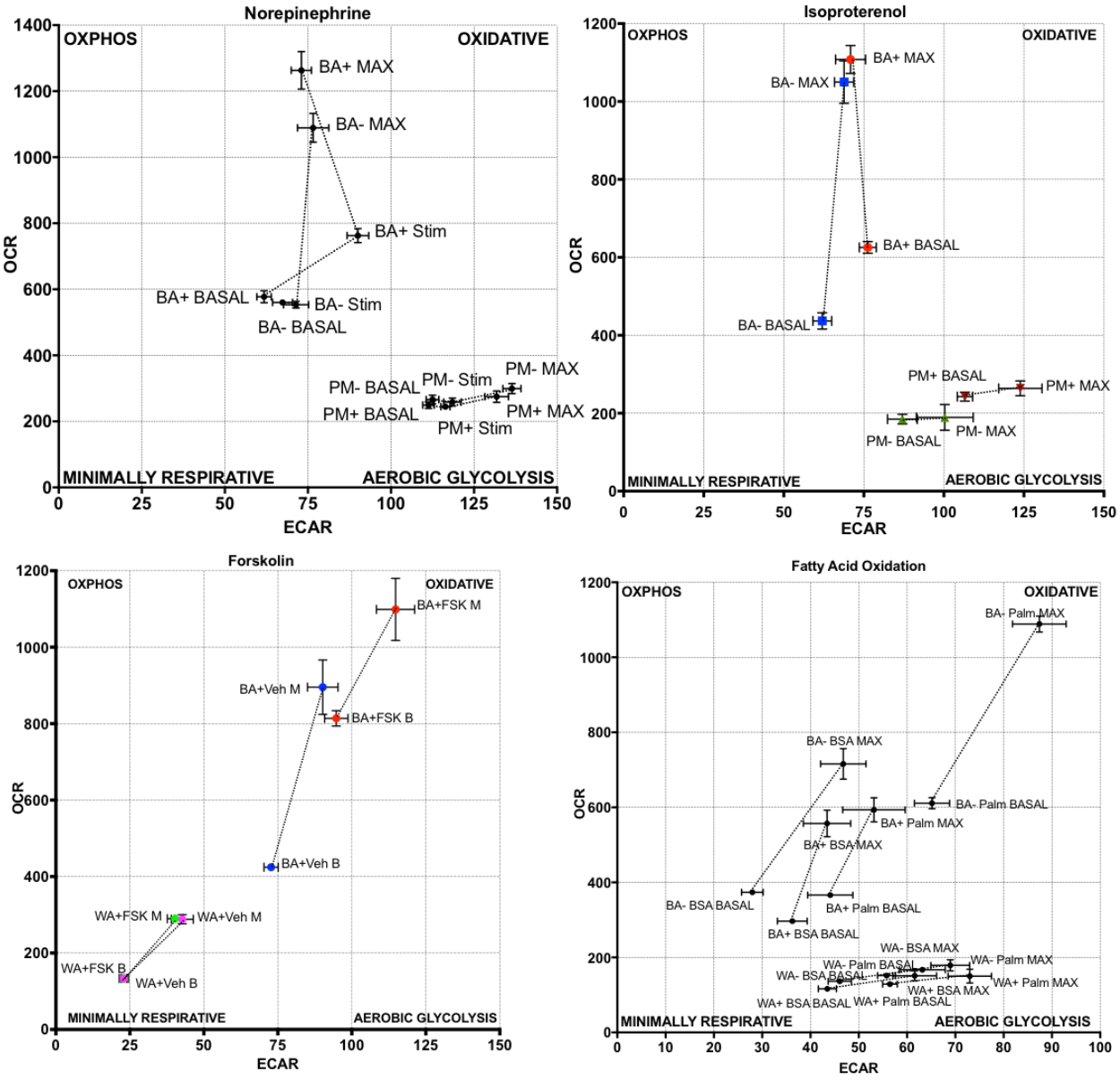

Figure 5.22- OCR:ECAR Energy phenotypes- Oxygen consumption versus extracellular acidification rates of each flux analysis assay are plotted on XY scatter plots. Basal and maximum stimulation OCR and ECAR values from treated versus untreated samples reveal the type of energy systems primarily utilized by each cell type in the basal and FCCP uncoupled state (maximum oxygen utilization) and traces their change during the transition from basal to maximal oxygen consumption.

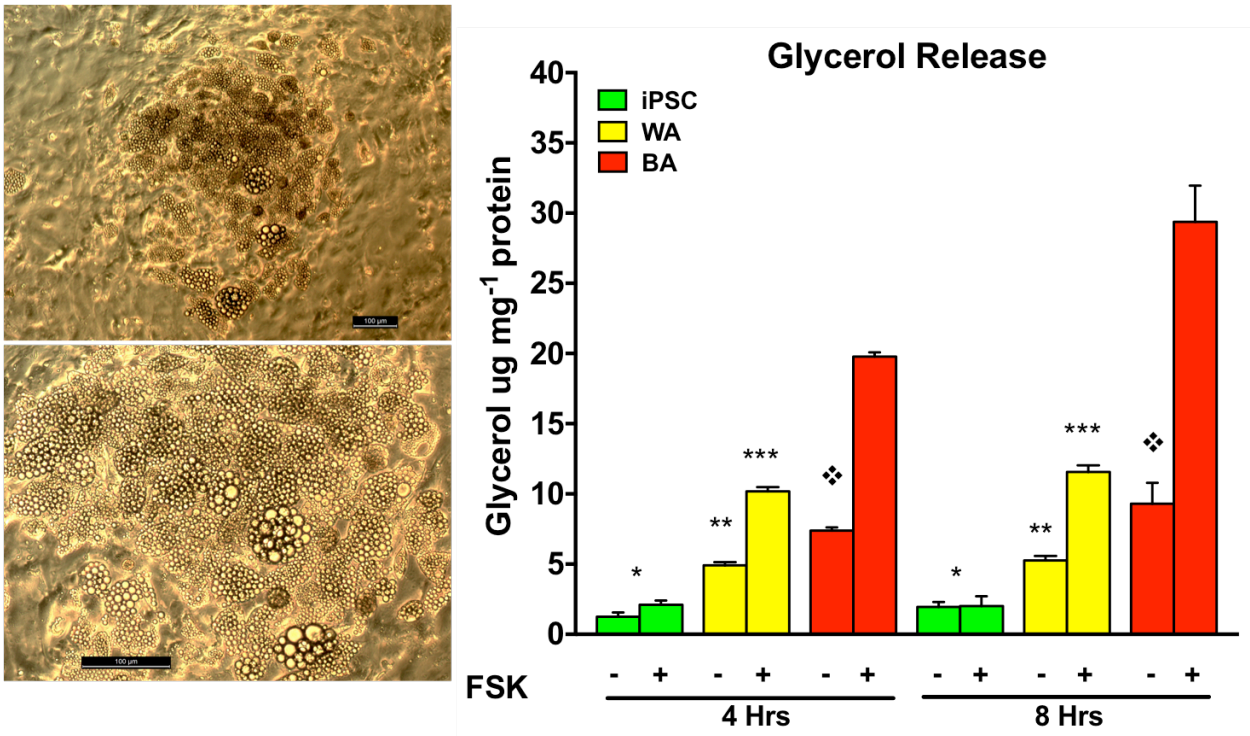

Figure 5.23- Lipolytic capacity of K3 Brown Adipocytes. Day 48 K3 brown adipocytes (pictured) were compared to day 4 iPSCs and Day 21 ADSC-derived white adipocytes. After 4 and 8 hours after stimulation with forskolin (FSK) or not in 12 well plates, free-glycerol was measured at 540nm absorbance and quantity of glycerol released normalized to protein content.

REFERENCES

Ahfeldt, T., Schinzel, R.T., Lee, Y.-K., Hendrickson, D., Kaplan, A., Lum, D.H., Camahort, R., Xia, F., Shay, J., Rhee, E.P., et al. (2012). Programming human pluripotent stem cells into white and brown adipocytes. Nature Publishing Group *14*, 209–219.

Atit, R., Sgaier, S.K., Mohamed, O.A., Taketo, M.M., Dufort, D., Joyner, A.L., Niswander, L., and Conlon, R.A. (2006). Beta-catenin activation is necessary and sufficient to specify the dorsal dermal fate in the mouse. Developmental Biology *296*, 164–176.

Bornfeldt, K.E., and Tabas, I. (2011). Insulin resistance, hyperglycemia, and atherosclerosis. Cell Metabolism *14*, 575–585.

Chen, Y.S., Pelekanos, R.A., Ellis, R.L., Horne, R., Wolvetang, E.J., and Fisk, N.M. (2012). Small molecule mesengenic induction of human induced pluripotent stem cells to generate mesenchymal stem/stromal cells. Stem Cells Transl Med *1*, 83–95.

Cheung, C., Bernardo, A.S., Pedersen, R.A., and Sinha, S. (2014). Directed differentiation of embryonic origin–specific vascular smooth muscle subtypes from human pluripotent stem cells. Nature Protocols *9*, 929–938.

Choy, L., and Derynck, R. (2003). Transforming growth factor-beta inhibits adipocyte differentiation by Smad3 interacting with CCAAT/enhancer-binding protein (C/EBP) and repressing C/EBP transactivation function. J. Biol. Chem. *278*, 9609–9619.

Collins, S., Yehuda-Shnaidman, E., and Wang, H. (2010). Positive and negative control of Ucp1 gene transcription and the role of β-adrenergic signaling networks. International Journal of Obesity *34 Suppl 1*, S28–S33.

Cypess, A.M., Lehman, S., Williams, G., Tal, I., Rodman, D., Goldfine, A.B., Kuo, F.C., Palmer, E.L., Tseng, Y.-H., Doria, A., et al. (2009). Identification and importance of brown adipose tissue in adult humans. N. Engl. J. Med. *360*, 1509–1517.

Elabd, C., Chiellini, C., Carmona, M., Galitzky, J., Cochet, O., Petersen, R., P nicaud, L., Kristiansen, K., Bouloumi, A., Casteilla, L., et al. (2009). Human Multipotent Adipose-Derived Stem Cells Differentiate into Functional Brown Adipocytes. Stem Cells *27*, 2753–2760.

Finkelstein, E.A., Trogdon, J.G., Cohen, J.W., and Dietz, W. (2009). Annual Medical Spending Attributable To Obesity: Payer-And Service-Specific Estimates. Health Affairs *28*, w822–w831.

GBD 2015 Obesity Collaborators (2017). Health Effects of Overweight and Obesity in 195 Countries over 25 Years. N. Engl. J. Med. NEJMoa1614362.

Gunawardana, S.C., and Piston, D.W. (2012). Reversal of type 1 diabetes in mice by brown adipose tissue transplant. Diabetes *61*, 674–682.

Gunawardana, S.C., and Piston, D.W. (2015). Insulin-independent reversal of type 1 diabetes in nonobese diabetic mice with brown adipose tissue transplant. Am. J. Physiol. Endocrinol. Metab. *308*, E1043–E1055.

Huttunen, R., and Syrjanen, J. (2013). Obesity and the risk and outcome of infection. Int J Obes (Lond) *37*, 333–340.

Karlsson, E.A., and Beck, M.A. (2010). The burden of obesity on infectious disease. Exp Biol Med (Maywood) *235*, 1412–1424.

Lee, Y.-H., Mottillo, E.P., and Granneman, J.G. (2013). Adipose tissue plasticity from WAT to BAT and in between. BBA - Molecular Basis of Disease 1–12.

Lepper, C., and Fan, C.-M. (2010). Inducible lineage tracing of Pax7-descendant cells reveals embryonic origin of adult satellite cells. Genesis *48*, 424–436.

Liu, X., Zheng, Z., Zhu, X., Meng, M., Li, L., Shen, Y., Chi, Q., Wang, D., Zhang, Z., Li, C., et al. (2013). Brown adipose tissue transplantation improves whole-body energy metabolism. Cell Research *23*, 851–854.

Lloyd-Jones, D., Adams, R., Carnethon, M., De Simone, G., Ferguson, T.B., Flegal, K., Ford, E., Furie, K., Go, A., Greenlund, K., et al. (2009). Heart disease and stroke statistics--2009 update: a report from the American Heart Association Statistics Committee and Stroke Statistics Subcommittee. Circulation *119*, 480–486.

Mottillo, E.P., Bloch, A.E., Leff, T., and Granneman, J.G. (2012). Lipolytic products activate peroxisome proliferator-activated receptor (PPAR) α and δ in brown adipocytes to match fatty acid oxidation with supply. Journal of Biological Chemistry *287*, 25038–25048.

Nedergaard, J., Petrovic, N., Lindgren, E.M., Jacobsson, A., and Cannon, B. (2005). PPARgamma in the control of brown adipocyte differentiation. Biochim. Biophys. Acta *1740*, 293–304.

Ng, M., Fleming, T., Robinson, M., Thomson, B., Graetz, N., Margono, C., Mullany, E.C., Biryukov, S., Abbafati, C., Abera, S.F., et al. (2014). Global, regional, and national prevalence of overweight and obesity in children and adults during 1980–2013: a systematic analysis for the Global Burden of Disease Study 2013. The Lancet *384*, 766–781.

Nishio, M., Yoneshiro, T., Nakahara, M., Suzuki, S., Saeki, K., Hasegawa, M., Kawai, Y., Akutsu, H., Umezawa, A., Yasuda, K., et al. (2012). Production of Functional Classical Brown Adipocytes from Human Pluripotent Stem Cells usingSpecific Hemopoietin Cocktail without Gene Transfer. Cell Metabolism *16*, 394–406.

Noguchi, M., Hosoda, K., Fujikura, J., Fujimoto, M., Iwakura, H., Tomita, T., Ishii, T., Arai, N., Hirata, M., Ebihara, K., et al. (2007). Genetic and Pharmacological Inhibition of Rho-associated Kinase II Enhances Adipogenesis. J. Biol. Chem. *282*, 29574–29583.

Pisani, D.F., Djedaini, M., Beranger, G.E., Elabd, C., Scheideler, M., Ailhaud, G., and Amri, E.-Z. (2011). Differentiation of Human Adipose-Derived Stem Cells into “Brite” (Brown-in-White) Adipocytes. Front Endocrinol (Lausanne) *2*, 87.

Roberts, J.L., Ashwell, M., and Enser, M. (1986). Brown adipose tissue triacylglycerol fatty acids of obese and lean mice: in situ and in transplants. Lipids *21*, 195–201.

Rubio, A., Raasmaja, A., and Silva, J.E. (1995). Thyroid hormone and norepinephrine signaling in brown adipose tissue. II: Differential effects of thyroid hormone on beta 3-adrenergic receptors in brown and white adipose tissue. Endocrinology *136*, 3277–3284.

Saito, M., Okamatsu-Ogura, Y., Matsushita, M., Watanabe, K., Yoneshiro, T., Nio-Kobayashi, J., Iwanaga, T., Miyagawa, M., Kameya, T., Nakada, K., et al. (2009). High incidence of metabolically active brown adipose tissue in healthy adult humans: effects of cold exposure and adiposity. Diabetes *58*, 1526–1531.

Sanchez-Gurmaches, J., and Guertin, D.A. (2014). Adipocytes arise from multiple lineages that are heterogeneously and dynamically distributed. Nature Communications *5*, 4099.

Sanchez-Gurmaches, J., Hung, C.-M., Sparks, C.A., Tang, Y., Li, H., and Guertin, D.A. (2012). PTEN loss in the Myf5 lineage redistributes body fat and reveals subsets of white adipocytes that arise from Myf5 precursors. Cell Metabolism *16*, 348–362.

Seale, P., Bjork, B., Yang, W., Kajimura, S., Chin, S., Kuang, S., Scimè, A., Devarakonda, S., Conroe, H.M., Erdjument-Bromage, H., et al. (2008). PRDM16 controls a brown fat/skeletal muscle switch. Nature *454*, 961–967.

Seamon, K.B., Padgett, W., and Daly, J.W. (1981). Forskolin: unique diterpene activator of adenylate cyclase in membranes and in intact cells. Proc. Natl. Acad. Sci. U.S.a. *78*, 3363–3367.

Shelton, M., Metz, J., Liu, J., Carpenedo, R.L., Demers, S.-P., Stanford, W.L., and Skerjanc, I.S. (2014). Derivation and expansion of PAX7-positive muscle progenitors from human and mouse embryonic stem cells. Stem Cell Reports *3*, 516–529.

Shinoda, K., Luijten, I.H.N., Hasegawa, Y., Hong, H., Sonne, S.B., Kim, M., Xue, R., Chondronikola, M., Cypess, A.M., Tseng, Y.-H., et al. (2015). Genetic and functional characterization of clonally derived adult human brown adipocytes. Nat Med *21*, 389–394.

Stanford, K.I., Middelbeek, R.J.W., Townsend, K.L., An, D., Nygaard, E.B., Hitchcox, K.M., Markan, K.R., Nakano, K., Hirshman, M.F., Tseng, Y.-H., et al. (2013). Brown adipose tissue regulates glucose homeostasis and insulin sensitivity. J. Clin. Invest. *123*, 215–223.

Timmons, J.A., Wennmalm, K., Larsson, O., Walden, T.B., Lassmann, T., Petrovic, N., Hamilton, D.L., Gimeno, R.E., Wahlestedt, C., Baar, K., et al. (2007). Myogenic gene expression signature establishes that brown and white adipocytes originate from distinct cell lineages. Proc. Natl. Acad. Sci. U.S.a. *104*, 4401–4406.

Townsend, K.L., and Tseng, Y.-H. (2014). Brown fat fuel utilization and thermogenesis. Trends in Endocrinology & Metabolism *25*, 168–177.

Tseng, Y.-H., Kokkotou, E., Schulz, T.J., Huang, T.L., Winnay, J.N., Taniguchi, C.M., Tran, T.T., Suzuki, R., Espinoza, D.O., Yamamoto, Y., et al. (2008). New role of bone morphogenetic protein 7 in brown adipogenesis and energy expenditure. Nature *454*, 1000–1004.

van Marken Lichtenbelt, W.D., Vanhommerig, J.W., Smulders, N.M., Drossaerts, J.M.A.F.L., Kemerink, G.J., Bouvy, N.D., Schrauwen, P., and Teule, G.J.J. (2009). Cold-activated brown adipose tissue in healthy men. N. Engl. J. Med. *360*, 1500–1508.

Virtanen, K.A., Lidell, M.E., Orava, J., Heglind, M., Westergren, R., Niemi, T., Taittonen, M., Laine, J., Savisto, N.-J., Enerbäck, S., et al. (2009). Functional brown adipose tissue in healthy adults. N. Engl. J. Med. *360*, 1518–1525.

Wang, W., Kissig, M., Rajakumari, S., Huang, L., Lim, H.-W., Won, K.-J., and Seale, P. (2014). Ebf2 is a selective marker of brown and beige adipogenic precursor cells. Proc. Natl. Acad. Sci. U.S.a. *111*, 14466–14471.

Xu, C., Tabebordbar, M., Iovino, S., Ciarlo, C., Liu, J., Castiglioni, A., Price, E., Liu, M., Barton, E.R., Kahn, C.R., et al. (2013). A Zebrafish Embryo Culture System Defines Factors that Promote Vertebrate Myogenesis across Species. Cell *155*, 909–921.

Xu, X., Browning, V.L., and Odorico, J.S. (2011). Activin, BMP and FGF pathways cooperate to promote endoderm and pancreatic lineage cell differentiation from human embryonic stem cells. Mechanisms of Development *128*, 412–427.

Yu, X.X., Lewin, D.A., Forrest, W., and Adams, S.H. (2002). Cold elicits the simultaneous induction of fatty acid synthesis and beta-oxidation in murine brown adipose tissue: prediction from differential gene expression and confirmation in vivo. Faseb J. *16*, 155–168.

Zhang, P., Li, J., Tan, Z., Wang, C., Liu, T., Chen, L., Yong, J., Jiang, W., Sun, X., Du, L., et al. (2008). Short-term BMP-4 treatment initiates mesoderm induction in human embryonic stem cells. Blood *111*, 1933–1941.

Zhou, J., Su, P., Wang, L., Chen, J., Zimmermann, M., Genbacev, O., Afonja, O., Horne, M.C., Tanaka, T., Duan, E., et al. (2009). mTOR supports long-term self-renewal and suppresses mesoderm and endoderm activities of human embryonic stem cells. Proceedings of the National Academy of Sciences *106*, 7840–7845.

CHAPTER 6

MATERIALS AND METHODS

Cell culture and differentiations

The human embryonic stem cell (hESCs) lines WA07 (WiCell, Madison, WI), WA09 (WiCell), induced pluripotent stem cell (hiPSCs) line K3, a gift from Stephen Duncan (Si-Tayeb et al., 2010), and de novo reprogrammed iPS cells generated from human neonatal foreskin fibroblasts (ATCC, Manassas, VA) were cultured as described previously (Singh et al., 2015). In detail, hESCs and hiPSCs were seeded at 50,000 cells/cm^2 on polystyrene culture plates (Thermo-Fisher, Waltham, MA) coated with Geltrex LDEV-Free hESC qualified reduced growth factor basement membrane matrix (Thermo-Fisher, Waltham, MA) at a 1:200 dilution in DMEM/F-12 w/o glutamine (Corning, Corning, NY). Media for PSC maintenance, sphere formation, paraxial mesoderm and brown adipocyte differentiations were accomplished using a chemically defined base medium (DBM) supplemented with specific factors. DBM was composed of DMEM/F-12 w/o glutamine supplemented with 2% Probumin (EMD Milipore, Billerica, MA), 1x Antibiotic-Antimyotic (Corning, Corning, NY), 1x MEM non-essential amino acids (Corning, Corning, NY), 1x Trace Elements A (Corning, Corning, NY), 1x Trace Elements B (Corning, Corning, NY), 1x Trace Elements C (Corning, Corning, NY) 50 ug/mL Ascorbic Acid (Sigma-Aldrich, St. Louis, MO), 10 ug/mL Transferrin (Athens Research and Technology, Athens, GA), 0.1 mM 2-mercaptoethanol (Therm-Fisher, Waltham, MA) and 1x Glutagro (Corning, Corning, NY). The PSC maintenance medium (MM) was composed of DBM

supplemented with 8 ng/mL human basic-FGF (R&D Systems, Minneapolis, MN), 200 ng/mL LONG® R3 human IGF-I (Sigma-Aldrich, St. Louis, MO), 10 ng/mL Activin A (R&D Systems, Minneapolis, MN) and 10 ng/mL human Heregulinβ-1 (Peprotech, Rocky Hill, NJ) to comprise a complete defied media (CDM). Human ESCs and hiPSCs were cultured in CDM with media changes every 24 hr up to 90% confluency, or 4 days, with 5% CO_2 in a 37 °C incubator. Human ESCs and iPSCs were removed from culture plates for passaging using Accutase® (Innovative Cell Technologies, San Diego, CA) at room temperature (RT) for 5-10 minutes. Following centrifugation at 1000 rpm for 4 minutes at RT, Accutase was aspirated off and the cell pellet was resuspened in CDM, cell number was then quantified using a hemocytometer. Cells were reseeded onto geltrex-coated plates as described above. Positive expression of OCT3/4, SOX2 and NANOG via quantitative polymerase chain reaction (qPCR), and immunofluorescence confirmed cell identity.

Definitive endoderm (DE) cells were generated by culturing hESCs or hiPSCs at 50,000 cells/cm^2 on geltrex, diluted 1:200 with DMEM/F-12, coated plates for 4 days in DBM supplemented with 100 ng/mL Activin A and 8 ng/mL human basic-FGF, with 25 ng/mL human Wnt-3a (R&D Systems, Minneapolis, MN) added to the media for the first 24 hr only. Medium was changed every 24 hr.

Paraxial Mesoderm (PM) cells were generated in a three-step process using rotational suspension culture. First a single-cell suspension containing $1x10^6$ cells/mL was seeded in 6-well suspension plates (Greiner Bio-One, Monroe, NC) at a volume of 5.5mL in sphere formation medium (SFM). The plate was then placed on an Innova 2000 platform shaker (New Brunswick Scientific, Edison, NJ) at 97 RPM in a 5% CO_2, 37°C incubator. Sphere formation medium was composed of hPSC MM supplemented with 10uM Y-27632 dihydrochloride (Tocris,

Minneapolis, MN) for 24 hours. Spent medium was changed by transferal of spheres and medium via pipette to a conical tube and spheres allowed to gravity sediment up to 10 minutes. Carefully, the spent medium was aspirated without disturbing the sedimented spheres. After 24 hours in SFM, the medium was replaced with only hPSC MM for an additional 24 hours and the spheres returned to the suspension plate and retuned to the orbital shaker. After 24 hours in MM, the medium was exchanged for paraxial mesoderm medium 1 (PMM1) via the medium exchange method above. PMM1 was composed of DBM supplemented with the final concentrations of the following factors: 10ng/mL BMP4 (R&D Systems, Minneapolis, MN), 20ng/mL bFGF (R&D Systems, Minneapolis, MN), 200ng/mL LONG® R3 IGF-I (Sigma-Aldrich, St. Louis MO), and 250 nM Rapamycin (Tocris, Minneapolis, MN). After 24 hours, fresh PMM1 was exchanged for spent PMM1 for another 24 hours. After a total of 48 hours in PMM1, the medium was exchanged with DBM to wash the cells. The cells were allowed to resediment, the DBM aspirated off and the spheres resuspended in PMM2 for an additional 96 hours with medium exchanges every 24 hours as above. As before the spheres were kept in suspension plates on the platform shaker. PMM2 was composed of DBM supplemented with the final concentrations of the following factors: 20ng/mL bFGF (R&D Systems, Minneapolis, MN), 200ng/mL LONG® R3 IGF-I (Sigma, Sigma-Aldrich, St. Louis MO), 250 nM Rapamycin (Tocris, Minneapolis, MN), 25ng/mL Wnt3a, 50ng/mL Noggin (R&D Systems, Minneapolis, MN), (R&D Systems, Minneapolis, MN), 2uM Bio (Tocris, Minneapolis, MN), and 5uM Forskolin (Tocris, Minneapolis, MN).

Brown adipocyte (BA) differentiation was accomplished using two sequential media formulations designated BAD1 and BAD2. BAs were derived by first dissociating the PM spheres into single-cell suspension. Briefly, PM spheres were removed from the suspension

plates and allowed to gravity sediment in a conical tube. The medium was aspirated carefully and the spheres gently washed once with excess DPBS without calcium or magnesium. The spheres were allowed to settle and the DPBS aspirated. The spheres were resuspended in 5mL of RT Accumax® (Innovative Cell Technologies, San Diego, CA) and placed on a single speed nutating mixer for 20-30 minutes until a single-cell suspension was achieved. The cells are subsequently filtered through a 100uM filter (ThermoFisher, Waltham, MA) into a 50mL conical tube, washed with DPBS and centrifuged at 200g for 4 minutes at RT; the resulting supernatant was aspirated and the cells resuspended in BAD1 medium for counting using a hemocytometer. BAD1 was composed of DBM supplemented with the final concentrations of the following factors: 8ng/mL bFGF (R&D Systems, Minneapolis, MN), 100ng/mL BMP7 (R&D Systems, Minneapolis, MN), 200ng/mL LONG® R3 IGF-I (Sigma-Aldrich, St. Louis, MO), 10uM Y-27632 dihydrochloride (Tocris, Minneapolis, MN), 2uM Rosiglitazone (Tocris, Minneapolis, MN), 1uM Dexamethasone (Tocris, Minneapolis, MN), 1nM LT-3 (3,3′,5-Triiodo-L-thyronine sodium salt) (Sigma-Aldrich, St. Louis, MO), 500uM IBMX (3-Isobutyl-1-methylxanthine) (Sigma-Aldrich, St. Louis, MO), and 10uM SB 431542 (Tocris, Minneapolis, MN). Cells were then seeded at a density of 90,000 cells/cm^2 on polystyrene culture plates (Thermo-Fisher, Waltham, MA) coated with Geltrex LDEV-Free hESC qualified reduced growth factor basement membrane matrix (Thermo-Fisher, Waltham, MA) at a 1:200 dilution in DMEM/F-12 w/o glutamine (Corning, Corning, NY). Cells were cultured in BAD1 until 100% confluence (8-10 days), with media changes every 24 hours. After 8-10 days, BAD1 was switched to BAD2. BAD2 is formulated the same as BAD1 excluding SB 431542 and supplemented with 1:500 Chemically Defined Lipid Concentrate (ThermoFisher, Waltham, MA). The cells are to remain in BAD2 until they are assayed or reaggregated for further use (transplants or further in vitro

analysis). BAD2 medium is changed daily. Reaggregation is achieved by first aspirating spent BAD2 medium and washing BA plates with DBPS; the cells are dissociated using a collagenase admixture containing 400 units each of collagenase I, II, and IV (ThermoFisher, Waltham, MA) diluted in HBSS without calcium and magnesium (Corning, Corning NY). The collagenase admixture was supplemented with 0.5mM $CaCl_2^+$ (Sigma-Aldrich, St. Louis, MO) to increase enzymatic activity. BA cells are incubated in the collagenase admixture at 37°C until the cells loosen from the plate (~20-30mins) at which point they were mainly in a sheet. The plates containing the cells and collagenase are rinsed with an equal volume of EDTA dissociation solution (Beers et al., 2012), transferred to a conical tube and centrifuged at 200g x 4 minutes at RT. The supernatant is removed and the cells are then resuspended in 5mL of Accumax® (Innovative Cell Technologies, San Diego, CA) and placed on a single speed nutating mixer for 20-30 minutes until a single-cell suspension was achieved. The cells are subsequently filtered through a 100uM filter (ThermoFisher, Waltham, MA) into a 50mL conical tube, washed with DPBS and centrifuged at 200g for 4 minutes at RT; the resulting supernatant was aspirated and the cells resuspended in BAD2 medium and placed in 6-well suspension plates (Greiner Bio-One, Monroe, NC) at a volume of 5.5mL/well. In general, one 10cm plate of BA will yield enough cells for two wells of a 6-well plate for reaggregation, as there is considerable loss between dissociation, filtration, wash, and cell death. The suspension plates are placed on an Innova 2000 platform shaker (New Brunswick Scientific, Edison, NJ) at 97 RPM in a 5% CO_2, 37°C incubator, and BAD2 replaced every other day by the gravity sedimentation medium exchange method above.

Adipocyte derived stem cells (ADSCs) were purchased from Thermofisher and cultured in MesenPRO™ RS medium (ThermoFisher, Waltham, MA) at a density of 5,000 cells/cm2

until reaching 70% confluence. The cells were dissociated with 1x TrypLe (ThermoFisher, Waltham, MA) and seeded at a density of 10,000 cells/cm2 for four days in MesenPRO™ RS medium. After four days the cells were at confluence and the medium was switched to StemPRO® Adipogenesis Differentiation Medium (ThermoFisher, Waltham, MA) to drive the cells toward a white adipocyte fate. The cells were culture for 21 days before being assayed.

qRT-PCR

Cells were lysed directly in the dish using TRK Lysis Buffer (Omega Bio-Tek, Norcross, GA) supplemented with 2-mercaptoethanol after DBPS wash and harvested with a on ice. E.Z.N.A RNA isolation kit (Omega Bio-Tek, Norcross, GA) was used to isolate RNA following the manufacturer's protocols and the RNA quantitated with a Biotek Synergy 2 plate reader. cDNA was synthesized using 1 μg of RNA via the Iscript cDNA synthesis kit (Bio-Rad, Hercules, CA) following the manufacturer's protocols. The cDNA was then diluted to a final volume of 500 μL with molecular grade water. ΔΔCt qRT-PCR analysis was performed using a ViiA7 Real-Time PCR System (Life Technologies, Carlsbad, California) in a 384 well plate with a reaction of 5 μL TaqMan Universal PCR Master Mix No AmpErase UNG (appliedbiosystems), 0.5 μL TaqMan primer (Life Technologies), 0.5 μL molecular grade water and 4 μL cDNA, see Table 6.1 for Taqman® probes used. Expression of each transcript was normalized to 18S ribosome, performed in triplicate and plotted as the mean ± standard error.

Immunofluorescent Microscopy

Human pluripotent stem cells were cultured in Labtek 4-well chamber slides (ThermoFisher, Waltham, MA) at a density of 50,000/cm2. Adipocyte derived stem cells were

seeded at 10,000 cells/cm2. Brown adipocytes were seeded as reaggregates at 15 reaggregates/cm2, or roughly one well of a 6-well suspension plate to eight Labtek slides. Paraxial mesoderm spheres were collected in 15 mL falcon tubes using gravity sedimentation (10mins), spent medium aspirated, spheres washed once with excess 1x DPBS without Ca2+ or Mg+ (Where from) and allowed to sediment again, supernatant aspirated and then fixed. The inclusion of MitoTracker® dye requires live cells with proper mitochondrial membrane potential. Therefore, if included, MitoTracker Deep Red dye was added to growth media at 200nM for 30-45 minutes prior to fixation. All cells were fixed with 4% paraformaldehyde (Electron Microscopy Sciences, Hatfield, PA) for 30 minutes at RT. Fixed spheres were washed once with excess 1x DPBS without Ca2+ or Mg+ and allowed to sediment. The wash was removed and a solution of 15% sucrose was added to a volume sufficient to cover the spheres. This entire volume of sucrose and spheres was then overlaid to the surface of a 2mL volume of 30% sucrose solution overnight at 4°C as a cryoprotectant. After overnight dehydration in sucrose, the spheres were removed via wide bore 200uL pipette tip and transferred into cryomolds filled with Tissue-Tek® O.C.T. Compound (Sakura Finetek, USA). The cryomolds were then transferred to liquid nitrogen gas phase for flash freezing for 5 minutes. Frozen cryomolds were stored at -80°C and were subsequently sectioned using a Leica CM 3050 S cryostat (Leica Biosystems, Buffalo Grove, IL) at a thickness of 7um onto microscope slides and stored at -80°C.

Human PSCs were cultured to 80% confluence before fixation. Human ADSCs were cultured in StemPRO® Adipogenesis Differentiation Medium for 21 days. Brown adipocytes were cultured 14 to 30 days after seeding reaggregates. All samples, fixed cells and sections, were washed with 1x DPBS without Ca2+ or Mg+ for 5 minutes. For hPSCs and PM the wash

was removed and replaced with permeabilization and blocking buffer containing PBST (1x PBS and 0.2% Triton X-100) (ThermoFisher, Waltham, MA), 10% donkey serum (Equitech-Bio), 0.3M glycine (Sigma-Aldrich, St. Louis, MO) for 1 hour at RT. For BA cells, the wash was removed and replaced with permeabilization and blocking buffer containing PBSS (1x PBS and 0.1% Saponin) (Millipore, Billerica, MA), 10% donkey serum, 0.3M glycine for 1 hour at RT. For all, permeabilization and blocking buffer was removed and the slides rinsed once with primary antibody incubation buffer containing PBST or PBSS and 10% donkey serum. Subsequent to removing the was the wash, primary antibodies, see Table 6.2 were prepared in primary antibody incubation buffer, added to samples and incubated overnight at 4°C. After overnight incubation with primary antibody, the samples were washed 3x with incubation buffer alone. Secondary antibodies were diluted in a 2.5% donkey serum, 0.2 M PBST/S solution and incubated for 1 hr at RT in the dark. Following removal of secondary antibodies, cells were washed twice with DPBS for 5 minutes each. If included, LipidTox Green/Red Dyes were added at 1:200 dilution in DPBS for 30 minutes. Subsequent to LipidTox dyes, 1 μg/mL 4′,6-Diamidino-2-phenylindole dihydrochloride (Sigma-Aldrich, St. Louis, MO) in DPBS was added to cells for 5 minutes. After 3 washes in DPBS, coverslips were mounted to slides with ProLong Gold Antifade (ThermoFisher, Waltham, MA). A Leica DM6000B microscope and Zeiss LSM 710 confocal microscope were used to obtain images. Images were processed with Slidebook 6 (Intelligent Imaging Solutions, Edmonton, Alberta).

Flow Cytometry

Cells were dissociated using methods listed above for normal dissociation for each cell type, washed with sterile DPBS and pelleted at 200 x g for 4 minutes. Cells were resuspended in 0.5 mL of Flow Cytometry Fixation Buffer (R&D Systems, Minneapolis MN) and incubated at

room temperature for 15 minutes. Following fixation cells were washed twice with DPBS, pelleted and resuspended in 200 μL of Flow Cytometry Permeabilization/Wash Buffer I (R&D Systems, Minneapolis, MN). Primary antibodies, see Table 4.1, were incubated with fixed cells for one hour at 4°C. Cells were then washed and incubated with secondary antibodies, see Table 4.2, for 30 minutes at 4°C. If included, LipidTox Green/Red Dyes were added at 1:200 dilution in DPBS for 30 minutes after secondary antibody addition. Analysis was performed on a Beckman Coulter CyAn and the results analyzed and plotted using FlowJo v10.

Western blotting

Cells were washed with ice cold DPBS, collected with a cell scrapper, pelleted via centrifugation at 200g for 4 minutes, flash-frozen in liquid nitrogen and stored at -80°C as cell pellets. Cell pellets were resuspended and lysed on ice for 30 minutes in 50μL of a buffer consisting of RIPA lysis buffer (Sigma), 1x protease inhibitor (Roche, Basel, CH), 1x phosphatase inhibitor (Millipore, Billerica, MA,) and 100mM dithiothreitol (Sigma-Aldrich, St. Louis, MO). Lysates were centrifuged at 20,000 x g for 10 min at 4°C with the supernatant collected. Protein concentrations within supernatants were determined via Bradford assay at 595nm on a Biotek Synergy 2 and diluted 1:1 with Laemmli buffer (Bio-Rad, Hercules, CA) supplemented with 5% 2-mercaptoethanol. Bolt bis-Tris precast gels (Life Technologies, Carlsbad, CA) were loaded with 20μg of protein, which was separated by electrophoresis at 165 V for 35 minutes. Protein was transferred to a nitrocellulose membrane via a Bolt transfer system (Life Technologies, Carlsbad, CA) at 100V for 60 minutes. Membranes were blocked with a solution of 2% nonfat blocking milk (Bio-Rad, Hercules, CA) in TBST, 0.5% (v/v) Tween-20 (Sigma-Aldrich, St. Louis, MO) in 25mM TBS, for 1hr at RT while rocking followed

by 3 washes with TBST. Primary antibodies, Table 6.1, were added to membranes in blocking solution and incubated overnight at 4 °C. Following incubation membranes were washed 3 times in TBST for 5 minutes at RT while rocking. Secondary antibodies were added to membranes in blocking solution and incubated for 1 hr at RT while rocking and then washed with TBST 3 times. Protein levels on membranes were detected with Amersham ECL detection kit (GE Healthcare Bioscience, Pittsburgh, PA) with Amersham hyperfilm (GE Healthcare Bioscience, Pittsburgh, PA).

Electron Microscopy

Both BA aggregates and ADSC-derived WA were cultured in their respective growth media on 15mm Nunc™ Thermanox™ Coverslips (TheroFisher, Waltham, MA) in 12-well plates for 21 days. Samples were fixed in 2% glutaraldehyde (v/v) and 5 mM $CaCl_2$ in 0.1 M cacodylate buffer (pH 7.2). The pieces were then washed in phosphate buffer saline (PBS) and post-fixed for 60 min in 1% OsO_4 in cacodylate buffer containing 5 mM $CaCl_2$ and 0.8% potassium ferricyanide. After washes in PBS, the sample material was dehydrated in acetone and embedded in Epon. Ultra-thin (70 nm) sections were stained with uranyl acetate and lead citrate and observed with a JEOL 1210 electron microscope.

Seahorse Extracellular Flux Analysis

Paraxial Mesoderm, BA and WA cells were plated on Seahorse XFe24 cell culture microplates (Agilent, Santa Clara, CA) under their normal culture conditions. Briefly, PM cells were plated at a density of 120,000/cm2 in PMM2 medium supplemented with Y-27632 dihydrochloride (Tocris, Minneapolis, MN) for 24 hours, then switched to PMM2 alone for an

additional 48 hours prior to flux analysis. Brown adipocytes were plated as reaggreagtes at a density of 15 aggregates/cm2 and cultured for 21 days in BAD2. For white adipocytes flux analysis, hADSCs were plated at a density of 10,000 cells/cm2 in MesenPRO™ RS (ThermoFisher, Waltham, MA) medium for four days and then switched to StemPRO® Adipogenesis Differentiation Medium (ThermoFisher, Waltham, MA) for 21 days. For BA cells, media was changed every other day. For the hADSCs fresh MesenPRO was added on the initial day of plating and not changed. During WA differentiation, StemPRO® Adipogenesis Differentiation Medium was changed every three days.

The Mito Stress Test Kit (Agilent, Santa Clara, CA) was utilized to analyze mitochondrial function. The drugs, oligomycin, FCCP and rotenone/antimycin A were titrated for maximal effect against brown adipocytes prior to establishing the flux analysis protocols for the PM and WA cells. Drug concentrations were unchanged throughout all extracellular flux assays: oligomycin was used at 2uM, FCCP, at 2uM, and rotenone/antimycin A used at 5uM.

For the norepinephrine stimulation analysis, the cells were kept in their respective differentiation media until immediately before the assay. For the isoproterenol stimulation assays the PM cells were given PMM2 medium without forskolin and with 100uM isoproterenol 18 hours prior to the assay. The BA cells were given BAD2 medium without IBMX and with 100uM isoproterenol for 18 hours prior to the assay. Because the white adipocytes were differentiated in a serum based medium, we sought to normalize any effects from serum on the BA cells by exposing both cells to the same medium for 48 hours for the forskolin stimulation assays. Both the BA and WA cells were given a minimal medium composed of DMEM/F-12 w/o glutamine (Corning, Corning, NY), 2% ESC-qualified FBS (Atlanta Biological, Flowery Branch, GA), 2mM glutagro™ (Corning, Corning, NY), 1x MEM non-essential amino acids (Corning,

Corning, NY), 200ng/mL LONG® R3 IGF-I (Sigma-Aldrich, St. Louis, MO), and 1uM Dexamethasone (Tocris, Minneapolis, MN). Twenty-four hours prior to the assay, this minimal medium was supplemented with 10uM forskolin. For the fatty acid oxidation assay, both BA and WA cells were given a substrate-limited medium for 24 hours prior to the flux assay. This substrate-limited medium was composed of DMEM w/o glucose, glutamine or sodium pyruvate (Corning, Corning, NY) supplemented with 0.5 mM glucose (Corning, Corning, NY), 1 mM glutagro™ (Corning, Corning, NY), 0.5 mM carnitine (Sigma-Aldrich, St. Louis, MO), and 2% ESC-qualified FBS (Atlanta Biological, Flowery Branch, GA).

Prior to the assay, the cells were given freshly prepared XF assay medium. This medium was composed of XF base medium (Agilent, Santa Clara, CA) and desired concentrations of substrates: glucose, glutamine, and sodium pyruvate. For the stimulation assays, XF assay medium contained base medium supplemented with 25mM glucose (Corning, Corning, NY), 2mM glutagro™ (Corning, Corning, NY), and 1mM sodium pyruvate. The medium was warmed to 37°C and the pH adjusted to 7.4 using sodium hydroxide and filtered through a 0.2μm Stericup® filter (Millipore, Billerica, MA). At least one hour prior to he start of a flux assay, the growth medium was removed from the XF24 plate and the cells washed three times per manufacturers protocol with XF assay medium and cells placed in a non-CO_2 incubator at 37°C. All drugs utilized during the flux analysis were also diluted from stocks into XF assay medium prior to loading into the assay cartridge ports. For the fatty acid oxidation assays, XF assay medium contained XF base medium supplemented with 5.5mM glucose and 0.5mM carnitine.

The 1.5mM conjugated palmitate-BSA solution was prepared sequentially in a two-step process. First a 1mM sodium palmitate (Sigma-Aldrich, St. Louis, MO) in 150mM NaCl solution was made followed by 0.34mM Fatty Acid Free BSA (Santa Cruz Biotechnology, Dallas, TX) in

150mM NaCl solution. The sodium palmitate solution was heated to from 37°C to 70°C in a water bath on heated stir plate until the solution was clear. Meanwhile, the BSA solution was heated in a water bath on a heated stir plate at 37C until it completely dissolved and then sterile filtered with a 0.2µm Stericup® filter (Millipore, Billerica, MA). Once filtered, the BSA solution was transferred to conical tubes and kept in a 37C water bath until ready to mix. For the BSA only control, half of the 0.34mM BSA NaCl solution was further diluted with an equal volume of 150mM NaCl solution for a final concentration of 0.17mM BSA. This solution was aliquoted and stored at -20C. To complete the palmitate conjugation, an equal volume of hot palmitate was added in 5mL increments to the remainder of the warm 0.34mM BSA solution (molar ratio between palmitate and BSA = 6:1). This solution was stirred at t 37°C for one hour. The pH was adjusted to 7.4 and the final solution aliquoted into 4mL glass vials and stored at − 20°C.

Following flux analysis, cells were lysed and protein content measured by Bradford assay. Briefly, at the completion of the flux assay, the plate was removed, medium aspirated and the wells rinse gently with ice cold DPBS. The wash was aspirated and the plate was then placed in liquid nitrogen gas phase while fresh lysis buffer was prepared. Lysis buffer was composed of 10mM Tris, pH 7.4 with 0.1% Triton X-100. The frozen plate was removed and room temperature lysis buffer immediately added. The freezing and addition of relatively warm lysis buffer assists the lysing of the adipocytes. To the lysed cells, 450uL of Bradford reagent (Bio-Rad, Hercules, CA) was added to each well. Protein concentration was determined using 100uL of the lysed cell-Bradford reagent admix at 595nm on a Biotek Synergy 2. Flux data was the processed via Wave software (Agilent, Santa Clara, CA) and standardized to protein content.

Lipolysis

Human PSCs, BA cells and hADSCs were plated in 12-well falcon plates (Fisher Scientific, Hampton, NH). Human PSCs were seeded at 50,000 cells/cm2 and cultured for four days until confluent in MM. Human ADSCs were seeded at 10,000 cells/cm2 and cultured first in MesenPRO™ RS (ThermoFisher, Waltham, MA) for four days until confluent. The medium was then switched to StemPRO® Adipogenesis Differentiation Medium (ThermoFisher, Waltham, MA) for 21 days. Brown adipocyte aggregates were plated in 12-well falcon plates (Fisher Scientific, Hampton, NH) at 15 aggregates/cm2 and cultured for 21 days in BAD2 medium. Lipolysis was measured by glycerol release into the cell culture medium using Free Glycerol Reagent (Sigma Aldrich, St. Louis, MO) according to manufacturer instructions. Prior to the assay, the growth medium from each cell type was removed and the cells washed with lipolysis base medium [DMEM (Corning, Corning, NY) supplemented with 2% FA-free BSA (Santa Cruz Biotechnology, Dallas, TX) three times to remove any residual fatty acids from the wells. Lipolysis was stimulated by addition 10μM Forskolin (Tocris, Minneapolis, MN) to lipolysis base medium at time "0" with sampling at 4 hours and 8 hours time points. Triacsin C (5 μM) was added to the base medium to inhibit acyl-CoA synthetases and subsequent reesterifciation of glycerol and released fatty acids. Lipolysis data were normalized to protein content as described in western blotting.

Table 6.1- Comprehensive List of Taqman Probes

Gene	Probe Number	Gene	Probe Number
ADIPOQ	Hs00605917_m1	*NKX2.5*	Hs00231763_m1
C/EBPα	Hs00269972_s1	*PAX3*	Hs00240950_m1
C/EBPδ	Hs00270931_s1	*PAX6*	Hs01088114_m1
C/EPBβ	Hs00270923_s1	*PAX7*	Hs00242962_m1
CD137	Hs00169409_m1	*PDK4*	Hs01037712_m1
CD36	Hs00169627_m1	*PLIN1*	Hs00160173_m1
CDH1	Hs00170423_m1	*PPARGC1α*	Hs01016724_m1
CIDEA	Hs00154455_m1	*PPARγ*	Hs00947536_m1
DIO2	Hs00988260_m1	*PRDM16*	Hs00922674_m1
EBF2	Hs00224081_m1	*PRRX1*	Hs00246567_m1
EDNRB	Hs00240747_m1	*SIX1*	Hs00195590_m1
ELOVL3	Hs00537016_m1	*SOX1*	Hs01057642_s1
FABP4	Hs01086177_m1	*SOX10*	Hs00366918_m1
FOXC1	Hs00559473_s1	*SOX9*	Hs01001343_g1
FOXC2	Hs00270951_s1	*TBX1*	Hs00962558_g1
FOXD3	Hs01027393_s1	*TBX6*	Hs00365539_m1
IRF4	Hs01056533_m1	*TCF15*	Hs00231821_m1
MRF4	Hs01547104_g1	*TFA2B*	Hs00231468_m1
MSGN1	Hs03405514_s1	*TMEM26*	Hs00415619_m1
MYF5	Hs00929416_g1	*UCP1*	Hs00222453_m1
NGFR	Hs00609977_m1	*ZIC1*	Hs006020749_m1

Table 6.2- Comprehensive List of Antibodies and Dyes

Primary Antibody/ Dye	Application	Dilution/ Concetration	Vendor	Catalog Number
CD29-APC	Flow	20uL/1x10^6 cells	BD Pharmingen	559883
CD34-PE	Flow	20uL/1x10^6 cells	BD Pharmingen	348057
PDGFRa-PE	Flow	20uL/1x10^6 cells	BD Pharmingen	556002
CDK2	WB	1:2000	Santa Cruz Biotechnology	sc-163
OCT3/4	IF	1:200	Santa Cruz Biotechnology	sc-8628
SOX2	IF	1:200	Santa Cruz Biotechnology	sc-17320
FOXC1	Flow/IF	1:50 (Flow); 1:500 (IF)	Millipore	ABD71
MYF5	Flow/IF	0.5 µg/10^6 cells (Flow); 1:50 (IF)	R&D Systems	AF4027
MYF5	WB	1:1000	Santa Cruz Biotechnology	sc-302
PAX3	Flow/IF	0.25ug/10^6 cells; 5µg/mL (IF)	R&D Systems	MAB2457
UCP1	IF	1:500	Abcam	ab10983
UCP1-PE	Flow	10uL/10^6 cells	R&D Systems	IC6158P
LipidTox Green	IF	1:200	ThermoFisher	H34475
LipidTox Red	Flow	1:200	ThermoFisher	H34477
MitoTracker Deep Red	IF	200nM	ThermoFisher	M22426
TCOF1/Treacle	WB	1:1500	proteintech	110003-1-AP
HNK1	Flow/IF	0.2uL/10^6 cells (Flow); 1:300 (IF)	Sigma	C6608
P75	Flow/IF	0.2uL/10^6 cells (Flow);1:100 (IF)	Advanced Targeting Systems	ABN07
AP2	IF	1:50	DSHB	3B5

REFERENCES

Beers, J., Gulbranson, D.R., George, N., Siniscalchi, L.I., Jones, J., Thomson, J.A., and Chen, G. (2012). Passaging and colony expansion of human pluripotent stem cells by enzyme-free dissociation in chemically defined culture conditions. Nature Protocols *7*, 2029–2040.

Si-Tayeb, K., Noto, F.K., Sepac, A., Sedlic, F., Bosnjak, Z.J., Lough, J.W., and Duncan, S.A. (2010). Generation of human induced pluripotent stem cells by simple transient transfection of plasmid DNA encoding reprogramming factors. BMC Dev Biol *10*, 81.

Singh, A.M., Sun, Y., Li, L., Zhang, W., Wu, T., Zhao, S., Qin, Z., and Dalton, S. (2015). Cell-Cycle Control of Bivalent Epigenetic Domains Regulates the Exit from Pluripotency. Stem Cell Reports *5*, 323–336.

CHAPTER 7

DISCUSSION

The effort to utilize human pluripotent stem cells (hPSCS) for human developmental studies and disease modeling began almost immediately after Thomson et al. described the isolation of such cells from the inner cell mass of human blastocysts in their seminal work nearly 20 years ago (Thomson et al., 1998). Human PSCs maintain two exceptional features that make them uniquely suited for these tasks: 1) the potential to generate cells from each of the three germ layers, and therefore every adult cell type; 2) capacity for unlimited self-renewal. These features offer benefits over animal studies and models based on isolated primary cells. Animal studies are limited in their relevance to humans, and isolated primary cells have limited differentiation, renewal, and scalability issue. Therefore, these approaches cannot faithfully recapitulate human disease, and are not suitable for scale-up needs, such as high throughput screening. By including induced pluripotent cell (iPSC), it is possible to further elucidate human specific disease etiology: patient-derived iPSC models are more likely to completely and faithfully recapitulate the human disease state, particularly in cases where the disease is cell autonomous. Additionally, access to patient-derived cells also allows for potential differences between individuals to be assessed. The work presented here took advantage of the beneficial characteristics of hPSCs and iPSCs to establish both a developmental model and a patient specific disease model. Both efforts were based on robust in vitro differentiation platforms that faithfully mimic embryonic development.

We developed a highly efficient, single-step method for the generation of neural crest cells (NCCs) from human pluripotent stem cells (Menendez et al., 2013; 2011). The protocol described herein is feeder-free and requires no enrichment steps with typical population yields of ≥ 90% NCC phenotype. To accomplish this, we coupled Smad inhibition to enhanced activation of the Wnt pathway by utilizing small-molecule inhibitors of TGF-β signaling (SB431542) and glycogen synthase kinase 3 [GSK3 inhibitor IX (BIO)]. This method was used to interrogate the suggested pathology of Treacher Collins Syndrome (TCS) in patient-derived cells. Preliminary studies in murine models of TCS have demonstrated that *Tcof1* haploinsufficiency results in decreased survival of NCCs. While these reports demonstrate craniofacial abnormalities, these studies have been characterized in genetically manipulated mice, which do not faithfully recapitulate TCS beyond late gestation, as this genotype is lethal. In addition these models demonstrate that burgeoning NCCs have defects in proliferation. Neither survival nor proliferation has ever been measured in developing human NCCs or subsequent cell types. However, our data suggest no difference in survival or proliferation upon NCC differentiation. In the human, TCS may manifest as a result of combined survival/proliferation abnormalities or as a consequence of one or the other. It is critical to establish what role *TCOF1* mutations in a human context has on the effect of neural crest cell lineage development. Neural crest cells differentiate to a vast number of other cell types, thus it is feasible that a defect may be discovered in the transition from NCC to these other cell types, specifically in the context of TCS: chondrocytes and osteocytes. If the evidence from murine models is translatable, TCS patient-derived cells should display reduced survivability/proliferation during their differentiation from NCCs.

Recent evidence suggests that the etiology of TCS may be a result of non cell-autonomous local environmental factors, specifically the generation and presence of reactive oxygen species (ROS) and the failure of an additional the function of Tcof1: suppressing apoptosis induced by oxidative stress (Ciccia et al., 2014; Larsen et al., 2014; Sakai and Trainor, 2016; Sakai et al., 2016). Importantly, Sakai et al. reported that neural crest cells endogenously generate ROS at relatively high levels compared with other tissues (Sakai et al., 2016). These ROS can lead to increased oxidative DNA damage. Evidence pointing to a function for treacle in DNA repair is mounting up: treacle has been shown to localize to sites of DNA damage and form DNA damage foci in response to X-ray irradiation (Ciccia et al., 2014; Larsen et al., 2014). Additionally, in utero treatment of Tcof-haploinsufficient embryos with N-acetyl-cysteine (NAC) quenched ROS and suppressed DNA damage (Sakai et al., 2016). The suppression of this damage diminished p53 accumulation and subsequent apoptosis (Sakai et al., 2016). Critically, prenatal supplementation with NAC decreased both incidence and severity of craniofacial abnormalities such that 30% of treated Tcof-haploinsufficient embryos were morphologically indistinguishable from wild-type littermates (Sakai et al., 2016). The observation of ROS involvement in TCS has also been demonstrated recently in zebrafish, and again, pharmacological amelioration of redox species through NAC in the fish medium, resulted in a reduction in abnormalities of craniofacial cartilages in Treacle-depleted 4 dpf zebrafish larvae (de Peralta et al., 2016).

With this new evidence in hand, it must be appreciated that our NCC differentiation medium contains several potent ROS scavengers and antioxidants including albumin, 2-mercaptoethanol, L-ascorbic acid and selenium (Yao and Asayama, 2017). It is feasible that our culture conditions do not permit the observance of a disease phenotype of TCS through

supplementation that artificially supports the survival and proliferation of neural crest cells by inhibiting ROS oxidative stress. Modulation of these agents within our culture conditions may permit the discovery of a TCS phenotype in the dish.

We also developed a highly efficient method to generate brown adipocytes from hPSCs through directed differentiation using a chemically defined medium. One of the hallmarks of hPSC cellular development models is the ability to model pathways as they occur in vivo. We are the first to report such a differentiation using a developmentally appropriate pathway deriving brown adipocytes through a paraxial mesoderm-resident dermomytome-like intermediate. Brown adipocytes arise from dermomytomal progenitors that also give rise to skeletal muscle (Atit et al., 2006; Lee et al., 2013; Lepper and Fan, 2010; Sanchez-Gurmaches and Guertin, 2014; Seale et al., 2008; Timmons et al., 2007). The dermomytomal-like identity of our intermediate cells is bolstered by the fact that we are able to generate skeletal myotubes along a differentiation path that transits from paraxial mesoderm to myoblast to myotube with appropriate sinusoidal kinetics of myogenic transcription factors such as PAX3, PAX7, MYF5, MYOD, and MYOG (Bentzinger et al., 2012; Buckingham, 2017; Buckingham and Relaix, 2007; Lagha et al., 2008; Le Grand and Rudnicki, 2007). This critical feature permits examination of the fate bifurcation point between brown adipocytes and skeletal muscle during human development. A current gap in knowledge is the mechanistic basis for the selective binding of factors such as PPARγ to their target genes that determine adipocyte identity and function. Moreover, these processes are likely to differ in a species specific manner, thus the use of human pluripotent cells to derive brown adipocytes to study transcriptional and epigenetic regulation of human adipogenesis in vitro is critical to our understanding of brown adipocyte development. The current lack of understanding of the molecular mechanisms of human

adipogenesis and difficulties in treating conditions related to excess adiposity represent an acute gap in knowledge. Defining the relationships between regulation and response of extracellular signals and transcriptional dynamics that lead to and occur during adipogenesis, with special consideration as to these factors as they relate to the specification of different adipocytes, white, brown, and brite alike, will be crucial to overcoming this gap. Obesity has become an enormous burden on human health and healthcare costs. Beyond the direct consequences of excess adipose, the chronic status of obesity leads to long-term sequelae such as cardiovascular disease, type II diabetes, and some cancers to name just a few. The discovery of active brown adipose tissue in adults and the positive health outcomes correlated to increase BAT quantity/activity have led to a great interest in discovering how this tissue forms and operates. The appeal of elucidating the method by which this tissue originates is the hope that we can ultimately derive anti-obesity therapies from the activities of this tissue, namely the utilization of stored lipids and serum glucose through uncoupled oxidation.

The study of adipogenesis has been accomplished mainly through murine studies. Most in vitro adipogenesis studies focus on deriving adipocytes from cellular populations collected from mature adipocyte depots in adult mice or humans. While these reports have been vital, a gap remains- we are still unacquainted with the mechanisms that drive the development of adipose tissue de novo. This is most grossly apparent in our understanding of brown adipogenesis. To date only one study has been able to develop brown adipocytes in vitro without gene transfer (Nishio et al., 2012) and this method derived brown adipocytes through hematopoietic means. A key goal of this work was to develop a model of brown adipogenesis using human pluripotent cells driven through distinct lineages that have been shown through lineage tracing experiments to be able to produce brown adipocyte tissue. Having developed

lipid droplet containing cells that express UCP1 from a dermomytome-like progenitor, we next sought to demonstrate the functional capacity of these adipocytes. Extracellular flux analyses revealed that differentiated brown adipocytes were responsive to stimuli known to activate brown adipocytes. These compounds included norepinephrine, isoproterenol and forskolin. Interestingly, the β-adrenergic agonists had no effect on the rate of glycolysis whereas forskolin had both a dramatic effect on oxygen consumption and a shift toward significant glycolytic increase. Forskolin administration also led to a significant increase in uncoupled oxidation. We next sought to determine the ability of our cells to utilize both endogenous and exogenous fatty acids to modulate mitochondrial function. Using a combination of palmitate and the irreversible inhibitor of carnitine palmitoyltransferase-1 (CPT-1), etomoxir, we showed that differentiated brown adipocytes drastically increase oxygen consumption upon addition of palmitate, indicating an increase in fatty acid β-oxidation. Palmitate increased basal respiration, and also significantly increased maximal respiration as well as uncoupled respiration. In addition to flux analysis, we also interrogated the ability of differentiated brown adipocytes to undergo increased lipolysis upon stimulation. Brown adipocytes displayed significantly more lipolysis than hiPSCs or ADSC-derived white adipocytes in both an unstimulated and stimulated state (forskolin). Having morphologic and functional similarity to classical human brown adipocytes, we are moving into in vitro and in vivo studies to demonstrate thermogenic capacity.

Another important feature of this brown adipocyte differentiation is the fact that these cells can be grown in adherent culture, survive passage and reaggregation, survive replating and go on to survive and proliferate for weeks after dissociation. This feature is unique to our culture system and permits gross scalability critical to high throughput screening efforts. Having completed this differentiation in both hESCs and hiPSCs, it may be possible to examine patient-

derived iPSCs to uncover if high BMI individuals have genetic features, which inhibit or retard their ability to activate their brown adipocyte tissue. If so, discovering pharmaceutical compounds through high through-put drug screening may be an attractive approach to designing therapies for this population. Moreover, the long-term survival of these cells and their ability to be removed from a matrix is an excellent prognostication that they will survive long-term engraftment in an animal host for in vivo studies.

Our use of hPSCs to develop a model of TCS in vitro failed. We were successful in deriving NCCs from patient-derived iPSCs. However, ultimately, our culture conditions that drive NCC identity may be inhibiting the development of the TCS phenotype. It remains to be determined if modulating these conditions will permit the appearance of such a phenotype. Thus, the choice of hiPSCs as a basis for this platform is still a sound model and the only way to accurately depict normal human development outside of animal models. The success of the brown adipocyte differentiation model is built on the ability to transit from hPSC to paraxial mesoderm to brown adipocyte in a developmentally mimicking manner coupled to the cells' functionality and flexibility in culture. These features make this differentiate suitable for developmental studies, as well as in vivo and high though-put analyses. To our knowledge it is the only human brown adipocyte system with such deep capabilities.

REFERENCES

Atit, R., Sgaier, S.K., Mohamed, O.A., Taketo, M.M., Dufort, D., Joyner, A.L., Niswander, L., and Conlon, R.A. (2006). Beta-catenin activation is necessary and sufficient to specify the dorsal dermal fate in the mouse. Developmental Biology *296*, 164–176.

Bentzinger, C.F., Wang, Y.X., and Rudnicki, M.A. (2012). Building Muscle: Molecular Regulation of Myogenesis. Cold Spring Harbor Perspectives in Biology *4*, a008342–a008342.

Buckingham, M. (2017). Gene regulatory networks and cell lineages that underlie the formation of skeletal muscle. Proceedings of the National Academy of Sciences *114*, 5830–5837.

Buckingham, M., and Relaix, F. (2007). The role of Pax genes in the development of tissues and organs: Pax3 and Pax7 regulate muscle progenitor cell functions. Annu. Rev. Cell Dev. Biol. *23*, 645–673.

Ciccia, A., Huang, J.-W., Izhar, L., Sowa, M.E., Harper, J.W., and Elledge, S.J. (2014). Treacher Collins syndrome TCOF1 protein cooperates with NBS1 in the DNA damage response. Proceedings of the National Academy of Sciences *111*, 18631–18636.

de Peralta, M.S.P., Mouguelar, V.S., Sdrigotti, M.A., Ishiy, F.A.A., Fanganiello, R.D., Passos-Bueno, M.R., Coux, G., and Calcaterra, N.B. (2016). Cnbp ameliorates Treacher Collins Syndrome craniofacial anomalies through a pathway that involves redox-responsive genes. Cell Death Dis *7*, e2397.

Lagha, M., Sato, T., Bajard, L., Daubas, P., Esner, M., Montarras, D., Relaix, F., and Buckingham, M. (2008). Regulation of Skeletal Muscle Stem Cell Behavior by Pax3 and Pax7. Cold Spring Harbor Symposia on Quantitative Biology *73*, 307–315.

Larsen, D.H., Hari, F., Clapperton, J.A., Gwerder, M., Gutsche, K., Altmeyer, M., Jungmichel, S., Toledo, L.I., Fink, D., Rask, M.-B., et al. (2014). The NBS1-Treacle complex controls ribosomal RNA transcription in response to DNA damage. Nat Cell Biol *16*, 792–803.

Le Grand, F., and Rudnicki, M.A. (2007). Skeletal muscle satellite cells and adult myogenesis. Current Opinion in Cell Biology *19*, 628–633.

Lee, Y.-H., Mottillo, E.P., and Granneman, J.G. (2013). Adipose tissue plasticity from WAT to BAT and in between. BBA - Molecular Basis of Disease 1–12.

Lepper, C., and Fan, C.-M. (2010). Inducible lineage tracing of Pax7-descendant cells reveals embryonic origin of adult satellite cells. Genesis *48*, 424–436.

Menendez, L., Kulik, M.J., Page, A.T., Park, S.S., Lauderdale, J.D., Cunningham, M.L., and Dalton, S. (2013). Directed differentiation of human pluripotent cells to neural crest stem cells. Nature Protocols *8*, 203–212.

Menendez, L., Yatskievych, T.A., Antin, P.B., and Dalton, S. (2011). Wnt signaling and a Smad pathway blockade direct the differentiation of human pluripotent stem cells to multipotent neural crest cells. Proceedings of the National Academy of Sciences *108*, 19240–19245.

Nishio, M., Yoneshiro, T., Nakahara, M., Suzuki, S., Saeki, K., Hasegawa, M., Kawai, Y., Akutsu, H., Umezawa, A., Yasuda, K., et al. (2012). Production of Functional Classical Brown Adipocytes from Human Pluripotent Stem Cells usingSpecific Hemopoietin Cocktail without Gene Transfer. Cell Metabolism *16*, 394–406.

Sakai, D., and Trainor, P.A. (2016). Face off against ROS: Tcof1/Treacle safeguards neuroepithelial cells and progenitor neural crest cells from oxidative stress during craniofacial development. Development, Growth & Differentiation *58*, 577–585.

Sakai, D., Dixon, J., Achilleos, A., Dixon, M., and Trainor, P.A. (2016). Prevention of Treacher Collins syndrome craniofacial anomalies in mouse models via maternal antioxidant supplementation. Nature Communications *7*, 10328.

Sanchez-Gurmaches, J., and Guertin, D.A. (2014). Adipocytes arise from multiple lineages that are heterogeneously and dynamically distributed. Nature Communications *5*, 4099.

Seale, P., Bjork, B., Yang, W., Kajimura, S., Chin, S., Kuang, S., Scimè, A., Devarakonda, S., Conroe, H.M., Erdjument-Bromage, H., et al. (2008). PRDM16 controls a brown fat/skeletal muscle switch. Nature *454*, 961–967.

Thomson, J.A., Itskovitz-Eldor, J., Shapiro, S.S., Waknitz, M.A., Swiergiel, J.J., Marshall, V.S., and Jones, J.M. (1998). Embryonic stem cell lines derived from human blastocysts. Science *282*, 1145–1147.

Timmons, J.A., Wennmalm, K., Larsson, O., Walden, T.B., Lassmann, T., Petrovic, N., Hamilton, D.L., Gimeno, R.E., Wahlestedt, C., Baar, K., et al. (2007). Myogenic gene expression signature establishes that brown and white adipocytes originate from distinct cell lineages. Proc. Natl. Acad. Sci. U.S.a. *104*, 4401–4406.

Yao, T., and Asayama, Y. (2017). Animal - cell culture media: History, characteristics, and current issues. Reproductive Medicine and Biology *16*, 99–117.